Formulation and Application of a Quasi-Static Material Point Method

Von der Fakultät für Bau- und Umweltingenieurwissenschaften
der Universität Stuttgart
zur Erlangung der Würde eines Doktors der Ingenieurwissenschaften (Dr.-Ing.)
genehmigte Abhandlung,

vorgelegt von

LARS BEUTH

aus Langen

Hauptberichter:	Prof. Dr.-Ing. Pieter A. Vermeer
Mitberichter:	Prof. Dr.-Ing. Zdzisław Więckowski

Tag der mündlichen Prüfung: 14. Februar 2012

Institut für Geotechnik der Universität Stuttgart

2012

Keywords: Quasi-static Material Point Method, interface elements, cone penetration testing, Anisotropic Undrained Clay model

(D93 - Dissertation, Universität Stuttgart)

Preface

Large deformation analysis is a central challenge in many fields of geomechanics such as geohazards, offshore foundations, collision problems, land reclamation or internal erosion, erosion of riverbeds and coastal areas. In managing problems in these fields, the classical Finite Element Method (FEM) which is often the method of choice in small deformation analysis is of limited use due to mesh tangling and inherent problems associated with modelling separation, breakage and slipping. Other numerical techniques such as the Element-Free Galerkin method, Smooth Particle Hydrodynamics and the Discrete Element Method likewise have significant technical and practical problems associated with their use in large deformation analysis in geomechanics.

On considering the need to proceed with large deformation analyses, I considered it of relatively low risk to remain within the realm of finite element modelling and use techniques such as the Arbitrary Lagrangian-Eulerian method or the related Coupled Eulerian-Lagrangian method. Finally, it was decided to use the Material Point Method (MPM) which is also a FEM related approach as it had been tested successfully by many researchers. In fact, it had been successfully applied in the field of dynamics of solids and fluids, but not to quasi-static problems of geomechanics. The first aim of this dissertation study was thus to extend the MPM to large deformation analysis for quasi-static problems.

The second aim of this study is to apply the new quasi-static MPM to cone penetration testing (CPT). Quasi-static penetration tests are used to estimate properties such as the undrained shear strength of clay layers. Present correlations are based on experiments as well as numerical simulations, but so far all simulations were performed on the basis of an isotropic elastic-plastic constitutive model; either the Tresca model or the Von Mises one. In recent years, however, it has been recognised that natural clays are highly anisotropic which results in significant stress-path dependency of the undrained shear stress. As a consequence, different types of laboratory tests will also yield different undrained shear strengths and which one of these correlates to the tip resistance as measured in CPT. In order to answer this question Lars Beuth performed CPT simulations on the basis of an advanced clay model which accounts for anisotropy.

It was a great pleasure to me to advise Lars Beuth during this challenging study, in which he directly proved to be excellent in the field of Information Technology when setting up the computer code. Subsequently, this study required increasing knowledge of continuum mechanics. For this reason, it was of great importance to have Professor Zdzisław Więckowski from the University of Łódź in Poland as a second advisor to this study. In particular as he is one of the founding fathers of the MPM.

Pieter A. Vermeer
Delft, February 2012

Acknowledgments

I wish to express first of all my deep gratitude to Professor Pieter Vermeer for his extensive, invaluable and steadfast guidance, for his support and patience, sharing his knowledge and experience, throughout my PhD studies. Likewise, I thank Professor Zdzisław Więckowski for his expert advise and feedback as my co-supervisor throughout the time of my studies. I feel indebted to Plaxis B.V. and Deltares, who supported the ongoing research project through funding and expert advise. Here, I am very grateful to Peter van den Berg and Hans Teunissen of Deltares for their kind support of my work. The author would especially like to thank Paul Bonnier from Plaxis B.V. who was of great assistance in the research presented in this thesis.
Throughout the years, I benefited from the cooperative and friendly support, advise, guidance of many others. With this regard, I would like to express my gratitude to Professor Thomas Benz, Professor Minna Karstunen, Professor Christian Moormann, Professor Dieter Stolle, Klaas-Jan Bakker, Ronald Brinkgreve, Corné Coetzee and to longtime colleagues at the University of Stuttgart and Deltares. Amongst them are Johannes Aschrafi, Golaleh Bazzaz, Alba Yerro Colom, John van Esch, Wiep Hellinga, Maximilian Huber, Issam Jassim, Annette Lächler, Martino Leoni, Axel Möllmann, Hilde Aas Nøst, Jitse Pruiksma, Ruth Rose, Tan Shuhong, Nadja Springer, Zsolt Szilvágyi, Yixing Yuan, Bernd Zweschper. Of those mentioned here and many others whom I met during the exciting years of my PhD studies I maintain invaluable good memories. I am very grateful to my parents, to my brother and to friends of many years in Germany and the Netherlands, who gave me indispensable support through their company and advise.

The research leading to these results has received funding from the European Community's Seventh Framework Programme FP7/2007-2013 under grant agreement n° PIAG-GA-2009-230638 (Geo-Install).
Furthermore, the Polish Ministry of Science and Higher Education and the German Academic Exchange Service kindly contributed through funding to this PhD study.

Lars Beuth
Delft, January 2012

Contents

Abstract

This thesis is concerned with the analysis of quasi-static large deformation problems such as the jacking of piles where inertia and damping effects can be neglected, as opposed to dynamic problems such as pile driving. To this end, a novel type of Material Point Method (MPM) that is specifically adapted to the analysis of quasi-static large deformation problems is developed.

The quasi-static MPM can be considered as an extension of the classical Updated Lagrangian Finite Element Method (UL-FEM). As with the UL-FEM, a solid body is discretised by finite elements, but in addition, the solid body is discretised by a cloud of material points which moves through the mesh in the course of a computation. The movement of material points represents the arbitrary large deformations of the solid body. The FE grid is used as with the UL-FEM to compute incremental displacements and strain increments at the locations of material points. In contrast to the UL-FEM, the mesh can be reset into its original state or changed arbitrarily if accumulated distortions of the FE grid cause numerical inaccuracies. Material and state parameters of the solid body as well as applied loads are stored in material points. In contrast to most existing implementations of the MPM, the developed quasi-static variant makes use of implicit rather than explicit time integration, which allows for a considerable reduction of the computation time in case of quasi-static problems.

The development of the quasi-static MPM and its validation for simple benchmark problems is the first aim of this thesis. This includes the modelling of soil-structure interaction within the developed method, a feature that is essential to many geotechnical analyses. Here, the novel approach of extending interface elements commonly used in small-strain Finite Element analyses for use with the Material Point Method has been taken.

The application of the quasi-static MPM to the simulation of cone penetration testing (CPT) forms the second aim. This widely-used in-situ test consists of pushing a steel rod with a measuring device attached to its tip into the ground with constant velocity. Numerical analyses of cone penetration testing improve the understanding of involved mechanical processes and allow to refine existing or establish new correlations between CPT measurements and soil properties. In the frame of this thesis, cone penetration testing in undrained soft clay is considered with the aim of investigating the relation between the tip resistance and the undrained shear strength of clay. Here, a new soil model that takes into consideration the anisotropic strength of clay has been applied. Thereby, the undrained shear strength of clay and thus measurements of tip resistance are reproduced with a significantly higher accuracy than with previously performed numerical analyses reported so far in literature.

Zusammenfassung

Numerische Methoden bilden seit mehr als einem halben Jahrhundert ein unverzichtbares Werkzeug bei der Analyse hochkomplexer mechanischer Probleme. Bei dem Versuch, akurate Vorhersagen zu dem alltäglichen Vorgang des Eindrückens eines Stahlstabes in den Untergrund zu treffen, stößt man jedoch schnell an die Grenzen selbst der leistungsfähigsten, derzeit verfügbaren Softwarepakete. Die Bestimmung des Widerstandes des Stabes erfordert Kenntnis des sich in der Umgebung des Stabes bildenden Spannungsfeldes. Die Schwierigkeiten der Spannungsberechnung liegen in der Modellierung der nichtlinearen Spannungs-Dehnungs-Beziehung von Boden sowie der komplexen Verformungsprozesse, die der eindringende Stab im Untergrund auslöst.

Diese Dissertation befaßt sich vornehmlich mit Letzterem, der numerischen Analyse großer Verformungsprozesse. Es werden ausschließlich quasi-statische Problemstellungen betrachtet, Problemstellungen bei denen Trägheits- und Dämpfungseffekte vernachläßigt werden können, wie etwa bei dem Eindrücken eines Pfahls.

Zu diesem Zweck wurde eine speziell für die Analyse quasi-statischer geotechnischer Problemstellungen geeignete Variante der Material-Punkt-Methode entwickelt.

Die Material-Punkt-Methode (MPM) kann als Erweiterung der klassischen Updated-Lagrangian Finite-Elemente-Methode (UL-FEM) betrachtet werden. Sie verwendet wie die UL-FEM ein FE-Netz zur Diskretisierung eines Festkörpers. Zusätzlich wird bei der MPM der Festkörper durch eine Punktmenge abgebildet, die sich im Verlauf einer Berechnung durch das FE-Netz bewegt. Die Verschiebungen der Punkte, Materialpunkte genannt, bilden die beliebig großen Verformungen des Festkörpers ab. Das FE-Netz wird wie bei der UL-FEM zur Berechnung inkrementeller Verschiebungen und Dehnungen an den Positionen der Materialpunkte verwendet. Im Unterschied zur UL-FEM kann das Netz in seinen ursprünglichen unverformten Zustand zurückgesetzt oder neu generiert werden, sobald die akkumulierten Verzerrungen des FE-Netzes zu numerischen Ungenauigkeiten führen: Sämtliche Materialeigenschaften und Zustandsgrößen des Festkörpers wie auch Lasten werden in den Materialpunkten gespeichert.

In den Neunziger Jahren entwickelten Schreyer und Sulsky *et al.* die MPM für die Simulation dynamischer Verformungsprozesse von Festkörpern [15, 51–53]. Ihre Arbeit basiert auf der Particle-In-Cell-Methode welche in den Sechziger Jahren von Harlow für die Analyse von Problemen der Fluidmechanik entwickelt wurde [25]. Seit ihren Anfängen erfuhr die MPM zahlreiche, mächtige Erweiterungen um Membranstrukturen [69], die Modellierung granularen Materialverhaltens [2, 17, 67, 68] und die Modellierung des Kontakts zwischen Festkörpern [3]. In den vergangenen Jahren bewies die MPM ihre Leistungsfähigkeit durch vielfältige Anwendungen wie beispielsweise der Entleerung eines Silos [68], dem Ziehen eines Ankers [18] oder der Verformung von Eisschollen [54].

Mit einer Ausnahme [23] handelt es sich bei allen existierenden Implementierungen der MPM um Varianten, die für dynamische Problemstellungen entwickelt wurden und ein explizites Zeitintegrationsschema einsetzen. Da explizite Zeitintegration nur sehr kleine Zeitschritte erlaubt, sind diese Implementierungen jedoch für quasi-statische Problemstellungen ungeeignet. Die entwickelte quasi-statische Variante der MPM verwendet ein implizites Integrationsschema [8, 9]. Hierdurch wird die bei dynamischen Varianten bestehende Begrenzung der Schrittgröße umgangen.

Die numerische Analyse der meisten geotechnischen Problemstellungen erfordert die Modellierung des Kontaktes zwischen einem Bauteil und dem umgebenden Boden. Dies wird auch in dieser Dissertation berücksichtigt. Die Nähe der quasi-statischen MPM zur UL-FEM bietet den Vorteil, durch den Einsatz in moderner FE-Software bewährte Technologien auf die quasi-statische MPM übertragen zu können. Unter der Voraussetzung kleiner Verformungen werden in Finite-Elemente-Berechnungen häufig Interface-Elemente zur Modellierung von Boden-Bauwerk-Interaktion eingesetzt. In der hier vorgestellten Forschungsarbeit wurden diese speziellen Elemente für den Einsatz mit der MPM erweitert [64].

Eine Vielzahl weiterer Technologien, die in der FEM zum Einsatz kommen, wurden für die MPM nutzbar gemacht. Hierzu zählen Techniken zur numerischen Integration und zur iterativen Lösung des Systems von Gleichgewichtsbedingungen, Materialmodelle sowie Ein- und Ausgabefunktionalitäten.

Die Entwicklung der quasi-statischen MPM bildet den ersten Teil dieser Forschungsarbeit. Im zweiten Teil erfolgt die erste Anwendung der entwickelten Methode auf eine geotechnische Problemstellung. Die Wahl fiel auf die Simulation von Drucksondierungen (Cone Penetration Testing, abgekürzt CPT). Dieses weitverbreitete Sondierverfahren besteht darin, einen Stahlstab mit konstanter Geschwindigkeit in den Untergrund zu drücken. An dem Stabende angebrachte Kraftaufnehmer messen den Druck auf die konische Stabspitze sowie auf eine oberhalb der Spitze angebrachte Manschette. Die so aufgenommenen Daten erlauben eine Abschätzung der Festigkeits- und Steifigkeitseigenschaften sondierter Bodenschichten.

Die Simulation von Drucksondierungen ermöglicht es, bestehende Korrelationen zwischen Messwerten und Bodeneigenschaften zu verbessern und neue Korrelationen zu erstellen. Im Rahmen dieser Forschungsarbeit wurden Drucksondierungen in wassergesättigtem undrainierten Ton untersucht. Das Ziel ist, die Beziehung zwischen Spitzendruck und der undrainierten Scherfestigkeit von Ton zu untersuchen. Hierbei wurde im Unterschied zu bisherigen Studien ein Bodenmodell eingesetzt, das die Anisotropie der Festigkeiteigenschaften von Tonböden berücksichtigt.

Der Inhalt dieser Dissertation gliedert sich wie folgt:

Als Einleitung in die behandelte Thematik folgen in **Kapitel 2** grundlegende Erläuterungen zur numerischen Mechanik.

Die Formulierung der quasi-statischen MPM wird in **Kapitel 3** behandelt. Eine Reihe von Benchmark-Berechnungen werden präsentiert: die Verformungen eines Kragträgers und einer Böschung sowie die Verschiebung einer Stützwand.

In **Kapitel 4** werden die mit der quasi-statischen MPM verwendeten Interface-Elemente vorgestellt. Die Funktionsweise der Interface-Elemente wird anhand der Simulation des Gleitens eines Blockes über eine ebene Fläche sowie der Verformungen einer Böschung demonstriert.

Die Modellierung undrainierten Tons wird, soweit relevant für die durchgeführten Simulationen von Drucksondierungen, in **Kapitel 5** beschrieben. Im ersten Teil dieses Kapitels werden gängige Techniken der Modellierung undrainierten Tons vorgestellt. Hierbei werden drei Stoffmodelle für isotropen Ton betrachtet: das Mohr-Coulomb-Modell, das Tresca-Modell sowie das Modified-Cam-Clay-Modell. Anschließend wird die Modellierung anisotropen Tons behandelt. Der Schwerpunkt liegt auf dem neuen Anisotropic-Undrained-Clay-Modell (AUC-Modell), welches speziell für die Modellierung der anisotropen Scherfestigkeit undrainierten Tons entwickelt wurde.

Die durchgeführten Simulationen von Drucksondierungen werden in **Kapitel 6** präsentiert. Nach einer detaillierten Beschreibung der durchgeführten Berechnungen folgt die Darstellung der erhaltenen Berechnungsergebnisse. Die zuerst vorgestellten Ergebnisse wurden anhand des Tresca-Modells berechnet. Diese werden mit Ergebnissen früherer Studien verglichen. Im nächsten Abschnitt werden anhand des Mohr-Coulomb-Modells erhaltene Ergebnisse präsentiert. Schließlich werden die Ergebnisse einer Berechnung vorgestellt, bei denen das AUC-Modell eingesetzt wurde, und mit Ergebnissen verglichen, die auf dem Mohr-Coulomb-Modell basieren.

Diese Dissertation schließt mit einem Ausblick auf mögliche weitere Arbeiten an der entwickelten quasi-statischen MPM und deren möglichen Anwendungen in **Kapitel 7**.

Chapter 1

Introduction

Since their first application in the middle of the last century, computational methods have evolved in engineering disciplines into an indispensable tool for analysing mechanical problems of ever increasing complexity. Yet, one still reaches the limits of the most advanced present-day software when trying to make accurate predictions on the common act of pushing a steel bar into soil. Determining the resistance of the bar requires not only knowledge of material properties, but also of the evolving stress field surrounding the bar. Predicting these stresses requires to take into account the highly non-linear stress-strain relationship of soil, as well as the complex deformation processes imposed by the bar on the surrounding soil. This thesis is mostly concerned with the latter, i.e. the proper reproduction of large deformations within soil in numerical analyses of geomechanical problems. Here, the focus lies on quasi-static problems where inertia and damping effects can be neglected. Present numerical approaches that are used for such analyses may be classified into three categories: Lagrangian, Eulerian and Arbitrary Lagrangian-Eulerian methods.

With Lagrangian methods, the numerical representation of a solid body, in any form whatsoever, is tied to the particles of the solid. Thus, the numerical representation follows the motion of the deforming body as if etched into the material. The widely-used Updated Lagrangian Finite Element Method falls under this category. Here, a deforming solid is subdivided by finite elements that are spanned by nodes. Interpolating functions which map data such as displacements between nodes and points in the interior of finite elements, as well as integration and differentiation over the volume or surface of a solid body, are well-defined on the basis of the underlying mesh. The boundary of the solid body is clearly defined through the mesh boundary which allows for an easy and accurate application of boundary conditions. However, the finite element grid might experience distortions which lead to numerical inaccuracies and can even render the calculation impossible.

Apart from this mesh-based Lagrangian method, various methods have been developed throughout the last decades that do without a mesh. With meshless Lagrangian methods a solid is described by a point set rather than a finite element grid. Each point represents a subregion of the deforming solid. The well-known Smooth Particle Hydrodynamics belongs to this category. A survey of meshless methods can be found, for example, in [6, 37, 38]. Meshless methods circumvent the problem of mesh distortions, but score badly with regard to the accurate application of boundary conditions and numerical integration. They also possess the disadvantage that the point set might not properly represent the considered solid body: if the density of the point set reduces

due to deformations, non-physical gaps might occur within the discretised solid body, numerical integration might become inaccurate or fail entirely in certain regions of the solid.

With Eulerian methods it is not a solid body that is subdivided into finite elements but the region of space it is moving through. This approach can be visualised by means of a grid that is etched into a glass pane with the material moving along the pane. Snapshots of a deforming solid body are taken at fixed positions in space. The Finite Volume Method is an example of a mesh-based Eulerian approach.

With Eulerian methods one may assess at a certain time the velocity or temperature change that a particle experiences when passing by a grid node or the amount of material that crosses an element boundary. However, it is not possible to determine from such computations, where a certain particle will be located or what temperature it has at a certain time. In contrast, Lagrangian methods do allow to trace state variables such as temperature or stresses throughout a computation for a certain particle of a solid because discretisation and solid body are tied together. With soil as with any solid, equilibrium equations are formulated with respect to the material rather than a region of space. Therefore, Lagrangian methods are more suited for geotechnical problems than Eulerian methods.

With Arbitrary Lagrangian-Eulerian (ALE) methods, the equilibrium equations are solved on the basis of a deforming mesh as with the UL-FEM. However, the displacements of nodes do not necessarily coincide with the movements of particles of the solid body throughout a computation. If mesh distortions become too large, nodes might be uncoupled from the particles that they follow. Thus, particles of the solid body — its state or material parameters — move relative to the nodes of the mesh, which corresponds to an Eulerian approach. The development of this concept goes back to the works of Hughes *et al.* [31], Donea [22] and Liu *et al.* [39]. Numerous implementations of this concept exist. Differences between them lie in the way how nodal coordinates are updated and in the mapping of state and material parameters from initial to new node locations. Nodes might be reset or the mesh might be regenerated, the interpolation might be performed on the basis of a global or local interpolation procedure.

In the frame of this thesis, the approach of the Material Point Method has been followed. This method belongs to the group of ALE methods. A distinct feature of the MPM is that it not only makes use of a finite element mesh as other ALE methods but also of a cloud of points, called material points, that move through the grid. These material points represent as with meshless Lagrangian methods subregions of a solid body and not individual particles such as sand grains. The movements of material points represent the deformations of the solid. They carry all properties and state parameters of the solid as well as external loads. The computational grid is used to determine incremental displacements and strain increments at material points as with the UL-FEM but it stores no permanent information. As with other ALE methods the mesh can be reset, moved or changed arbitrarily.

In the 1990s, Schreyer and Sulsky *et al.* developed the MPM for the simulation of dy-

namic deformation processes of solid bodies [15, 51–53]. Their work is based on the Particle-In-Cell Method which was devised in the 1960s by Harlow for the analysis of problems of fluid dynamics [25]. The applicability of the MPM has been extended considerably in recent years by including membrane structures [69], flow of granular material [2, 17, 67, 68] and contact between solid bodies [3]. It proved its potential through a wide range of applications such as silo discharge [68], anchor pull-out [18] and sea-ice dynamics [54].

With one exception [23], existing implementations of the MPM are dynamic codes that employ an explicit time integration scheme. Using these codes for the analysis of quasi-static problems is computationally inefficient as explicit integration requires very small time steps. The variant of the MPM that has been developed in the frame of this thesis for the analysis of geomechanical problems makes use of an implicit integration scheme and thus circumvents the limitation on step size of dynamic codes [8].

The closeness of the quasi-static MPM to the UL-FEM allows to reuse well-proven, sophisticated technologies applied in present-day FEM codes. Ample use has been made of this advantage, which reflects in nearly all chapters of this thesis. They relate to numerical integration as also reported in [9], solving the system of equilibrium equations, the modelling of soil-structure interaction as published in [64], constitutive modelling as well as pre- and post-processing.

The arrangement of the contents of this thesis is as follows: At first, a basic introduction to computational mechanics is given in **Chapter 2**. Subsequently, the formulation of the quasi-static MPM and a series of benchmark problems is presented in **Chapter 3**. The formulation of the interface elements used with the quasi-static MPM and their validation is presented in **Chapter 4**.

Soil modelling of undrained clay as relevant to the performed simulations of cone penetration testing is presented in **Chapter 5**. In the first part of this chapter, typical features of the modelling of undrained clay behaviour are reviewed. Here, constitutive models for isotropic clay are considered; the Mohr-Coulomb model, the Tresca model and the Modified Cam Clay model. Subsequently, the modelling of anisotropic clay is treated. Attention is focussed on the new Anisotropic Undrained Clay (AUC) model which has been specifically developed for the accurate simulation of the anisotropic shear strength of undrained natural clay.

The simulation of cone penetration testing is presented in **Chapter 6**. After a detailed description of the setup of the numerical analyses, results are presented in three steps. At first, results obtained with the Tresca model are presented and compared to results of previous studies. Afterwards, results for computations with the Mohr-Coulomb and the AUC model are presented and evaluated.

This dissertation concludes with an outlook on possible further works on and with the developed quasi-static MPM in **Chapter 7**.

Chapter 2

Introduction to computational mechanics of solids and structures

Computational mechanics of solids and structures focusses on the approximation of partial differential equations by a set of algebraic equations which involves tensor and matrix operations. In this chapter, the ordinary differential equation of a simple spring-mass-system is considered, so that tensor and matrix operations are avoided. In this manner, basic concepts of this thesis are explained for a relatively wide group of readers.

With the help of the simple spring-mass-system, the following two aspects of numerical analysis that are relevant to the formulation of the quasi-static MPM are presented. At first, implicit and explicit time integration are described in Section 2.1. Subsequently, non-linear quasi-static problems are treated in Section 2.2. Section 2.3 provides a brief introduction to large deformation theory, a matter which is essential to the mechanical problems treated in this thesis, by means of another simple mechanical system. The subjects of space-discretisation and numerical integration with respect to space are left out as scalar problems are considered. For in-depth presentations of the subjects treated here, the reader is referred to [7], [57], [44] and [42].

For the considered spring-mass-system illustrated in Figure 2.1, the spring elongation $x(t)$ can be simply computed from an analytical solution for the equation of motion

$$m\,\ddot{x} \;=\; -k\,x \;+\; b \tag{2.1}$$

with k being the spring stiffness with units [N/m]. The mass m is attached to a weightless spring and is loaded by an external force b, for example a gravitational force mg. The two superposed dots denote the second derivative with respect to time. For most problems encountered in geomechanics, however, analytical solutions are not available due to the complexity of the involved geometry, material behaviour, loading and deformation processes. Numerical analyses are used instead.

2.1 Implicit versus explicit time integration

With numerical analyses, discrete values are determined for the unknown function $x(t)$ at times $t, t+\Delta t$, etc. Such discretisation with respect to time can be performed either by an explicit or implicit integration scheme. In case of **explicit time integration**, the spring elongation at time $t+\Delta t$ is determined from consideration of the state of the system at time t. The equation of motion thus takes the form

$$m\,\ddot{x}^t \;=\; -k\,x^t \;+\; b^t \tag{2.2}$$

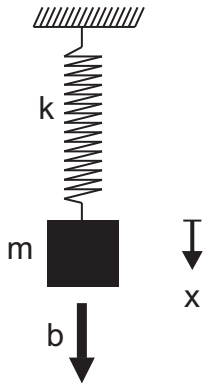

Figure 2.1: Schematic illustration of a spring-mass-system

where the notation of a superscript t is used to indicate a discrete value at time t rather than a function of time. At first, the acceleration at time t is computed from Equation 2.2

$$\ddot{x}^t \;=\; m^{-1}\,\left(-k\,x^t \;+\; b^t\right) \tag{2.3}$$

The elongation of the spring at time $t + \Delta t$ is then determined from the known velocity and acceleration at time t by means of the finite difference approximations for velocity and accleration

$$\dot{x}^{t+\Delta t} \;\approx\; \dot{x}^t \;+\; \Delta t\,\ddot{x}^t \quad \text{and} \quad x^{t+\Delta t} \;\approx\; x^t \;+\; \Delta t\,\dot{x}^t \tag{2.4}$$

In the second equation, the velocity $\dot{x}^{t+\Delta t}$ may also be used instead of $\dot{x}^t$.

In contrast, with **implicit time integration**, the solution for $t + \Delta t$ is obtained by considering the initially unknown state of the system at time $t + \Delta t$ rather than at time t

$$m\,\ddot{x}^{t+\Delta t} \;=\; -k\,x^{t+\Delta t} \;+\; b^{t+\Delta t} \tag{2.5}$$

Likewise, the finite difference approximations for velocity and acceleration are considered at time $t + \Delta t$

$$\dot{x}^{t+\Delta t} \;\approx\; \dot{x}^t \;+\; \Delta t\,\ddot{x}^{t+\Delta t} \quad \text{and} \quad x^{t+\Delta t} \;\approx\; x^t \;+\; \Delta t\,\dot{x}^{t+\Delta t} \tag{2.6}$$

With Equations 2.6 the spring elongation at time $t + \Delta t$ can be expressed as

$$x^{t+\Delta t} \;=\; x^t \;+\; \Delta t\,\dot{x}^t \;+\; \Delta t^2\,\ddot{x}^{t+\Delta t} \tag{2.7}$$

Introducing Equation 2.7 into Equation 2.5 renders

$$m\,\ddot{x}^{t+\Delta t} \;=\; -k\,\left(\,x^t \;+\; \Delta t\,\dot{x}^t \;+\; \Delta t^2\,\ddot{x}^{t+\Delta t}\,\right) \;+\; b^{t+\Delta t} \tag{2.8}$$

Rearranging for $\ddot{x}^{t+\Delta t}$ gives

$$\ddot{x}^{t+\Delta t} \;=\; \left(\,m \;+\; \Delta t^2 k\,\right)^{-1}\,\left[\,-k\,\left(\,x^t \;+\; \Delta t\,\dot{x}^t\,\right) \;+\; b^{t+\Delta t}\,\right] \tag{2.9}$$

which allows to compute the spring elongation $x^{t+\Delta t}$ through two integration steps by means of Equations 2.6.

The **advantages and disadvantages** of the above two time integration schemes become obvious when considering their application to problems with more than one degree of freedom. In this case, the terms x and b are vectors and k and m are matrices, in the following denoted by bold uppercase letters.

Implicit time integration requires inversion of the matrix that is assembled from matrices $\mathbf{M}$ and $\mathbf{K}$ for each time step, which renders this approach expensive with respect to both computation time and memory consumption. In contrast, computation of an explicitly integrated time step can be performed with considerably less effort. The reason is that it is generally possible to turn matrix $\mathbf{M}$ through lumping into a diagonal matrix without significant loss of accuracy. Thus, inversion of this matrix and the consequent computation of acceleration, velocity and spring elongation is trivial.

Explicit time integration is conditionally stable, which means that a reasonably accurate solution can be obtained for each time step as long as the size of time steps lies below a limit value, the so-called critical time step. With mesh-based numerical methods such as the UL-FEM, the critical time step size depends on the dimensions of the smallest finite element and the speed of waves travelling through the discretised continuum. The latter in turn depends on the mass and stiffness of the material. Thus, the finer the finite element grid and the stiffer the discretised material, the smaller the critical time step. Implicit time integration is unconditionally stable, there is no limitation on the step size.

With the formulation of the MPM presented in this thesis, implicit integration is used. As loading processes are considered that extend over long periods of time, an integration scheme that limits the size of time steps would obviously be of disadvantage.

2.2 Non-linear versus linear quasi-static mechanical problems

In case of mechanical problems that involve slow loading and consequently slow deformation processes, effects of inertia can be neglected. The right hand side term of Equation 2.5 can then be set to zero. This renders the quasi-static equilibrium equation $k\,x = b$, where b may be time dependent. For this linear problem, obtaining the spring elongation of the spring-mass-system for a load b is trivial.

However, many mechanical problems exhibit a non-linear relation between loading and deformations which renders the solution more difficult. Non-linearity is introduced to mechanical problems either by a change of geometry, i.e. geometric non-linearity, or through dependence of material properties of a continuum on state variables such as stresses and strains, i.e. material non-linearity. A quasi-static problem that exhibits geometric non-linearity will be considered in the next section.

Material non-linearity can be easily introduced to the aforementioned spring-mass-system by making the spring stiffness dependent on the spring elongation x. This exam-

ple will be used in the following to elaborate on the solution of non-linear quasi-static problems. Figure 2.2 shows the spring elongation plotted over the applied load for the three cases of k remaining constant, increasing and decreasing with elongation of the spring.

With non-linear problems, finding the spring elongation for which the spring force is in equilibrium with a specific applied load b requires finding the root from the equation $g(x) = x\,k(x) - b = 0$. In general, an iterative method is needed to find the spring elongation x for which $g = 0$. Ortega and Rheinboldt [44] describe a very simple method which they refer to as the parallel-chord method. This method approximates the root of g starting from an initial guess x^0 by replacing g at x^0 by a linear function h with slope κ

$$h(x) = g\left(x^0\right) + \kappa\left(x - x^0\right) \tag{2.10}$$

Setting h to zero gives

$$x = x^0 - \kappa^{-1}\, g\left(x^0\right) \tag{2.11}$$

The obtained value x forms a closer approximation of the root as illustrated in Figure 2.3 (left). Repeating this approximation of the root by using x as new approximation renders

$$x^{j+1} = x^j - \frac{g\left(x^j\right)}{\kappa^j} \tag{2.12}$$

where the superscript j denotes the iteration number. Iterations are continued until the value of g, the difference between spring force and applied load, lies below a threshold value. For the first iteration, x^j may be chosen as zero. Using the derivative $\frac{dg}{dx}$ of g at x^0 as the slope κ for all iterations j corresponds to a simplified, also called modified Newton-Raphson method [44]. Figure 2.3 (left) illustrates the method, which is used with the quasi-static MPM presented in the following chapter.

Alternatively, κ can be updated for each iteration j to the tangent of g at x^j as shown in Figure 2.3 (right). This is known as the regular or full Newton-Raphson method. Clearly, the former approach possesses the disadvantage of slower convergence. However, when considering a matrix $\boldsymbol{\kappa}$ instead of a scalar κ, the inversion of this matrix is only performed once which reduces computation time considerably.

Solving geomechanical problems requires an incremental approach. Here, in terms of the treated spring-mass-system, equilibrium points (x, b) are determined for successively applied load increments Δb. Soil exhibits a path-dependent stress-strain relation: a stress state not only depends on the magnitude of straining but also on the sequence in which strain increments occur. Thus, obtaining accurate results requires proper reproduction of the straining history as possible with an incremental approach.

The Newton-Raphson procedure then starts at a previously computed equilibrium point (x, b) rather than at $x^0 = 0$ as illustrated in Figure 2.3 (right).

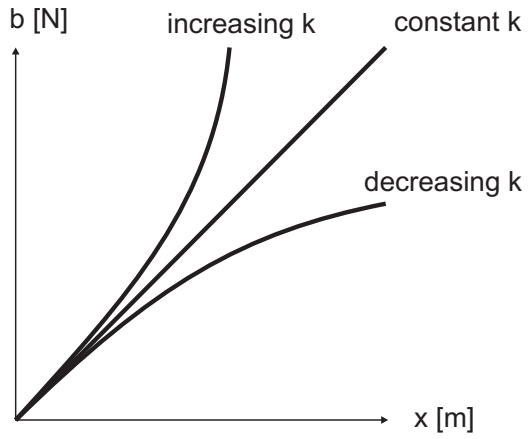

Figure 2.2: Load-displacement curves for a spring-mass-system with dependence of stiffness k on spring elongation

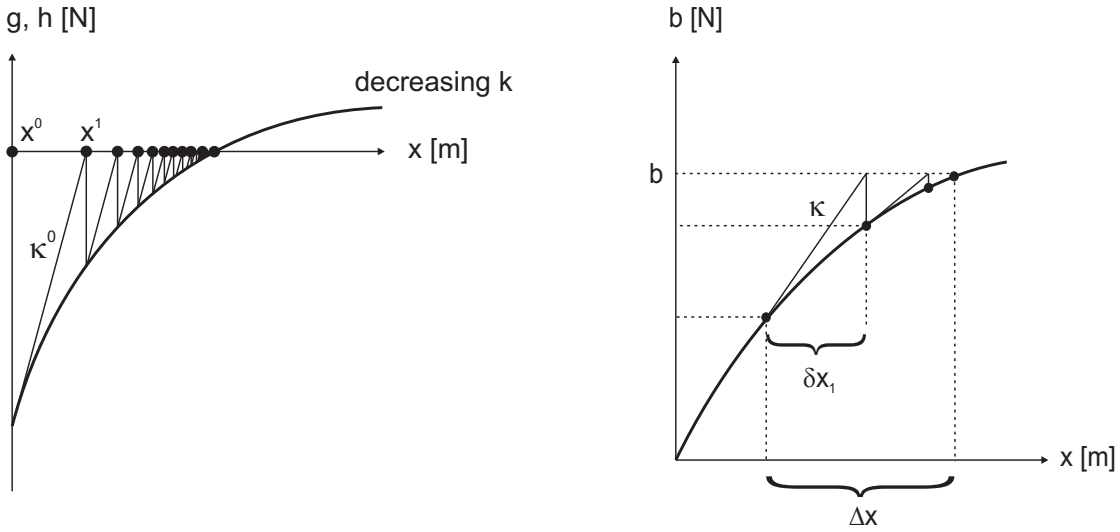

Figure 2.3: (left) Simplified Newton-Raphson method; (right) regular Newton-Raphson method for a load increment

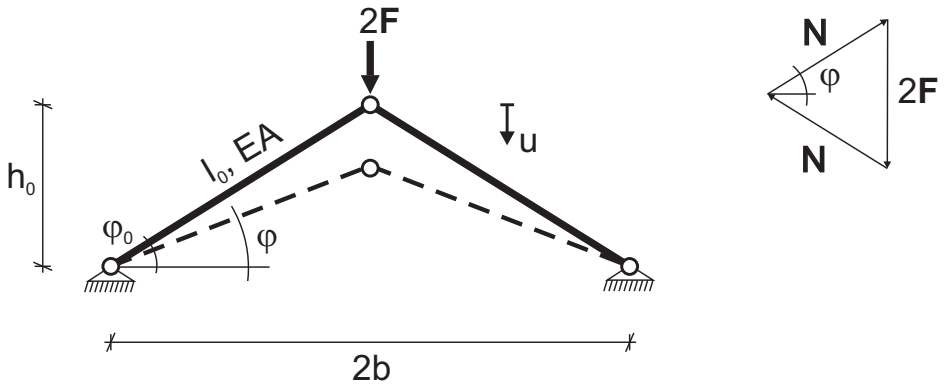

Figure 2.4: System of two bars exhibiting a non-linear relationship between forces and applied load due to a change of geometry

2.3 Geometric non-linearity

In the following, the quasi-static system depicted in Figure 2.4 is considered. A vertical load of $2F$ is applied at the top joint of two bars. E denotes the Young's modulus of the bars and A their cross sectional area. It is assumed that the two inclined bars will experience changes in length Δl but no bending due to the applied load. Compression of the bars thus only results in axial stresses σ. The forces in the bars N can be computed from simple equilibrium considerations

$$N = -\frac{F}{\sin\phi} \qquad \text{with} \quad \sin\phi = \frac{h_0 - u}{l} \tag{2.13}$$

where l written without subscript denotes the length of the bars for a certain vertical displacement u of the top joint. The forces in the bars relate to the relative change of length of the bars by

$$N = EA\,\frac{\Delta l}{l_0} \tag{2.14}$$

Combining Equations 2.13 and 2.14 renders the following cubic relationship between the vertical displacement of the top joint u and the applied force F

$$F = -EA\,(h_0 - u)\,\frac{l - l_0}{l\,l_0} \quad \text{with} \quad l^2 = b^2 + (h_0 - u)^2 \tag{2.15}$$

It should be noted that in the presented solution higher-order terms of the non-linear relation between forces N and the change of length of the bars are neglected for simplification. However, the overall mechanical behaviour of the truss-system is reproduced with sufficient accuracy by the simplified solution for the illustration of geometric non-linearity.

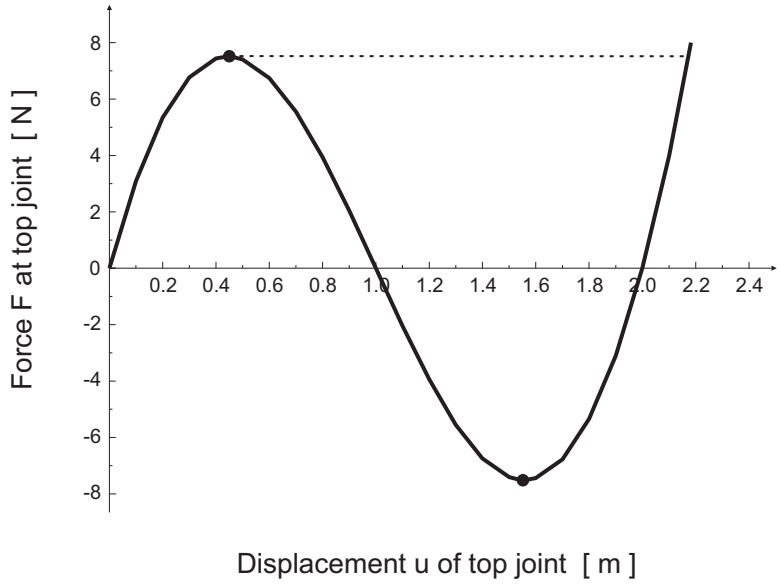

Figure 2.5: Load-displacement curve for the top joint of the truss-system

Figure 2.5 shows the load-displacement curve for the top joint of the truss-system for $E = 100$ kN/m^2, $A = 1$ m^2, $h_0 = 1$ m, $l_0 = \sqrt{2}$ m and $b = 1$ m. Clearly, a linear increase of the external load does not lead to a linear change of displacement u. In the range $0 \leq u \leq 2h_0$ the tangent stiffness $\frac{dF}{du}$ to the load-displacement curve varies between 31 and -21 N/m.

Dots mark so-called limit points at which the tangent stiffness is zero. Between the limit points, the tangent stiffness is negative, which corresponds to softening. Beyond the second limit point, hardening sets in. Under load-control, the system exhibits a snap-through instability. After applying a load that corresponds to the first limit point, the truss-system will snap through dynamically along the dashed line to an equilibrium state for the same load at $u \approx 2.2$ m. Under displacement-control, the top joint obviously follows the entire load-displacement curve. Here, for $u < h_0$, the bars are under compression, beyond $u = h_0$, the bars experience tension and, accordingly, the force F changes orientation.

One can easily see that the tangent stiffness is a function of u. In the range of small displacements of the joint of up to ≈ 10 cm, this dependency is negligible and the response of the system to loading can be described with reasonable accuracy by a linear relation. However, in case of large deformations, modelling the response of the system to loading requires consideration of the change of geometry.

A limit value for deformations, beyond which the change of geometry must be considered when analysing a mechanical problem cannot be uniquely defined. Generally speaking, effects of large deformations must be considered at strains beyond approximately 5 percent.

Chapter 3

Formulation of the quasi-static Material Point Method

The Material Point Method can be considered as a variant of the Finite Element Method. As with the latter method, the final system of equations of the MPM is derived by the discretisation of the virtual work equation with respect to time and space as presented in the first 3 sections of this chapter. These sections apply identically to both the FEM and MPM. The additional discretisation by means of material points that is specific to the MPM is described in Section 3.5. In the succeeding Section 3.6 the numerical integration is treated. The iterative procedure used to solve the non-linear system of equilibrium equations for a load increment is presented in Section 3.7. Section 3.8 provides an overview of the MPM calculation process.

This chapter concludes with the presentation of benchmark problems. In the first benchmark, the MPM solution is compared with FEM results for a large deformations problem involving only relatively small strains. Thereafter, results for large strain geomechanical problems of a slope stability and retaining wall are presented.

3.1 Virtual work formulation of the quasi-static problem

The following notation will be used. Let σ_{ij} and τ_{ij} denote the Cauchy and Kirchhoff stress tensors, respectively, and let v_i denote the velocity vector, while d_{ij} and $\dot{\omega}_{ij}$ represent the rate-of-deformation and spin tensors, defined as

$$d_{ij} \;=\; \frac{1}{2}\left(v_{i,j} + v_{j,i}\right) \qquad\qquad \dot{\omega}_{ij} \;=\; \frac{1}{2}\left(v_{i,j} - v_{j,i}\right) \tag{3.1}$$

respectively, where the superposed dot implies a material time derivative and the comma in $(\cdot)_{,i}$ denotes a partial derivative with respect to coordinate x_i.

Assuming that the reference and current configurations coincide instantaneously, the incremental form of the principle of virtual work for dead loading can be written as [43]

$$\int_V \left(\overset{\nabla}{\tau}_{ij}\, \delta d_{ij} - \sigma_{ij}\, \delta(d_{ik}\, d_{kj} \;-\; \frac{1}{2}\, v_{k,i}\, v_{k,j}) \right) \mathrm{d}V \;=\; \int_V \dot{b}_i\, \delta v_i \,\mathrm{d}V \;+\; \int_{S_t} \dot{t}_i\, \delta v_i \,\mathrm{d}S \tag{3.2}$$

which is valid for an arbitrary vector, δv_i, satisfying homogeneous kinematic boundary conditions vanishing on the part of the boundary surface where displacements are prescribed. Vectors $\dot{b}_i$ and $\dot{t}_i$ correspond to body forces and tractions, respectively. V is the

volume of the body, the part of the boundary with prescribed tractions is denoted as S_t. The co-rotational rate of the Kirchhoff stress tensor, $\overset{\nabla}{\tau}_{ij}$, is related to the Cauchy stress tensor by [27]

$$\overset{\nabla}{\tau}_{ij} \;=\; \overset{\nabla}{\sigma}_{ij} + \sigma_{ij}\, d_{kk} \tag{3.3}$$

where the Jaumann rate of the Cauchy stress tensor is defined as

$$\overset{\nabla}{\sigma}_{ij} \;=\; \dot{\sigma}_{ij} - \dot{\omega}_{ik}\, \sigma_{kj} + \sigma_{ik}\, \dot{\omega}_{kj} \tag{3.4}$$

The constitutive relation is written in hypoelastic form as

$$\overset{\nabla}{\tau}_{ij} \;=\; D_{ijkl}\, d_{kl} \tag{3.5}$$

where D_{ijkl} denotes the constitutive tensor.

3.2 Time discretisation

The quasi-static problem being considered is solved in an incremental way, i.e. the solution is found for a number of finite time steps. Considering an arbitrary step, stress, strain and displacement increments are denoted as

$$\Delta\overset{\nabla}{\tau}_{ij} \;=\; \overset{\nabla}{\tau}_{ij}\Delta t + h.o.t. \qquad \Delta\varepsilon_{ij} \;=\; d_{ij}\Delta t + h.o.t. \qquad \Delta u_i \;=\; v_i\Delta t + h.o.t. \tag{3.6}$$

where the symbol Δ is used to indicate finite differences, u_i denotes the displacement vector and $h.o.t.$ stands for higher-order terms, which originate from geometric non-linearity within a time step. Virtual displacements are denoted as δu_i and $\delta\varepsilon_{ij}$ are virtual strains. The virtual work equation 3.2 can now be written as

$$\begin{aligned}\int_V \left(\Delta\overset{\nabla}{\tau}_{ij}\,\delta\varepsilon_{ij} - \sigma_{ij}\,\delta(\Delta\varepsilon_{ik}\,\Delta\varepsilon_{kj} \;-\frac{1}{2}\,\Delta u_{k,i}\,\Delta u_{k,j})\right)\mathrm{d}V \;+\; h.o.t. \;=\\ \int_V \Delta b_i\,\delta u_i\,\mathrm{d}V \;+\; \int_{S_t} \Delta t_i\,\delta u_i\,\mathrm{d}S\end{aligned} \tag{3.7}$$

Here, V refers to the configuration at the beginning of the time step Δt. Similarly, the stresses σ_{ij} denote stresses at the end of the previous time step. Additional higher-order terms originate from material non-linearity by writing

$$\Delta\overset{\nabla}{\tau}_{ij} \;=\; D_{ijkl}\Delta\varepsilon_{kl} + h.o.t. \tag{3.8}$$

This equation can now be inserted into Equation 3.7 to obtain

$$\begin{aligned}\int_V (D_{ijkl}\,\Delta\varepsilon_{kl}\,\delta\varepsilon_{ij} + \sigma_{ij}\,\Delta u_{k,i}\,\delta u_{k,j} - 2\,\sigma_{ik}\,\Delta\varepsilon_{kj}\,\delta\varepsilon_{ij})\,\mathrm{d}V \;+\; h.o.t. \;=\\ \int_V \Delta b_i\,\delta u_i\,\mathrm{d}V \;+\; \int_{S_t} \Delta t_i\,\delta u_i\,\mathrm{d}S\end{aligned} \tag{3.9}$$

In quasi-static analyses of elastoplastic solids it is efficient not to neglect the higher-order terms and to apply relatively large time steps with equilibrium iterations, as also done in this study. In fact, elastoplastic stress-strain relationships will be integrated implicitly, giving significant non-linearity within a time step.

3.3 Space discretisation

With both the FEM and MPM, a computational mesh is used for arriving at the system of equilibrium equations. Referring to this computational mesh, the interpolation functions, $\boldsymbol{N}$, the degrees of freedom, $\Delta\boldsymbol{a}$, and the displacement increment vector, $\Delta\boldsymbol{u}$, are related by the equation

$$\Delta\boldsymbol{u}(x_1, x_2, x_3) \;=\; \boldsymbol{N}(\xi, \eta, \zeta)\, \Delta\boldsymbol{a} \tag{3.10}$$

where

$$\Delta\boldsymbol{u} \;=\; \left[\; \Delta u_1 \quad \Delta u_2 \quad \Delta u_3 \;\right]^{\mathrm{T}} \qquad \Delta\boldsymbol{a} \;=\; \left[\; \Delta a_{11} \quad \Delta a_{12} \quad \Delta a_{13} \quad \Delta a_{21} \quad \ldots \quad \Delta a_{n3} \;\right]^{\mathrm{T}} \tag{3.11}$$

and the coordinates ξ, η and ζ refer to the local coordinate system of the used finite elements. With regard to the definition of the components Δa_{ij} of $\Delta\boldsymbol{a}$, the first index denotes the number of the node and the second one the number of the coordinate, with n being the number of (active) nodes in the mesh. Likewise, the global coordinates $\boldsymbol{x}$ of a point inside an element can be computed from nodal coordinates $\boldsymbol{X}$ by means of

$$\boldsymbol{x} \;=\; \boldsymbol{N}\,\boldsymbol{X} \tag{3.12}$$

Matrix $\boldsymbol{N}$ takes the form

$$\begin{bmatrix} N_1 & 0 & 0 & N_2 & 0 & 0 & \ldots & N_n & 0 & 0 \\ 0 & N_1 & 0 & 0 & N_2 & 0 & \ldots & 0 & N_n & 0 \\ 0 & 0 & N_1 & 0 & 0 & N_2 & \ldots & 0 & 0 & N_n \end{bmatrix}$$

The components N_i are specified in Appendix A for the isoparametric elements used in this study along with the respective geometry and local coordinate system. In this thesis, 15-noded prismatic, 10-noded tetrahedral elements with quadratic interpolation of displacements as well as 4-noded tetrahedral elements with linear interpolation of displacements have been used (see Figure 3.1).

As common in the finite element literature, stress and strain increments are written using matrix notation

$$\begin{aligned} \boldsymbol{\sigma} \;&=\; \left[\; \sigma_{11} \quad \sigma_{22} \quad \sigma_{33} \quad \sigma_{23} \quad \sigma_{13} \quad \sigma_{12} \;\right]^{\mathrm{T}} \\ \Delta\boldsymbol{\varepsilon} \;&=\; \left[\; \Delta\varepsilon_{11} \quad \Delta\varepsilon_{22} \quad \Delta\varepsilon_{33} \quad 2\,\Delta\varepsilon_{23} \quad 2\,\Delta\varepsilon_{13} \quad 2\,\Delta\varepsilon_{12} \;\right]^{\mathrm{T}} \end{aligned} \tag{3.13}$$

Thus the strain increment vector and its variation can be expressed as

$$\Delta\boldsymbol{\varepsilon} \;=\; \boldsymbol{B}\,\Delta\boldsymbol{a} \qquad \delta\boldsymbol{\varepsilon} \;=\; \boldsymbol{B}\,\delta\boldsymbol{a} \tag{3.14}$$

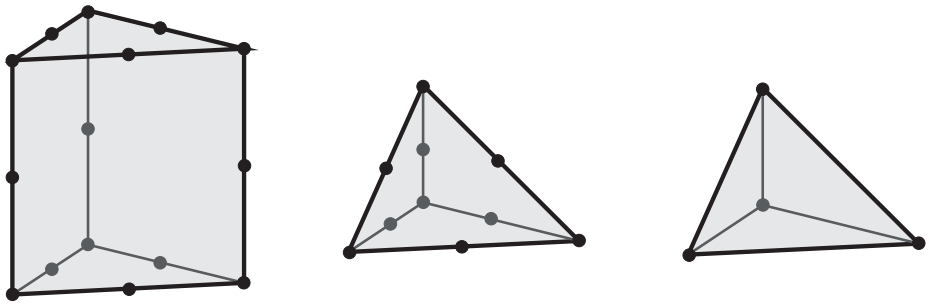

Figure 3.1: Used elements; (left) 15-noded prismatic element; (center) 10-noded tetrahedral element; (right) 4-noded tetrahedral element

where $\boldsymbol{B}$ is the strain-displacement matrix defined as

$$\begin{bmatrix} \frac{\partial N_1}{\partial x_1} & 0 & 0 & \dots & \frac{\partial N_n}{\partial x_1} & 0 & 0 \\ 0 & \frac{\partial N_1}{\partial x_2} & 0 & \dots & 0 & \frac{\partial N_n}{\partial x_2} & 0 \\ 0 & 0 & \frac{\partial N_1}{\partial x_3} & \dots & 0 & 0 & \frac{\partial N_n}{\partial x_3} \\ \frac{\partial N_1}{\partial x_2} & \frac{\partial N_1}{\partial x_1} & 0 & \dots & \frac{\partial N_n}{\partial x_2} & \frac{\partial N_n}{\partial x_1} & 0 \\ 0 & \frac{\partial N_1}{\partial x_3} & \frac{\partial N_1}{\partial x_2} & \dots & 0 & \frac{\partial N_n}{\partial x_3} & \frac{\partial N_n}{\partial x_2} \\ \frac{\partial N_1}{\partial x_3} & 0 & \frac{\partial N_1}{\partial x_1} & \dots & \frac{\partial N_1}{\partial x_3} & 0 & \frac{\partial N_1}{\partial x_1} \end{bmatrix}$$

Substituting Equations 3.10 to 3.14 into Equation 3.9 gives the equation

$$\delta \boldsymbol{a}^T (\boldsymbol{K} + \boldsymbol{K}^g)\, \Delta \boldsymbol{a} \;+\; h.o.t. \;=\; \delta \boldsymbol{a}^T \Delta \boldsymbol{F} \tag{3.15}$$

As this equation holds for any kinematically admissible displacement variation, it can be written as

$$(\boldsymbol{K} + \boldsymbol{K}^g)\, \Delta \boldsymbol{a} \;+\; h.o.t. \;=\; \Delta \boldsymbol{F} \tag{3.16}$$

Here,

$$\Delta \boldsymbol{F} \;=\; \int_V \boldsymbol{N}^{\mathrm{T}}\, \Delta \boldsymbol{b}\, \mathrm{d}V \;+\; \int_{S_t} \boldsymbol{N}^{\mathrm{T}}\, \Delta \boldsymbol{t}\, \mathrm{d}S \tag{3.17}$$

and

$$\boldsymbol{K} \;=\; \int_V \boldsymbol{B}^{\mathrm{T}}\, \boldsymbol{D}\, \boldsymbol{B}\, \mathrm{d}V \qquad\qquad \boldsymbol{K}^g \;=\; \int_V (\boldsymbol{B}_n^{\mathrm{T}}\, \tilde{\boldsymbol{\sigma}}\, \boldsymbol{B}_n - 2\, \boldsymbol{B}^{\mathrm{T}}\, \tilde{\tilde{\boldsymbol{\sigma}}}\, \boldsymbol{B})\, \mathrm{d}V \tag{3.18}$$

Vectors $\Delta \boldsymbol{b}$ and $\Delta \boldsymbol{t}$ correspond to body forces and tractions, respectively. Matrix $\boldsymbol{D}$ which appears in the expression for $\boldsymbol{K}$ represents the components of tangential material stiffness moduli while $\boldsymbol{K}^g$ is a geometric stiffness matrix. The latter is important as

soon as the stresses are of the same order as the material stiffness moduli. Matrix $\boldsymbol{B}_n$ has the following form

$$\boldsymbol{B}_n = \begin{bmatrix} \tilde{\boldsymbol{B}}_n & \tilde{\mathbf{0}} & \tilde{\mathbf{0}} \\ \tilde{\mathbf{0}} & \tilde{\boldsymbol{B}}_n & \tilde{\mathbf{0}} \\ \tilde{\mathbf{0}} & \tilde{\mathbf{0}} & \tilde{\boldsymbol{B}}_n \end{bmatrix} \quad \text{with} \quad \tilde{\boldsymbol{B}}_n = \begin{bmatrix} \frac{\partial N_1}{\partial \xi} & 0 & 0 & \frac{\partial N_2}{\partial \xi} & 0 & 0 & \dots & \frac{\partial N_{ne}}{\partial \xi} \\ \frac{\partial N_1}{\partial \eta} & 0 & 0 & \frac{\partial N_2}{\partial \eta} & 0 & 0 & \dots & \frac{\partial N_{ne}}{\partial \eta} \\ \frac{\partial N_1}{\partial \zeta} & 0 & 0 & \frac{\partial N_2}{\partial \zeta} & 0 & 0 & \dots & \frac{\partial N_{ne}}{\partial \zeta} \end{bmatrix}$$

and $\tilde{\mathbf{0}} = \begin{bmatrix} 0 & 0 & 0 \end{bmatrix}^{\mathrm{T}}$ while matrix $\tilde{\boldsymbol{\sigma}}$ appearing in the first term of the integrand of matrix $\boldsymbol{K}^g$ is

$$\tilde{\boldsymbol{\sigma}} = \begin{bmatrix} \bar{\boldsymbol{\sigma}} & \bar{\mathbf{0}} & \bar{\mathbf{0}} \\ \bar{\mathbf{0}} & \bar{\boldsymbol{\sigma}} & \bar{\mathbf{0}} \\ \bar{\mathbf{0}} & \bar{\mathbf{0}} & \bar{\boldsymbol{\sigma}} \end{bmatrix} \quad \text{with} \quad \bar{\boldsymbol{\sigma}} = \begin{bmatrix} \sigma_{11} & \sigma_{12} & \sigma_{13} \\ \sigma_{21} & \sigma_{22} & \sigma_{23} \\ \sigma_{31} & \sigma_{32} & \sigma_{33} \end{bmatrix} \quad \text{and} \quad \bar{\mathbf{0}} = \begin{bmatrix} 0 & 0 & 0 \\ 0 & 0 & 0 \\ 0 & 0 & 0 \end{bmatrix}$$

Matrix $\tilde{\tilde{\boldsymbol{\sigma}}}$ used in the second term of the integrand of $\boldsymbol{K}^g$ is defined as

$$\tilde{\tilde{\boldsymbol{\sigma}}} = \begin{bmatrix} \sigma_{11} & 0 & 0 & 0 & \sigma_{13} & \sigma_{12} \\ 0 & \sigma_{22} & 0 & \sigma_{23} & 0 & \sigma_{12} \\ 0 & 0 & \sigma_{33} & \sigma_{23} & \sigma_{13} & 0 \\ 0 & \sigma_{23} & \sigma_{23} & \sigma_{22} + \sigma_{33} & \sigma_{12} & \sigma_{13} \\ \sigma_{13} & 0 & \sigma_{13} & \sigma_{12} & \sigma_{11} + \sigma_{33} & \sigma_{23} \\ \sigma_{12} & \sigma_{12} & 0 & \sigma_{13} & \sigma_{23} & \sigma_{11} + \sigma_{22} \end{bmatrix}$$

3.4 Mitigation of volumetric locking

Incompressible material behaviour forms an ingredient of many geomechanical problems. It occurs in undrained saturated soil. Furthermore, it is assumed in case of fully plastic flow. Modelling such material behaviour implies that material experiences no change in volume which requires special attention when discretising a problem by means of constant-strain elements such as the used 4-noded tetrahedral elements.

In the following, the example shown in Figure 3.2 (left) is considered. Here, only one node of a tetrahedral element is free to move in directions 1, 2 and 3 by a displacement increment $\Delta \boldsymbol{u}^4$. The element might be located inside a larger mesh, but in the following explanations only one element is considered. Writing out Equation 3.14 renders

$$\Delta \boldsymbol{\varepsilon} = \begin{bmatrix} 0 & \Delta\varepsilon_{12} & 0 \\ \Delta\varepsilon_{21} & \Delta\varepsilon_{22} & \Delta\varepsilon_{13} \\ 0 & \Delta\varepsilon_{31} & 0 \end{bmatrix} \tag{3.19}$$

where $\Delta\varepsilon_{22}$ is only a function of the vertical displacement Δu_{42} of node 4. Assuming incompressible deformation, the additional constraint

$$\Delta\varepsilon_{11} + \Delta\varepsilon_{22} + \Delta\varepsilon_{33} = 0 \tag{3.20}$$

requires $\Delta u_{42} = 0$. Thus, the displacement of node 4 is limited to a horizontal plane. Now, a slightly tilted element as shown in Figure 3.2 (right) is considered so that two

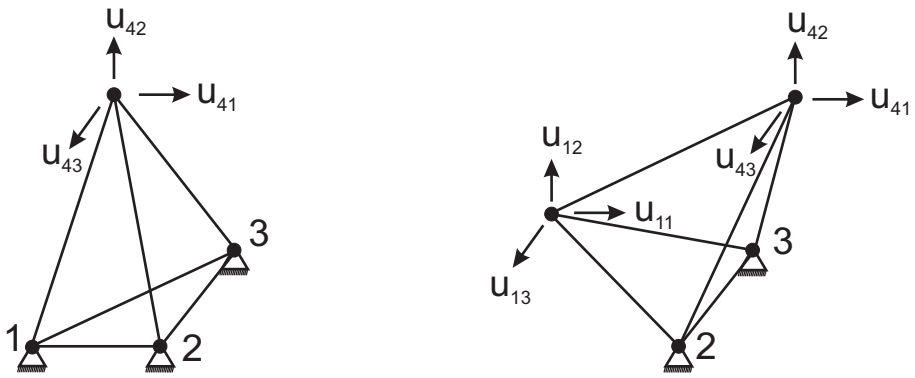

Figure 3.2: Volumetric locking; (left) tetrahedral element with all but three degrees of freedom fixed; (right) alternative discretisation with two nodes free to move

nodes 1 and 4 are free to move. Writing out the strain tensor components shows that the volumetric strain is now a function of Δu_{42} as well as Δu_{11}, Δu_{12}, Δu_{13}, which forms a less restrictive constraint on the element deformation.

Thus, depending on the used discretisation, incompressible material behaviour translates into a more or less severe restriction on the deformation of an element. In the extreme case of an element with only one node free to move, the severe restriction on element deformations shows in results of numerical analyses as a non-physical stiffness. Figure 3.13 (left) in Section 3.9.2 illustrates the occurrence of such so-called volumetric locking for the problem of an elastic-plastic slope.

Volumetric locking can be reduced by means of a Nodal Mixed Discretization technique as proposed by Detournay and Dzik [21]. This technique has been successfully introduced by Stolle, Jassim and Vermeer [50] to a 3D dynamic MPM code with explicit time integration using the same 4-noded tetrahedral elements. With the Nodal Mixed Discretization technique the number of degrees of freedom per element is increased by incorporating information of surrounding elements into the determination of element volumetric strain rates $\dot{e}$ defined as

$$\dot{e} = \dot{\varepsilon}_{11} + \dot{\varepsilon}_{22} + \dot{\varepsilon}_{33} \tag{3.21}$$

The algorithm forms an intermediate step between the element-wise determination of strain rates from the kinematic relation and the computation of stresses. The deviatoric strain components $\dot{\varepsilon}^D$ remain unchanged while the volumetric strain component is modified through an averaging procedure.

Let $\overset{\triangle}{\dot{e}}$ denote nodal volumetric strain rates obtained by weighted averaging of the volumetric strain rates $\dot{e}_l$ of all elements connected to a node

$$\overset{\triangle}{\dot{e}} = \frac{\sum \dot{e}_l V_l}{\sum V_l} \tag{3.22}$$

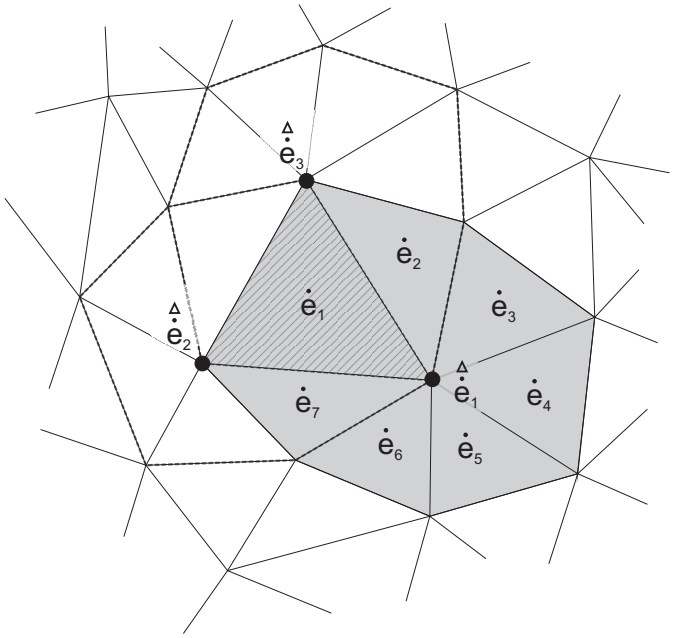

Figure 3.3: Nodal Mixed Discretization technique for the example of a 3-noded triangular element

where V_l denotes the volume of element l. Figure 3.3 illustrates the averaging procedure for the hatched triangular element, one of its nodes, respectively. Averaged volumetric strain rates $\bar{\dot{e}}$ are then computed for each element by averaging the nodal volumetric strain rates $\overset{\triangle}{\dot{e}}$ of all nodes connected to an element

$$\bar{\dot{e}} = \frac{\sum \overset{\triangle}{\dot{e}}_k}{n} \tag{3.23}$$

where n denotes the number of nodes per element (4 in case of the low-order tetrahedral elements). From the averaged element volumetric strain rates the updated strain rates $\dot{\varepsilon}'_{ij}$ are computed by means of

$$\begin{aligned} \dot{\varepsilon}'_{ij} &= \dot{\varepsilon}_{ij} - \frac{1}{3}\,\delta_{ij}\,(\dot{e} - \bar{\dot{e}}) \\ &= \dot{\varepsilon}^{D}_{ij} + \frac{1}{3}\,\delta_{ij}\bar{\dot{e}} \end{aligned} \tag{3.24}$$

where δ_{ij} is the Kronecker delta. The averaging is performed separately for different material domains. On the basis of the modified strain rates, stresses are computed from

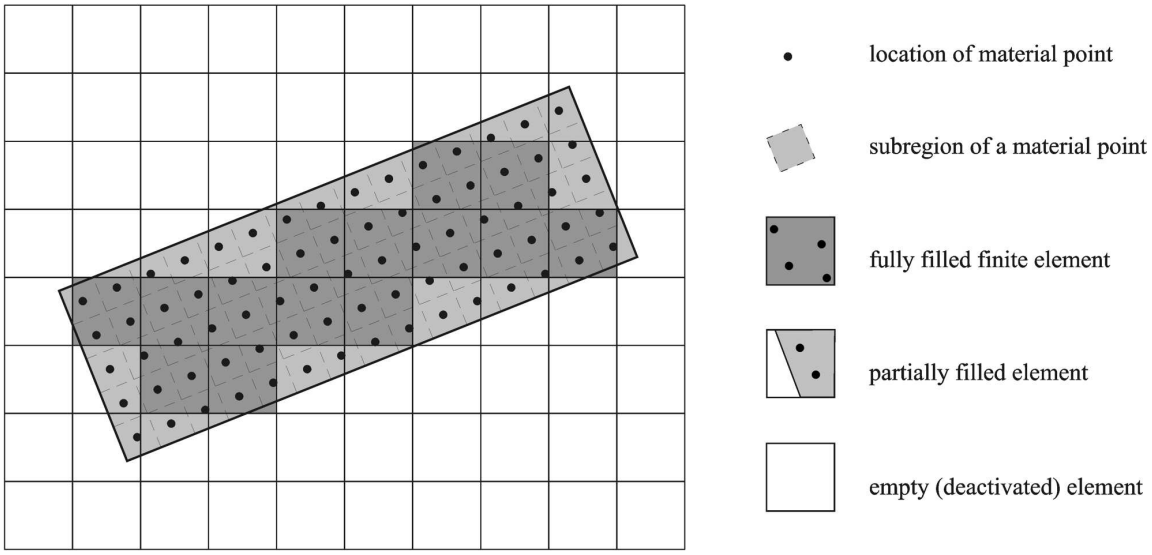

Figure 3.4: Finite element grid and solid body with material points

the constitutive stress-strain relation as with the standard FEM. In contrast to [21] no averaging procedure is applied on stress rates, because an averaging of stresses is already performed in the MPM calculation procedure as detailed in Section 3.6.

The performance of the described technique is illustrated in Section 3.9.2 with the benchmark of an elastic-plastic slope.

3.5 Material point discretisation

The essential difference between the standard FEM and the MPM is that, in the latter one, stresses and other state variables are not calculated and traced for Gaussian integration points, but for so-called material points flowing through the mesh. This means that the MPM does not only involve a finite element discretisation of space, but also a set of material points representing small subregions of the deformable body. The mass and volume of subregions are memorised for these points, but changes in the shape of the subregions are not traced.

Initialisation of the material point discretisation Figure 3.4 shows the undeformed state of a body that is divided into uniformly distributed subregions inside a regular computational mesh of squares. The finite element mesh covers the solid in its initial configuration as well as the region into which the solid is expected to move. In this example, the computational grid is completely independent of the initial state of the body, so that the analysis begins with fully filled as well as partially filled elements. In general, however, one will use meshes that largely match the initial undeformed state to avoid partially filled elements for the initial state of the discretisation. In this case, initial volumes V_p are assigned to subregions, material points respectively, such that the

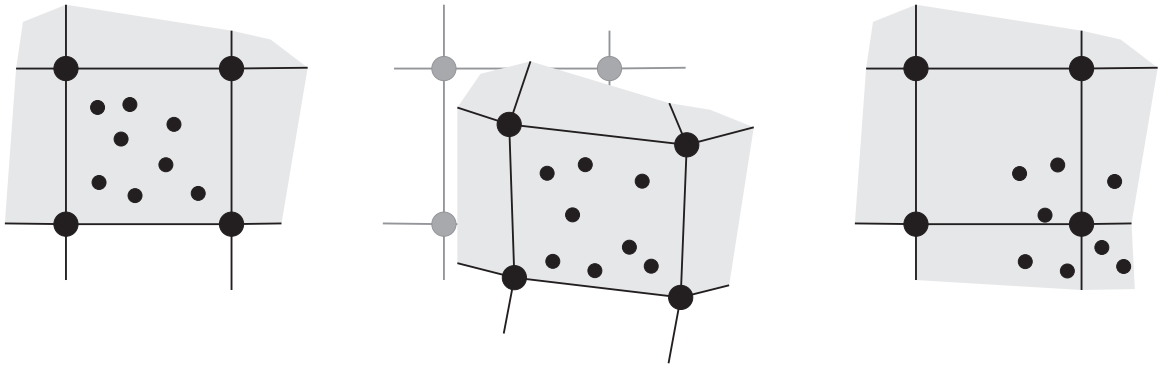

Figure 3.5: Movement of material points through the computational grid for a time step; (left) initial configuration; (center) incrementally deformed mesh; (right) reset mesh

summed volume of subregions inside an element equals the volume of the element

$$V_p = V_e/n_e \tag{3.25}$$

where n_e stands for the number of material points within the element considered and V_e is the element volume. Furthermore, material properties and state variables such as initial stresses are assigned to the material points.

An arbitrary distribution of material points may be used. In this study, 18 material points are initially assigned to the considered 15-noded prismatic elements, 10 material points to 10-noded tetrahedral volume elements and either 4 or 10 material points to 4-noded tetrahedral elements. In Appendix A the initial location of material points is shown.

Linkage with the finite element discretisation During the deformation process, elements initially filled with material points will eventually become void of material points and vice versa. Throughout the calculation process, elements void of material points are marked as deactivated, elements containing material points are marked as activated. The same distinction is applied to grid nodes, where nodes not attached to any activated element are marked as deactivated.

For each time step, the equations of equilibrium are assembled and solved for nodal displacement increments as usual within the numerical analysis of nonlinear problems (see Section 3.7). Here, only the changing set of activated elements and nodes is considered. The solution of the governing equations is Lagrangian in the sense that the computational mesh is deforming. As illustrated in Figure 3.5, material points thereby move relative to the global coordinate system. At the end of a time step elements are distorted. In case of significant distortions the computational mesh has to be adjusted. With the MPM it is usual to reset the distorted mesh back to its initial configuration as shown in Figure 3.5, but it is also possible to apply mesh refinement or other changes to the mesh. Material points, however, maintain the positions that they took up within the deformed mesh. Thus, the assignment of material points to finite elements is updated after the adjustment of the mesh.

The finite element and material point discretisation are linked by the mapping of data between the two discretisations on the basis of polynomial interpolation functions defined for the finite element grid. For example, the incremental movement of material points through the mesh is computed from nodal displacement increments by means of Equation 3.10.

Application of boundary conditions As with the standard FEM, prescribed displacements are assigned to nodes of the mesh. In anticipation of the movement of material through the discretised space, they are also applied to (boundary) nodes that might become activated in the course of the calculation.

With the MPM, it is common to apply prescribed forces not on boundary nodes but on material points [23]. With the presented implementation, tractions are assigned to material points in two steps. At first, prescribed tractions $\boldsymbol{t}$ are assigned to element surfaces S_t of the finite element mesh in its initial configuration. This can be done without difficulty, because, as stated above, the finite element mesh matches the initial undeformed state of the discretised body. When inserting material points into the mesh, these tractions are translated for each volume element into forces $\boldsymbol{F}^t$ attached to those material points that lie next to the loaded surface. This is done by means of

$$\boldsymbol{F}^t = \boldsymbol{t}\,\frac{S_t}{n_t} \tag{3.26}$$

Here, n_t is the number of material points next to the loaded element surface. This even distribution of traction over material points is justified for the presented implementation because material points are evenly spread across the volume elements in the initial configuration. Furthermore, at present, only constant surface tractions are considered.

The disadvantage of applying tractions to material points arises when computing the vector of external forces (Equation 3.17). Material point forces $\boldsymbol{F}_i^t$ are mapped to nodes on the surface as well as nodes slightly inside the solid body by

$$\boldsymbol{F} = \sum_{e=1}^{n_{fe}} \sum_{i=1}^{n_e} \boldsymbol{N}_i^T\, \boldsymbol{F}_i^t \tag{3.27}$$

where $\boldsymbol{F}$ is a vector of nodal external forces, n_{fe} denotes the number of finite elements that contain load-carrying material points and n_e is the number of load-carrying material points inside each element. So, boundary tractions are finally distributed over a boundary zone rather than over a surface. In case of non-structured meshes the thickness of this zone is variable. In order to avoid resulting inaccuracies, it is also possible to stick to the FEM way of applying traction at nodes. However, to maintain nodes on the boundary with the MPM, the computational mesh would have to be adjusted after each time step.

Updated locations of material points are computed from interpolation functions of the underlying deformed mesh. While material points might approach element sides whose normal displacements are fixed, crossing these fixed surfaces is thereby explicitly prohibited.

Adaptation of the material point discretisation With a fixed number of material points, empty finite elements and thus deactivated nodes might occur temporarily within the interior of a body during the calculation process. Such deactivated elements introduce non-physical discontinuities. This might happen in case of an extremely large stretching of the body by which the density of its material point discretisation decreases. One might also think of strongly irregular meshes, in which small elements enclosed by large elements might become void of material points.

In order to guarantee a proper discretisation of a body, material points are inserted within the body into elements that would otherwise become void of material points. In case of low-order elements 1 material point is inserted into each empty element at the location of the Gaussian integration point, in case of high-order elements 4 material points are inserted in an identical fashion. State variables such as stresses are assigned to these points from a sphere of surrounding material points by means of the method of least squares. Furthermore, incremental displacements of the previous time step are computed for these inserted material points. This is done by back-calculating the coordinates of inserted material points at the beginning of the previous time step from the nodal displacement increments obtained at the end of the time step. These inserted material points get no volume and consequently no weight so that the distribution of weight inside the solid body is not altered. If the distribution of material points inside elements becomes too dense at a later stage of the calculation process, these inserted material points can simply be removed.

Apart from these weight-less material points, material points that do carry a weight are inserted into the mesh during computations in which the entire mesh is displaced. Such an approach is taken when a structure such as a pile or anchor is moved through soil. Figure 3.6 illustrates this adjustment of the mesh and the insertion of material points with the example of a rigid pile pushed vertically into soil by a distributed load at the top. At the end of a time step, the finite element mesh is deformed incrementally. Instead of resetting the mesh to its initial configuration, the elements discretising the rigid pile are updated as in the conventional updated Lagrangian FEM. Thereby, the boundary of the pile coincides with element boundaries at all stages of the analysis. Thus, material points of pile elements do not experience a movement relative to their respective element boundaries. The distributed load is always applied on the pile boundary. Now, the remaining mesh is adjusted so that the undeformed geometry of elements is recovered. All coordinates of mesh nodes are updated so that the mesh moves step by step as a fixed entity with the displacement of the rigid pile. As shown on the right hand side of Figure 3.6, finite elements at the bottom of the mesh would eventually become empty. However, with this problem, the grid moves over a material point discretisation representing soil that extends beyond the boundaries of the mesh as indicated by the greyed surface below the mesh. During the computation, material points are thus continuously entering the mesh along its lower boundary.

The extended soil body, material point discretisation respectively, is initialised in two steps as shown in Figure 3.7. In a first step, the entire material point discretisation is initialised on the basis of a finite element grid as presented in this chapter (left side image). The finite element discretisation is then discarded while the initialised material points

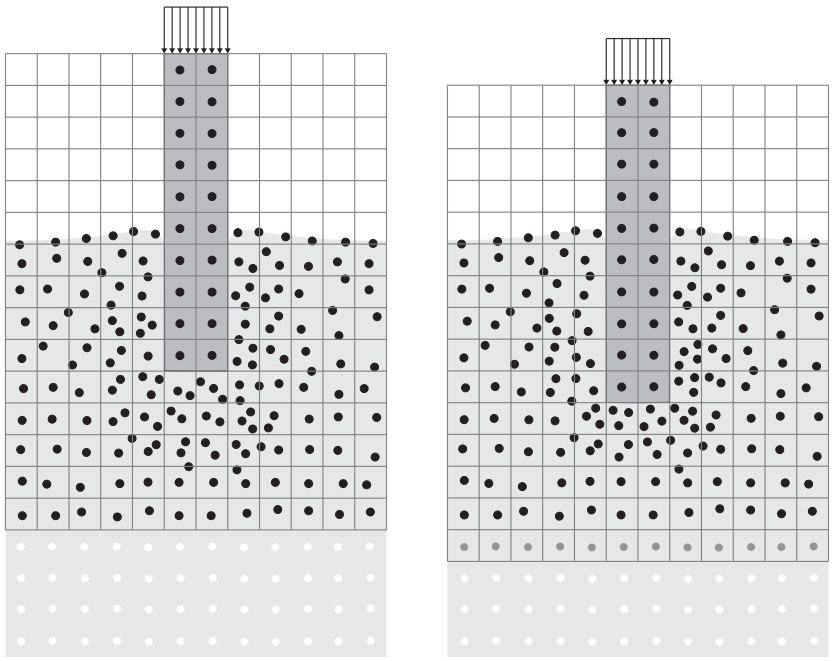

Figure 3.6: Insertion of material points into the discretised space; (left) initial mesh; (right) moved mesh

are kept (center image). In the second step, the (smaller) finite element discretisation of the considered problem is initialised (right side image). Material points inside this new discretisation are initialised as usual. Material points outside the grid are taken from the previously generated extended material point cloud and marked as deactivated. After the mesh has experienced an incremental displacement, it is checked which deactivated material points crossed the boundary surfaces of the finite element mesh and which activated material points might have left the grid. For those material points that entered the mesh, the elements they moved into are determined.

Through this approach, state variables are properly initialised for inserted material points. Thus, a mapping of stresses from surrounding material points as done with weight-less material points does not apply. Obviously, the region discretised by finite elements must be sufficiently large so that the initial state of material that lies outside the mesh would not be altered throughout the calculation. More importantly, the material point discretisation forms a continuous medium with respect to the volume and mass of material points inserted into the mesh. A small inaccuracy might evolve along the boundary of the mesh because the volume covered by material points might lie to some extend outside the mesh, so that the gravitational load of the solid body would be slightly overestimated.

Throughout the calculation process, no distinction is made between inserted material points and the initial material point discretisation, with one exception related to numerical integration that is described in the following section.

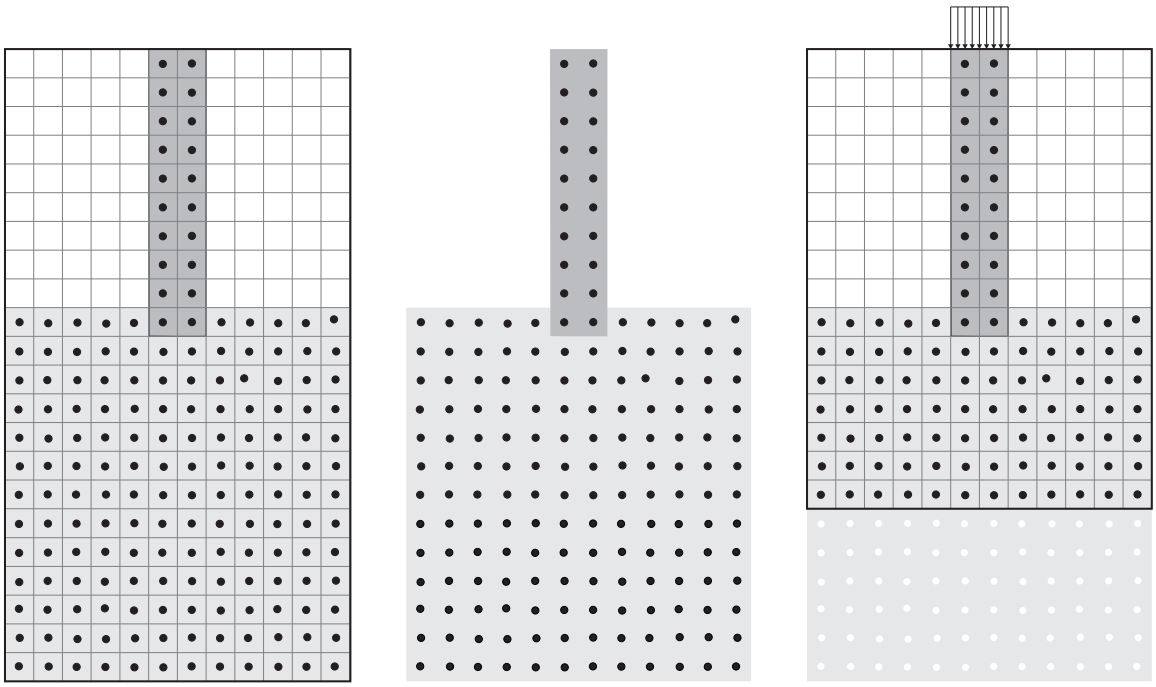

Figure 3.7: Generation of extended material point discretisation

3.6 Numerical integration

In finite element analyses, Gaussian integration points are generally used for the numerical integration of Equations 3.18 and 3.17 but this is not usual for the MPM. In most existing MPM implementations [15, 51–53, 67, 68] numerical integration is not performed by using Gaussian integration points, but by an element-wise summation over the material points. Considering for example evaluation of the material stiffness matrix, the material point based integration yields

$$\int_V \boldsymbol{B}^{\mathrm{T}}\,\boldsymbol{D}\,\boldsymbol{B}\;\mathrm{d}V \;\approx\; \sum_{e=1}^{n_{fe}} \sum_{p=1}^{n_p} \boldsymbol{B}^{\mathrm{T}}\,\boldsymbol{D}\,\boldsymbol{B}\;V_p \tag{3.28}$$

where n_{fe} denotes the number of finite elements containing material points and n_p the number of material points inside each element.

In the example shown in Figure 3.4 the finite element mesh is completely independent of the state of the body, so that the mesh contains fully filled as well as partially filled elements. The advantage of material point based integration is that it applies to elements that are either fully or partially filled with material. However, stress oscillations were observed with material point based integration during benchmark calculations as illustrated in Figure 3.8 for the example of an oedometer that is subjected to traction. The geometry and boundary conditions of the problem are sketched on the left hand side of the figure. In the charts, vertical stresses computed at material points are plotted across the height of the oedometer in its final deformed state. The dashed frame indicates the

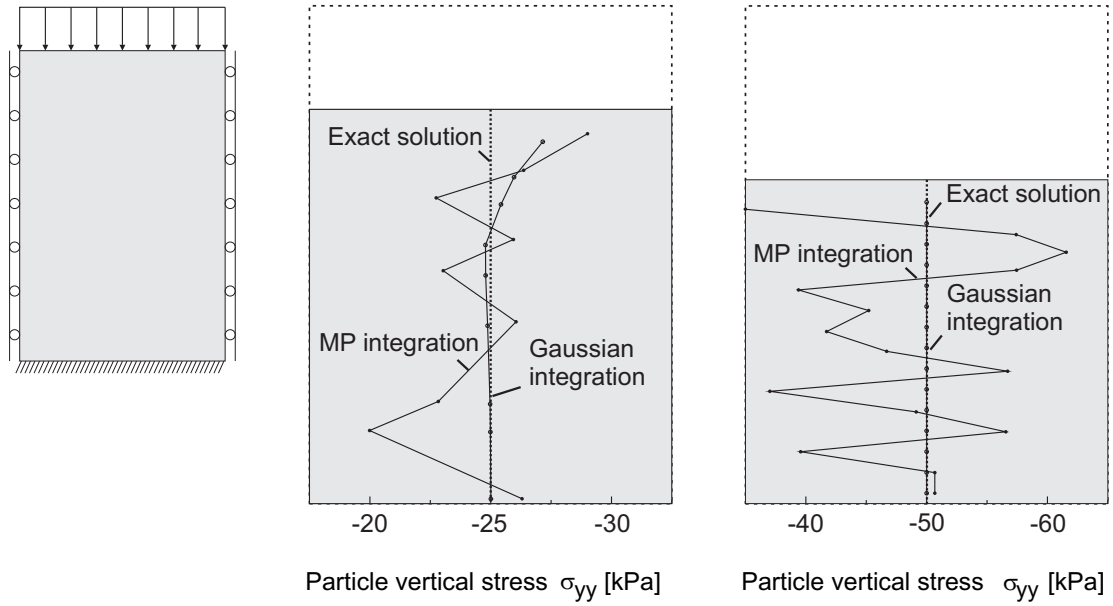

Figure 3.8: Vertical stresses at material points plotted over the height of an oedometer for material point based integration and Gaussian integration; (left) geometry of the considered problem; (center) discretisation with low-order tetrahedral elements; (right) discretisation with high-order tetrahedral elements

initial height of the oedometer. The image in the center shows stresses for a discretisation with low-order tetrahedral elements at a traction load of 25 kPa, the one on the right hand side shows stresses for a discretisation with high-order prismatic elements at a load of 50 kPa. Because traction is applied on the top layer of material points, stresses near the oedometer surface are not accurate and are therefore not shown in the charts. The computation using material point based integration shows severe oscillations of stresses, though the average taken over the oedometer height corresponds reasonably well to the exact value. In order to eliminate these oscillations, Gaussian integration is applied to all elements that are fully filled with material, whereas material point based integration is only adopted for partially filled elements. The stresses obtained with this extension of the Material Point Method are also shown in Figure 3.8. They correspond well to the exact solution. The deviation of material point stresses from the exact solution in case of the discretisation with low-order elements must be attributed to the material point based load application.

As stated before, elements in the interior of a body are assumed to be fully filled. Conversely, partially filled elements are assumed to occur only along the boundary of a body. From Figure 3.6 it becomes evident that a mesh boundary is not considered as a boundary of the body as though the body extends beyond the mesh.

For elements along the boundary of a body, partially filled elements satisfy the condition

$$\sum_{p=1}^{n_e} V_p \; < \; \beta \, V_e \tag{3.29}$$

The constant β was chosen to be 0.9, as sensitivity calculations showed very little influence on computational results for variations of β around this particular value.

Similar to the material stiffness matrix, $\boldsymbol{K}$, the geometric stiffness matrix, $\boldsymbol{K}^g$, in Equation 3.18 is computed by Gaussian integration of fully filled elements and material point based integration of partially filled elements. However, in the case of body forces, material point based integration is used in all elements instead of distinguishing between partially and fully filled elements. In doing so, it is made sure that the total body weight is exactly retrieved.

Inserted material points that carry no weight are not considered for the integration of partially filled elements. This evolves automatically from the material point discretisation because such material points are only placed in the interior of a body, whereas the occurrence of partially filled elements is limited to the boundary of a solid. Weight-less material points in the vicinity of the boundary of a body are removed.

Because Gaussian integration of fully filled elements needs the integrand values, e.g. stresses, for Gaussian integration points, data has to be mapped from the material points to the Gaussian integration points at the beginning of every time step. Conversely, state variables computed at Gaussian integration points have to be mapped to material points at the end of a time step for fully filled elements. In the following, the mapping of state variables from Gaussian integration points to material points is presented. In the succeeding paragraph, the mapping of state variables from material points to Gaussian integration points is explained. For illustration of the used algorithms, the mapping of stresses will be considered as representative for any state variable that is required for a used constitutive model.

Mapping of state variables from Gaussian integration points to material points In case of 4-noded tetrahedral elements with constant stress distribution, stresses are mapped from Gaussian integration points to material points by simple averaging. Considering quadratic interpolation of displacements within 10-noded tetrahedral elements, the strain interpolation is linear and it is thus consistent to choose a linear stress interpolation for the high-order elements as used in this study.

Stresses at any point within a finite element in terms of Gauss point stresses can be determined from

$$\sigma_{ij}(\xi, \eta, \zeta) \;=\; H_k \, S_{kij} \tag{3.30}$$

where H_k are interpolation functions, S_{kij} are known stresses at Gauss points k, the range of k is the number of Gauss points denoted as n_{GP}. Likewise, stresses at a point inside an element can be described by the following polynomial

$$\sigma_{ij}(\xi, \eta, \zeta) \;=\; p_l \, a_{lij} \tag{3.31}$$

where p_l are polynomial basis functions and a_{lij} are constant coefficients. In case of 10-noded tetrahedral elements $p_l \in \{1, \xi, \eta, \zeta\}$. For the high-order prismatic elements, the stress interpolation is not linear and has to be extended by two extra terms — details are left to the reader. The coefficients a_{lij} can be determined from a system of n_{GP} equations that is assembled from Equation 3.31 for known stresses S_{kij} at Gauss point locations

$$S_{kij} \;=\; P_{kl} \, a_{lij} \tag{3.32}$$

where P_{kl} is assembled from p_l for the known Gauss point coordinates. Because the number of Gauss points within the elements used in this study is equal to the number of coefficients a_{lij}, Equation 3.32 has a unique solution. Combining Equations 3.30, 3.31 and 3.32 renders the sought-after shape functions

$$H_k \;=\; p_l\,(P^{-1})_{kl} \tag{3.33}$$

The shape functions for 15-noded prismatic elements and 10-noded tetrahedral elements are listed in Appendix A.

Mapping of state variables from material points to Gaussian integration points For low-order constant-stress elements, the mapping of stresses from material points to Gaussian integration points is trivial, as the element stress is simply an average of material point stresses within the element considered. This will be a weighted average in the most general case that the subregions of material points are of different volumes, V_P. In this study, also in case of non-structured meshes, no weighting has been applied, as initial tests with varying weights showed a negative effect on the numerical stability of performed calculations. This (weighted) averaging is in fact a least square fitting, as also applicable to high-order elements. Considering a linear stress interpolation for the high-order elements used in this study an arbitrary component of stress is assumed to vary within a particular element according to the function

$$\sigma_{ij}(\boldsymbol{x}) \;=\; \alpha_0 + \alpha_1 x_1 + \alpha_2 x_2 + \alpha_3 x_3 \tag{3.34}$$

where the constants α_i are found by a least-square of all material point stresses $S_{p\,ij}$ within the element. Hence, coefficients α_i are calculated by minimising the quadratic function

$$J \;=\; \sum_{p=1}^{n_e} (S_{p\,ij} \;-\; (\alpha_0 + \alpha_1 x_{p1} + \alpha_2 x_{p2} + \alpha_3 x_{p3})\,)^2 \; V_p \tag{3.35}$$

The coefficients α_i can now be computed from the four linear equations

$$\frac{\partial J}{\partial \alpha_i} \;=\; 0 \tag{3.36}$$

at least if the equations are linearly independent. This will not be the case when an element contains less than four material points or in the very special case that all these material points happen to be aligned. In such cases, it is possible to take more material points from a wider volume than the element considered.

Having evaluated the coefficients α_i for the fully-filled high-order element considered, the stresses in the Gaussian integration points can be straightforwardly computed from the function $\sigma_{ij}(\boldsymbol{x})$. For the 15-noded prismatic elements, the stress interpolation is not linear and has to be extended by two extra terms.

3.7 Iterative procedure within a load step

For elastic-plastic constitutive models as considered in this study, finite increments of stress may be written in the form of Equation 3.8 or alternatively as

$$\Delta \overset{\triangledown}{\boldsymbol{\tau}} = \boldsymbol{D}^e \left(\Delta \boldsymbol{\varepsilon} - \Delta \boldsymbol{\varepsilon}^p \right) = \boldsymbol{D}^e \, \Delta \boldsymbol{\varepsilon} - \boldsymbol{h}(\boldsymbol{\sigma}, \Delta \boldsymbol{\varepsilon}) \tag{3.37}$$

where $\boldsymbol{D}^{\mathrm{e}}$ is the elastic material stiffness and $\boldsymbol{h}$ a correction function for the plastic strains, $\Delta \boldsymbol{\varepsilon}^p$, that depend on a yield function and a plastic potential function. Using the above expression, Equation 3.16 may be put into the form

$$\left(\boldsymbol{K}^e + \boldsymbol{K}^g \right) \Delta \boldsymbol{a} = \Delta \boldsymbol{F} + \Delta \boldsymbol{F}_p \tag{3.38}$$

with

$$\Delta \boldsymbol{F}_p = \int_{V^*} \boldsymbol{B}^{\mathrm{T}} \, \boldsymbol{h} \, \mathrm{d}V \tag{3.39}$$

where $\boldsymbol{K}^e$ is the global elastic stiffness matrix and all material non-linearity is contained in the function $\boldsymbol{h}$. Geometric non-linearity is captured by defining V^* and S_t^* as the deformed body at the end of the load step and writing

$$\Delta \boldsymbol{F} = \boldsymbol{F}_{ex} - \boldsymbol{F}_{int} \tag{3.40}$$

where

$$\boldsymbol{F}_{ex} = \int_{V^*} \boldsymbol{N}^{\mathrm{T}} \left(\boldsymbol{b} + \Delta \boldsymbol{b} \right) \mathrm{d}V + \int_{S_t^*} \boldsymbol{N}^{\mathrm{T}} \left(\boldsymbol{t} + \Delta \boldsymbol{t} \right) \mathrm{d}S \qquad \boldsymbol{F}_{int} = \int_{V^*} \boldsymbol{B}^{\mathrm{T}} \left(\boldsymbol{\sigma} + \Delta \boldsymbol{\sigma} \right) \mathrm{d}V \tag{3.41}$$

The global iteration process as used in this study can be written as

$$\left(\boldsymbol{K}^e + \boldsymbol{K}^g \right) \Delta \boldsymbol{a}^{k+1} = \boldsymbol{F}_{ex} - \boldsymbol{F}_{int}^k + \Delta \boldsymbol{F}_p^k \tag{3.42}$$

where k refers to the iteration number. Hence, $\boldsymbol{F}_{int}^k$ and $\Delta \boldsymbol{F}_p^k$ are computed from $\Delta \boldsymbol{\varepsilon}^k$, being evaluated for the deformed state at the end of the kth iteration. During the iteration process within a load step, the computational mesh is continuously updated, but the matrices $\boldsymbol{K}^e$ and $\boldsymbol{K}^g$ are kept constant, i.e. are only updated for the very first iteration. This iterative procedure is continued until the relative equilibrium error of

$$\text{error} = || \, \boldsymbol{F}_{ex} - \boldsymbol{F}_{int}^k \, || \, / \, || \, \boldsymbol{F}_{ex} \, || \tag{3.43}$$

has reached a value below a particular tolerated error. In this study the tolerated error has been generally set to a value of 0.01 unless otherwise stated.

The use of a constant matrix requires only a single (time-consuming) decomposition and is thus considered to be computationally attractive. On the other hand, it would seem to be inefficient to use the elasticity matrix, $\boldsymbol{K}^e$, rather than the elastoplastic stiffness matrix, $\boldsymbol{K}$. Indeed, a (modified) Newton-Raphson iterative procedure with a constant elastoplastic tangent stiffness matrix is very efficient for regular elastoplastic models. In this study, however, the Mohr-Coulomb elastic-plastic model is used, which involves an irregular yield surface so that there is no unique elastoplastic stiffness matrix.

In such a case the elastoplastic stiffness matrix might be estimated from the previous load step, but it would seem that this is only converging in combination with relatively small load steps. Moreover, the elastoplastic stiffness matrix is generally non-symmetric, at least for non-associated plasticity models. For this reason, the standard iterative procedure with the elastic stiffness matrix, as applied in Plaxis codes [12], has been adopted.

The efficiency of the iteration process depends on the size of the load steps. The use of very small steps requires many matrix decompositions in combination with only a few iterations per step, whereas the use of very large steps will imply the opposite, i.e. less matrix decompositions and more iterations per step. Considering results from some benchmark problems, Van Langen and Vermeer [59] suggested to use step sizes that require 4 to 10 iterations with a quasi-static FEM. On the basis of a desired minimum and maximum number of iterations, they also proposed an automatic step size correction procedure. If the number of iterations exceeds an upper limit, the step size is scaled down by half. The load step is then recomputed with the scaled load vector. In case the number of iterations lies below a lower threshold, the step size is doubled. This procedure has been successfully applied to the quasi-static MPM as well. However, a recommendation for a maximum and minimum number of iterations requires assessment of a broader set of benchmark problems.

Although the mesh experiences only incremental deformations, these might nonetheless become extensive in case of large load steps. Therefore, in order to keep distortions of the finite element mesh small, an additional criteria for scaling down the size of load steps is introduced. If the change of the determinant of the Jacobian ΔJ at any Gaussian integration point of the activated finite elements

$$\Delta J \;=\; 1 \;-\; \frac{\min(J^{\text{deformed}}, J^{\text{undeformed}})}{\max(J^{\text{deformed}}, J^{\text{undeformed}})} \tag{3.44}$$

exceeds a given threshold value, then the load step is scaled down. Here, J^{deformed} and $J^{\text{undeformed}}$ denote the determinant of the Jacobian of the deformed element, the undeformed element respectively. For computations of this study a threshold value of 0.3 has been used. The Jacobian $\boldsymbol{J}$ is defined as

$$\boldsymbol{J} \;=\; \begin{bmatrix} \frac{\partial x_1}{\partial \xi} & \frac{\partial x_2}{\partial \xi} & \frac{\partial x_3}{\partial \xi} \\ \frac{\partial x_1}{\partial \eta} & \frac{\partial x_2}{\partial \eta} & \frac{\partial x_3}{\partial \eta} \\ \frac{\partial x_1}{\partial \zeta} & \frac{\partial x_2}{\partial \zeta} & \frac{\partial x_3}{\partial \zeta} \end{bmatrix} \tag{3.45}$$

where the terms x_1, x_2 and x_3 are computed from Equation 3.12.

The iteration process can be accelerated by estimating the first iterate, $\Delta \boldsymbol{a}^1$, from the previous load step. Instead of solving the governing equations of the first iteration, nodal displacement increments are estimated from the displacement field of the previous load step that is stored with material points. For each activated node, incremental displacements are interpolated by weighted averaging from displacement increments of material points in the vicinity of the node. Weighting is done by distance. For computations presented in Chapter 6 such load step extrapolation showed a reduction of the number of iterations by a factor of 0.88.

3.8 Overview of the calculation process

In the initialisation phase of an MPM analysis, the finite element mesh and material point discretisation are generated and boundary conditions are applied to the finite element mesh as explained in Section 3.5.

Load stepping: After initialisation, the calculation process of stepwise load increase is started. For each load step, the equations of equilibrium are assembled and solved as described in Section 3.7. For fully filled elements, Gaussian integration is applied and stresses are computed at integration points. For partially filled elements, material point integration is applied and stresses are directly computed at these points identical to the computation at integration points (see Section 3.6).

After reaching the required accuracy of the iterative solution, a calculation phase termed Convective Phase is performed [51]. For fully filled elements, stresses are mapped from Gaussian integration points to material points element-wise as presented in Section 3.6. In case of significant distortions of finite elements the computational mesh is reset to its initial position or otherwise adjusted while material points maintain the positions they took up in the deformed mesh. Consequently, the assignment of material points to finite elements is updated. For the Gaussian integration of fully filled elements, material point stresses are mapped to the Gauss points of these elements (see Section 3.6). Eventually, material points are inserted into elements, redundant material points are removed. Subsequently, the next load increment is applied on the updated material point configuration.

Those steps of the calculation process that are related to the resetting or adjustment of the mesh introduce non-physical out-of-balance forces at activated nodes. Here, both the external as well as the internal load vector defined in Equation 3.41 are subject to changes. As also found by Hu and Randolph [28], these out-of-balance forces degrade the numerical stability, at least if they exceed the tolerated error used for the iterative procedure. In order to eliminate this adverse effect, a so-called zero load step is inserted in between two load steps as proposed by Sheng [48]. With zero load steps, no additional load increment is applied. The nodal out-of-balance forces are reduced as with a standard FEM load step. Material points do no move through the mesh, i.e. nodal displacements are reset to zero. Stresses obtained from a zero load step have no physical meaning and are overwritten by results obtained in the succeeding load step.

3.9 Validation

The first benchmark for validation of the quasi-static MPM is the bending of a cantilever beam. It involves large displacements rather than large strains so that the UL-FEM is well suited for solving this problem. It is thus used to compare results obtained with the MPM against a proven numerical solution. Thereafter, results for two geomechanical problems involving extremely large deformations of soil are shown, a slope under gravity loading and a retaining wall moved along the ground. The latter two examples illustrate the advantage of the presented numerical method compared to the UL-FEM.

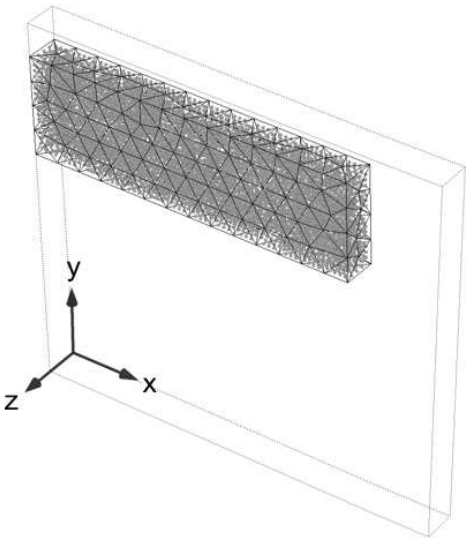

Figure 3.9: Non-structured mesh for a cantilever beam with material points, initially activated elements

3.9.1 Linear-elastic cantilever beam: comparison to FEM

A linearly elastic cantilever beam subjected to gravity loading is analysed. It is assumed that the load is applied quasi-statically. The beam has a length of 1 m, a height of 0.3 m and a width of 0.1 m. The weight of the material is increased up to a value of 4 kN/m^3. A linear-elastic material with Young's modulus of 100 kPa and Poisson's ratio of 0 is assigned to the beam.

Tetrahedral elements with quadratic interpolation functions are employed in the calculations. Figure 3.9 shows the active elements (those where material points are located) inside the discretised space at the onset of loading. Initially 10 material points are placed inside each activated element. The boundary nodes are fixed in the z-direction in order to obtain the plane strain solution.

Figure 3.10 shows the computed material point positions both for a body weight of 2 kN/m^3 and for the final weight of 4 kN/m^3. In Figure 3.10 (left), the partially filled elements along the boundary of the beam are indicated by coloring the contained material points in red. In Figure 3.10 (right), horizontal stresses are indicated. As a large-displacement but small-strain problem is considered, the UL-FEM calculation provides accurate results, which can thus be used for validation of the MPM. The minimum and maximum value of horizontal stress of -47.0 and 32.7 kPa are in good agreement with results of an UL-FEM analysis. The load-displacement curves for the vertical and horizontal displacement averaged over the tip of the cantilever beam for both the MPM and UL-FEM calculation are presented in Figure 3.11. This figure shows results for 20 load steps. For a tolerated error of 0.03 and manual presetting of the step size the average

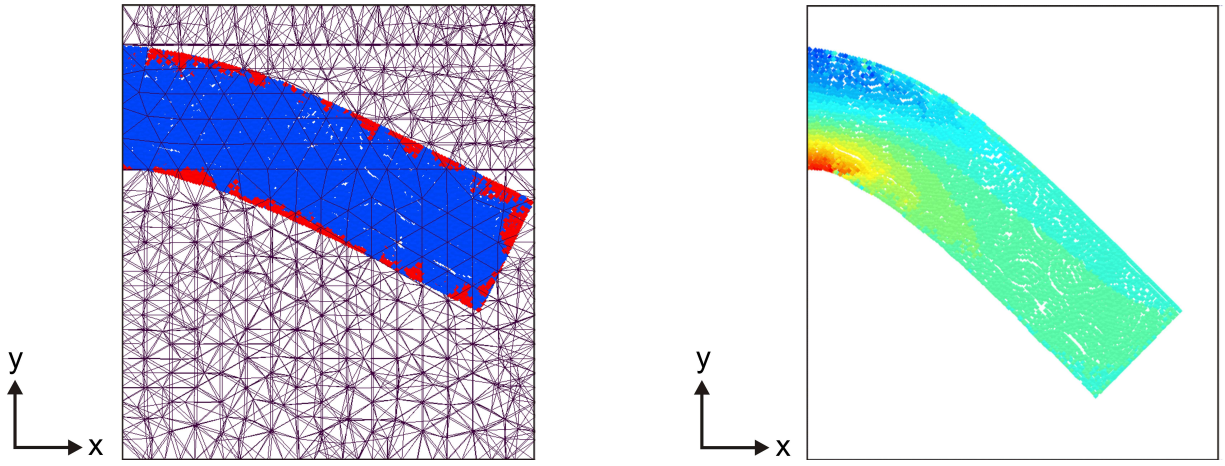

Figure 3.10: Deflection of the cantilever beam: (left) location of material points relative to the computational mesh for a body weight of 2 kN/m^3; (right) shading of horizontal stresses at an applied body weight of 4 kN/m^3

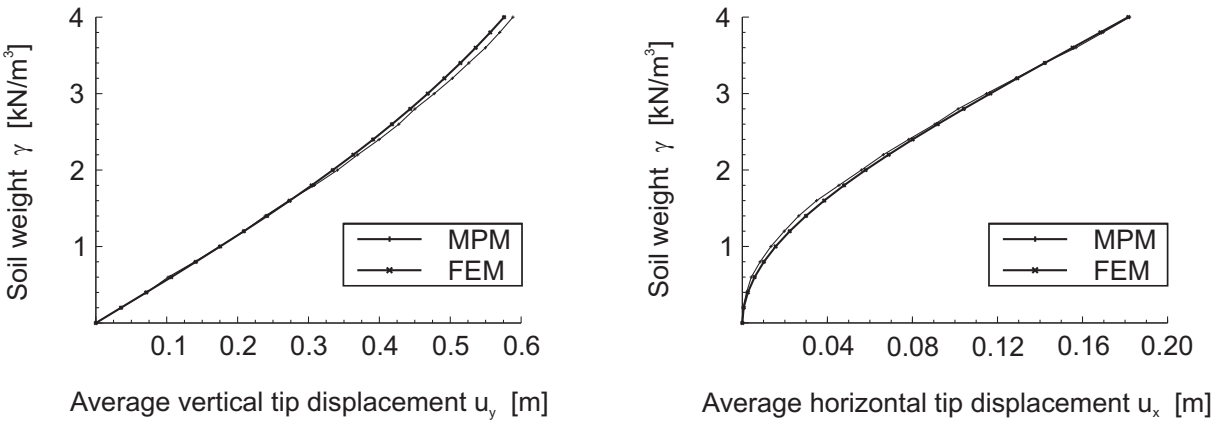

Figure 3.11: Load-displacement curves calculated with UL-FEM and MPM for (left) vertical and (right) horizontal tip displacement averaged over the height of the cantilever beam

number of iterations per step was about 12.

As can be seen from Figure 3.11, good agreement is obtained between the UL-FEM and MPM results. The slight deviation of the MPM curves from the UL-FEM results may very well be attributed to the less accurate integration procedure used for partially filled elements along the boundary of the material point discretisation.

3.9.2 Elastic-plastic slope problem

For an elastoplastic slope under gravity loading, as depicted in Figure 3.12, the UL-FEM meets its limitations as large distortions of elements occur inside the developing shear bands and at the foot of the slope during the calculation process.

The slope has been discretised using 15-noded prismatic elements with initially 18 material points inside, 10-noded tetrahedral elements with initially 10 material points and 4-noded tetrahedral elements with initially 10 material points. It possesses an inclination of 60° and a height of 1 m. The Tresca yield criterion is used [61], with Young's modulus of 100 kPa, Poisson's ratio of 0.33 and cohesion of 1 kPa. As for the case of the beam, the plane strain problem was analysed as a 3D slice with a thickness of 0.1 m. Nodal displacements are fixed at the bottom of the mesh and horizontal nodal displacements are fixed at the left side of the mesh. The weight of the material is increased up to $\gamma = 10$ kN/m^3.

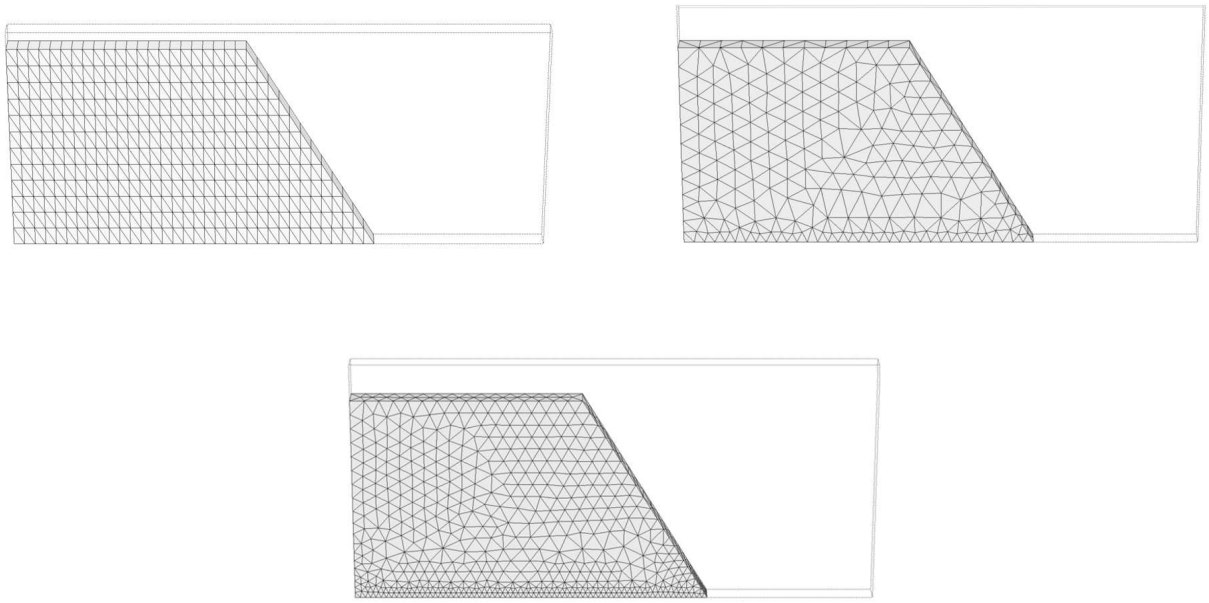

Figure 3.12: Geometry and discretisation of the slope: (top left) structured mesh of prismatic elements; (top right) non-structured mesh of 10-noded tetrahedral elements; (bottom) non-structured mesh of 4-noded tetrahedral elements

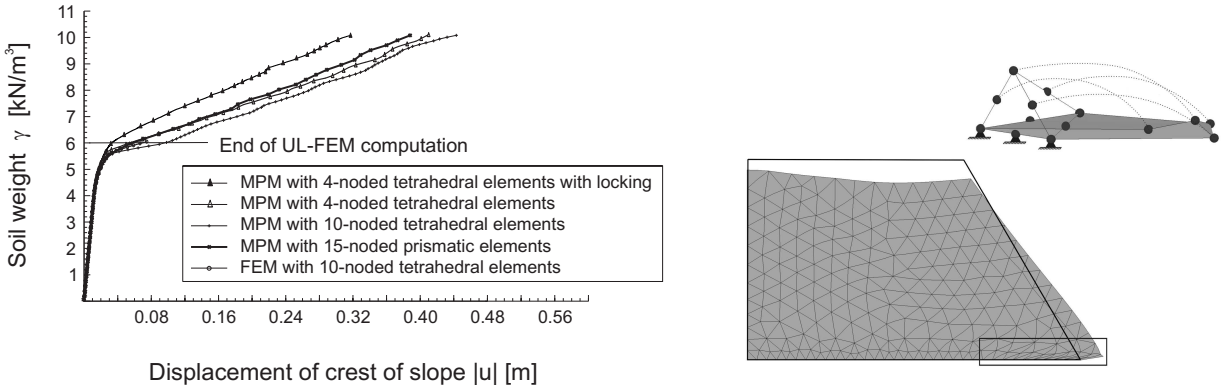

Figure 3.13: (left) Load-displacement curves for the slope for prismatic and tetrahedral elements; (right) deformed mesh for FEM

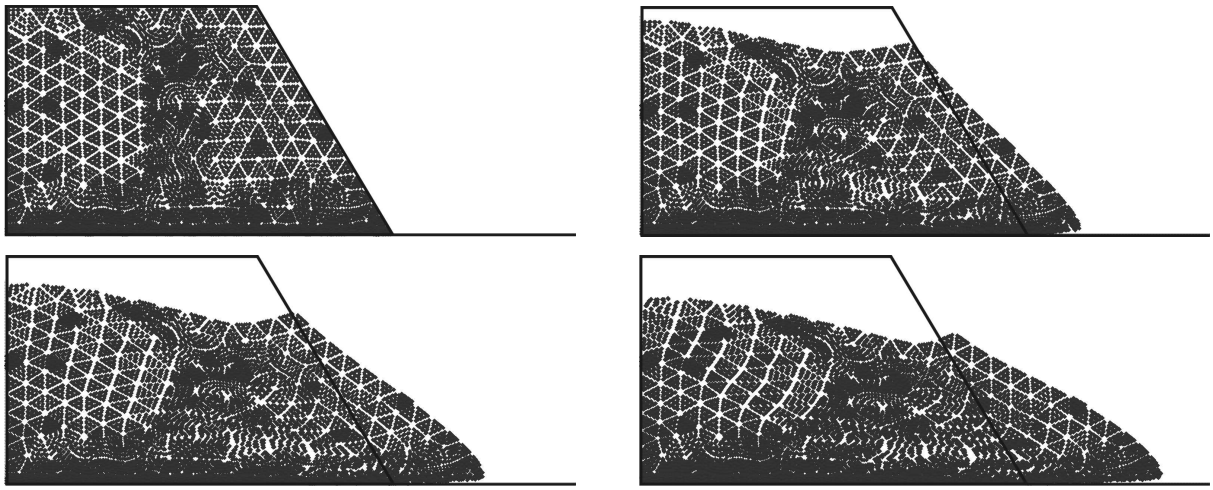

Figure 3.14: Deformation of the slope represented by material point positions at soil weight γ = 0, 7, 8.5 and 10 kN/m^3

The tetrahedral element analyses were carried out with manual presetting of the step size which rendered on average 14 iterations per step, whereas a much higher number was needed for the prismatic element analysis.

Figure 3.13 (left) shows the unit soil weight as a function of the displacement of the crest of the slope both for prismatic and tetrahedral elements. Up to a soil weight of approximately γ = 5.25 kN/m^3, elastic deformations dominate the deformation process. With regard to the MPM calculations, the slightly softer response of the tetrahedral elements compared to the prismatic elements is attributed to the mesh refinement at the bottom of the slope (see Figure 3.12). The load-displacement curve for a computation with 4-noded tetrahedral elements without application of the Nodal Mixed Discretization technique (see Section 3.3) is also plotted. This curve shows a considerably stiffer response due to volumetric locking compared to the result for the computation with 4-noded elements that makes use of this technique. The latter corresponds well to results obtained with high-order elements that are less prone to locking effects. Furthermore,

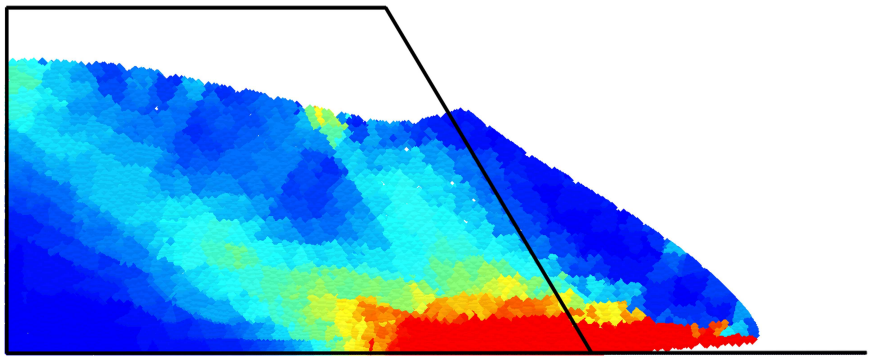

Figure 3.15: Incremental shear strains for the slope in the final deformed state

the load-displacement curve from an UL-FEM calculation using tetrahedral elements is provided. The UL-FEM computation did not converge towards a solution when reaching a soil weight of $\gamma = 6$ kN/m^3. Figure 3.13 (right) depicts the deformed mesh for the UL-FEM computation at this applied soil weight. As can be seen, strong distortions of elements occur in the region of the mesh highlighted by the rectangular box such that the determinant of the Jacobian of these elements becomes negative. The deformed shape of one of these elements is shown enlarged. The results of the FE analysis as shown in Figure 3.13 (right) happen to give the impression that the material is also supported beyond the toe point, but this is not the case; only the six bottom nodes of the (enlarged) element are supported.

Figure 3.14 shows the computed deformation of the slope represented by material points at different loading stages for a MPM computation using 10-noded tetrahedral elements. One observes that material points move into elements that become newly activated in front of the initial slope. Thereby, the MPM correctly reproduces the support given to the slope by material deposited in front of its toe even without remeshing and/or a contact algorithm.

Figure 3.15 shows the incremental shear strains inside the slope of the final load increment. A localisation of deformations occurs along the bottom of the slope. Two shear bands that diagonally extend through the body of the slope develop from this zone.

A possible load-step dependency of results has been investigated for this problem by performing computations with 200, 600 and 1000 load steps. However, a comparison of the obtained results did not reveal any load-step dependency.

3.9.3 Retaining wall problem

A retaining wall problem consisting of a stiff block being pushed against soil is investigated in the last example. The soil is modelled by an elastic-plastic Mohr-Coulomb constitutive law and the stiff block by a linear-elastic material. Figure 3.16 shows the geometry and discretisation of the problem. Like in the previous examples, it is a plane

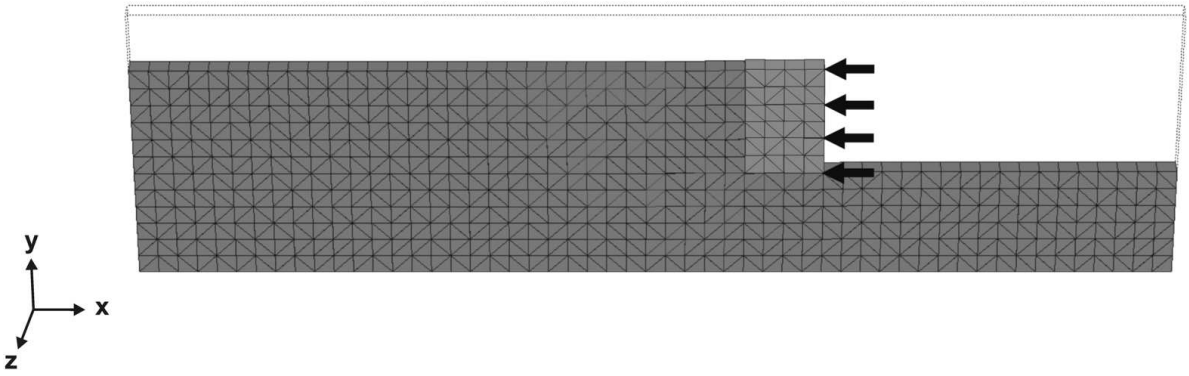

Figure 3.16: Geometry and discretisation of the retaining wall problem by prismatic elements

strain problem with a width of 0.1 m perpendicular to the plane of deformation. The total domain has the dimensions 5.3 $\times$ 1.2 m. Full fixity is applied along the lower edge, and a free-slip condition is applied on the left and right sides. The domain is discretised with 15-noded prismatic elements, each element containing 18 material points initially. The stiff block, lightly shaded in Figure 3.16, has the dimensions 0.6 $\times$ 0.4 m and a material weight of 20 kN/m^3, a Young's modulus of 100 MPa and a Poisson ratio of 0. The remaining active elements are soil elements with a material weight of 20 kN/m^3, elastic modulus of 10 MPa and Poisson's ratio of 0.3, cohesion of 10 kPa, internal friction angle of 30° and dilatancy angle of 0°.

The calculation is performed in two phases: firstly, gravity loading is applied, secondly, prescribed displacements of 600 mm are applied in equally sized increments on the stiff block. Here, use is made of the fact that with the MPM, the finite element mesh can be arbitrarily modified after each time step. Thus, the elements discretising the stiff block are updated as in the conventional updated Lagrangian FEM such that the boundary of the block coincides with element boundaries at all stages of the analysis. The finite element mesh is updated as described in Section 3.5.

Figure 3.17 shows the computational results of the considered earth pressure problem. A completely rough wall is considered with full adhesion, so that the soil just in front is sticking to the wall, but a wedge further in front is pressed out. One observes that some of the soil is falling on top of the stiff block. Shear bands in front of the stiff block occur as well as significant shear deformations at the bottom of the wall. A third shear band develops near the end of the simulation.

Figure 3.18 displays the computed load-displacement curve. The force consists of the horizontal earth pressure in front of the wall and the horizontal shear force below the stiff block (for a wall length of 0.1 m). Large displacements cause soil heave in front of the block and consequently an increase in earth pressure. For small deformations the force amounts to 5.6 kN which complies well with the analytical solution from classical earth pressure theory and the sliding force below the block.

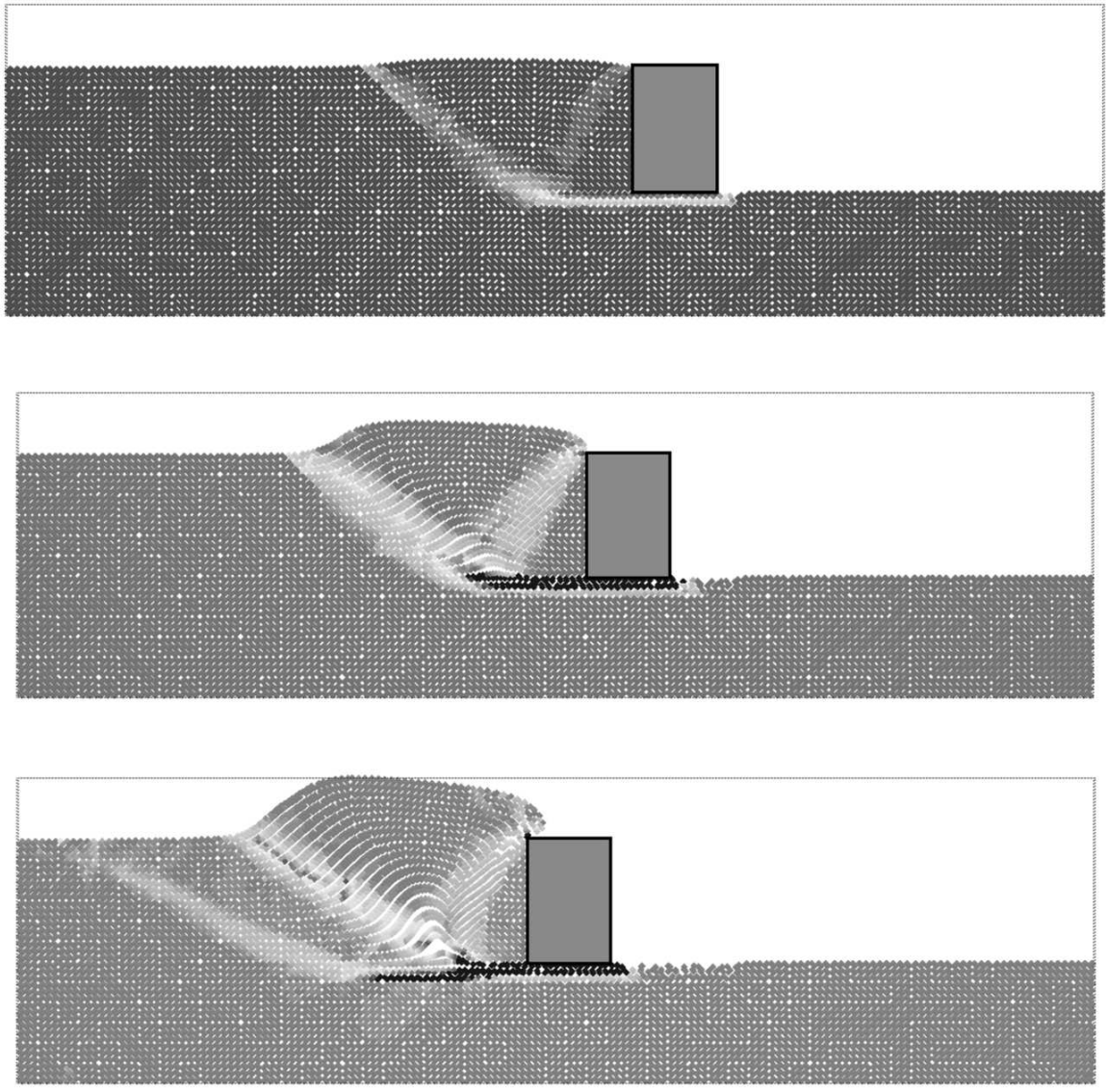

Figure 3.17: Deformation and incremental shear strains after a wall movement of 0, 300 and 600 mm

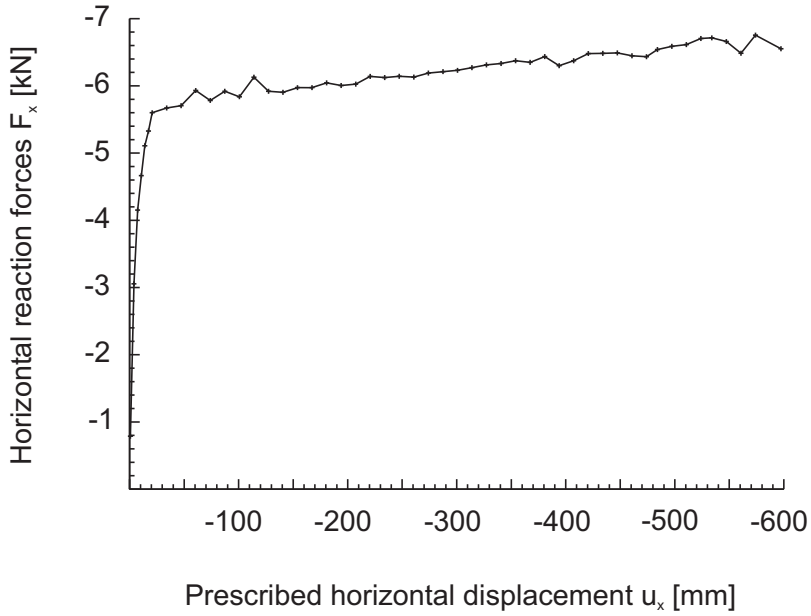

Figure 3.18: Computed load-displacement curve for the retaining wall

Chapter 4

Soil-structure interaction

Modelling contact between structures and surrounding soil is of importance in many geotechnical problems, since such contact significantly contributes to the mechanical behaviour of the structure. For example, piles being driven or jacked into soil generally carry their loads to a large extend through skin friction.

In conventional small-deformation finite element analyses of geotechnical problems, such soil-structure interaction is generally modelled by interface elements. This approach proved to be both robust and efficient [58]. Interface elements model contact by relating relative displacements between pairs of surface nodes of two bodies (dual nodes) through constitutive equations to contact stresses. For large deformations, however, this approach cannot be used in a straightforward manner, as the dual nodes of interface elements have to remain in direct contact. Indeed, interface elements cannot be used with an UL-FEM analysis, as relative displacements between dual nodes and subsequent remeshing destroy the required contact between dual nodes. For illustration, Figure 4.1 shows principal stresses for a rigid, elastic block subjected to gravity loading that displaces horizontally over a flat surface. Interface elements are placed beneath the block. Considerable relative displacements occur between the dual nodes of the interface elements: the top plane sticks to the block, while the bottom layer remains at its initial location. Consequently, the stresses induced by the block into the soil remain at the initial position of the block, whereas they should move with the sliding block. For this reason, (master-slave) contact algorithms tend to be applied in Total and Updated Lagrangian FE formulations [48]. With the MPM, however, large deformations do not require (full) remeshing so that the usage of interface elements forms an attractive extension of this method for solving soil-structure interaction problems, as will be shown in this chapter.

At first a brief introduction to the formulation of interface elements is given that identically applies to both the FEM and MPM. For a more extensive treatment of interface elements, the reader is referred to [58]. In Section 4.2 the adaptation of interface elements to the MPM is outlined. In Section 4.3 benchmark problems of a block sliding over a purely adhesive as well as a purely frictional surface and of a slope under gravity loading that is placed on an adhesive surface are presented.

4.1 Formulation of interface elements

In the present study, 3D interface elements compatible to both 4-noded and 10-noded tetrahedral volume elements were considered. However, computations with high-order

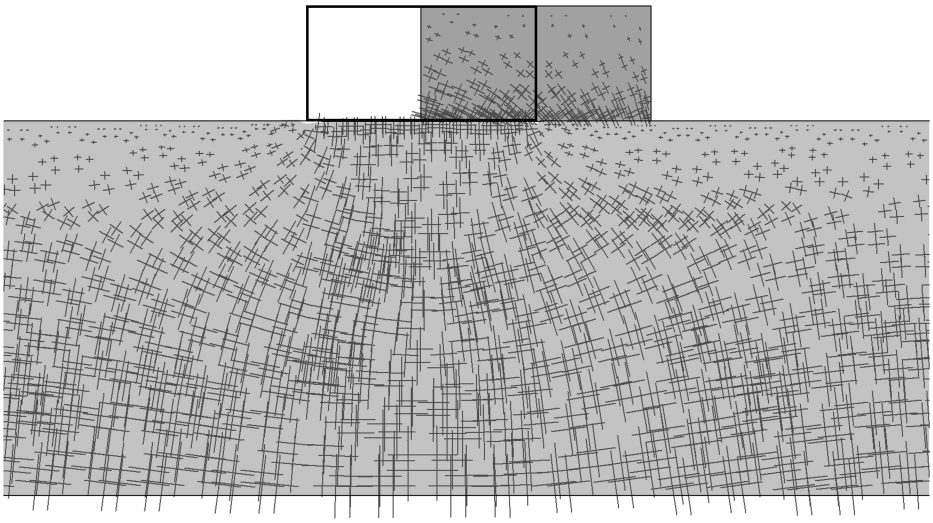

Figure 4.1: Principal stresses for a block-pushing test using interface elements in an UL-FEM analysis

interface elements proved considerably less stable than those with low-order interface elements. Therefore, only the use of low-order interface elements was further pursued and thus consequently also the use of corresponding low-order volume elements.

Interface elements consist of two 'faces'. In the most general case each face shares nodes with adjacent tetrahedral elements as illustrated in Figure 4.2 (left). Interface elements might also be placed along the boundary of a finite element mesh so that boundary conditions are applied on the nodes of the outer face. However, this case does not require any special treatment. Interface elements do not possess a finite thickness within the mesh and in the present implementation they do not keep track of the width of a possible gap between surfaces.

Slip is modelled through a relative displacement $\boldsymbol{w}$ between the two faces being related to the stress vector $\boldsymbol{t}$

$$\boldsymbol{w} = [w_n \;\; w_s \;\; w_t]^T \qquad \boldsymbol{t} = [\tau_n \;\; \tau_s \;\; \tau_t]^T \tag{4.1}$$

where $\boldsymbol{w}$ consists of a component w_n in normal direction and two tangential components w_s, w_t. The vector $\boldsymbol{t}$ contains the normal stress component τ_n and the two shear stress components τ_s and τ_t. Tensile stresses are defined to be positive. Interpolation of the relative displacement field inside interface elements from nodal displacements is performed by means of shape functions $\boldsymbol{N}$. Appendix A.4 provides a detailed description of the considered 6-noded interface elements including the shape functions.

In contrast to the volume elements which make use of Gaussian integration, Newton-Cotes integration is used with interface elements. Therefore, the locations of pairs of dual

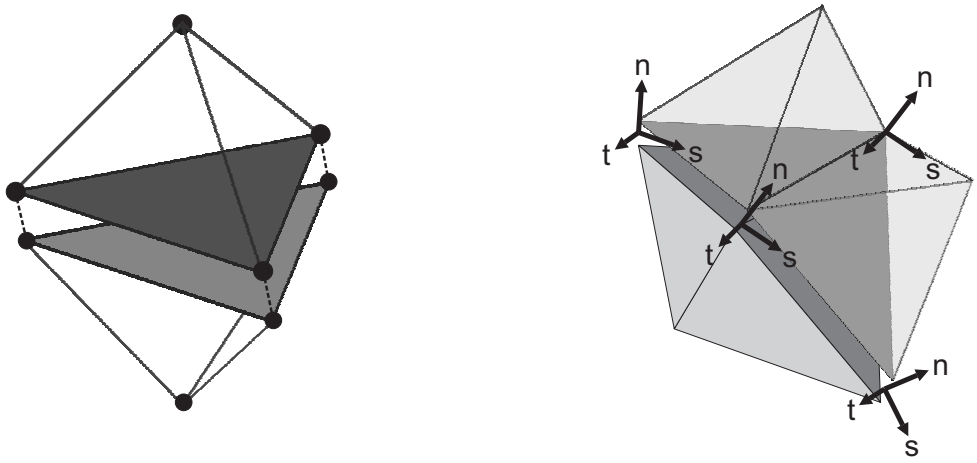

Figure 4.2: (left) Interface element placed between two 4-noded tetrahedral elements; (right) local coordinates for pairs of dual nodes, Newton-Cotes integration points respectively

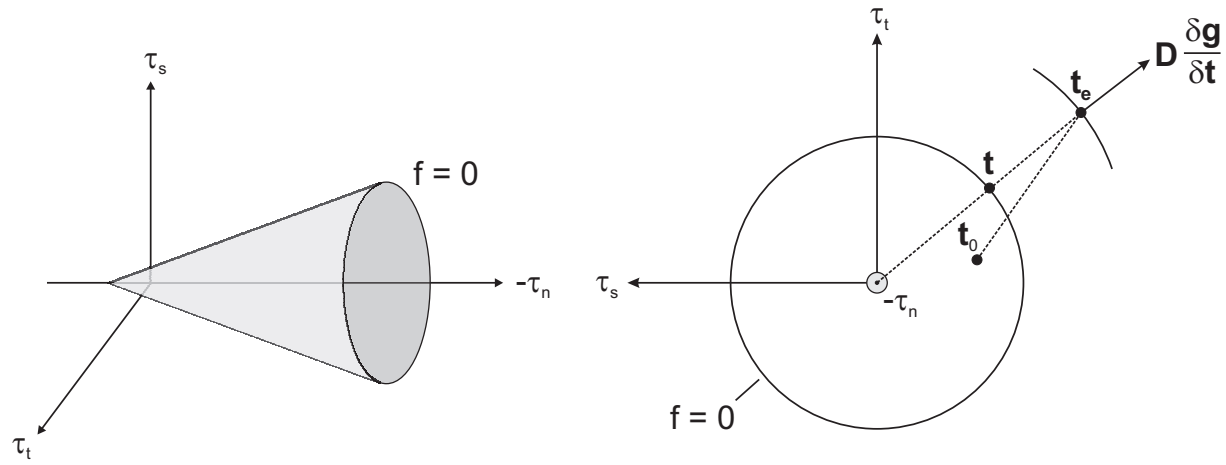

Figure 4.3: (left) Illustration of the yield function $f = 0$; (right) radial return mapping illustrated for cross-section through the yield surface

nodes and integration points coincide. In case of a curved slip surface, the normal and tangential directions are not identical at all pairs of dual nodes of an interface element, integration points respectively. Therefore, local coordinate systems are assigned to each pair of dual nodes as illustrated in Figure 4.2 (right). The computation of the normals at pairs of dual nodes is described in Appendix A.4.

With $\dot{\boldsymbol{w}}^p$ denoting the irreversible slip rate between two faces, the elastic-plastic constitutive relation in rate form reads

$$\dot{\boldsymbol{t}} = \boldsymbol{D}\left(\dot{\boldsymbol{w}} - \dot{\boldsymbol{w}}^p\right) \tag{4.2}$$

where $\boldsymbol{D}$ is a diagonal matrix of elastic spring constants, whose diagonal entries D_n, D_s and D_t are in [N/m^3]. It should be noted that, in contrast to volume elements, no shape function derivatives are involved in the stress-displacement relation. Thus, the stress distribution of the low-order interface elements is linear whereas adjacent volume elements exhibit a constant stress distribution. The irreversible slip rate $\dot{\boldsymbol{w}}^p$ corresponds to the flow rule [63]

$$\dot{\boldsymbol{w}}^p = \dot{\lambda}\frac{\partial g}{\partial \boldsymbol{t}} \tag{4.3}$$

where $\frac{\partial g}{\partial \boldsymbol{t}}$ determines the direction of plastic slip and $\dot{\lambda}$ is the magnitude of the plastic slip rate. The plastic potential function g is defined as

$$g\left(\boldsymbol{t}\right) = \sqrt{\tau_s^2 + \tau_t^2} + \tau_n \tan\psi_i \tag{4.4}$$

where ψ_i is an interface angle of dilatancy that relates plastic volume change to plastic slip. On substituting Equation 4.3 into 4.2, it is found that

$$\dot{\boldsymbol{t}} = \boldsymbol{D}\left(\dot{\boldsymbol{w}} - \dot{\lambda}\frac{\partial g}{\partial \boldsymbol{t}}\right) \tag{4.5}$$

Irreversible slip occurs if the condition

$$f\left(\boldsymbol{t}\right) = \sqrt{\tau_s^2 + \tau_t^2} + \tau_n \tan\phi_i - a = 0 \tag{4.6}$$

is fulfilled. Here, f denotes the yield function, ϕ_i the interface friction angle and a the adhesive interface strength. Equation 4.6 takes the form of a cone in the three-dimensional stress space as shown in Figure 4.3 (left). In case of $f < 0$ only elastic deformations occur, which requires no further consideration. A state $f > 0$ is not allowed. Thus, stress states are either located on the cone surface of Figure 4.3 (left) or in the elastic range represented by the interior of the cone. If $f = 0$, distinction must be made between the case that loading shifts the stress state into the elastic range ($\dot{f} < 0$) and the case that loading keeps the soil in a plastic state ($\dot{f} = 0$). Only the latter case produces irreversible slip. Writing out the consistency condition $\dot{f} = 0$ gives

$$\frac{\partial f}{\partial \boldsymbol{t}}^T \dot{\boldsymbol{t}} = 0 \tag{4.7}$$

Inserting Equation 4.5 into Equation 4.7 renders

$$\frac{\partial f}{\partial \boldsymbol{t}}^T \boldsymbol{D} \left(\dot{\boldsymbol{w}} - \dot{\lambda} \frac{\partial g}{\partial \boldsymbol{t}} \right) = 0 \tag{4.8}$$

From it, $\dot{\lambda}$ can be determined to be

$$\dot{\lambda} = \frac{1}{d} \frac{\partial f}{\partial \boldsymbol{t}}^T \boldsymbol{D}\, \dot{\boldsymbol{w}} \quad \text{with} \quad d = \frac{\partial g}{\partial \boldsymbol{t}}^T \boldsymbol{D} \frac{\partial f}{\partial \boldsymbol{t}} \tag{4.9}$$

Insertion of this equation for $\dot{\lambda}$ into Equation 4.5 gives the following relation between stress and relative displacement

$$\dot{\boldsymbol{t}} = \boldsymbol{M}\, \dot{\boldsymbol{w}} \quad \text{with} \quad \boldsymbol{M} = \boldsymbol{D} - \frac{1}{d} \boldsymbol{D} \frac{\partial g}{\partial \boldsymbol{t}} \frac{\partial f}{\partial \boldsymbol{t}}^T \boldsymbol{D} \tag{4.10}$$

4.1.1 Time integration of the constitutive equation

What remains to be done is integration of Equation 4.10 over a load step. Writing Equation 4.2 in incremental form renders

$$\Delta \boldsymbol{t} = \boldsymbol{D} \left(\Delta \boldsymbol{w} - \Delta \boldsymbol{w}^p \right) = \boldsymbol{D} \left(\Delta \boldsymbol{w} - \Delta\lambda \frac{\partial g}{\partial \boldsymbol{t}} \right) = \boldsymbol{D}\, \Delta \boldsymbol{w} - \Delta\lambda\, \boldsymbol{D} \frac{\partial g}{\partial \boldsymbol{t}} \tag{4.11}$$

Stresses at the end of a load step $\boldsymbol{t}$ can be computed from interface stresses $\boldsymbol{t}_0$ at the beginning of a load step by means of $\boldsymbol{t} = \boldsymbol{t}_0 + \Delta \boldsymbol{t}$. Inserting Equation 4.11 gives

$$\boldsymbol{t} = \boldsymbol{t}_e - \Delta\lambda\, \boldsymbol{D} \frac{\partial g}{\partial \boldsymbol{t}} \quad \text{with} \quad \boldsymbol{t}_e = \boldsymbol{t}_0 + \boldsymbol{D}\, \Delta \boldsymbol{w} \tag{4.12}$$

Let $\boldsymbol{t}^*$ denote the stress state where a stress path starting from $\boldsymbol{t}_0$ crosses the yield surface. Depending on the choice of integration scheme, the terms $\frac{\partial f}{\partial \boldsymbol{t}}$ and $\frac{\partial g}{\partial \boldsymbol{t}}$ might be evaluated for $\boldsymbol{t}^*$ (explicit integration), $\boldsymbol{t}$ (implicit integration) or for instance the average of $\boldsymbol{t}^*$ and $\boldsymbol{t}$. Vermeer and Van Langen [63] argue that the most stable time integration is obtained when evaluating the term $\frac{\partial g}{\partial \boldsymbol{t}}$ for the final stress state $\boldsymbol{t}$ of a load step. As $\boldsymbol{t}$ is of course not known in advance, evaluation is performed for $\boldsymbol{t}_e$ instead. But Figure 4.3 (right) shows that this renders the same gradient $\frac{\partial g}{\partial \boldsymbol{t}}$.

A solution for $\Delta\lambda$ is derived from the yield condition $f(\boldsymbol{t}) = 0$ [63] with $\boldsymbol{t}$ taken from Equation 4.12. This gives

$$\Delta\lambda = \frac{1}{d} f(\boldsymbol{t}_e) \quad \text{with} \quad d = \frac{\partial f}{\partial \boldsymbol{t}}^T \boldsymbol{D} \frac{\partial g}{\partial \boldsymbol{t}} \tag{4.13}$$

and together with Equation 4.12 one obtains

$$\boldsymbol{t} = \boldsymbol{t}_e - \frac{\langle f(\boldsymbol{t}_e) \rangle}{d} \boldsymbol{D} \frac{\partial g}{\partial \boldsymbol{t}} \tag{4.14}$$

where $\frac{\partial g}{\partial \boldsymbol{t}}$ is evaluated for $\boldsymbol{t}_e$. The brackets $\langle . \rangle$ imply $\langle x \rangle = 0$ for $x < 0$ and $\langle x \rangle = 1$ for $x \geq 0$.

Special attention must be paid to the apex point of the yield surface. Here,

$$\tau_n = a \cot \phi_i \quad \text{and} \quad \tau_{s/t} = 0 \tag{4.15}$$

for $f(\boldsymbol{t}_e) > 0$. Even closing a gap might be accounted for, but this is not considered in the present study.

4.1.2 Evaluation of the elastic stiffness matrix

The definition of the elastic stiffness matrix $\boldsymbol{D}$, the diagonal terms D_n, D_s and D_t respectively, may be evaluated by considering deformations of a thin soil sample in a simple shear test. To this end, a virtual interface thickness δ is introduced that corresponds to the height of a simple shear sample. The virtual thickness represents the thickness of the shear zone along the slip surface. The stiffness terms in normal and tangential direction may now be written as

$$D_n = \frac{E_{\text{oed}}}{\delta} \quad \text{and} \quad D_s = D_t = \frac{G}{\delta} \tag{4.16}$$

where E_{oed} denotes the constrained modulus and G the soil's shear modulus. The Poisson ratio ν is set to a value of 0.45 in order to prevent interface elements from inverting: nodes of one face would cross the opposite face which would imply a negative thickness. Thereby, D_n is roughly 10 times larger than $D_{s/t}$. The specification of the virtual thickness would require calibration for a specific soil-structure problem through testing. Setting the virtual thickness to one tenth of the average element size proved to be a good compromise. A large virtual thickness induces unrealistic large deformations in the elastic range of deformation. A small virtual thickness might lead to an ill-conditioning of the global stiffness matrix.

Computation of the linear-elastic element stiffness matrix $K_{\text{interface}}$ and internal force vector $F_{\text{interface}}$ is straightforward

$$\boldsymbol{K}_{\text{interface}} = \int_S \boldsymbol{N}^T \boldsymbol{D} \boldsymbol{N} \, \mathrm{d}S = \sum_{e=1}^{n_{ife}} \sum_{i=1}^{n_{ip}} \boldsymbol{N}_i^T \boldsymbol{D} \boldsymbol{N}_i \, \Delta S_i \tag{4.17}$$

$$\boldsymbol{F}_{\text{interface}} = \int_S \boldsymbol{N}^T \boldsymbol{t} \, \mathrm{d}S = \sum_{e=1}^{n_{ife}} \sum_{i=1}^{n_{ip}} \boldsymbol{N}_i^T \boldsymbol{t}_i \, \Delta S_i \tag{4.18}$$

where n_{ife} denotes the number of considered interface elements, n_{ip} is the number of integration points per interface element and ΔS_i stands for the weight of integration point i which is computed as described in Appendix A.4.

Newton-Cotes integration is used with interface elements because it proved convenient with regard to the adaptation of the interface elements to the MPM. Furthermore, as reported by [58], Newton-Cotes integration reduces oscillations at stress concentrations, produces a continuous stress distribution across element boundaries and keeps disturbances confined to small regions.

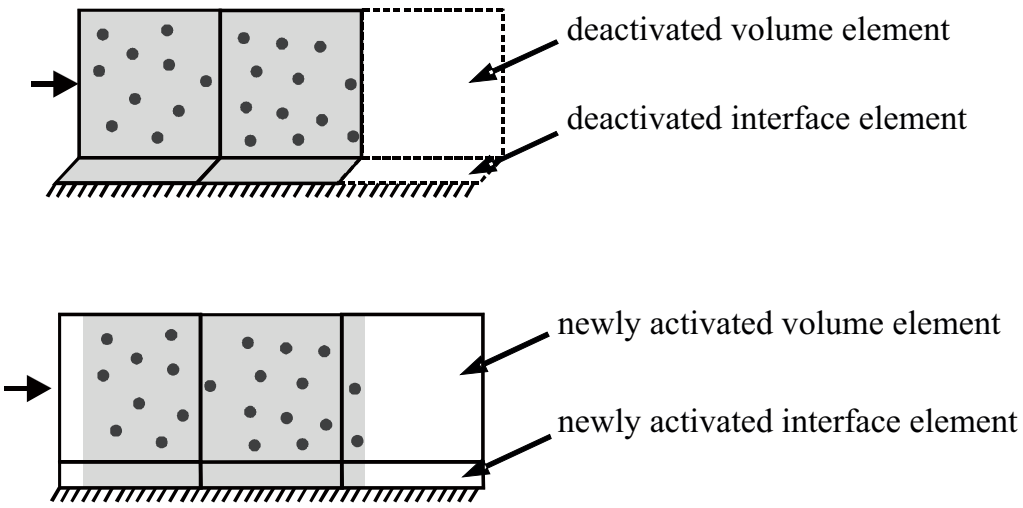

Figure 4.4: Usage of interface elements with the MPM; (left) deformed state as result of the Lagrangian phase of a calculation step; (right) reset mesh directly after each Lagrangian phase

4.2 Adaptation of interfaces to the Material Point Method

In most cases, interface elements are used in between a soil and a stiffer body, where both bodies have a finite element discretisation. In the following, the special situation of Figure 4.4 is considered where interface elements are located at a fixed boundary.

With the MPM only small deformations of the mesh occur as the mesh is frequently reset to its initial configuration. Consequently, interface elements attached to the mesh must likewise be reset. As indicated in Figure 4.4 (right), material points might eventually enter volume elements adjacent to interface elements that were initially empty. Inversely, initially filled volume elements might become void of material points. Thus, interface elements must cover the entire surface along which material is expected to move. According to the approach taken with volume elements, interface elements that are adjacent to activated soil elements are marked as activated while all other interface elements are marked as deactivated.

In contrast to volume elements, interface elements do not make use of material points. Thus, when resetting the mesh, interface stresses cannot be computed from moving interface material poins. Nevertheless, interface stresses must be computed after resetting the mesh. This can be done by considering equilibrium of forces acting on the interface nodes in contact with the soil. Here, use is made of the fact that accurate stresses are available in the material points of the soil adjacent to the interface. Accurate interface

stresses can then be computed from the nodal force equilibrium equation

$$\boldsymbol{F}_{\text{interface}} \;=\; \boldsymbol{F}_{\text{external}} \;-\; \boldsymbol{F}_{\text{soil}} \tag{4.19}$$

where

$$\boldsymbol{F}_{\text{soil}} \;=\; \int_V \boldsymbol{B}^T\,\boldsymbol{\sigma}\;\mathrm{d}V \qquad\qquad \boldsymbol{F}_{\text{external}} \;=\; \int_V \boldsymbol{N}^T\,\boldsymbol{b}\;\mathrm{d}V$$

In the following, interface stresses at pairs of dual nodes $\hat{\boldsymbol{t}}$ are considered which relate to the interface stresses $\boldsymbol{t}_i$ at integration points i by

$$\boldsymbol{t}_i \;=\; \sum_{j=1}^{n_n} \boldsymbol{N}_{ij}\,\hat{\boldsymbol{t}}_j \tag{4.20}$$

where n_n is the number of pairs of interface dual nodes. The contribution of $\boldsymbol{F}_{\text{interface}}$ to the nodal force equilibrium is then

$$\boldsymbol{F}_{\text{interface}} \;=\; \int_S \boldsymbol{N}^T\,\boldsymbol{N}\,\hat{\boldsymbol{t}}\;\mathrm{d}S \;=\; \sum_{e=1}^{n_{ife}} \sum_{i=1}^{n_{ip}} \boldsymbol{N}_i^T\,\boldsymbol{N}_i\,\hat{\boldsymbol{t}}\;\Delta S_i \tag{4.21}$$

After resetting the mesh at the end of a loading step, all above quantities are known with the exception of the interface stresses $\hat{\boldsymbol{t}}$. Hence one is left with the calculation of $\hat{\boldsymbol{t}}$. For further consideration, it is convenient to assemble all stresses of pairs of interface dual nodes into a super vector

$$\boldsymbol{T} \;=\; \left[\hat{\tau}_{n\,1}\;\; \hat{\tau}_{s\,1}\;\; \hat{\tau}_{t\,1}\;\; \ldots\;\; \hat{\tau}_{t\,n_I}\right]^T \tag{4.22}$$

where n_I is the number of pairs of dual nodes of all interfaces. Now Equation 4.21 can be written as

$$\boldsymbol{F}_{\text{interface}} \;=\; \boldsymbol{M}\;\cdot\;\boldsymbol{T} \qquad\qquad \boldsymbol{M} \;=\; \sum_{e=1}^{n_{ife}} \sum_{i=1}^{n_{ip}} \boldsymbol{N}_i^T\,\boldsymbol{N}_i\,\Delta S_i \tag{4.23}$$

For the situation of Figure 4.4, vector $\boldsymbol{T}$ has a length of three times the number of pairs of interface dual nodes, i.e. $3\;n_I$. The matrix $\boldsymbol{M}$ has dimension $3\;(n_{ife}\,n_{ip}\;\times\;n_I)$. Hence, Equation 4.19 can only be solved for $\hat{\boldsymbol{t}}$ in the special case of $n_I \;=\; n_{ife}\,n_{ip}$, when the number of pairs of dual nodes coincides with the number of interface integration points. This special case is obtained for Newton-Cotes integration, being thus most suitable for the devised algorithm. Another convenient property of Newton-Cotes integration lies in the fact that it results in a diagonal matrix $\boldsymbol{M}$ so that Equation 4.23 is extremely easy to solve for $\hat{\boldsymbol{t}}$.

In the case that interface elements are placed in between solid bodies rather than on the boundary of the mesh, the mesh cannot simply be reset to its initial configuration, as in contrast to Figure 4.4 the interface moves inside a soil body. Rather than resetting the mesh to its initial position it is now possible to rotate and translate the mesh according to the new position of the structural body. The stress recovery algorithm will now yield two possibly slightly different solutions for the interface stress; one solution is obtained from the nodal forces on the soil-side nodes and another from nodal forces on the side of

the structural body. In case of significant differences between both solutions, the average of both solutions may be computed and a zero load step may be performed, in which all loads are kept constant. This intermediate load step has no physical meaning and resulting deformations are neglected. However, in the frame of the presented study only the situation of interface elements placed along a mesh boundary has been considered.

4.3 Validation

4.3.1 Block-pushing test

For validation, the sliding of a rigid block discretised by material points over a surface featuring interface elements has been simulated. The cases of a purely adhesive and a purely frictional sliding surface have been considered.

The block has a length of 4 m and a height of 2 m. Only a thin slice with a width of 0.5 m is considered. The block material is linear-elastic with a Young's modulus of 15 MPa and a Poisson ratio of 0. The geometry and discretisation of the block in its initial configuration are shown in Figure 4.5 (top). The block is pushed along the bottom surface by a uniformly distributed load acting on the side of the block. In case of frictional contact, a self-weight of 5 kN/m^3 is applied on the block before it is pushed along the bottom surface. With this benchmark, the distributed load is not applied on nodes which would imply adjustment of the mesh to the moving boundary of the block but on material points as described in Chapter 3. The resulting smearing out of the applied traction across a layer of block elements appears not to have a significant impact on results.

In case of adhesive contact, an adhesion of a = 10 kPa has been applied and tensile stresses are allowed to occur in the sliding surface. In case of frictional contact a friction angle of ϕ_i = 45° has been used and, for numerical reasons, a small value of adhesion of 0.001 kPa. With the benchmarks presented in this chapter, the interface dilatancy angle ψ_i is set equal to zero which implies non-dilatant behaviour. In both computations, interface stiffnesses of D_n = 10 MN/m^3 and $D_{s/t}$ = 1 MN/m^3 have been used which render a very soft sliding surface.

Figure 4.5 (center) shows the final deformed state of the block after it has been moved by a distance of 1.2 m. The load-displacement curves for a point on the right side of the block are shown in Figure 4.6 for the cases of frictional and adhesive contact. After reaching the threshold value of plastic slip, a constant reaction force of 20 kN is obtained for both computations that corresponds well to the theoretical sliding resistance

$$R = (\gamma h \tan\phi + a)\ s = 20\ kN \tag{4.24}$$

with s = 2 m^2 being the area covered by the block.

On considering adhesive interfaces, it is important to distinguish between fully filled and partially filled interfaces. Partially filled elements will occur just in front and just behind the block as shown in Figure 4.5 (bottom). In order to take into account such partially filled interface elements, the adhesion of interface elements adjacent to partially filled block elements is reduced. The degree of filling of an adjacent volume element is used as reduction factor for the adhesion of the interface element.

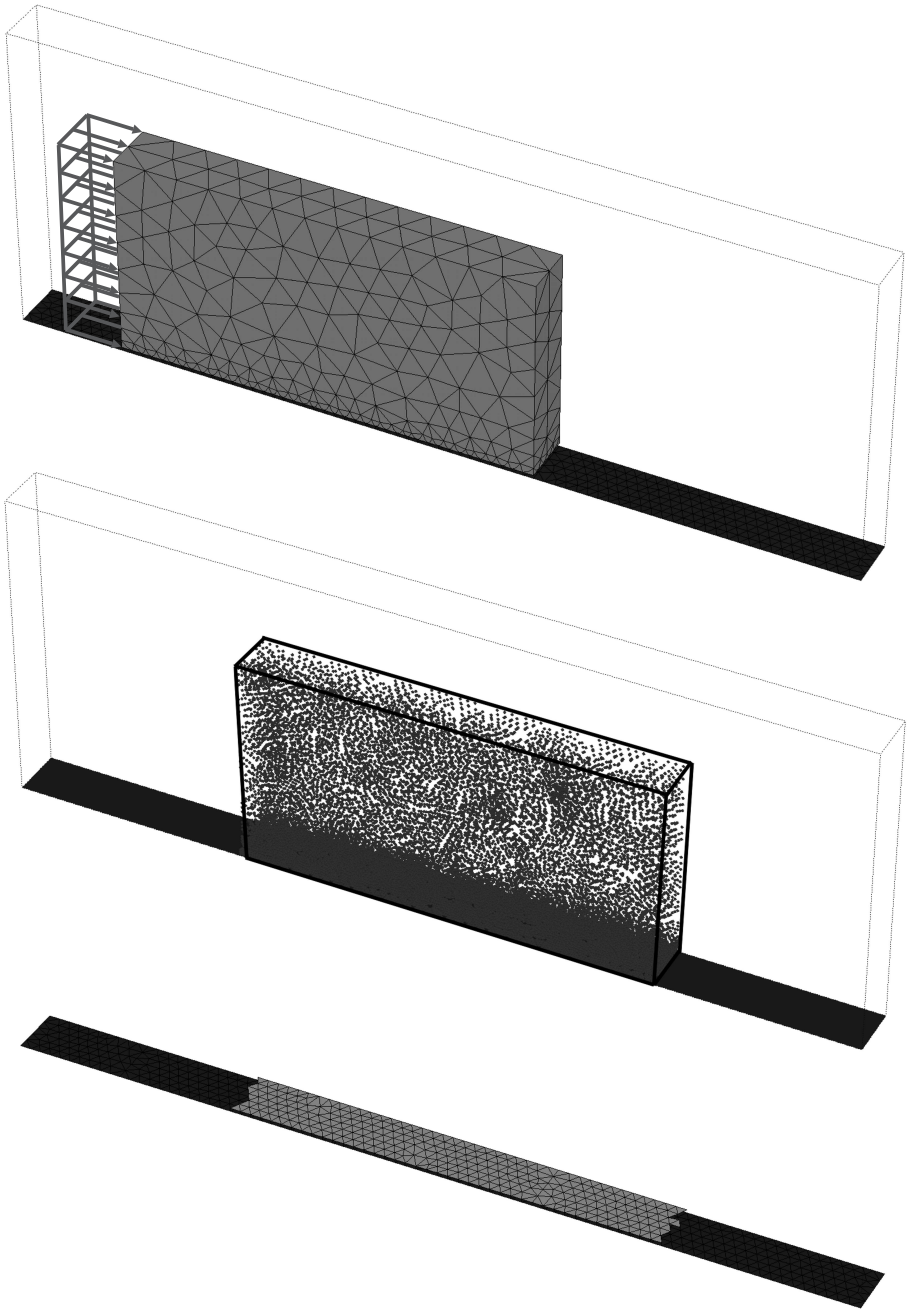

Figure 4.5: Block-pushing test; (top) discretisation of block with 4-noded tetrahedral elements; (center) material point discretisation after block displacement of 1.2 m; (bottom) activated interface elements in final deformed state

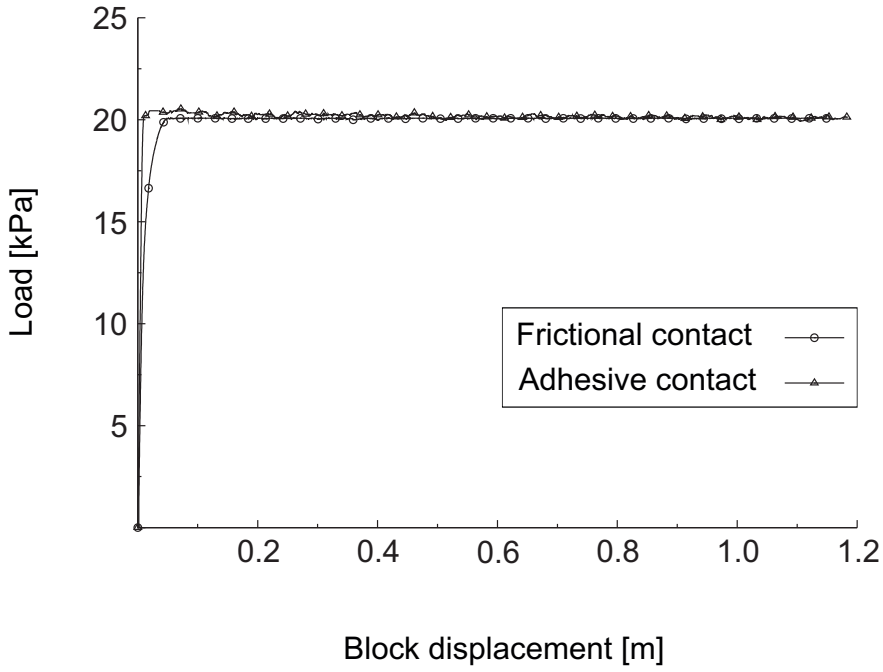

Figure 4.6: Load-displacement curves for block with adhesive and frictional contact

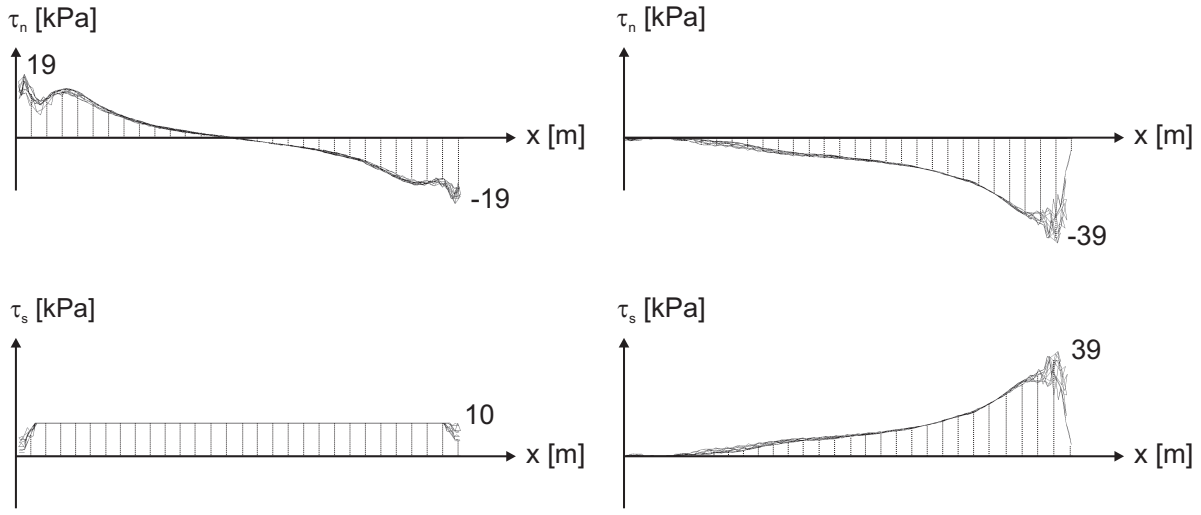

Figure 4.7: Stress distributions of activated interface elements along the bottom of the slope in the final deformed state; (left side) adhesive contact and (right side) frictional contact; (top) normal stresses and (bottom) shear stresses

Figure 4.7 shows the resulting normal and shear stress distributions of the activated interface elements at the final deformed state of the block for the cases of adhesive and frictional contact. It should be noted that the presented stress distributions are 'raw' data computed at interface nodes rather than results postprocessed by means of smoothing techniques commonly used with the FEM. The normal stress distributions reflect the momentum induced by the applied distributed load. As may be expected, the normal and shear stress distributions are approximately the same in case of the pure frictional contact. Oscillations occur locally at the front and back of the active sliding surface that coincide with stress peaks inside the block.

4.3.2 Slope analysis

The second analysed boundary value problem consists of a slope with the same dimensions and material properties as the problem considered in Chapter 3: a Young's modulus of 100 kPa, a Poisson ratio of 0.33 and the Tresca failure criterion with a cohesion of 1 kPa. The weight of the material is gradually increased up to a value of 10 kN/m^3. The slope is discretised with 4-noded tetrahedral elements, each containing initially 10 material points. Horizontal nodal displacements are fixed at the left and right side of the mesh. Figure 4.8 shows the used discretisation. The frame indicates the size of the space that is discretised by finite elements.

However, now, interface elements are placed at the bottom of the mesh to model adhesive contact with an adhesion of 0.5 kPa as well as an adhesion equal to the soil's cohesion of 1 kPa. The normal stiffness of the interface elements is set to $D_n = 76$ MN/m^3 and the tangential stiffness to a value of $D_s = D_t = 7.6$ MN/m^3. Tensile stresses are allowed to occur both in interface as well as volume elements.

Figure 4.9 shows the load-displacement curves for the computations of the slope with adhesive bottom surface plotted for an identical sample point at the head of the slope.

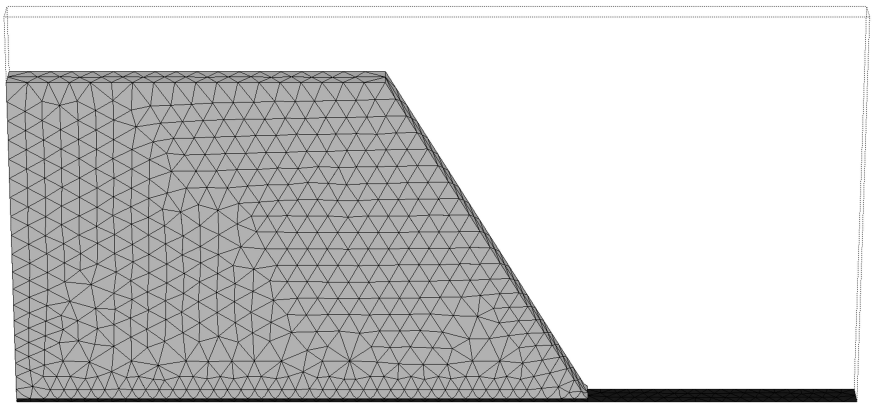

Figure 4.8: Discretisation of slope with 4-noded tetrahedral elements

Furthermore, the curve for the computation with a fixed bottom boundary of the mesh of Figure 3.12 (bottom) is plotted. The obtained results indicate that the deformation mechanisms for the computation with interfaces and $a = c$ is largely identical to the one without interfaces. The insertion of interface elements corresponds to a local mesh refinement at the bottom of the mesh. Given that both computations produce similar results, the degree of refinement used along the fixed bottom of the mesh, shown in Figure 3.12 (c), appears to be comparable to the insertion of interface elements. In case of the computation with $a = c$ / 2, plastic deformation starts to dominate the deformation process at a smaller soil weight compared to the computation with fully rough contact whereas the subsequent displacement increments are identical in magnitude — the load-displacement curve is just shifted downward. The final deformed state of the slope is compared in Figure 4.10 for the cases of $a = c$ / 2 and $a = c$ through plotting the respective material point discretisations inside the discretised space. In case of the computation with $a = c$ / 2, one layer of deactivated elements separates the toe of the slope from the mesh boundary so that the boundary is not just yet 'felt' by the advancing slope. In case of the computation without interface elements, material topples over the (fixed) toe of the slope as shown in Figure 3.14. When employing interface elements, soil material slides along the bottom of the mesh, which yields a somewhat more realistic deformation process. This can be seen in Figure 4.10, where material points lie closer to the bottom surface compared to the computation with a fixed boundary. This is even more pronounced in case of $a = c$ / 2 than $a = c$.

Figure 4.11 shows the incremental shear strains of the final load increment for the two computations with interface elements. The development of shear bands in case of $a = c$ agrees with the one shown in Figure 3.15 for the computation without interface elements. This confirms that both deformation processes are very similar. For $a = c$ / 2, incremental shear strains concentrate in inclined shear bands rather than in a shear band that extends along the bottom of the mesh from the very toe of the slope to the back as with fully rough contact. With both computations, some mesh dependency can be observed in the development of shear bands. It should be noted that different color legends are used for the two figures so that the coloring does not reflect identical magnitudes of straining for the two computations. When displaying incremental strains that may vary significantly from one load step to the next, comparing the magnitudes of shear strain increments would not be very meaningful.

Figure 4.12 depicts the accumulated shear strains for all three slope computations in the final deformed state. The color legends used for the computations without interface elements and with interfaces and $a = c$ are identical. Because the accumulated shear strains of the computation with $a = c$ / 2 are far smaller than those for the fully rough contact, a different legend has been chosen for the bottom figure. In compliance with the observed similarity of the two computations with a fully rough bottom boundary, the layer of heavy shear strains is only slightly wider in case of the computation without interface elements. For the computation with $a = c$ / 2, maximum shear strains concentrate further in the interior of the slope. The toe of the slope is pushed forward as a more or less rigid block. The maximum shear strain is only one sixth of the maximum shear strain of the computation without interface elements.

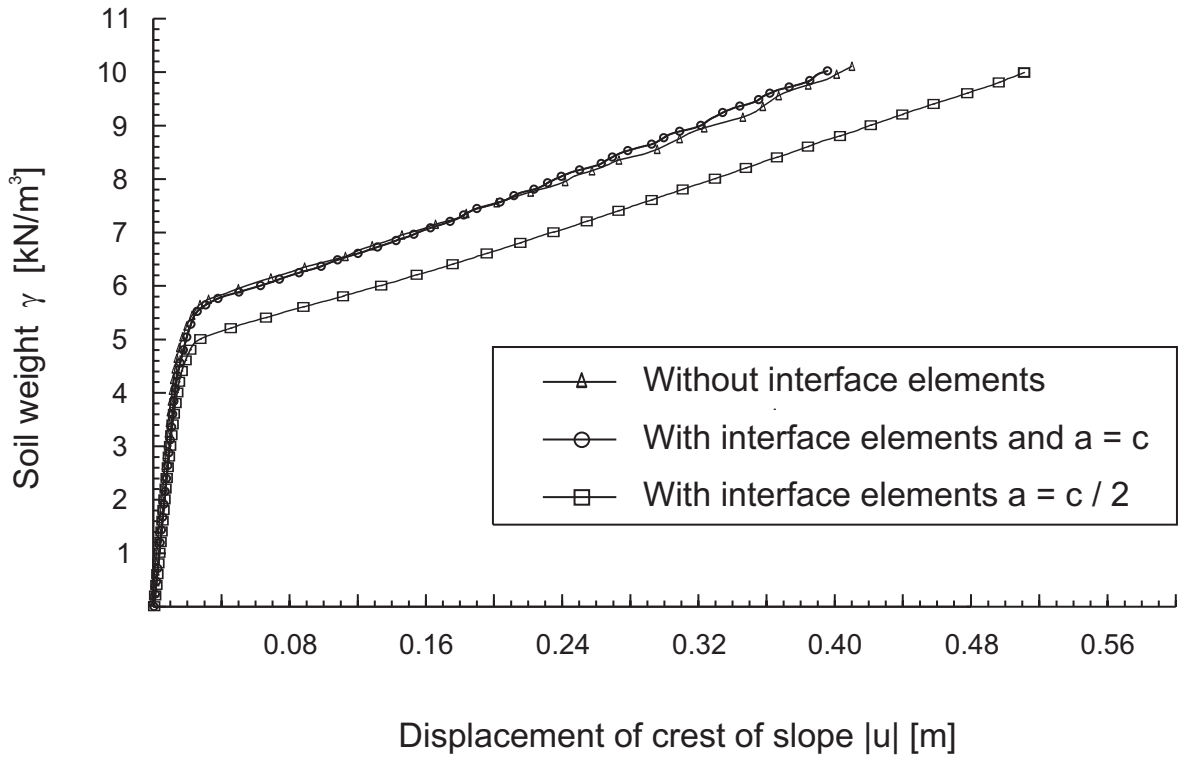

Figure 4.9: Load-displacement curves for the slope computed with the MPM using 4-noded tetrahedral elements

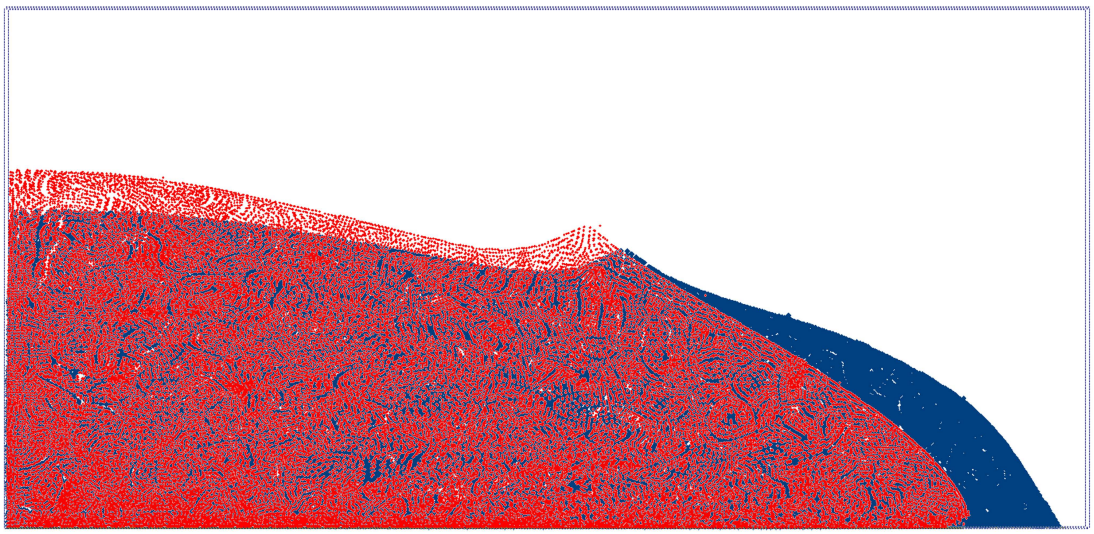

Figure 4.10: Location of material points for the deformed slope for $a = c$ and $a = c$ / 2

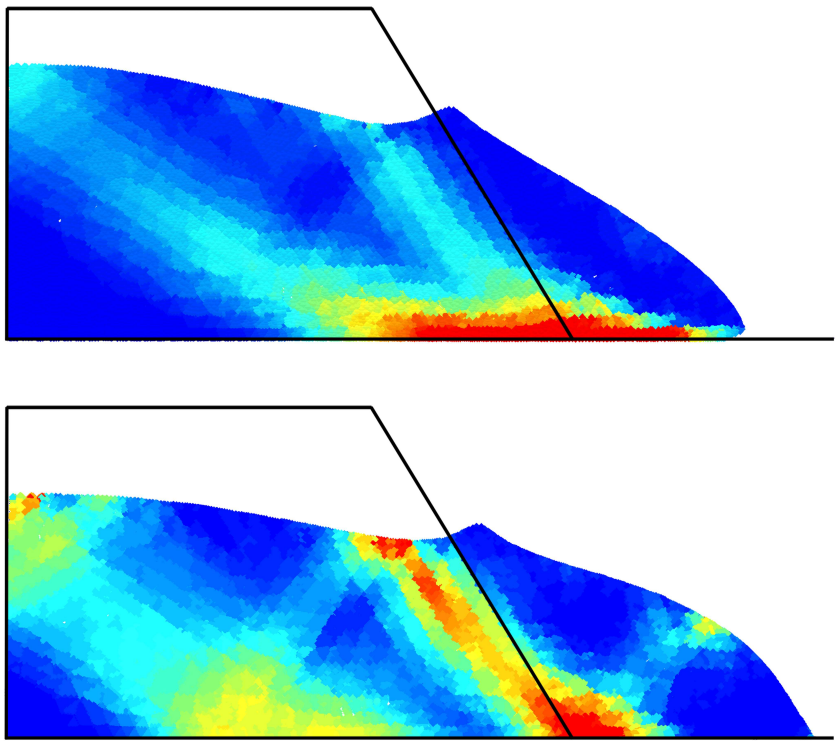

Figure 4.11: Incremental shear strains for the slope in the final deformed state with interface elements placed along the bottom boundary with (top) $a = c$ and (bottom) $a = c$ / 2

Figures 4.13, 4.14 and 4.15 show the normal and shear stress distributions along the bottom surface of the slope for the final deformed state of the slope. In case of the computation without interface elements, stresses are plotted for a horizontal cross section drawn slightly above the bottom surface. Here, σ_{xy} inside the soil is plotted instead of the shear stress within the interface elements. For all three computations, the maximum value of the normal stress of about -8 kPa corresponds well to the expected stress value that can be roughly estimated from a final height of the slope at the left boundary of the mesh of approximately 0.8 m. As can be seen in Figure 4.10, the height of the slope is slightly lower in case of the computation with $a = c$ / 2, which reflects in the lower normal stresses of the interface elements. Throughout the zones of heavy shear strain shown in Figure 4.12, the maximum shear stress imposed by the respective limit is reached. Shear stresses gradually decrease towards the back of the slope, where only a small lateral movement of soil occurs. In case of the computations with a fully rough bottom surface, with or without interface elements, slight oscillations of normal and shear stresses occur.

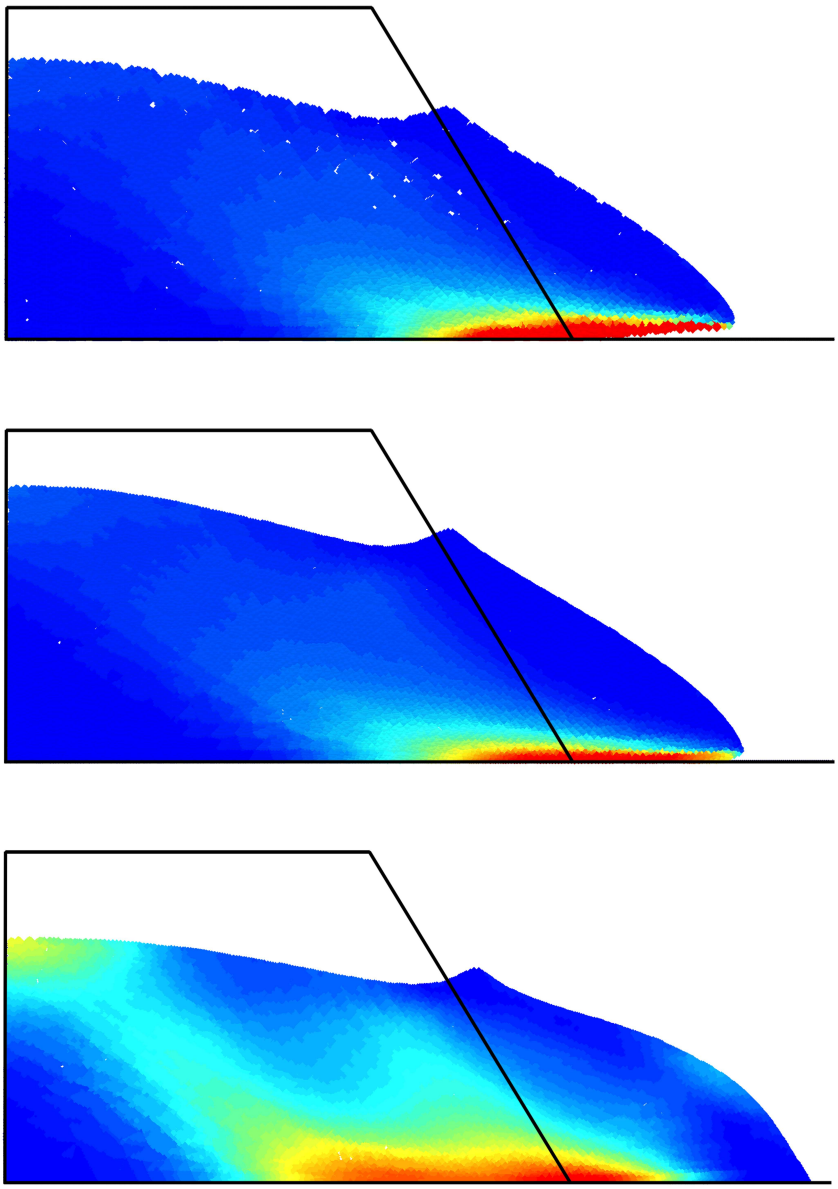

Figure 4.12: Accumulated shear strains for the slope in the final deformed state: (top) analysis without interface elements; (center) with interface elements and a = c and (bottom) a = c / 2

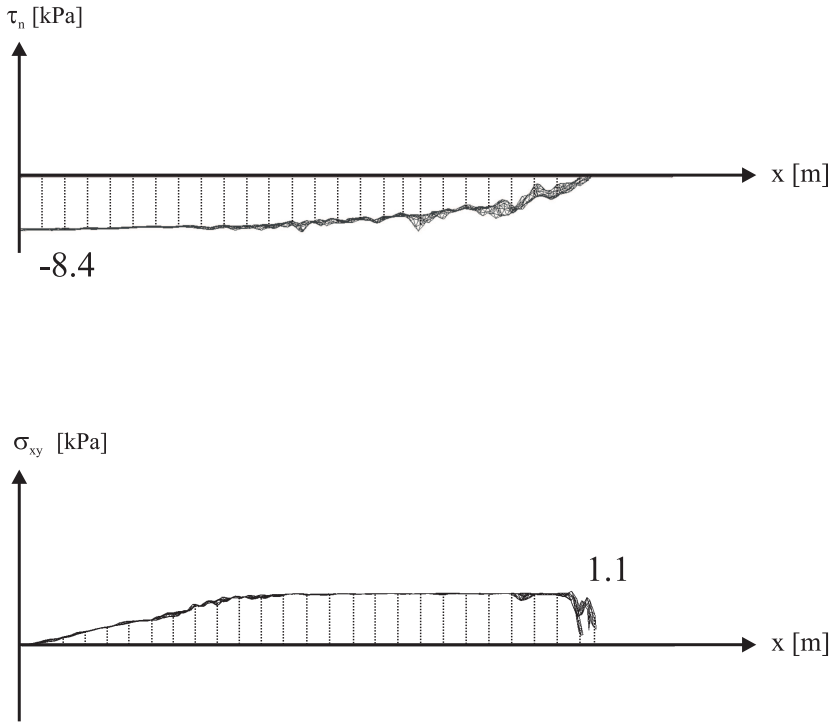

Figure 4.13: Distribution of normal (top) and shear stresses (bottom) along the bottom of the slope in the final deformed state without interface elements for a cross section just above the bottom surface

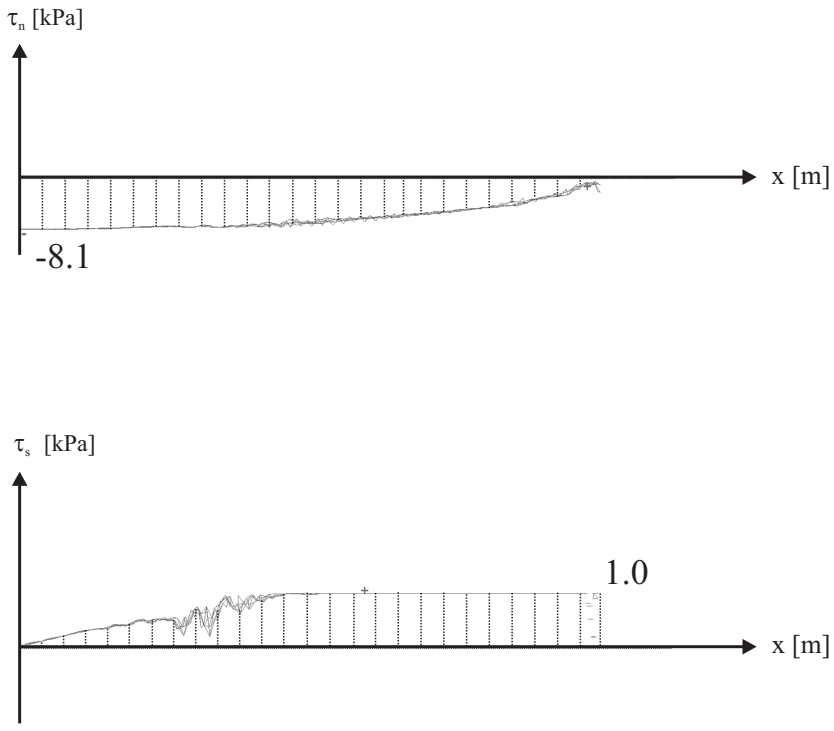

Figure 4.14: Distribution of normal (top) and shear stresses (bottom) along the bottom of the slope in the final deformed state within interface elements for $a = c$

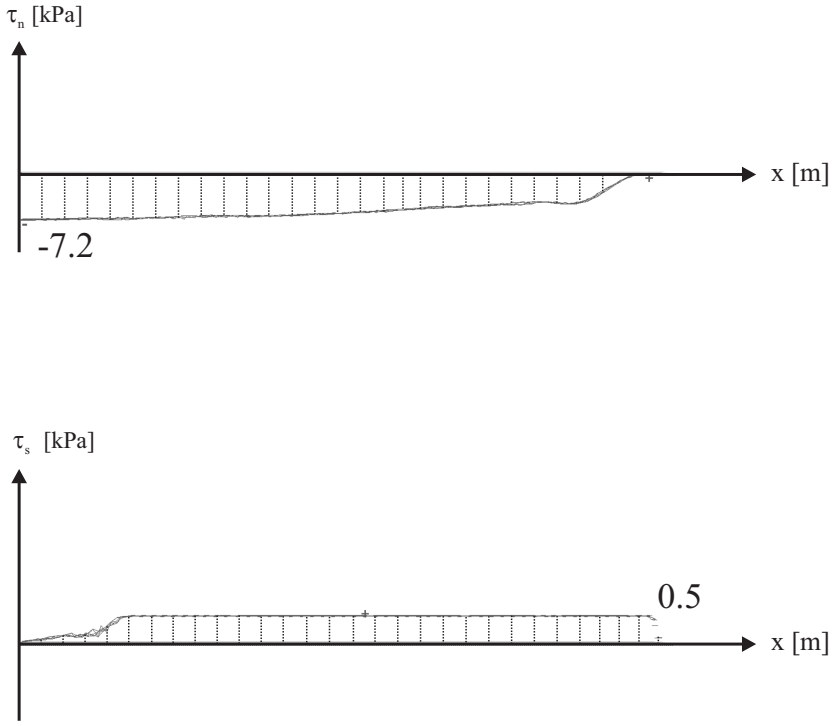

Figure 4.15: Distribution of normal (top) and shear stresses (bottom) along the bottom of the slope in the final deformed state within interface elements for $a = c / 2$

Chapter 5

Constitutive modelling of undrained clay

The numerical analyses of cone penetration testing as presented in this thesis are performed for fully saturated clay. When the rate at which a load is applied on soil is much faster than the rate at which pore water is able to dissipate out of the soil, volume change is prohibited and pore water pressures are generated that balance, together with effective stresses, the applied load. With cone penetration testing, a steel bar is pushed into the ground at a velocity of $2 \cdot 10^{-2}$ m/s. When considering clay that generally possesses a permeability below 10^{-6} m/s such undrained conditions occur in the vicinity of the advancing cone [16].

In the following three sections, aspects of constitutive modelling of undrained clay are covered that are relevant to the numerical analyses presented in Chapter 6. For a broader treatment of the matter, the reader is referred to [20] and [47].

In Section 5.1, general definitions that form the basis for subsequent elaborations on the modelling of undrained clay are provided. In Section 5.2, the modelling of stiffness of undrained clay is considered and in Section 5.3 the modelling of strength of undrained clay. With regard to the latter, the Mohr-Coulomb, Tresca as well as a new more advanced material model called Anisotropic Undrained Clay model are treated. The Anisotropic Undrained Clay model which has recently been developed by Vermeer and Teunissen, first reported in [65], takes into account the anisotropic strength of clay. In Chapter 6, these models will be used for the simulation of cone penetration testing. Only the case of normally-consolidated clay is considered.

5.1 General definitions

The distribution of total stresses $\dot{\boldsymbol{\sigma}}$ over effective stresses of the soil skeleton $\dot{\boldsymbol{\sigma}}'$ and pore water pressures $\dot{p}_w$ can be written as

$$\dot{\boldsymbol{\sigma}} = \dot{\boldsymbol{\sigma}}' + \dot{p}_w \boldsymbol{I} \quad \text{and} \quad \dot{p} = \dot{p}' + \dot{p}_w \tag{5.1}$$

where $\boldsymbol{I}$ denotes the identity matrix with components $I_{ij} = 1$ for $i = j = 1, 2, 3$ else 0, $\dot{p}$ is the total mean stress rate given by $\dot{p} = (\dot{\sigma}_{11} + \dot{\sigma}_{22} + \dot{\sigma}_{33})/3$ and $\dot{p}'$ the effective mean stress rate computed from $\dot{\boldsymbol{\sigma}}'$.

With the used sign convention, compressive stresses are negative. Because the strength of soil is related to effective stresses that act on the soil skeleton rather than total stresses, only effective stress measures are considered in the following.

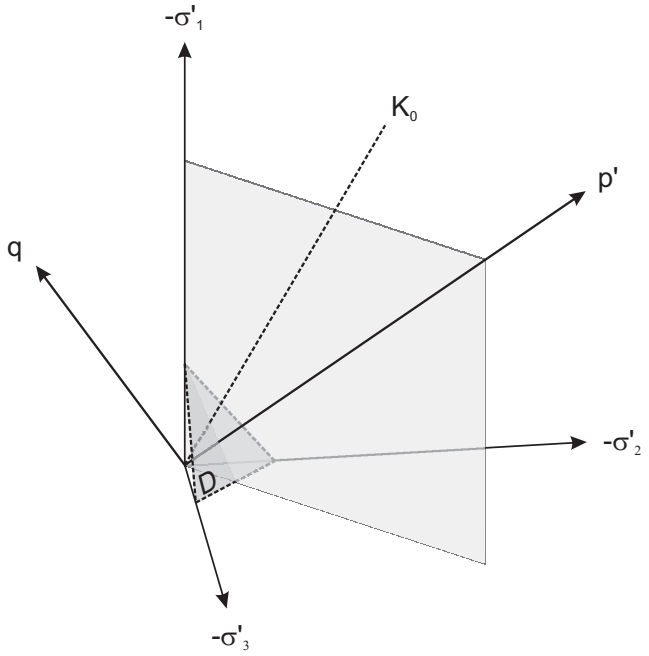

Figure 5.1: Illustration of principal stress space

Any stress tensor $\boldsymbol{\sigma}'$ can be split into an isotropic stress $p'\boldsymbol{I}$ and a deviatoric stress $\boldsymbol{s}$ defined as

$$\boldsymbol{s} = \boldsymbol{\sigma}' - p'\,\boldsymbol{I} \tag{5.2}$$

From the second invariant of the deviatoric stress tensor J_2, a deviatoric stress measure q^* can be derived which quantifies the shear stress intensity

$$\begin{aligned} q^* &= \sqrt{3\,J_2} = \sqrt{\frac{3}{2}\,(\boldsymbol{s}^T : \boldsymbol{s})} = \sqrt{\frac{3}{2}\,s_{ij}\,s_{ji}} \\ &= \sqrt{\frac{1}{2}\left((\sigma_1' - \sigma_2')^2 + (\sigma_2' - \sigma_3')^2 + (\sigma_3' - \sigma_1')^2\right)} \end{aligned} \tag{5.3}$$

where σ_1', σ_2' and σ_3' denote principal stresses.

For the special case of $\sigma_2' = \sigma_3'$, the deviatoric stress measure reduces to $\mid \sigma_1' - \sigma_3' \mid$. In the following, the deviatoric stress measure q will be used, defined as $\sigma_1' - \sigma_3'$.

Figure 5.1 illustrates the principal stress space generally used to visualise stresses and stress paths. Here, negative signs are used for denoting the axes of principal stress space because in the following explanations compressive rather than tensile stresses are considered. Lines p' and q form the p'-q-coordinate system, referred to as p'-q-space. Letter D denotes the deviatoric plane. A change of stress with $\dot{\sigma}_2' = \dot{\sigma}_3'$ and $\dot{\sigma}_1' = K_0\,\dot{\sigma}_3'$ follows a line denoted in Figure 5.1 as K_0 line.

The orientation of a deviatoric stress vector (s_1, s_2, s_3) within the deviatoric plane can be described by means of the Lode angle Θ. Figure 5.2 shows the Lode angle for the six sections of the deviatoric plane that are created through the projected axes of σ_1', σ_2' and σ_3'. More than one definition of this angle exists. The definition of the Lode angle used

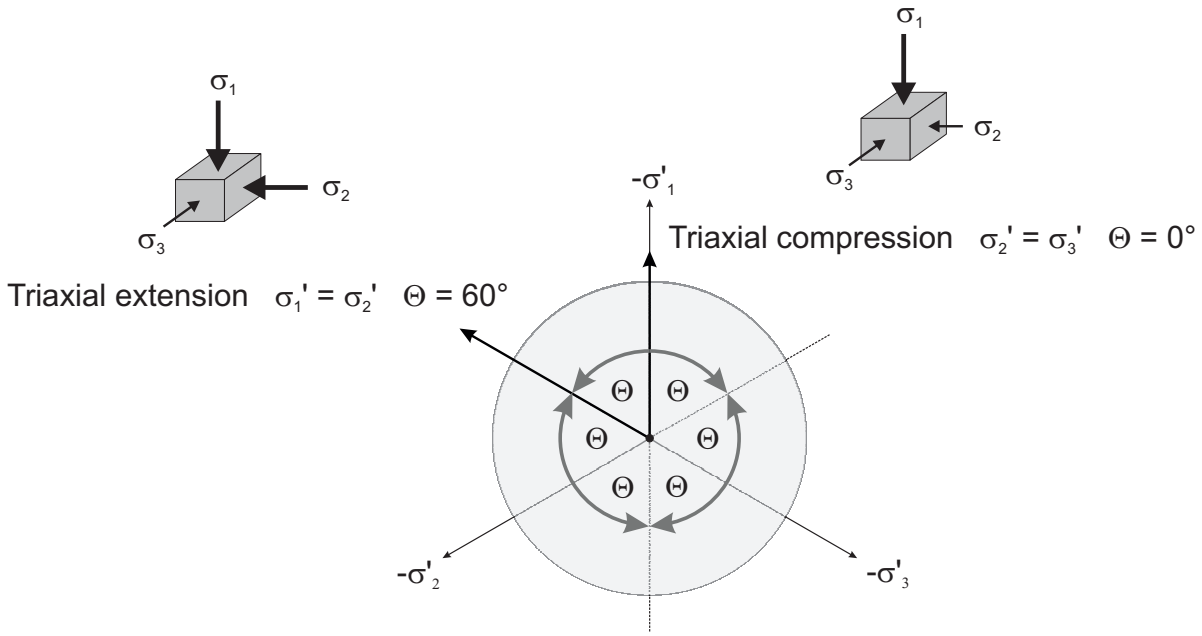

Figure 5.2: Definition of the Lode angle in the deviatoric plane

here is

$$\cos\Theta = -\frac{3}{2}\frac{s_1}{q} \tag{5.4}$$

with $\mid \sigma_1' \mid \geq \mid \sigma_2' \mid \geq \mid \sigma_3' \mid$. For $\Theta = 0°$, the intermediate principal stress σ_2' is equal to the minimum principal stress σ_3'. For $\Theta = 60°$, the intermediate principal stress σ_2' is equal to the maximum principal stress σ_1'. The angle can be defined correspondingly for all principal axes.

Figure 5.3 depicts the triaxial compression and triaxial extension test. In triaxial compression tests, a soil sample is first subjected to K_0 loading and then sheared by increasing the vertical load σ_1 while keeping the horizontal stresses $\sigma_{2/3}$ constant. In triaxial extension tests, a soil sample is sheared after initial K_0 loading by increasing the horizontal stresses $\sigma_{2/3}$ while keeping σ_1 constant. Alternatively, σ_1 might be reduced in triaxial extension tests. Figure 5.3 also illustrates a simple shear test which will be considered later on. In simple shear tests, a vertical load is initially applied on a laterally confined soil sample. In a second step, the soil sample is sheared. When considering undrained conditions, these tests are performed in a slightly different manner. After initial loading under drained conditions, the soil probe is sheared under undrained conditions. As shown in Figure 5.4, triaxial compression and extension as well as simple shear tests reproduce loading paths that occur for example at different locations along the surface of a slip circle.

For triaxial tests, σ_2' is equal to σ_3', principal stress directions coincide with the directions of the applied vertical and horizontal loads and do not change throughout the loading process. Thus, stress states occurring in triaxial tests can be illustrated in p'-q-space — unlike stress states found in simple shear. Figure 5.5 (left) shows stress paths for triaxial compression and extension tests under drained conditions. Here, the stress

paths first follow the p' axis ($K_0 = 1$) and then deviate from it when shearing the sample. In the deviatoric plane, a Lode angle of $\Theta = 0°$ corresponds to triaxial compression, a Lode angle of $\Theta = 60°$ corresponds to triaxial extension (see Figure 5.2).

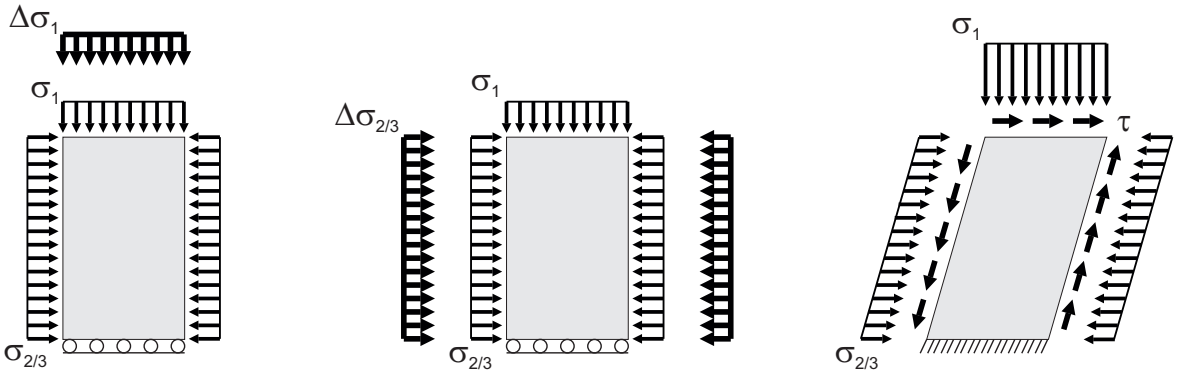

Figure 5.3: Triaxial compression (left), triaxial extension (center) and simple-shear test (right)

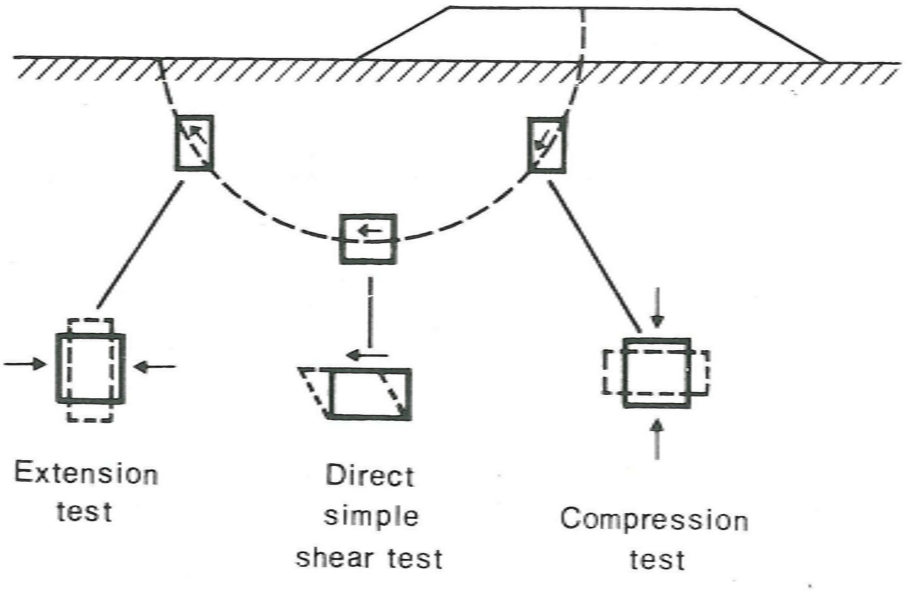

Figure 5.4: Loading types found along slip circle [11]

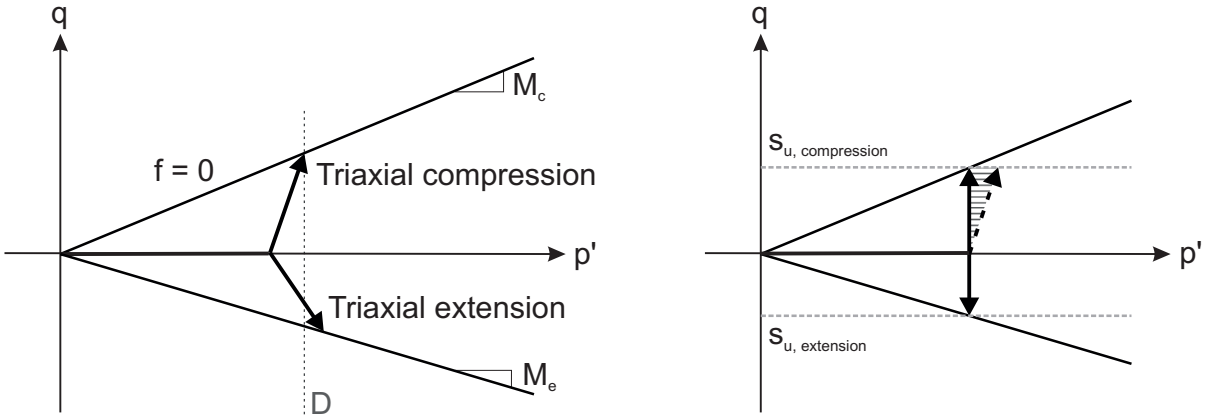

Figure 5.5: Stress paths for triaxial compression and extension in p'-q-space and yield loci of the Mohr-Coulomb model for $c' = 0$; (left) drained conditions; (right) undrained stress paths according to the Mohr-Coulomb model for incompressible undrained soil ($\nu_u = 0.5$)

5.2 Stiffness of undrained clay

Which fraction of an applied incremental load is carried by the soil skeleton and which fraction is carried by the pore water follows from the consideration of strain compatibility between the two materials and, thus, the consideration of the stiffnesses of the soil skeleton, the soil minerals and the pore water. This, of course, only holds for undrained conditions when no dissipation of water with time is considered. Equation 5.1 implies that only the distribution of pressures p' and p_w inside the soil body requires further consideration. The bulk modulus of water K_{water} is approximately 2.1 GPa, the bulk modulus of the soil minerals K_s lies in the range of 36 to 69 GPa and the bulk modulus of the soil skeleton K' lies between 3 and 30 MPa [55]. In view of these values, the soil minerals can be considered as incompressible so that only K_{water} and K' are of relevance for the distribution of stresses within the soil. Pore water is mostly assumed to be slightly more compressible than pure water because the pore space is generally filled to some extend with air even for a fully saturated soil. Strain compatibility requires that the change of volume of the soil-water mixture due to loading $\dot{\varepsilon}_{\text{vol}}$ corresponds to the change of volume of the soil skeleton due to effective pressure and to the change of volume of the water-filled pores due to pore water pressure. This is illustrated in Figure 5.6. Thus,

$$\dot{\varepsilon}_{\text{vol}} = \frac{\dot{p}_w}{\frac{K_{water}}{n}} = \frac{\dot{p}'}{K'} \quad \text{with} \quad n = \frac{V_0}{V} \tag{5.5}$$

where $\dot{\varepsilon}_{\text{vol}} = \dot{\varepsilon}_{11} + \dot{\varepsilon}_{22} + \dot{\varepsilon}_{33}$, n is the porosity of the soil, V_0 is the pore volume and V the total volume of a soil body. Introducing the porosity n takes into account the above mentioned reduction of the bulk modulus of the pore water. This approach goes back to Bruggeman [13] as reported by Bishop in [10].

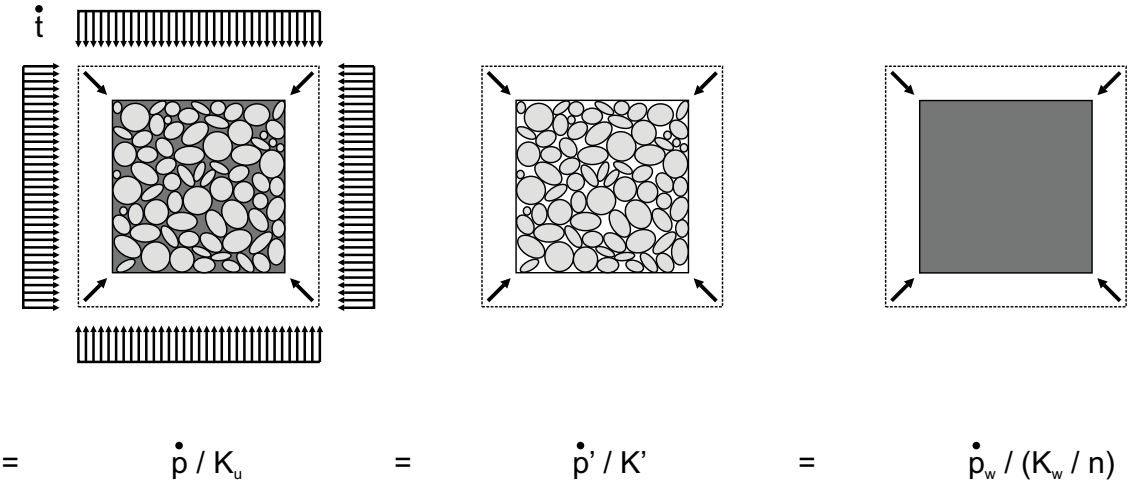

Figure 5.6: Illustration of strain compatibility considerations for the modelling of undrained clay

Rearranging Equation 5.5 gives

$$\dot{p}_w = \frac{K_{water}}{n}\,\dot{\varepsilon}_{\mathrm{vol}} \quad \text{and} \quad \dot{p}' = K'\,\dot{\varepsilon}_{\mathrm{vol}} \tag{5.6}$$

With these equations and $\dot{\varepsilon}_{\mathrm{vol}}$ as input, the excess pore pressures as well as the effective and total stresses can be computed.

For an elastic soil skeleton, the bulk modulus K' can be computed from the shear modulus and Poisson ratio by means of

$$K' = \frac{2G\,(1+\nu')}{3\,(1-2\,\nu')} \tag{5.7}$$

Similarly, a so-called undrained bulk modulus K_u can be written as [60]

$$K_u = \frac{2G\,(1+\nu_u)}{3\,(1-2\nu_u)} \tag{5.8}$$

where ν_u is an undrained Poisson ratio. It yields

$$\dot{p} = K_u\,\dot{\varepsilon}_{\mathrm{vol}} \tag{5.9}$$

Inserting Equations 5.6 and 5.9 into Equation 5.1 renders

$$K_u = K' + \frac{K_{water}}{n} \tag{5.10}$$

Combining Equations 5.7, 5.8 and 5.10 gives

$$\frac{K_{water}}{n} = \frac{3\,(\nu_u - \nu')}{(1-2\,\nu_u)\,(1+\nu')}\,K' \tag{5.11}$$

which relates the bulk modulus of the pore water to the effective bulk modulus by means of the effective Poisson ratio and the undrained Poisson ratio.

Upon sudden oedometric loading a fully saturated soil shows no noteworthy change of volume and the applied load is found to be carried almost entirely by the pore water. This implies incompressibility of the soil and thus ν_u being close to 0.5. The bulk modulus of the pore water $\frac{K_{\mathrm{water}}}{n}$ would be almost equal to K_u and K' relatively small. The applied load would then indeed be carried almost entirely by the pore water.

On the other hand, assuming slight compressibility of the pore water is of advantage for numerical analyses, because a high stiffness of the pore water resulting in a near-incompressible material causes numerical problems such as volumetric locking and a severe ill-conditioning of the stiffness matrix. In order to prevent numerical problems, the undrained Poisson ratio is generally set to a value between 0.485 and 0.495.

In Figure 5.7 the ratio of $\frac{K_{\mathrm{water}}}{n}$ and K_u is plotted over the undrained Poisson ratio for different values of the drained Poisson ratio. For a drained Poisson ratio of 0.25 and an undrained Poisson ratio of 0.495 Figure 5.7 shows that 98 percent of the applied external load is carried by the pore water. Changing the undrained Poisson ratio to 0.485 causes an increase of 3 percent of the part of the load that is carried by the soil skeleton. The higher the drained Poisson ratio, the smaller the percentage of the load carried by the pore water. Thus, besides specifying an undrained Poisson ratio in the range of 0.485 to 0.495, the drained Poisson ratio should preferably lie below a value of 0.35.

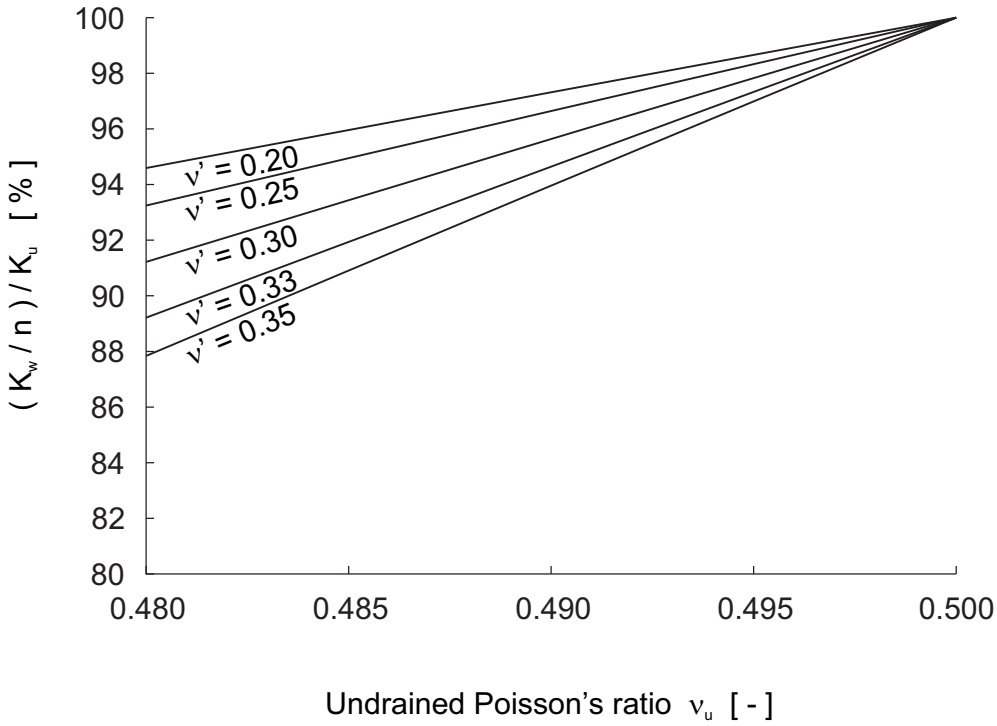

Figure 5.7: Ratio of pore pressure bulk modulus over bulk modulus of the soil-water mixture plotted over the undrained Poisson ratio ν_u for different Poisson ratios of the drained soil ν'

5.3 Strength of undrained clay

In Subsections 5.3.1 and 5.3.2 the modelling of the strength of undrained clay by means of the Mohr-Coulomb and Tresca models is presented. Subsequently, the concept of critical state soil mechanics as used with the Anisotropic Undrained Clay model is introduced in Subsection 5.3.3 by means of the Modified Cam Clay model. Here, too, focus lies on the modelling of undrained clay. Finally, the Anisotropic Undrained Clay model itself is presented in Subsection 5.3.4. Only normally-consolidated clay will be treated.

5.3.1 The Mohr-Coulomb model

Section 4.1 covers in detail the stress-strain relationship for an elastic-plastic constitutive model used with the interface elements. These derivations of plastic slip rate and stress rate apply in similar manner to the models described below so that they are not repeated here. In contrast to the smooth yield locus presented in Section 4.1, the Mohr-Coulomb yield locus is a cone with a hexagonal cross section as shown in Figure 5.8 (left). The Tresca yield function is a prism with six sides shown in Figure 5.8 (right). At the intersections of the sides, the direction of mapping of stresses onto the yield loci is not uniquely defined. The mapping for these intersections is not presented here. The reader is referred to [34].

The Mohr-Coulomb model possesses three strength parameters: the friction angle ϕ', the cohesion c' and the dilation angle ψ'. Its yield functions are

$$\begin{aligned} f &= |\sigma'_1 - \sigma'_2| - (\sigma'_1 + \sigma'_2)\sin\phi' - 2\,c'\cos\phi' = 0 \\ f &= |\sigma'_2 - \sigma'_3| - (\sigma'_2 + \sigma'_3)\sin\phi' - 2\,c'\cos\phi' = 0 \\ f &= |\sigma'_3 - \sigma'_1| - (\sigma'_3 + \sigma'_1)\sin\phi' - 2\,c'\cos\phi' = 0 \end{aligned} \tag{5.12}$$

and its plastic potential functions are

$$\begin{aligned} g &= |\sigma'_1 - \sigma'_2| - (\sigma'_1 + \sigma'_2)\sin\psi' \\ g &= |\sigma'_2 - \sigma'_3| - (\sigma'_2 + \sigma'_3)\sin\psi' \\ g &= |\sigma'_3 - \sigma'_1| - (\sigma'_3 + \sigma'_1)\sin\psi' \end{aligned} \tag{5.13}$$

With the computations presented in Chapter 6 that use the Mohr-Coulomb model, no cohesion is considered so that it is also left out in the following explanations. Figure 5.5 (left) and (right) depict the yield locus of the Mohr-Coulomb model in p'-q-space for a purely frictional soil (c' = 0). The upper line with inclination M_c limits elastic deformations for triaxial compression, the line below the p' axis with inclination M_e elastic deformations for triaxial extension. The inclinations M_c and M_e are given by

$$M_c = \frac{6\,\sin\phi'}{3 - \sin\phi'} \quad \text{and} \quad M_e = \frac{6\,\sin\phi'}{3 + \sin\phi'} \tag{5.14}$$

Figure 5.9 shows the yield locus of the Mohr-Coulomb model and circles with radii M_c and M_e in the deviatoric plane for a friction angle of 30°. Furthermore, stress paths for triaxial compression and extension are indicated.

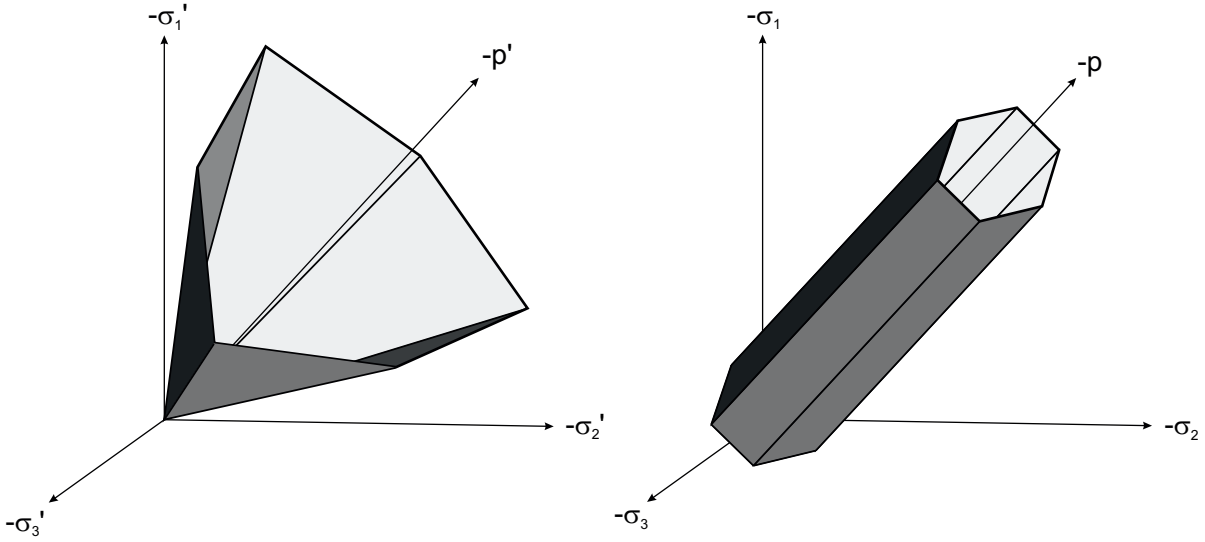

Figure 5.8: Mohr-Coulomb yield locus in principal stress space for $c' = 0$ (left) and Tresca yield locus (right)

With the cone penetration simulations that use the Mohr-Coulomb model, non-associated plasticity with $\psi' = 0°$ is considered. Figure 5.10 (left) shows the orientation of the plastic potential function g in p'-q-space and the orientation of the plastic strain rates derived from it for the Mohr-Coulomb model. A dilation angle ψ' equal to zero results in plastic deformations with no change of volume of the soil.

Figure 5.5 (right) shows stress paths up to failure for undrained triaxial compression and extension tests on the basis of the Mohr-Coulomb model for $c' = 0$ and $\nu_u = 0.5$. In contrast to the drained stress paths shown on the left, the increase of the mean stress is carried by the excess pore pressure whose magnitudes are also indicated in Figure 5.5 (right). The Mohr-Coulomb model predicts a larger shear strength for triaxial compression $s_{\mathrm{u,compression}}$ than for triaxial extension $s_{\mathrm{u,extension}}$. This corresponds to measurements of laboratory tests. However, for reasons explained below, the magnitudes of shear strength obtained with the Mohr-Coulomb model are higher than measured shear strengths. The shear strengths $s_{\mathrm{u,compression}}$ and $s_{\mathrm{u,extension}}$ are indicated in Figure 5.5 (right). They are generally referred to as undrained shear strengths. It should be emphasised, that the widely-used term 'undrained shear strength' represents no unique soil parameter, but depends on the type of loading considered and on the effective mean stress. Obviously, without the generation of effective stresses through initial drained loading, the undrained shear strengths would be zero, at least for $c' = 0$. Furthermore, laboratory tests show that undrained shear strengths are influenced by the rate of shearing, but this is not considered here. Besides undrained shear strengths for triaxial compression and extension, simple shear tests render an undrained shear strength $s_{\mathrm{u,simpleshear}}$ that lies in between $s_{\mathrm{u,compression}}$ and $s_{\mathrm{u,extension}}$.

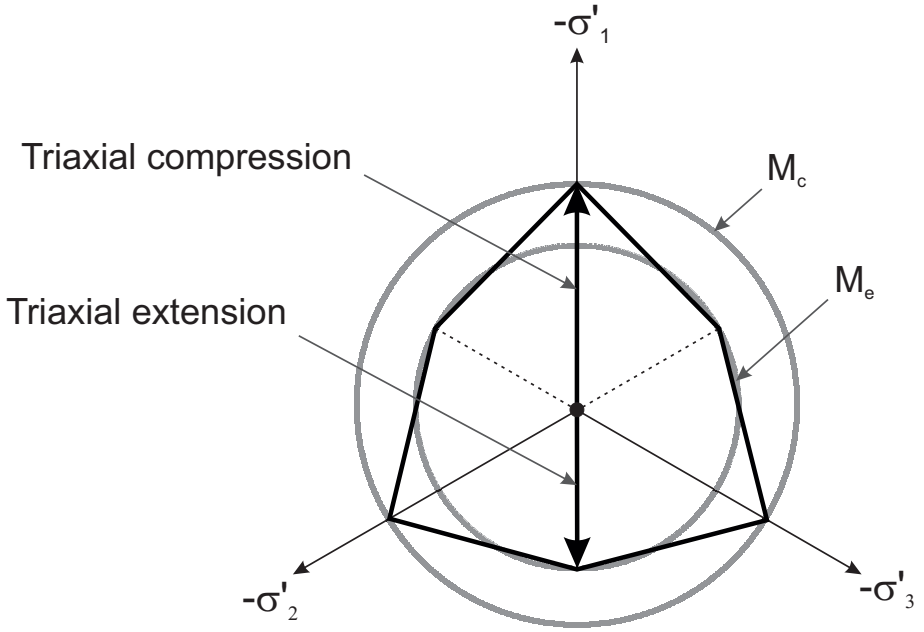

Figure 5.9: Mohr-Coulomb failure envelope in the deviatoric plane

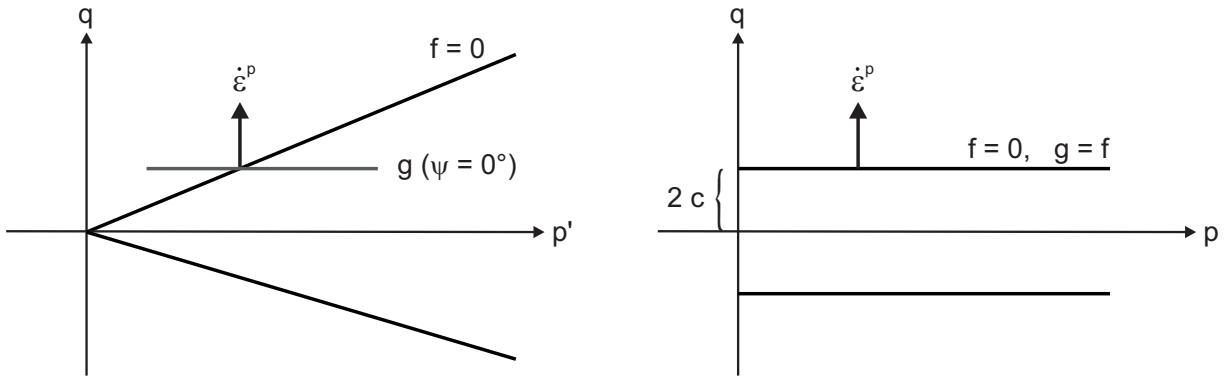

Figure 5.10: Yield loci, plastic potential functions and directions of the rate of plastic strain $\dot{\varepsilon}^p$ for the Mohr-Coulomb model with $c' = 0$ for non-associated plasticity with $\psi' = 0°$ (left) and for the Tresca model for associated plasticity (right)

5.3.2 The Tresca model

The Tresca model, originally developed for metal plasticity, does not incorporate frictional strength but assumes a constant, pressure-independent strength. The yield functions of the Tresca model correspond to those of the Mohr-Coulomb model when setting the friction angle to zero. The yield locus in principal stress space is illustrated in Figure 5.8 (right). In p-q-space, the yield locus shows up as two lines parallel to the p axis at distances of twice the specified cohesion.

The Tresca material model can be used instead of the Mohr-Coulomb model for undrained analyses by setting the cohesion to an undrained shear strength s_u. Under undrained conditions the undrained shear strength remains constant throughout the loading process as described above. The formulation of the Tresca model reflects such strength behaviour.

Obviously, the initial effective stresses must be known as well as the loading type in order to specify the undrained shear strength. It might for example be determined on the basis of a triaxial compression or extension test. For numerous geotechnical problems such as the one depicted in Figure 5.4, a unique loading type cannot be specified. Any choice of s_u will then either under- or overestimate the soil's undrained shear strength in some part of the modelled soil body. As a kind of average, an undrained shear strength obtained from simple shear tests is generally used.

Undrained analyses with the Tresca model can be performed with or without distinguishing between effective stresses and excess pore pressures. The Tresca yield criterion can be formulated identically on the basis of both the total as well as the effective stress tensor: plastic yielding is predicted to occur once q^* reaches a value of 2 s_u. When total stresses are split into effective stresses and excess pore pressures as described in Section 5.2, the analysis is referred to as 'effective stress analysis'. Analyses that only consider total stresses are in the following referred to as 'total stress analyses'. With total stress analyses, the specified Poisson ratio corresponds to the undrained Poisson ratio ν_u used in effective stress analyses. First computations presented in Chapter 6 follow the approach of the total stress analysis.

With simulations that use the Tresca model, an associated flow rule is used, so that $g = f$. Figure 5.10 (right) depicts the orientation of plastic strain rates for the associated Tresca model that produce no plastic volumetric straining.

5.3.3 The Modified Cam Clay model

Figure 5.11 shows the undrained stress paths for triaxial compression and extension, both for the Mohr-Coulomb model and from tests on isotropically consolidated clays (without over-consolidation). Tests result in lower undrained shear strengths than the values predicted with the Mohr-Coulomb model. The measured undrained shear strengths are indicated in Figure 5.11 by dashed horizontal lines for triaxial compression and extension. On the right, the change of deviatoric stress with vertical compression / extension of the soil sample is plotted for these two cases.

Reason for this discrepancy between measurement and prediction is that the Mohr-Coulomb model underestimates the generation of pore pressure observed in laboratory

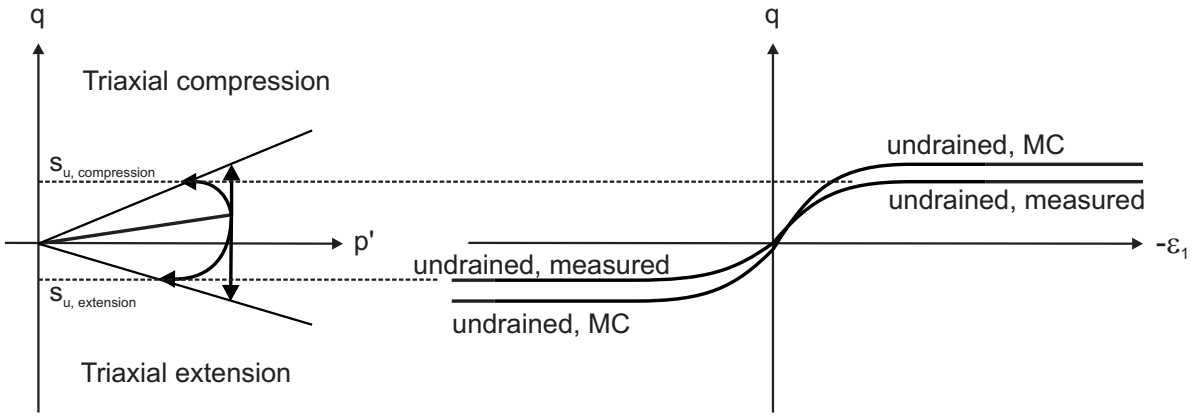

Figure 5.11: (left) Stress path for triaxial compression and extension in p'-q-space; (right) deviatoric stresses plotted over the vertical strain for triaxial compression (negative strain) and triaxial extension (positive strain)

tests when shearing normally-consolidated clay under undrained conditions. Under drained conditions, normally-consolidated clay exhibits contractant behaviour when sheared, being not captured by the Mohr-Coulomb model. Under undrained conditions, contractant behaviour gives rise to pore pressures. The evolving pore pressures in turn act on the soil skeleton resulting in a decrease of effective pressure. This leads to the reduction of the undrained shear strengths in triaxial compression as well as extension shown in Figure 5.11.

Soil models that are based on the concept of critical state soil mechanics such as the Cam Clay and Modified Cam Clay model do better than the Mohr-Coulomb and Tresca models in reproducing results of triaxial compression and extension tests on undrained clay. They take into account the shear-induced volume change. The concept of critical state soil mechanics is presented in detail by amongst others Schofield and Wroth [47]. In the following, general aspects of critical state soil mechanics that apply to the modelling of undrained clay will be explained. The attention will be focussed on the Modified Cam Clay (MCC) model.

Figure 5.12 shows the yield locus of the MCC model in p'-q-space. The shape of the yield locus is specified through an isotropic preconsolidation pressure p'_p and peak points whose locations are given by the intersections of the yield locus with critical state lines. The critical state lines are fixed so that the extend of the yield locus solely depends on p'_p. The yield locus has vertical tangents at p' = 0 and p' = -p'_p. The yield function is

$$f = p' + \frac{q^2}{M^2\, p'} - p'_p = 0 \tag{5.15}$$

where the parameter M is defined below. Under the assumption of normally-consolidated clay, stress states initially lie for K_0 loading conditions at the point where the K_0 line intersects with the yield locus. For this case, the initial yield locus, the isotropic preconsolidation pressure p'_p respectively, can be initialised from the condition f = 0.

The elliptic shape of the yield locus stems from experimental results as shown in Figure 5.13. Compaction of normally-consolidated clay occurs either through isotropic load-

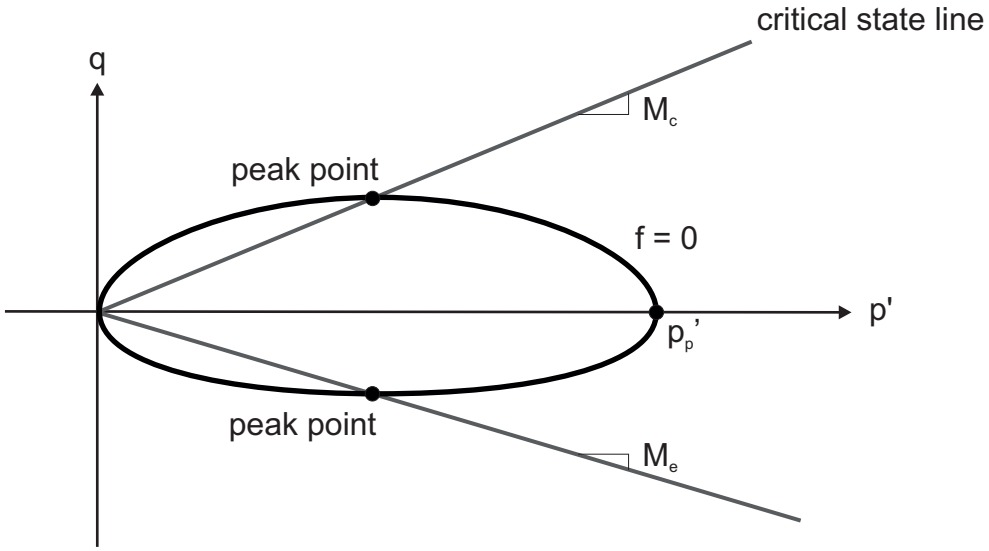

Figure 5.12: Yield locus of the MCC model with critical state specified through the Mohr-Coulomb yield functions

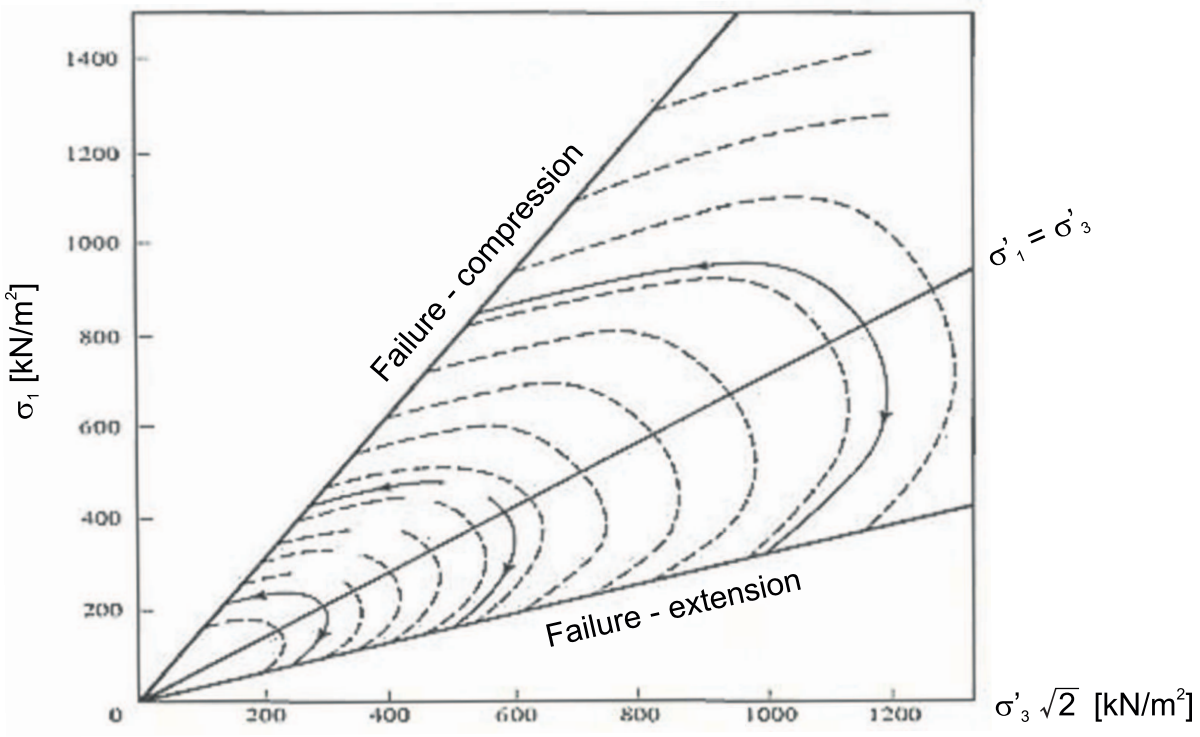

Figure 5.13: Contourlines of equal volumetric strain found in triaxial compression and extension tests for clay by Henkel [26]

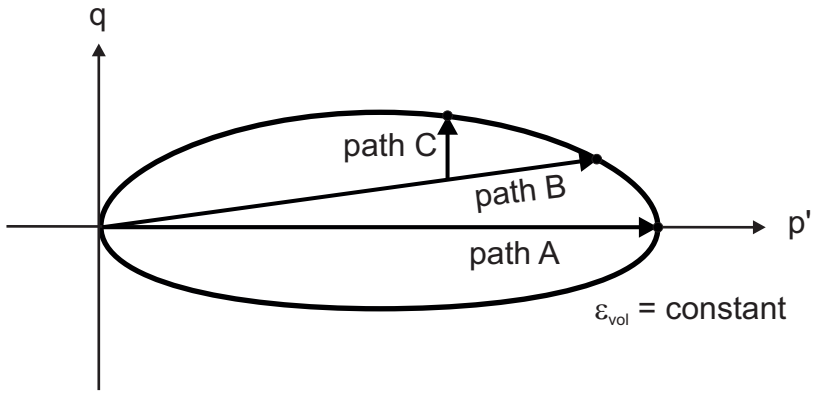

Figure 5.14: Illustration of a contourline of equal volumetric strain in p'-q-space and of different stress paths resulting in the same volumetric straining: (A) isotropic loading, (B) K_0 loading, (C) shearing in triaxial compression under undrained conditions

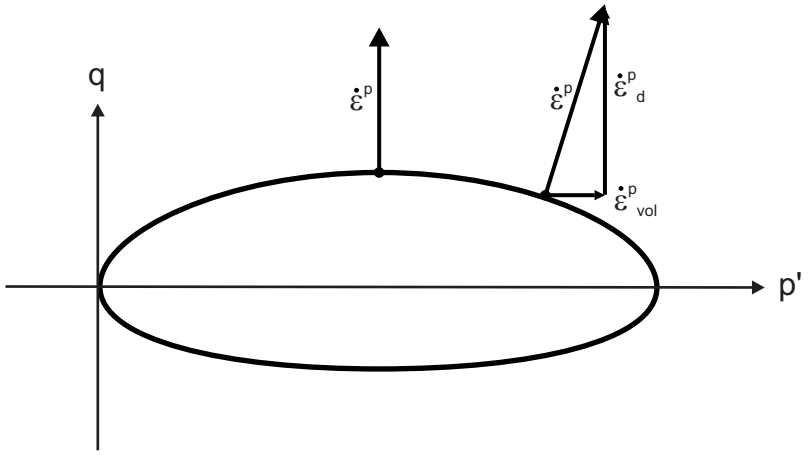

Figure 5.15: Direction and volumetric and deviatoric components of plastic strain rates for an associated flow rule

ing or through shearing. Thus, a certain degree of volumetric straining can be produced through different stress paths. As shown in Figure 5.13, stress states of equal compaction of soil lie for triaxial tests on curved lines that ressemble ellipses. Figure 5.14 illustrates how such an idealised contour of equal volumetric strain is reached for different stress paths. The extend of these contourlines can be specified through the isotropic preconsolidation pressure p'_p, which is related to the maximum applied compaction of the soil. Once loading moves a stress state beyond such a contourline, the soil is compacted beyond any previous level of compaction which implies irreversible volumetric straining. The elliptic yield locus is based on these contours of constant volumetric strain.

Figure 5.15 shows directions of plastic straining $\dot{\boldsymbol{\varepsilon}}^p$ for an associated flow rule. As indicated in Figure 5.15, $\dot{\boldsymbol{\varepsilon}}^p$ can be split into a volumetric component $\dot{\varepsilon}^p_{\text{vol}}$ and a deviatoric component $\dot{\varepsilon}^p_d$. At the peak point, the soil is sheared without any volume change which

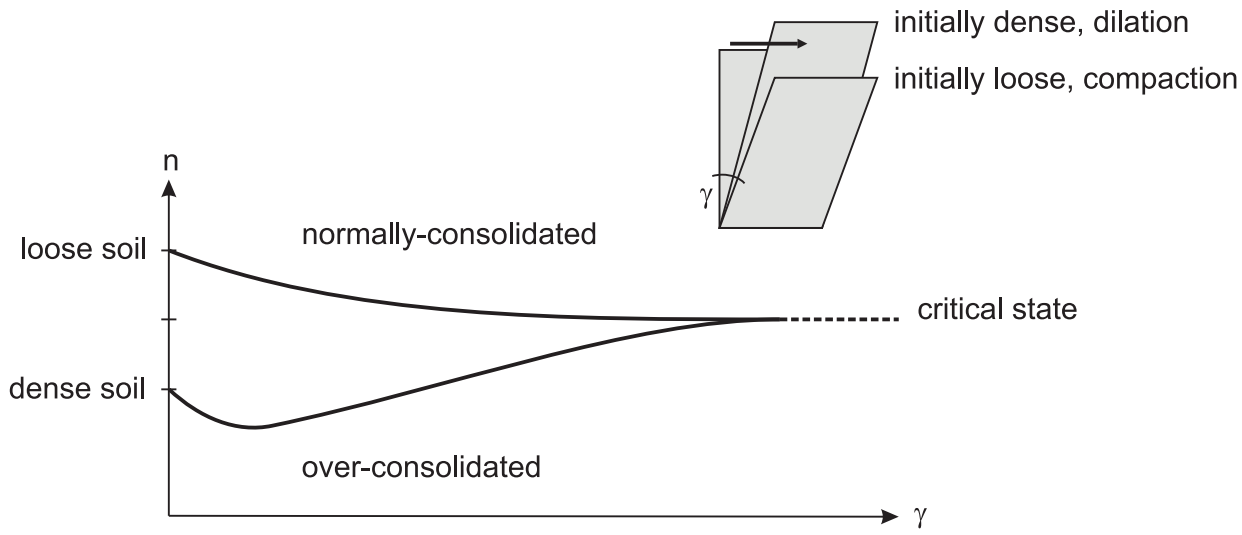

Figure 5.16: Change of porosity for normally-consolidated and over-consolidated clay through shearing

corresponds to a soil being in a critical state.

Normally-consolidated clay with a high initial porosity will experience a decrease of its pore volume upon shearing. When shearing over-consolidated clay that possesses a low porosity, its particles are tightly packed and shear deformations are accompanied by an increase of the soil volume. On continued shearing a limit porosity is reached for both normally- and over-consolidated clay. No further volume change is observed during shearing of the soil which corresponds to the soil being in a critical state. This is illustrated in Figure 5.16. The MCC model predicts such behaviour for a stress state that reached a peak point of the ellipse.

The critical state lines that cross the yield locus at its peak points correspond to stress states with a ratio q/p' for which soil is in a critical state. With the implementation of the concept of critical state soil mechanics, the Mohr-Coulomb yield functions often serve for specification of the critical state. In p'-q-space the two critical state lines for triaxial compression and extension then possess inclinations of M_c, M_e respectively, defined in Equations 5.14 (see Figure 5.12). Here, the friction angle ϕ' must be replaced by a friction angle for the critical state ϕ'_{cs}. Congruence between the peak points of the yield locus for both triaxial compression and extension with the critical state lines can be obtained by defining M in Equation 5.15 as a function of the Lode angle Θ so that M varies between M_c for triaxial compression and M_e for triaxial extension. Figure 5.17 exemplifies this yield locus and the critical state lines in the deviatoric plane for an arbitrary p'.

Yielding of soil that is accompanied by dilation is related to softening behaviour as observed with densely packed over-consolidated clays. However, these are not considered here. Irreversible compaction ($\dot{\varepsilon}^p_{\text{vol}} < 0$) is related to hardening behaviour of soil. It is associated with normally-consolidated clays and modelled through an expansion of the yield locus. The respective amount of hardening depends on the plastic volumetric strain rate.

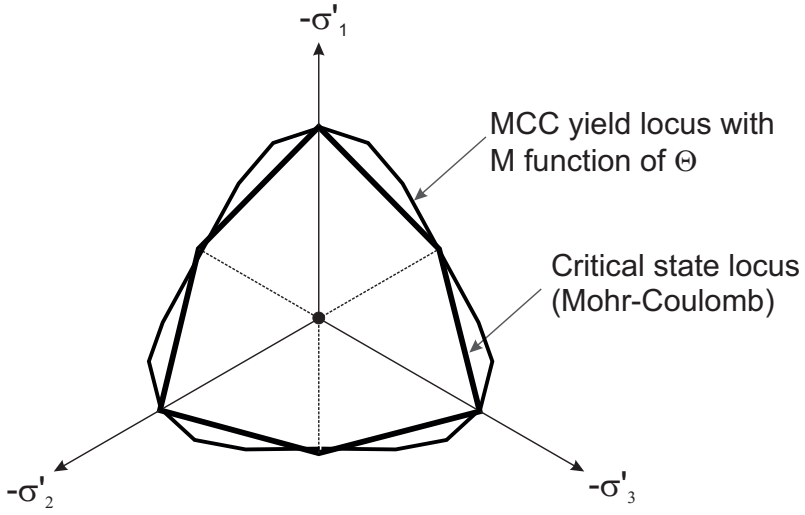

Figure 5.17: Yield locus and critical state locus for the MCC model in the deviatoric plane

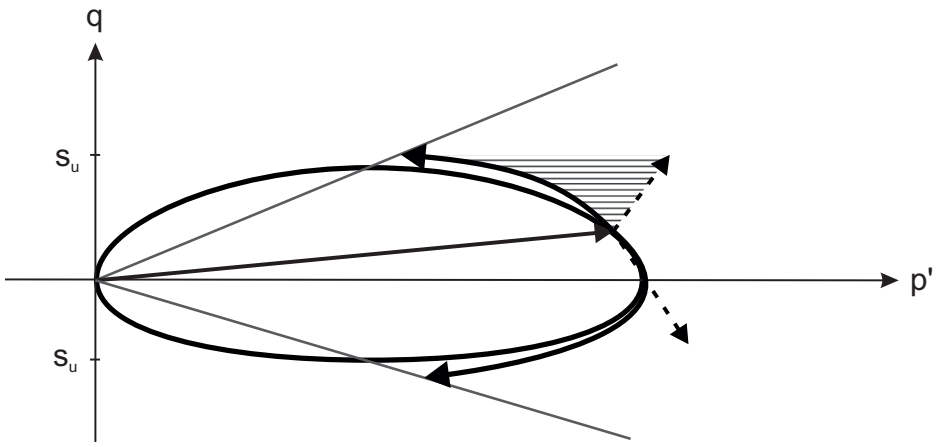

Figure 5.18: Stress paths for triaxial compression and extension as predicted by the MCC model

For undrained conditions, only slight hardening or softening occurs because a change of volume is constrained and instead translates into the generation of excess pore pressures. With the MCC model, effective stress states thus only deviate slightly from the initial yield locus upon shearing. Figure 5.18 illustrates the resulting respective stress paths for triaxial compression and extension. Clearly, the thus obtained stress paths correspond to measurements of triaxial compression and extension tests as indicated in Figure 5.11.

The slight expansion of the yield locus found with the MCC model occurs because prohibited plastic volumetric strains $\dot{\varepsilon}^{p}_{\mathrm{vol}}$ translate into inversely oriented elastic strains ($\dot{\varepsilon}^{p}_{\mathrm{vol}} = -\dot{\varepsilon}^{e}_{\mathrm{vol}}$). Consequently, the yield locus expands to a new isotropic preconsolidation pressure p'_p.

5.3.4 Consideration of the strength anisotropy of clay with the Anisotropic Undrained Clay model

In case of clay, the proper reproduction of the pore pressures generated through shearing requires to take into consideration anisotropy. During deposition, clay is generally compacted vertically under its self-weight, which leads to the arrangement of clay particles in layers rather than a random configuration. As a consequence, natural clay generally shows a different strength in horizontal directions than in vertical direction. This special case of anisotropic material behaviour is referred to as cross-anisotropy or transverse anisotropy.

In the frame of this thesis, the Anisotropic Undrained Clay (AUC) model developed by Vermeer and Teunissen is considered for the simulation of cone penetration testing in order to capture the cross-anisotropic strength of clay and to properly predict the magnitude of excess pore pressures generated during cone penetration. The AUC model is largely based on the S-CLAY1 model developed by Wheeler *et al.* [66] which will be presented first in the following.

The S-CLAY1 model This elastoplastic anisotropic model forms a considerable extension of the MCC model. It is amongst others based on the works of Dafalias [19] and Korhonen *et al.* [35]. It takes into account the initial anisotropic strength of clay as well as the development and erasure of fabric anisotropy through volumetric and shear strains by means of a rotational hardening law.

The yield function of the S-CLAY1 model is

$$f \;=\; p' \;+\; \frac{3/2\;(\boldsymbol{s} \;-\; p'\,\boldsymbol{\alpha}_d)^T \;:\; (\boldsymbol{s} \;-\; p'\,\boldsymbol{\alpha}_d)}{(M^2 \;-\; 3/2\,\boldsymbol{\alpha}_d^T \;:\; \boldsymbol{\alpha}_d)\;p'} \;-\; p'_p \tag{5.16}$$

The deviatoric fabric tensor $\boldsymbol{\alpha}_d$ takes into account the anisotropic strength of the soil. For initialisation, it is related to $\boldsymbol{s}_0$, q_0 computed on the basis of the initial stress state and a parameter α_0 by means of

$$\boldsymbol{\alpha}_{d,0} \;=\; \frac{\alpha_0}{q_0}\,\boldsymbol{s}_0 \tag{5.17}$$

Tying the initial deviatoric fabric tensor to the initial deviatoric stress tensor takes into account that the anisotropic initial stresses of a clay largely define the formation of its fabric. For normally-consolidated clay, Wheeler *et al.* relate α_0 to K_0 with K_0 estimated from Jaky's formula $K_0 \approx 1 - \sin\phi'$. This results in

$$\alpha_0 \;=\; 3\left(\left(\frac{\sin\phi'}{3-2\sin\phi'}\right)^2 + \left(\frac{\sin\phi'}{3-2\sin\phi'}\right) - 12\left(\frac{\sin\phi'}{3-\sin\phi'}\right)^2\right) \tag{5.18}$$

Expressing Equation 5.16 in terms of p'_0 and q_0 as well as α_0 renders

$$f_0 \;=\; p'_0 \;+\; \frac{(q_0 \;-\; \alpha_0\,p'_0)^2}{(M^2 \;-\; \alpha_0^2)\;p'_0} \;-\; p'_{p,0} \tag{5.19}$$

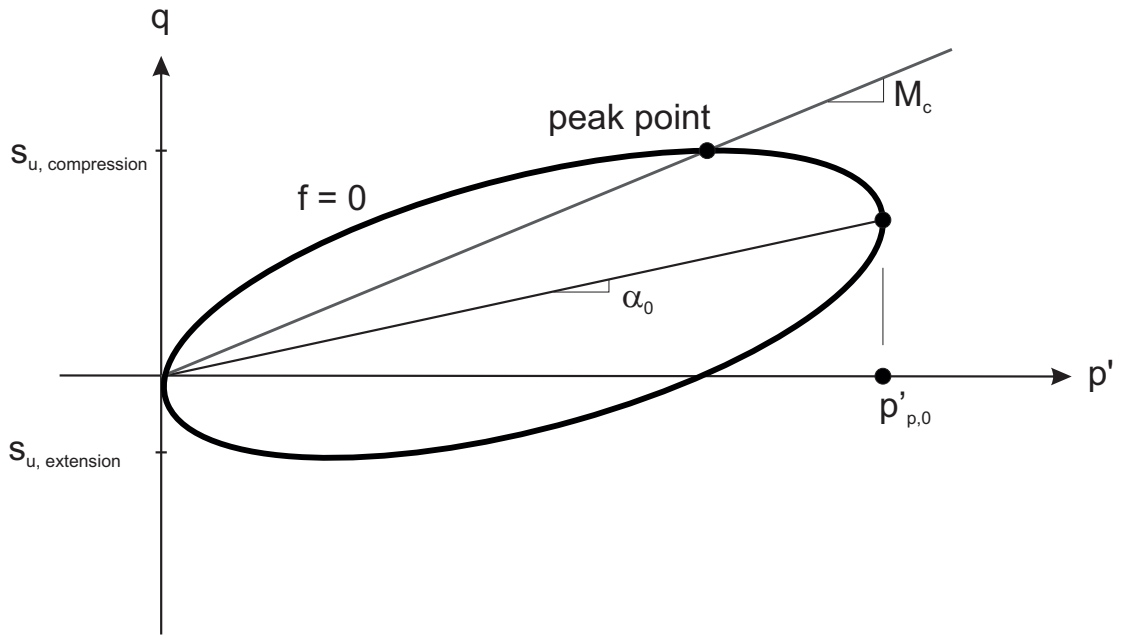

Figure 5.19: Initial yield locus of the AUC and S-CLAY1 models in p'-q-space

which is illustrated in Figure 5.19.

As shown in Figure 5.19, the yield locus produces a higher undrained shear strength for triaxial compression compared to the yield locus of the MCC model. Inversely, the undrained shear strength for triaxial extension decreases.

Wheeler *et al.* as well as Leoni *et al.* [36] present, amongst others, extensive results of laboratory testing on natural clays and convincingly show that such a yield locus matches well the yield behaviour of the tested clays.

Simulating undrained loading with the S-CLAY1 model gives negligible hardening and softening as explained above for the MCC model. So, it behaves for undrained conditions nearly as an elastic, perfectly plastic model. On reducing the model to perfect plasticity, one obtains the AUC model which is described in the following.

The AUC model The AUC model [62] is tailored for the modelling of the anisotropic strength of clay under undrained conditions. Density and rotational hardening as well as softening are not considered which reduces the number of soil parameters required for the AUC model compared to the S-CLAY1 model. The AUC model requires only 4 input parameters, namely E', ν', ϕ'_{cs} and the overconsolidation ratio OCR. OCR is defined as the preconsolidation stress divided by the vertical effective stress. This makes the AUC model more adapted to engineering practice of undrained analyses than the S-CLAY1 model which covers a much broader range of applications but entails a much higher level of complexity that is not needed for the modelling of undrained clay.

The stiffness and shear strength parameters are generally well known or can be estimated relatively easily. However, the sensitive overconsolidation ratio of soil is often

difficult to assess accurately. This parameter might be determined for undrained conditions from evaluation of the undrained shear strength $s_{\mathrm{u,simpleshear}}$ obtained from simple shear tests as suggested by Vermeer [65]. Alternatively, an undrained shear strength obtained from cone penetration testing could be used which can be related to $s_{\mathrm{u,simpleshear}}$ through empirical or theoretical correlations. Such an extension would make the model even easier to use in practice.

With the AUC model, the isotropic preconsolidation pressure and deviatoric stress tensor $\boldsymbol{s}_0$ remain fixed after initialisation. The yield function of the AUC model then takes the form

$$f \;=\; p' \;+\; \frac{3/2 \left(\boldsymbol{s} \;-\; p' \,\frac{\alpha_0}{q_0}\, \boldsymbol{s}_0\right)^T \;:\; \left(\boldsymbol{s} \;-\; p' \,\frac{\alpha_0}{q_0}\, \boldsymbol{s}_0\right)}{\left(M^2 \;-\; \alpha_0^2\right)\, p'} \;-\; p'_{p,0} \tag{5.20}$$

Initialisation of $p'_{p,0}$ follows the procedure presented above for the MCC model for normally-consolidated clay.

Equation 5.20 can likewise be written in terms of p', q and α_0

$$f \;=\; p' \;+\; \frac{\left(q \;-\; \alpha_0\, p'\right)^2}{\left(M^2 \;-\; \alpha_0^2\right)\, p'} \;-\; p'_{p,0} \tag{5.21}$$

provided that $\boldsymbol{s} \;=\; \lambda\, \boldsymbol{s}_0$ and $q \;=\; \lambda\, q_0$ where λ is an arbitrary scalar. This condition applies to triaxial compression and extension.

A change of M depending on the Lode angle Θ is not considered with the AUC model in contrast to the S-CLAY1 model. The factor M is initialised to M_c with

$$M_c \;=\; \frac{6\, \sin \phi'_{cs}}{3 \;-\; \sin \phi'_{cs}} \tag{5.22}$$

The peak point of the yield locus shown in Figure 5.19 therefore only coincides with the critical state locus for triaxial compression, not for triaxial extension.

Referring to results of laboratory tests, Wheeler *et al.* conclude that associated plasticity is a reasonable assumption for natural clays with the considered yield function. Here, too, only associated plasticity is considered, so that a separate specification of a plastic potential function is not needed. With the AUC model as with the S-CLAY1 model, elastic behaviour is assumed to be isotropic rather than anisotropic.

In addition to stresses, the AUC model requires two more state parameters that define the shape of its yield locus. With the computations performed in Chapter 6, only uniform initial stresses are considered so that the latter two state parameters are identical throughout the soil body. Furthermore, they are constant throughout the computation. Whereas stresses are mapped with the quasi-static MPM between material points and Gaussian integration points as described in Section 3.5, these two state parameters are therefore only mapped from material points to Gaussian integration points but not from Gaussian integration points to material points. The mapping of the state parameters is trivial for the 4-noded tetrahedral elements considered in Chapter 6.

Validation of the Anisotropic Undrained Clay model In the following, results obtained from numerical analyses of triaxial compression, triaxial extension and direct shear tests are presented to illustrate the performance of the AUC model. These analyses were performed with the quasi-static Plaxis 2D FEM code as well as the quasi-static MPM code. With the former, the triaxial tests were simulated as axisymmetric problems and the direct shear tests as a plane-strain problem. With the quasi-static MPM, these soil tests were modelled as fully three-dimensional problems. Given that failure of the soil is already obtained for small deformations, the computations with the quasi-static MPM correspond to FEM computations because material points do not show any notable displacements. Correspondingly, results for both methods were found to render the same undrained shear strengths.

For triaxial compression and extension, a vertical load σ_v of 10 kPa and horizontal loads σ_h of 5 kPa ($K_0 = 0.5$) are applied in a first computation stage under drained conditions. For triaxial compression, the soil body is afterwards compressed in the direction of σ_v under undrained conditions. For triaxial extension, the soil body is extended in a second stage in the direction of σ_v under undrained conditions. The computations were performed for the Mohr-Coulomb material model and the AUC model. For the Mohr-Coulomb and the AUC model, a Young's modulus of 6 MN/m^2, a Poisson's ratio of 0.2 and an undrained Poisson's ratio of 0.495 were specified which results in a bulk modulus $\frac{K_{\text{water}}}{n}$ = 235.2 MN/m^2. The friction angle ϕ' in case of the Mohr-Coulomb model and the friction angle for the critical state ϕ'_{cs} in case of the AUC model are set to 30°. For the Mohr-Coulomb model a dilation angle of 0° is specified. The generated initial stress state results with the AUC model in a rotation angle α_0 of -0.458.

The same material parameters were used for the simple shear test. Here, initially, a vertical load of 10 kPa is applied on the drained soil body. Afterwards, the soil body is sheared horizontally under undrained conditions.

Figure 5.20 shows stress-strain-curves for the numerical analyses of the triaxial tests. The obtained curves correspond to the illustration of Figure 5.11 (right). The Mohr-Coulomb soil yields for triaxial compression at q = 4 kPa and for triaxial extension at q = 2.8 kPa. The AUC model renders an undrained strength of 3 kPa for triaxial compression and 1.2 kPa for triaxial extension.

Figure 5.21 shows stress-strain-curves for the simulation of the simple shear test with the Mohr-Coulomb and AUC models. The Mohr-Coulomb model gives an undrained shear strength of 3.8 kPa, the AUC model gives an undrained shear strength of 2.15 kPa.

Figure 5.22 shows the loading type dependency of normally-consolidated clay reported by Hansen and Clough [24] for laboratory tests on different natural clays. Here the abbreviation CK_0UC stands for triaxial compression under undrained conditions after drained K_0 loading, DSS denotes direct simple shear conditions and CK_0UE stands for triaxial extension under undrained conditions after drained K_0 loading. The undrained shear strength normalised by the vertical initial stress is plotted relative to the undrained shear strength obtained for triaxial compression. The ratio of $s_{\text{u,extension}}$ over $s_{\text{u,compression}}$ of 0.4 as well as the ratio of $s_{\text{u,simpleshear}}$ over $s_{\text{u,compression}}$ of 0.72 found for the AUC model correspond well to results presented in Figure 5.22. For the ratio of $s_{\text{u,simpleshear}}/\sigma_v$ a value of 0.22 is obtained. As reported in [65], this value corresponds well

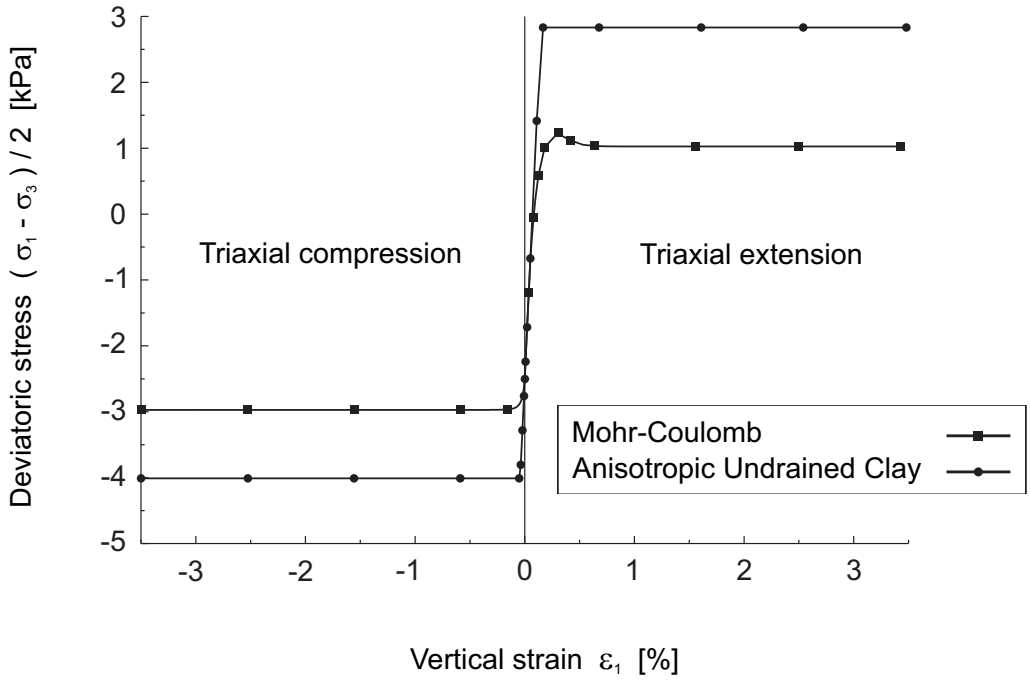

Figure 5.20: Stress-strain-curves of 2D axisymmetric FE analyses of drained consolidation, undrained triaxial compression and extension tests with different material models

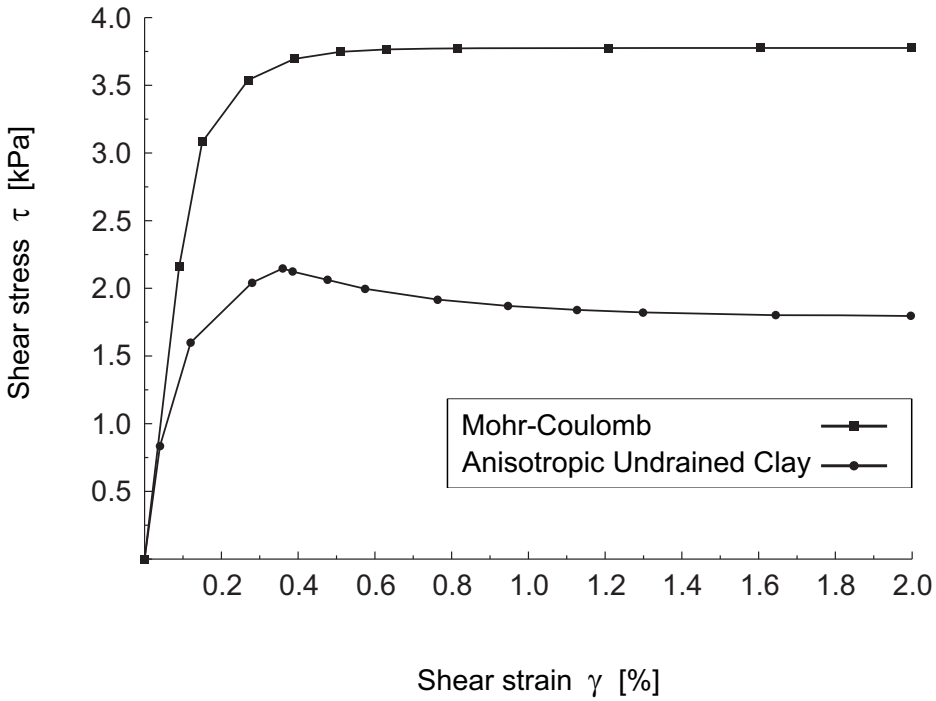

Figure 5.21: Stress-strain-curves of 2D plane strain FE analyses of undrained simple shear with different material models

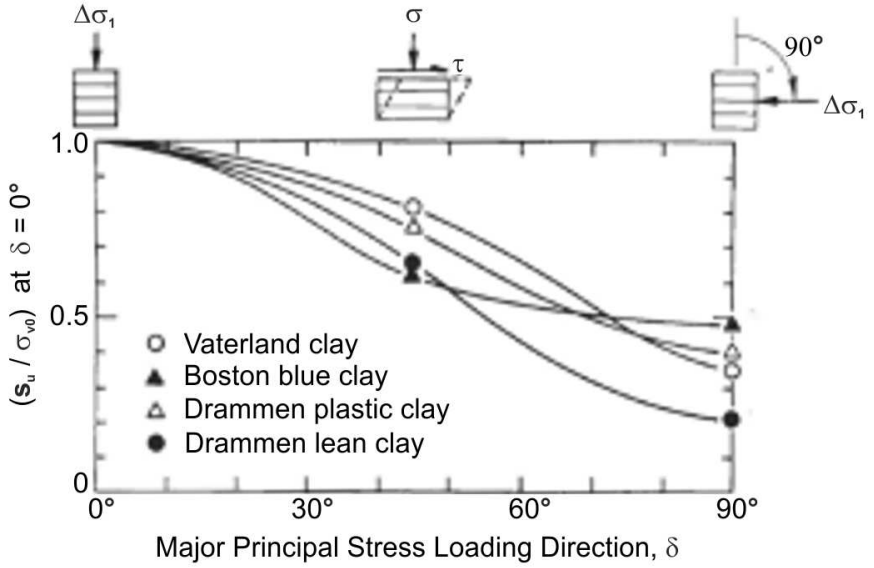

Figure 5.22: Measured undrained shear strengths of clay for different loading types [24]

to experimental results reported by Jamiolkowski *et al.* [33] for normally-consolidated clay.

Chapter 6

Analysis of cone penetration testing in undrained saturated clay

Invention, first employment and early enhancements of the cone penetration test go back to the works of Buisman [14], Barentsen [4], Huizinga [32] and Begemann [5]. Nowadays, cone penetration testing is a widely used in-situ test for soil profiling as well as estimating soil properties of strength and stiffness. The cone penetration test is performed by pushing a measuring device, the cone penetrometer, that is attached to the tip of a steel cylindrical rod into the ground with a constant rate of penetration of 2 cm/s. The standardised cone penetrometer features a conical tip with an apex angle of 60° and a base area of 10 cm^2 (corresponding to a diameter D of 3.57 cm). A friction sleeve with an area of 150 cm^2 is located above the cone. Load cells allow for continuous measurement of the vertical pressure q_c on the cone (tip or cone resistance) and of the horizontal pressure on the friction sleeve while the cone is pushed into the ground. Pore pressures are measured through a pressure sensor that is located either on the cone or just above it. Figure 6.1 provides an overview of the terminology for the cone penetrometer. For a detailed description of penetrometer designs the reader is referred to Lunne *et al.* [41].

In many cases, cone penetration testing is supplemented by laboratory tests on probes taken from the investigated site. This allows to assemble empirical correlations between in-situ CPT measurements and soil properties such as density, permeability, strength or stiffness. For an overview of empirical correlations the reader is again referred to Lunne *et al.* [41].

In the frame of this thesis, the relation between tip resistance and undrained shear strength of clay is investigated. Generally, the tip resistance is related to an undrained shear strength s_u by means of

$$q_c = N_c\, s_u + \sigma_0 \tag{6.1}$$

Here, N_c denotes a cone factor and σ_0 the overburden stress, which is at present not uniquely defined and can be either the vertical stress, horizontal stress or mean stress [45]. In the following, σ_0 is equated with the vertical stress. Empirical cone factors are determined for clay deposits from measured cone tip resistances and values of undrained shear strength that are obtained through laboratory testing on samples taken from the considered deposits. As described in Chapter 5, no unique undrained shear strength exists. Lunne *et al.* [41] therefore recommend to assemble cone factors not as stand-alone values but to complement them by information on how the underlying undrained shear strengths were obtained (triaxial compression test, triaxial extension test, simple shear test ...).

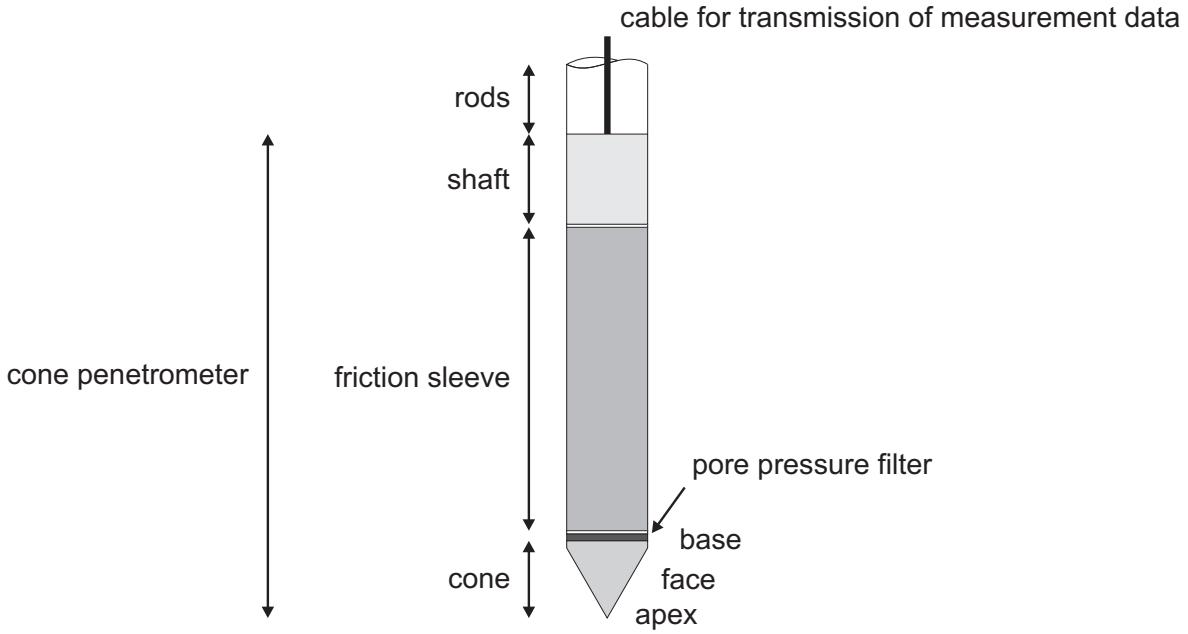

Figure 6.1: Terminology for the cone penetrometer

Empirical correlations are supplemented with theoretical correlations based on analytical or numerical models of the cone penetration process. Undoubtedly, theoretical approaches are necessarily based on simplifications so that obtained results form a mere approximation of in-situ measurements and soil properties. However, numerical approaches reproduce mechanical processes along the lines of a framework of equilibrium equations, boundary conditions, kinematic relations and constitutive relations that is well-founded on physical principles. Obtained results thus provide a sound basis for corroborating field observations and experimental correlations.

The cone tip resistance for undrained clay is determined by a number of soil properties. Numerous studies such as those by Robertson and Campanella [45], Van den Berg [56], Schneider *et al.* [46] and others summarised by Lunne *et al.* [41] address the investigation and quantification of relations between cone tip resistance and soil properties. Penetrometer roughness, the relation between vertical and horizontal initial stresses, soil strength as well as stiffness have an impact on the measured tip resistance. When relating the cone tip resistance to the undrained shear strength of soil, these aspects have to be addressed properly.

As demonstrated in Chapter 3, the implemented quasi-static MPM is well suited to reproduce the evolving stress field for the steady-state penetration process and thus its impact on the recorded cone tip resistance. Investigating the impact of penetrometer roughness on the tip resistance is made possible through the interface elements presented in Chapter 4. With the analyses presented in this chapter, the undrained clay is modelled by means of the AUC model described in Chapter 5. Thus, all of the above listed aspects that determine the cone tip resistance are addressed. As shown in Chapter 5, incorporating anisotropy into the material model allows to model undrained clay with a considerably higher accuracy than with the Mohr-Coulomb, Tresca or Modified

Cam Clay models. At this, the performed simulations distinguish from past numerical analyses.

In Section 6.1, at first, numerical analysis of cone penetration testing in undrained clay by Van den Berg [56] is presented. His work plays a prominent role for the performed analyses, as his computations serve as a archetype. In Section 6.2, the set up of the performed computations is presented in detail, the geometry of the considered problem, applied boundary conditions, the discretisation by means of finite elements and material points. Results of the performed computations are presented and evaluated in Section 6.3.

6.1 Numerical analysis of cone penetration in undrained clay by Van den Berg

In the dissertation of Van den Berg [56], cone penetration testing is simulated by means of an ALE implementation called DIEKA which has been developed by Huétink (see [29] and [30]). With this code, the equilibrium equations are solved for a load increment as with the UL-FEM. The mesh is reset to its initial configuration after each load increment. Stresses are then computed at the locations of Gaussian integration points in the reset mesh on the basis of generated global stress fields.

Van den Berg investigated cone penetration into homogeneous undrained clay, homogeneous drained sand as well as layered soil. For clay, he investigated the dependence of the cone factor N_c on the undrained shear strength and the stiffness of clay, the roughness of the penetrometer surface and the initial stress state. He compared his results with other theoretical correlations.

The undrained clay is modelled by means of the Tresca material model. Van den Berg performed total stress analyses, thus no distinction is made between effective stresses and excess pore pressures. The specified soil cohesion is equal to the assumed undrained shear strength. Incompressibility is modelled through a high Poisson ratio of 0.49.

Figure 6.2 (left) shows the 2D discretisation of the axisymmetric problem used by Van den Berg. The penetrometer itself is not discretised, its surface coincides with the boundary of the mesh. Penetration is simulated by pushing the soil upwards against the penetrometer surface through prescribed displacements that are applied along the bottom of the mesh.

The discretisation consists of 360 elements. 4-noded quadrilateral elements are used. In order to reduce locking, the constant volume condition that applies to undrained soil is fullfilled in an average sense rather than at all integration points with the used elements. Elements with a reduced stiffness are placed along the right boundary of the mesh in order to eliminate boundary effects.

Adhesive contact between penetrometer and soil is modelled by placing 4-noded interface elements along the penetrometer surface as shown in Figure 6.2 (right). As with the interface elements implemented with the quasi-static MPM, these elements make use of a Coulomb-type friction law. Gapping between penetrometer and soil is not considered. Van den Berg considered adhesive contact with adhesion a equal to s_u as well as a

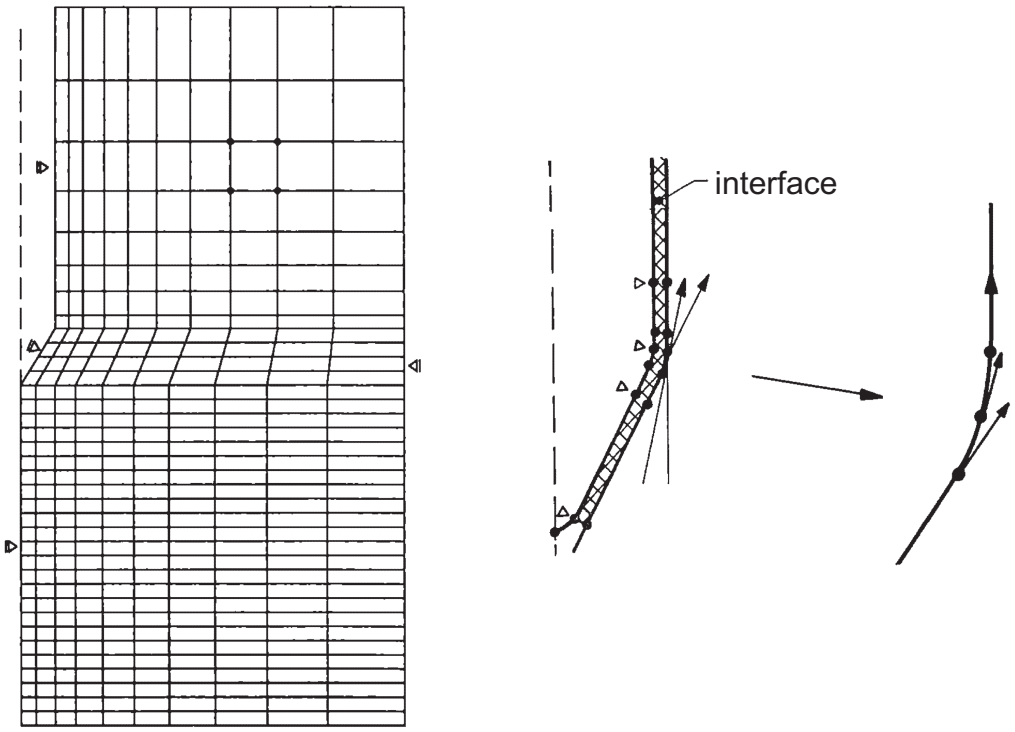

Figure 6.2: Discretisation of the cone penetration problem (left) and application of interface elements along the penetrometer (right) by Van den Berg [56]

equal to s_u / 2. Smooth contact is modelled by setting a to 0.

The standard CPT device possesses a discontinuous edge at the base of the cone. At this location, boundary conditions are not uniquely defined. Van den Berg investigated three possible solutions to this discretisation problem illustrated in Figure 6.2 (right). Either, the node at the base of the cone moves vertically upwards, in the direction of the slope of the cone tip or along an intermediate prescribed displacement. In case of smooth contact, Van den Berg followed the approach of the intermediate solution whereas no boundary conditions were prescribed on the soil-side nodes of the interface elements. Furthermore, he introduced a slight curvature at the base of the cone in order to reduce stress oscillations that are introduced through discontinuities within the displacement field.

The cone is initially located inside a pre-bored hole at a depth of 4.5 cone diameters D measured from the base of the cone (D is 0.0357 m). For penetration of the cone at greater depths, the gradient of vertical stresses due to soil weight is small compared to the magnitude of stresses. Therefore, uniform initial stresses are considered.

In the performed series of computations, Van den Berg varied the stiffness of the soil, the undrained shear strength, the adhesion of the contact surface between penetrometer and soil as well as the K_0 factor. Results for variation of soil stiffness and penetrometer roughness are summarised and compared to theoretical solutions in Figure 6.3. Here, the obtained cone factors are plotted over the rigidity index I_r which is defined as G/s_u. The results obtained with the ALE method are represented by the hatched area. The up-

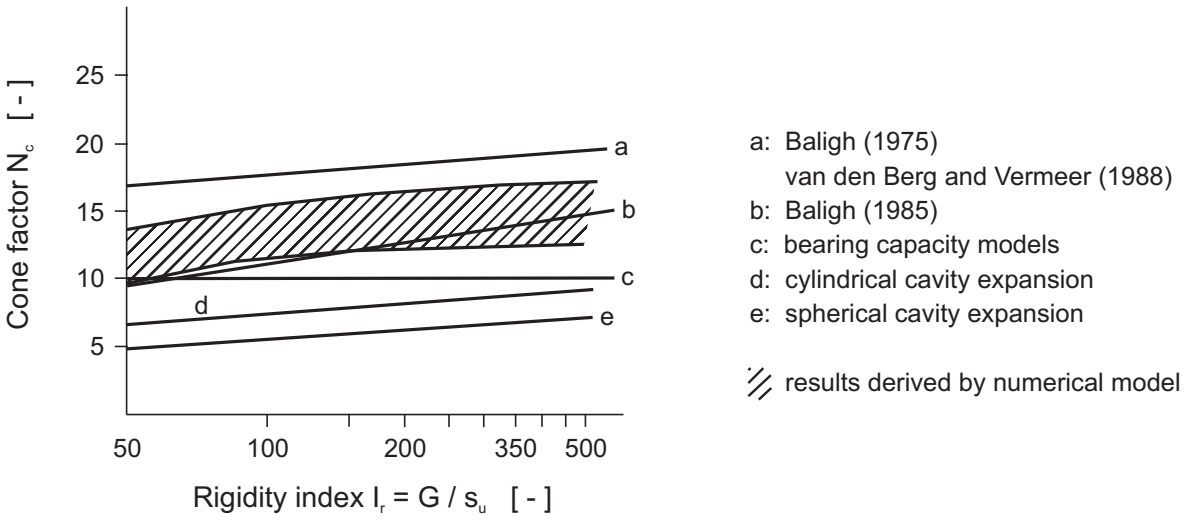

Figure 6.3: Relation between cone factor N_c and rigidity index I_r according to different models and numerical analyses with the ALE method, Van den Berg [56]

per bound of the hatched area corresponds to computational results for a rough contact surface, the lower bound to results for a smooth contact surface.

6.2 Geometry and discretisation

Geometry The geometry of the problem is shown in Figure 6.4. It is closely based on the analyses made by Van den Berg in order to allow for comparison of results. Differences with regard to geometry and discretisation of the problem are noted in the following.

A 20° slice of the axisymmetric problem is considered. With smaller angles, finite elements near the longitudinal axis exhibit extreme aspect ratios that are known to produce numerical inaccuracies. The slice possesses a triangular base area rather than the shape of a cylindrical segment as might be expected for an axisymmetric problem. Advantage of the chosen geometry is that it simplifies the application of boundary conditions on the planar outer boundary surface. Van den Berg states that a width of the discretised space of 20 to 25 cone diameters D is needed for his analyses to eliminate boundary effects. Lu *et al.* mention that a mesh width of 0.75 $\sqrt{I_r}\ D$ represents a safe estimate [40]. Check analyses showed that this equation provides a good estimate for the required mesh width when considering the prevention of any boundary effect. Some of the performed computations would require according to this equation a mesh width of 18 and 26 D. However, such large grids could not be used for extensive series of computations due to the high involved computation times and memory consumption. With all computations, the mesh extends outwards by 14 D at the shorter edge. This represents the limit of what is feasible with the present implementation of the quasi-static MPM. With some of the performed computations, stresses along the boundary slightly deviate from the initial stresses. However, they subside sufficiently so as not to alter the occurring

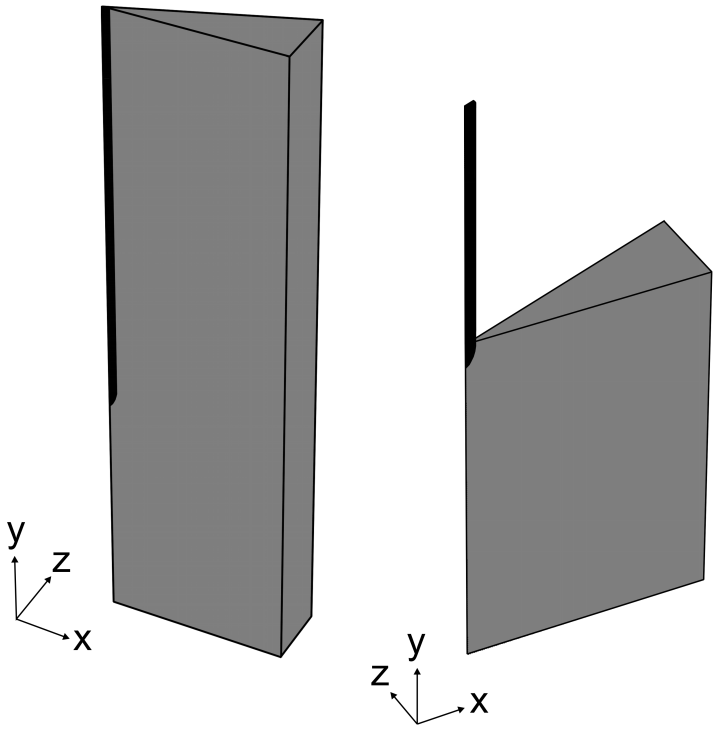

Figure 6.4: Geometry of the discretised space (left) and initial configuration (right)

mechanical processes. This is confirmed by check analyses with a mesh width of 19 D which showed that the tip stress is not influenced by the mesh width with any computation.

In the initial configuration, the cone of the penetrometer is located inside the soil up to its base as shown in Figure 6.5 (left). Here, the cone tip initially lies 1.37 D below the soil surface. In contrast, Van den Berg placed the cone initially at a depth of 4.5 D measured from its base. Placing the cone initially inside the soil complicates the generation of initial stresses within the soil body. In order to obtain an even stress field, the location of the rigid cone has to be adapted to the deformations of the adjacent soil due to the applied initial loading. Alternatively, computations with the cone initially located 1 D above the soil surface were performed as illustrated in Figure 6.5 (right). However, when increasing the complexity of the simulations, for example by taking into consideration the anisotropy of clay, the penetration of the cone tip into the ground brought considerable numerical complications with it. Therefore, this approach was abandoned. The implemented approach to the generation of soil stresses for initial loading is presented below when elaborating on boundary conditions.

The chosen geometry of the cone is shown in Figure 6.6 (left). As with Van den Berg the cone is slightly rounded in order to circumvent numerical problems induced by a discontinuous edge at the base of the cone. Hence, the cone features a double-curvature

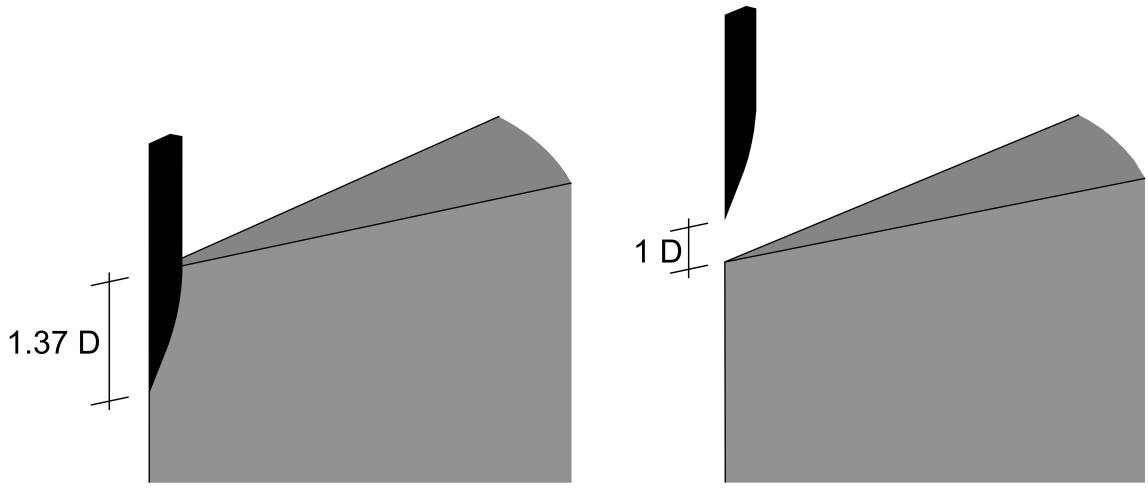

Figure 6.5: Considered initial configurations; (left) cone initially located inside soil; (right) cone initially located above the soil

surface. For comparison, the true geometry of the standardised cone is shown. Apart from this modification, the dimensions of the penetrometer correspond to those of a standard penetrometer. The apex of the cone likewise exhibits a discontinuity in the displacement field. The treatment of this discontinuity will be considered below.

The height of the discretised space has been chosen so as to accomodate for a penetration depth of up to 18 D measured from the base of the cone. This penetration depth ensures that the influence of the soil surface on the evolving steady-state deformation process is eliminated for any of the performed computations in the final deformed state.

With the performed computations, only rectilinear penetration is considered and the cone penetrometer is rigid. As laid out in Chapter 3, the surface of the penetrometer preferably coincides throughout the computation with finite element boundaries. Consequently, there is no need to discretise the penetrometer itself, analogous to the approach taken by Van den Berg. This simplifies the application of boundary conditions, interface elements respectively, along the penetrometer surface. To this end, the approach of moving the finite element discretisation relative to the material point discretisation as presented in Chapter 3 is used, though in a slightly altered manner.

Rather than incrementally moving the penetrometer surface downwards into the ground, and with it the entire finite element discretisation, the soil is pushed upwards against the fixed penetrometer surface. The upward displacement of the material point discretisation is realised by prescribed displacements applied on the bottom boundary of the mesh. At the end of an increment, the deformed finite element mesh is reset to its initial configuration while material points maintain their displacements. Obviously, elements along the bottom boundary would become void of material points. Therefore, material points are continuously fed along the lower boundary into the mesh from a cloud of material points that is initially located outside the discretised region as presented in Chapter 3.

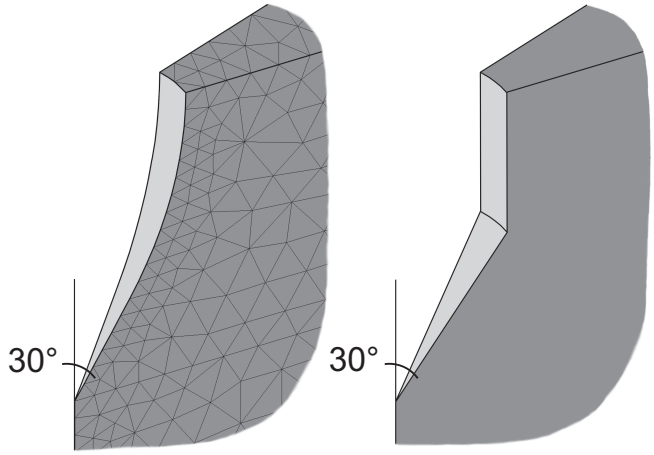

Figure 6.6: Used double-curved geometry of the cone tip (left) and geometry of the standard CPT (right)

In order to ensure that the change of the stress field due to the penetration process does not extend to the bottom boundary of the finite element discretisation with any of the performed computations, the lower mesh boundary is located 18 D below the tip of the cone. According to [41], the cone senses a layer at a distance of 10 to 20 D ahead, depending on the stiffness of the soil, which supports this choice.

Boundary conditions Along the sides of the mesh, displacements are fixed normal to the vertical planes (roller boundaries).

Smooth contact between soil and penetrometer is modelled by prescribing roller boundaries along the penetrometer surface as shown in Figure 6.7 (left). The degrees of freedom along the surface are rotated such that nodal displacements are fixed normal to the penetrometer surface and free in tangential directions. Here, the tangential directions are averaged from the orientations of the (plane) element sides that lie on the penetrometer surface. This approach corresponds to the averaged orientation of boundary conditions along the penetrometer used by Van den Berg. The apex of the cone exihibits a discontinuity of the displacement field similar to the one at the base of the cone. Here, the apex node is fixed as otherwise the shape of the cone would be altered during the deformation process.

Frictional and adhesive contact between penetrometer and soil is modelled by placing interface elements on the penetrometer surface. No special attention is paid to boundary conditions along this surface: the structure-side nodes are fully fixed, the soil-side nodes are free to move. This also holds for the soil-side node of the apex dual node. Figure 6.7 (center and right) shows the placement of the interface elements along the cone which corresponds to the approach taken by Van den Berg.

Computations with the AUC model require initial stresses for initialisation of the extend and orientation of the yield surface in principal stress space. Therefore, surface traction is considered with some of the presented computations. Anisotropic initial stresses

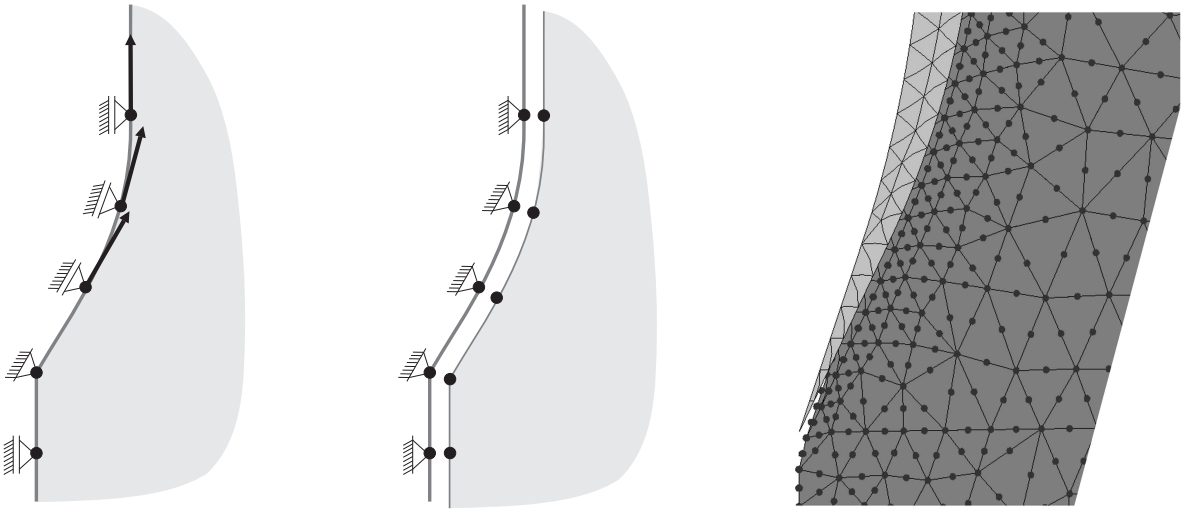

Figure 6.7: Application of roller boundaries along the penetrometer surface for modelling of smooth contact (left), placement of interface elements along the penetrometer surface for modelling of adhesive contact (center) and FE discretisation of the cone with interface elements (right)

are generated for a K_0 value of 0.5. To this end, two initialisation phases are performed before the penetration of the cone is simulated in a third computation stage.

In order to achieve a K_0 value of 0.5, the Poisson ratio of the soil is set to a value of 0.333 in the first initialisation phase, which gives for deformations in the elastic range by means of $\sigma_2 = \sigma_3 = \frac{\nu}{1-\nu}\sigma_1$ the desired K_0 value. Afterwards, in a "soil replacement" phase, the initial material model, soil parameters respectively, are replaced by those used during the cone penetration phase. The three phases of the computation, stress initialisation phase, soil replacement phase and cone penetration phase, are illustrated from left to right in Figure 6.8. During the two initialisation phases, drained conditions are considered, whereas during the cone penetration phase the soil is considered undrained.

When the tip of the penetrometer is initially located inside the soil, the application of surface traction cannot be performed in a straightforward manner. As explained above, the relative displacement between the fixed cone and soil due to initial loading introduces inaccurate stresses within the soil. Therefore, an alternative approach was chosen. In the two initialisation phases, nodes at the initial top surface of the soil are fixed and the surface traction $\boldsymbol{t}$ is applied along the bottom boundary of the mesh (see Figure 6.8 (left)). That way, soil displacements in the vicinity of the cone remain relatively small and thus the stress field shows only a small deviation from the uniform stress field.

In the cone penetration phase, incremental prescribed displacements $\delta\boldsymbol{u}$ are applied at the bottom boundary of the mesh to simulate the cone penetration process and traction is applied on the top soil surface as shown in Figure 6.8 (right). Now, traction forces are assigned to material points as described in Chapter 3 so that the load moves upwards together with the soil surface. Along the penetrometer surface either roller boundaries or interface elements are applied in this phase.

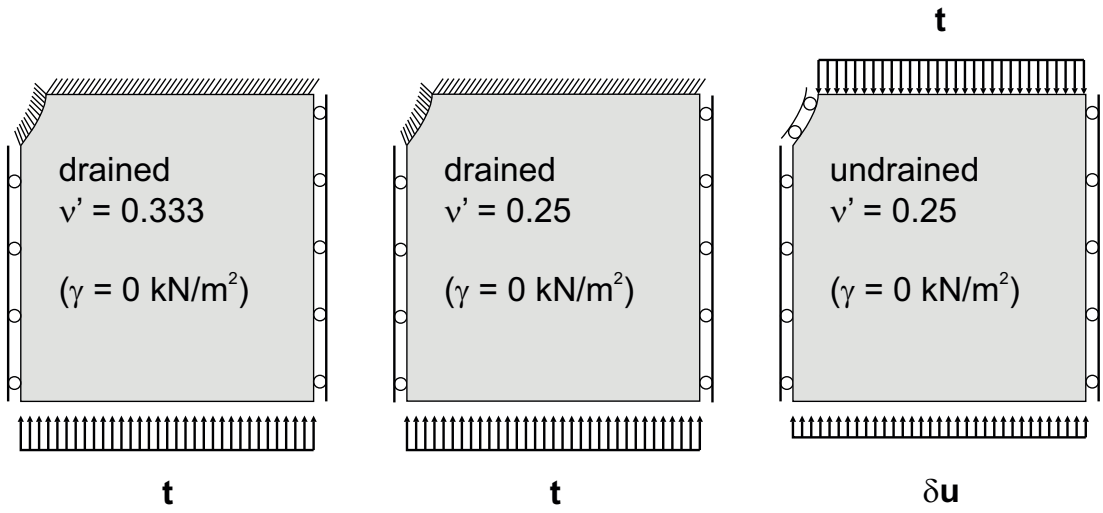

Figure 6.8: Calculation phases for CPT computations with applied traction from left to right: 1. application of traction along bottom boundary, generation of K_0 stresses for drained soil, 2. change of material model and soil parameters, 3. application of traction on top soil surface, application of incremental prescribed displacements along bottom boundary

As described in Chapter 3, the application of traction forces on material points introduces local inaccuracies. Furthermore, the occurrence of slightly inaccurate initial stresses in the vicinity of the cone cannot be prevented with the taken approach. However, because these disturbances are limited to a small region near the soil surface, they have only a limited impact on the outcome of computations. Once a steady-state penetration process evolved, the top soil surface is located more than 6 D above the cone base and has no influence anymore on the stress field near the cone tip.

Soil weight is not considered with the presented computations although it poses no technical problem — computations with soil weight have been performed recently without additional difficulty.

Finite element discretisation All computations were performed with 4-noded tetrahedral elements. Only two different finite element discretisations were used: one with interface elements and one without interface elements for modelling smooth contact. The two meshes are depicted in Figure 6.9. Table 6.1 lists the key figures of the used discretisations.

The number of degrees of freedom of the discretisation must be sufficiently large in order to properly reproduce the displacement field of the problem, the stress field respectively, with the used constant-strain elements. Here, special attention must be paid to the region around the penetrometer cone which exhibits large stress gradients. This is especially true for the apex and the base of the cone, where high stress peaks occur. At the apex of the cone, element deformations are severly restricted through boundary conditions which introduces an unrealistically high stress peak. In case of the discretisation with interface elements, a refinement of the mesh is required along the entire length

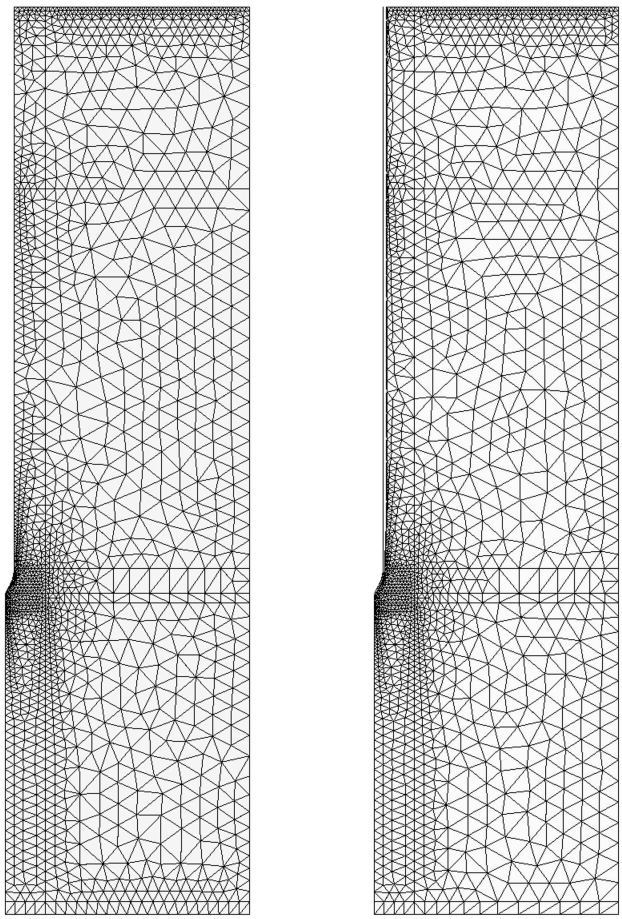

Figure 6.9: FE discretisations (left) without interface elements and (right) with interface elements

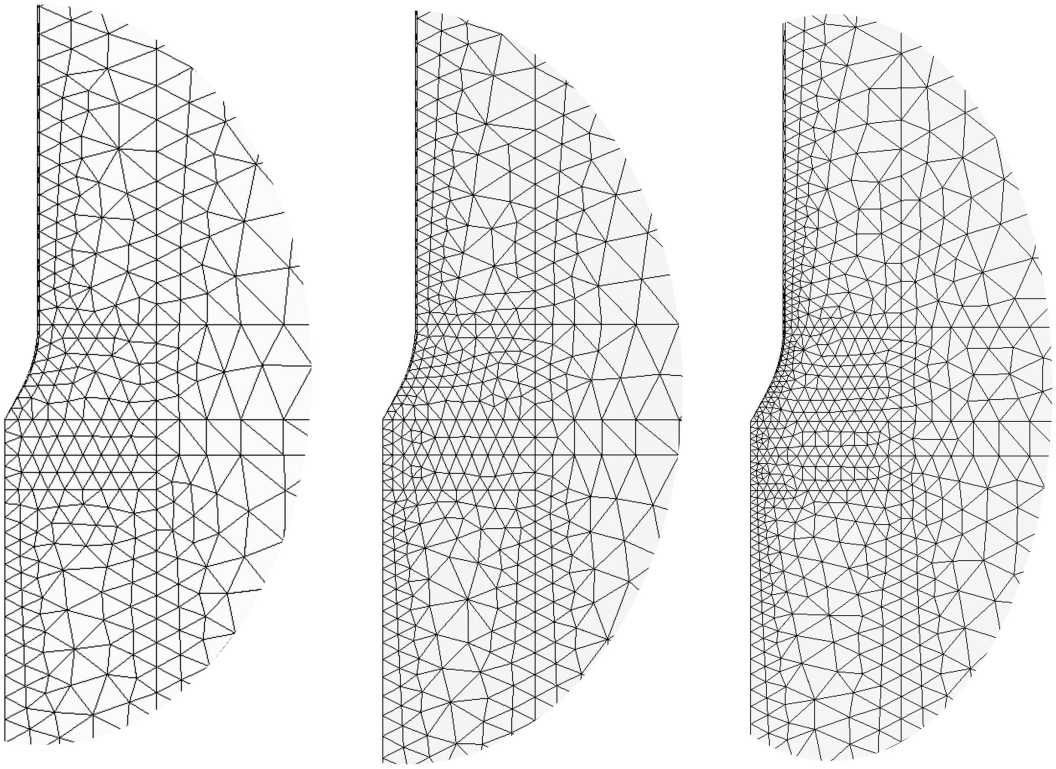

Figure 6.10: FE discretisation without interface elements with (left) 10,902 degrees of freedom, (center) 11,859 degrees of freedom and (right) 15,678 degrees of freedom

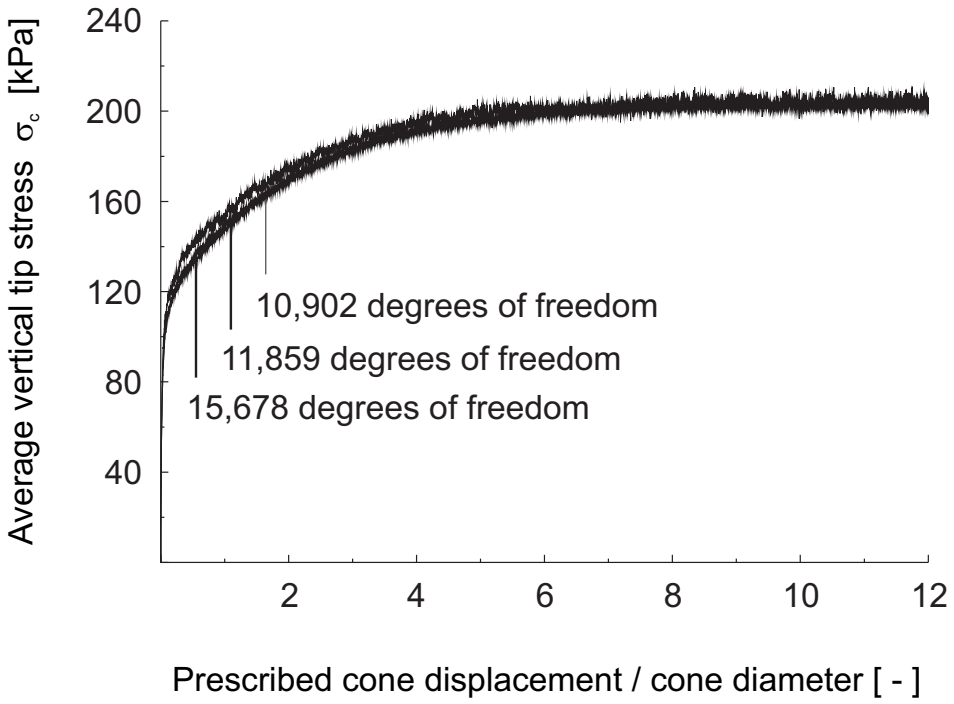

Figure 6.11: Average vertical tip stress plotted over the cone penetration for different FE discretisations without interface elements

of the penetrometer in order to accomodate for the heavy shear strains that occur due to the adhesive contact between soil and penetrometer. Furthermore, a mesh refinement is required on the narrow edge along the longitudinal axis of the discretised slice. If the edge were discretised by only a small number of elements, nodal displacements of these elements would be severly constrained because, in general, most nodes would lie on either one of the converging mesh boundaries. Towards the outer side of the discretisation a rather coarse mesh proved to be sufficient.

In order to determine the required level of refinement, analyses were performed with different numbers of degrees of freedom of the mesh. The check was performed without consideration of interface elements. The mesh refinement concentrated on the region around the cone. Figure 6.10 shows close–ups of this region for three levels of mesh refinement. The parameters of the three discretisations are listed in Table 6.1. Figure 6.11 shows the vertical tip stress plotted over the relative cone penetration for the three meshes. Only a slight difference in results can be observed between the discretisations with 15,678 and 11,859 degrees of freedom, the obtained steady-state vertical tip stress is identical. The computation with 10,902 degrees of freedom shows significant oscillations and gives a slightly larger vertical tip stress. Thus, a discretisation with 11,859 degrees of freedom would seem sufficient.

Due to the complex geometry of the considered problem, elements of the discretisation tend to exhibit large aspect ratios. All generated discretisations showed a small number of 5 to 10 tetrahedral elements whose minimum angle between boundary surfaces lies between 1 and 5°. As the discretisation with 15,678 degrees of freedom showed some-

	Number of degrees of freedom	Number of elements	Number of material points
Without interface elements	15,678	24,777	286,410
	11,859	17,950	255,060
	10,902	16,392	243,030
With interface elements	18,779	23,880	279,340

Table 6.1: Discretisation data

what fewer elements with small minimum angles in the vicinity of the cone, this level of refinement was chosen for further numerical analyses.

Material point discretisation With the implemented quasi-static MPM, an equal number of 10 material points is initially placed inside each finite element. Additionally, an external cloud of material points is generated in a preliminary calculation step as presented in Chapter 3. Allowing for an upward movement of the soil of 18 D from the cone base onwards gives a height of 18 D for the external material point cloud. Figure 6.12 illustrates the material point discretisation including the generated external cloud of material points in its initial and final configuration for the mesh with a width of 14 D. For the computations with a grid width of 19 D, the external cloud of material points has a height of only 12 D due to limitations on memory consumption. Consequently, computations with this grid are limited to a penetration depth of 12 D. Rather dense external clouds of material points are generated in order to prevent the occurrence of empty elements within the discretisation. Table 6.1 lists the total number of material points, including those of the external material point cloud.

The used finite element and material point discretisations reach the limits of the possible with the present implementation of the quasi-static MPM due to the considerable memory consumption and computation time required with the performed analyses. A standard 32-bit DuoCore personal computer was used whose RAM is limited to 3 GB.

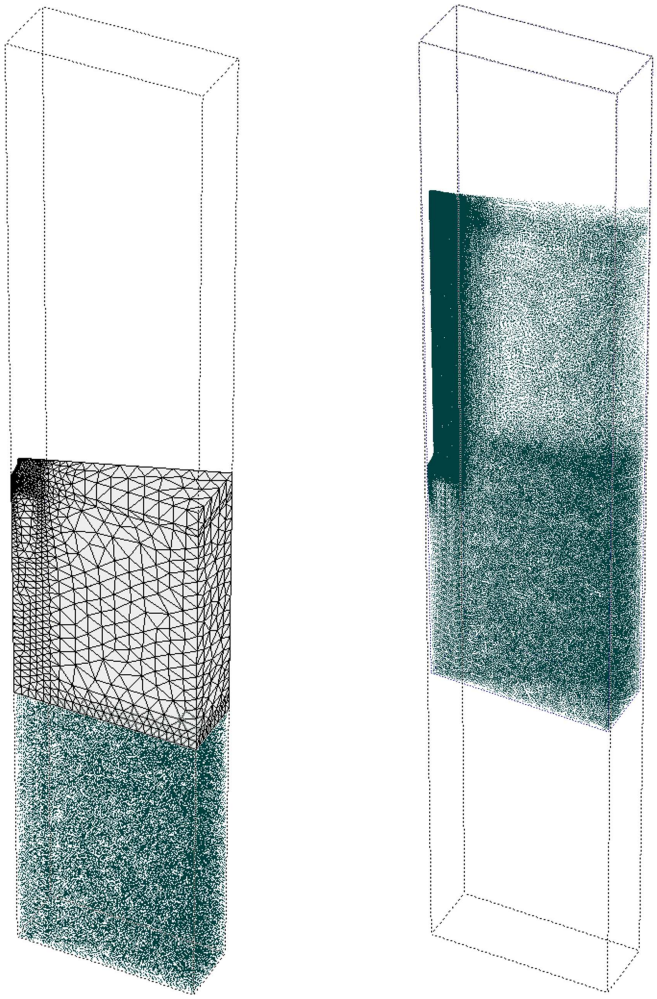

Figure 6.12: Material point discretisation for the initial configuration including the external cloud of material points (left) and final configuration of the material point discretisation at a penetration depth of 18 D for a representative computation (right)

6.3 Results

In a first step, computations with material parameters that closely match those by Van den Berg [56] were performed in order to check the proper functioning of the quasi-static MPM for CPT analyses. In a second step, the Mohr-Coulomb model is introduced to the simulation of cone penetration testing and, finally, the AUC model.

6.3.1 Analyses with the Tresca material model

At first, the performed series of computations are presented. Subsequently, obtained cone factors are compared to values presented by Van den Berg. Lu *et al.* [40] likwise performed an extensive parameter study on cone penetration in undrained clay by means of an ALE method. Their results will be considered, too. Afterwards, aspects of the simulated penetration process such as the generation of shear strains and pore pressures are presented.

The presented computations as well as those by Van den Berg are based on the Tresca material model. An undrained shear strength s_u of 20 kPa is specified. No soil weight or overburden stress is considered. The used material parameters and those of three reference computations by Van den Berg are listed in Table 6.2.

Computations were performed for smooth as well as adhesive contact between soil and penetrometer surface in compliance with Van den Berg's analyses. With regard to adhesive contact, the adhesion was set to both half the undrained shear strength and equal to the undrained shear strength of the soil as specified in Table 6.2. As reported by Lu *et al.* in [40], field values for adhesion between penetrometer surface and soil are found to lie between 0.2 and 0.6 s_u. The stiffness of interface elements in normal and tangential directions has been set to 4,644 MN/m^3, 410 MN/m^3 respectively, for all computations. It should be noted that these stiffness parameters only affect deformations in the elastic range. With the performed computations for both, soil and interfaces, tensile stresses are allowed.

The computations are split into two groups identified by Roman numerals (I and II). The first series comprises total stress analyses as done by Van den Berg, effective stress analyses are pooled in the second series. With the latter, as described in Chapter 5, distinction is made between effective stresses and excess pore pressures, whereas the former only render total stresses.

Unfortunately, an exact match of material parameters with those used by Van den Berg was not possible for the total stress analyses. Van den Berg used a high Poisson ratio of 0.49 for his computations. Due to numerical problems, the total stress analyses with interface elements required a Poisson ratio of 0.4. Thus, the incompressibility condition of undrained behaviour is only roughly observed with these computations. With computation I.1, the impact of a smaller Poisson ratio on the cone factor has been investigated by setting the Poisson ratio to 0.485 for a computation with smooth contact. With all total stress analyses the rigidity index corresponds to the one of the reference computations by Van den Berg ($I_r \approx 101$).

For the effective stress analyses (series II), the stiffness of the pore water must be speci-

Computation	E	ν'	s_u	ν_u	K_w/n	I_r	a	N_c
	$[\mathrm{kN/m^2}]$	$[-]$	$[\mathrm{kN/m^2}]$	$[-]$	$[\mathrm{kN/m^2}]$	$[-]$	$[\mathrm{kN/m^2}]$	$[-]$
V. d. Berg	6,000	-	20	0.490	-	100.7	0.0	11.0
V. d. Berg	6,000	-	20	0.490	-	100.7	10.0	12.2
V. d. Berg	6,000	-	20	0.490	-	100.7	20.0	12.9
I.1	6,000	-	20	0.485	-	101.0	0.0	9.9
I.2	5,656	-	20	0.400	-	101.0	0.0	9.4
I.3	5,656	-	20	0.400	-	101.0	10.0	11.3
I.4	5,656	-	20	0.400	-	101.0	20.0	12.9
II.1	5,050	0.250	20	0.485	63,970	101.0	0.0	10.2
II.2	5,050	0.250	20	0.490	92,820	101.0	0.0	10.2
II.3	5,050	0.250	20	0.490	92,820	101.0	10.0	11.8
II.4	5,050	0.250	20	0.490	92,820	101.0	20.0	13.4
II.5	6,000	0.250	20	0.490	110,300	120.0	0.0	10.2
II.6	6,000	0.250	20	0.490	110,300	120.0	10.0	12.0
II.7	6,000	0.250	20	0.490	110,300	120.0	20.0	13.8

Table 6.2: Soil material parameters and obtained cone factors N_c for series I and II as well as the reference computation by Van den Berg [56]

fied. This is done by means of an undrained Poisson ratio as explained in Chapter 5. For the performed analyses, an undrained Poisson ratio of 0.49 has been used. The effective Poisson ratio of the soil has been set to 0.25 in order to ensure that the bulk modulus of the pore water is sufficiently high compared to the stiffness of the soil skeleton. In computation II.1 a slightly lower undrained Poisson ratio of 0.485 has been used in order to investigate the impact of this parameter on results.

The effective stress analyses II.2 to II.4 correspond to the total stress analyses I.2 to I.4. Both sets exhibit a rigidity index of 101. In the second set of computations II.5 to II.7, a higher rigidity index of 120 is considered to investigate the effect a change of I_r has on the cone factor.

The last column of Table 6.2 lists the cone factors N_c obtained for the respective computations. The cone factors provided for the reference computations are explicitly stated by Van den Berg in his thesis. He does not provide discrete cone factors nor material parameters for computations with I_r = 120. Here, Figure 6.3 is used as a reference.

The cone factor is obtained by plotting the relative tip stress σ_c/s_u over the cone displacement normalised by the cone diameter. Once the influence of the soil surface on the movement of soil particles around the penetrating structure subsides, a steady-state deformation process evolves. The tip stress σ_c for the fully developed steady-state penetration process corresponds to the tip resistance q_c measured during cone penetration testing and thus renders the cone factor.

The tip stress of the cone penetrometer is computed by summing up the vertical reaction forces at nodes of the cone up to its base. The nodal reaction forces are computed

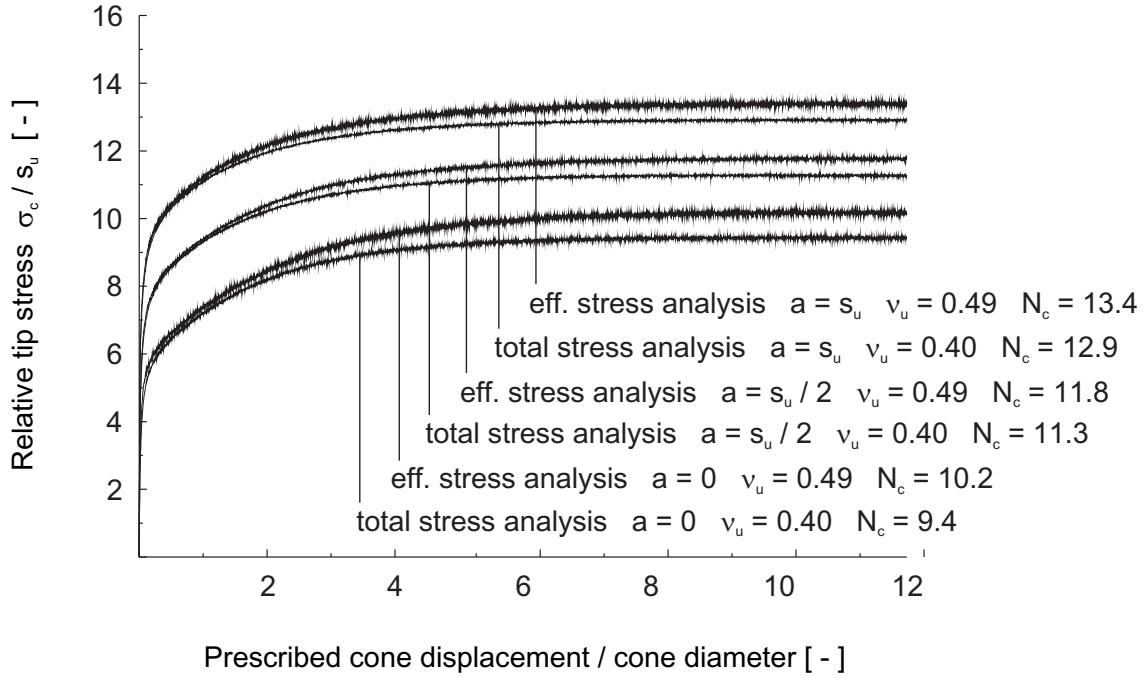

Figure 6.13: Relative tip stress plotted over the relative cone displacement for computations I.2, I.3, I.4 (total stress analyses) and II.2, II.3, II.4 (effective stress analyses) for I_r = 101

from

$$\boldsymbol{F}_{\text{reaction}} = \int_V \boldsymbol{B}^{\mathrm{T}}\,\boldsymbol{\sigma}\,\mathrm{d}V \tag{6.2}$$

The resulting force is then divided by the base area of the cone segment, which equals 0.556 cm^2 for the considered 20° slice. The obtained value represents an average vertical tip stress. The cone displacement is taken from the accumulated displacement increments that are prescribed at the bottom of the mesh. This value only approximates the assumed true movement of the cone as the compression of the soil is not taken into account. However, in case of the considered undrained soil, the compression of the soil is rather small so that the prescribed displacement gives a reasonable measurement of the penetration depth with reference to the base of the cone.

Comparison of results with analyses by Van den Berg [56] and Lu et al. [40] Figure 6.13 shows the tip stress plotted over the cone penetration for the total and effective stress analyses I.2, I.3, I.4 and II.2., II.3, II.4 (all with I_r = 101) for a = 0, $a = s_u/2$ and $a = s_u$. With all computations, a steady-state penetration process has fully developed at a depth of approximately 6 D. The roughness of the penetrometer surface does not appear to have an impact on the depth at which a steady-state occurs. The cone factors for the effective stress analyses lie above the values of the total stress analyses. The difference is somewhat larger for the smooth contact surface than the rough contact surface. The analyses with rough contact render the highest cone factors of 12.9 and 13.4 compared

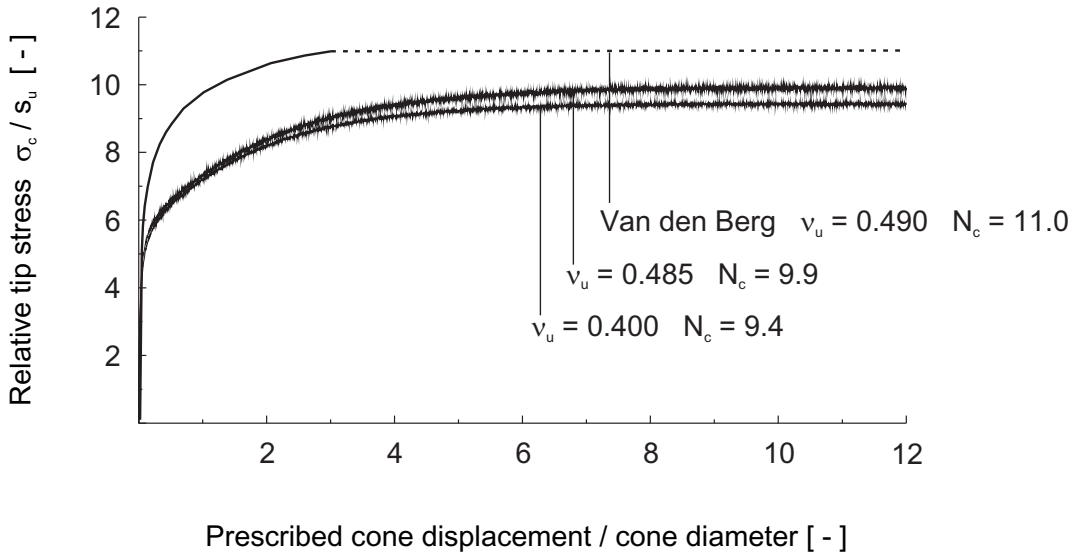

Figure 6.14: Relative tip stress plotted over the relative cone displacement for computations I.1, I.2, I.3 (total stress analyses) for I_r = 101

to a value of 12.9 reported by Van den Berg. The computations with $a = s_u/2$ give cone factors of 11.3 and 11.8 compared to 12.2 found by Van den Berg, for smooth contact the cone factors are 9.4 and 10.2 compared to 11.

The differences between the cone factors of the total and effective stress analyses appear to have a simple cause. Figure 6.14 shows the tip stress plotted over the cone penetration for total stress analyses with a variation of the Poisson ratio whereas the rigidity index is kept at 101. Here, smooth contact is considered. The dashed line extrapolates the tip stress of the computation by Van den Berg which was stopped at 3 D. With increasing Poisson ratio, the cone factor increases from 9.4 for a Poisson ratio of 0.4 to a value of 9.9 for a Poisson ratio of 0.485. The cone factor for a Poisson ratio of 0.49 would thus lie slightly below a value of 10 which corresponds reasonably well to the cone factor of 10.2 found with the effective stress analyses. Obviously, total and effective stress analyses show good agreement for a proper choice of Poisson's ratio. However, for smooth contact the reference value by Van den Berg is not reached.

Figure 6.15 shows results for a variation of the undrained Poisson ratio as well as for a computation with the cone initially placed above the soil rather than inside. The curves are obtained for effective stress analyses and smooth contact. The initial location of the cone has only a slight impact on the resulting tip stress at steady-state deformation. A change of the undrained Poisson ratio from 0.49 to 0.485 has no significant impact on results. The same was found for adhesive contact.

Table 6.3 lists cone factors obtained by Van den Berg, by Lu *et al.* [40] and results of the performed effective stress analyses. Results by Van den Berg for I_r = 120 are taken from Figure 6.3.

Lu *et al.* use an ALE method called RITSS which has been developed by Hu and Randolph [28]. As with other ALE implementations, it solves the equilibrium equations identical to the FEM. With RITSS, a complete remeshing is performed to circumvent

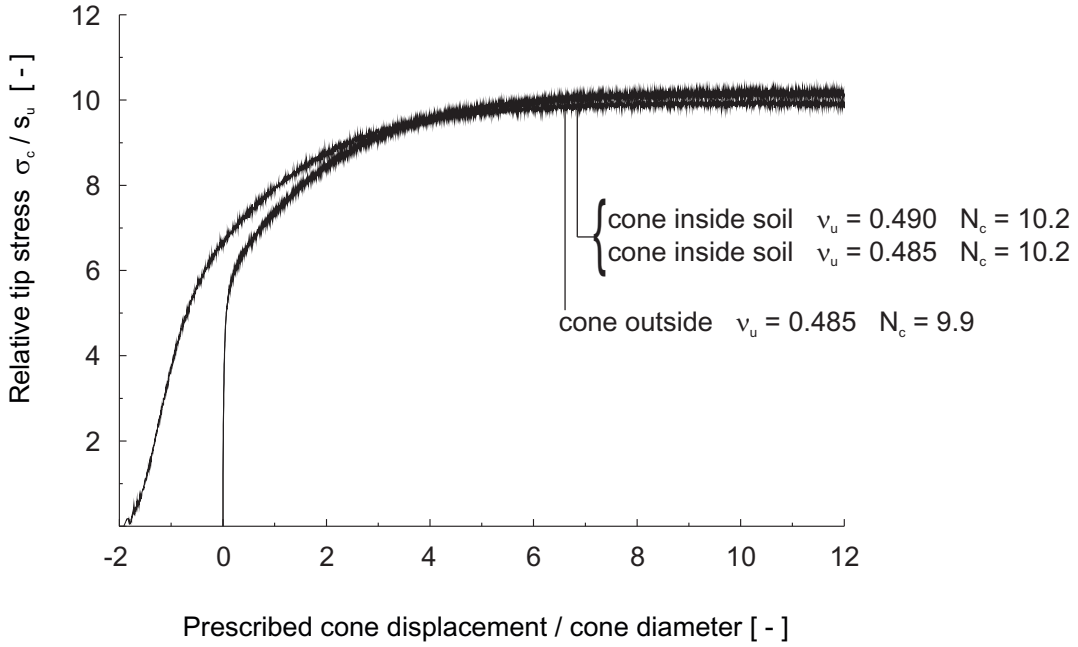

Figure 6.15: Relative tip stress plotted over the relative cone displacement for computations II.1 (ν_u = 0.485) with cone initially placed above the soil surface, II.1 with the cone initially placed inside the soil and II.2 (ν_u = 0.490)

Author	$I_r = 101$ $a = 0$	$I_r = 101$ $a = s_u/2$	$I_r = 101$ $a = s_u$	$I_r = 120$ $a = 0$	$I_r = 120$ $a = s_u/2$	$I_r = 120$ $a = s_u$
V. d. Berg	11	12.2	12.9	11.4	13.4	15.5
Lu *et al.*	10.8	11.4	12.1	11.1	11.7	12.4
this study	10.2	11.8	13.4	10.2	12	13.8

Table 6.3: Cone factors obtained by Lu *et al.* [40], Van den Berg [56] and for series II

mesh distortions after an arbitrary number of load steps. Stresses at Gaussian integration points of the new mesh are determined on the basis of the stress fields within elements of the old mesh that new integration points are located in. On the basis of their numerical analyses, they developed an equation for the cone factor which takes into account I_r, penetrometer roughness and initial stress anisotropy

$$N_c = 3.4 + 1.6 \ln I_r - 1.9\Delta + 1.3\,\alpha_c \quad \text{with} \quad \Delta = \frac{\sigma_{v0} - \sigma_{h0}}{2\,s_u} \tag{6.3}$$

where σ_{v0} and σ_{h0} are the initial vertical and horizontal stresses and α_c represents the friction ratio a/s_u that lies between 0 for a smooth contact surface and 1 for a fully rough contact surface.

Figure 6.16 shows the results for effective stress analyses with rigidity indices of 101 (circles) and 120 (squares) added to a chart that is generated from Equation 6.3. A further

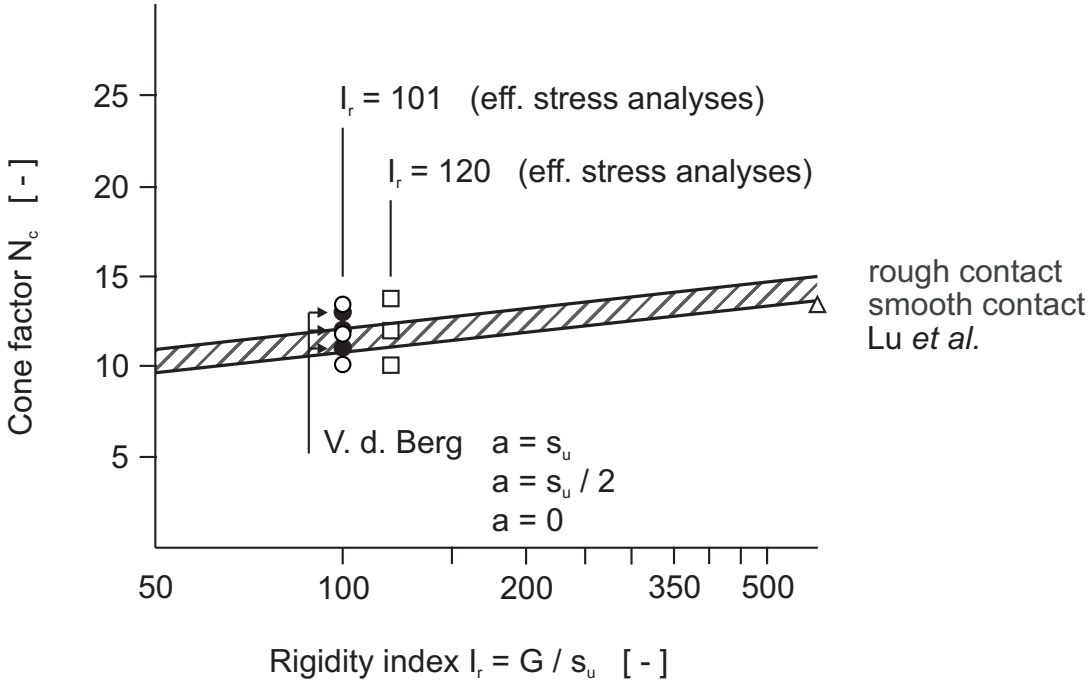

Figure 6.16: Comparison of results of computations II.2, II.3, II.4, II.5, II.6 and II.7 with results obtained by Van Den Berg and Lu *et al.*

computation that has been performed with a rigidity index of 600 is added to the chart (triangle). The filled circles indicate cone factors stated by Van den Berg in his thesis, the white symbols correspond to results found with the quasi-static MPM. The symbols of each column mark from top to bottom cone factors for a contact surface with $a = s_u$, $a = s_u/2$ and $a = 0$. Clearly, the change of rigidity index from 101 to 120 does not have an impact on the cone factor for the smooth contact — both computations render the same cone factor of 10.2. In case of adhesive contact, a slight increase of the cone factors can be observed that corresponds to the increase indicated through the hatched region.

For a smooth contact surface, cone factors according to Lu *et al.* lie slightly below values obtained by Van den Berg and above the values obtained with the quasi-static MPM. For adhesive contact, the equation of Lu *et al.* gives cone factors that are considerably lower than those obtained by Van den Berg. The difference with results of the quasi-static MPM are somewhat smaller. As a general trend, differences in results increase with increasing roughness of the penetrometer surface. Furthermore, from the considered computations, it would seem that results deviate more, the larger the stiffness of the soil: the largest differences in cone factors are found for $I_r = 120$ and a fully rough contact surface.

The found differences can be attributed to numerous sources, which are difficult to quantify. Differences might be attributed to differences of the employed numerical methods, especially with regard to the contact and smoothing algorithms. Furthermore, the interpolation of computational results for obtaining Equation 6.3 and the chart provided by Van den Berg introduces deviations from raw numerical results. With this regard,

the cone factors provided by Van den Berg for $I_r \approx 101$ form the best reference for the performed numerical analyses.

Differences in the discretisation of the problem form another source. With the quasi-static MPM a significantly finer mesh has been used compared to the discretisation by Van den Berg. This is especially true for the region above the cone. Here, a mesh refinement is of relevance for the case of adhesive contact when large shear strains do not only occur at the tip of the cone but also along the shaft.

Van den Berg modelled smooth contact by setting the adhesion of the interface elements to zero, whereas roller boundaries have been used with the quasi-static MPM. This would explain why the difference of results is larger for smooth contact than for adhesive contact.

As shown in Figure 6.15, the initial location of the cone (inside or above the soil) does not have a significant impact on results.

All computations are based on the Tresca material model so that the constitutive modelling can be excluded as a source of differences.

Van den Berg specified a tolerated error of 0.1 percent for his computations. With the quasi-static MPM, a tolerated error of 1 percent was used instead which might also contribute to the difference in results.

Considering the difficulty of quantifying the numerous possible sources of differences between the numerical analyses listed in Table 6.3, it seems justified to state that the results of the quasi-static MPM agree well with those of the reference computations within the range of accuracy that can be obtained by any numerical method.

Soil strains and stresses for steady-state penetration The following illustrations are a snapshot of the steady-state penetration process taken at a penetration depth of 10 D.

If not otherwise stated, the figures depict soil strains and stresses that are post-processed by mapping data of Gaussian integration points onto element surfaces as common with Finite Element post-processors. With this procedure, smoothing is applied to the raw Gauss point data. For the used constant-strain elements, material points of an element and Gauss points carry the same stresses. This approach proved very convenient as the full functionality of the used FEM post-processing application could be used that way without any modification. Generally, the surface between active and inactive finite elements will not be even in case of the used irregularly shaped tetrahedral elements. For better illustration, the top layer of partially-filled elements is removed in the following plots. Most images of this section show a plot of soil strains or stresses for smooth contact on the left half and next to it mirrored on the right half of the image the corresponding plot for fully rough contact.

Figure 6.17 shows the incremental displacements δu_y and δu_x of the soil for the total stress analysis I.1 with smooth contact surface. Here, nodal displacement values form the basis for the shown plots. As is to be expected, incremental soil displacements (relative to the penetrometer displacement) concentrate in the vicinity of the cone. Soil particles below the cone are compacted vertically, soil particles next to the cone experience lateral compression. With regard to vertical displacement increments, the region that is colored red corresponds to the vertical prescribed displacement δu_y applied along

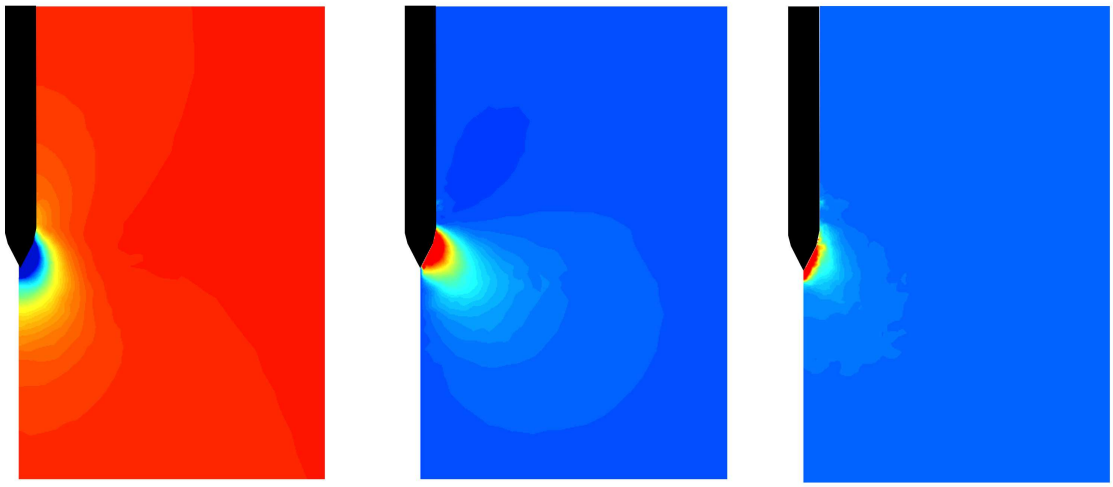

Figure 6.17: Incremental deformations for total stress analysis I.1 with smooth contact surface: (left) vertical displacement increments; (center) horizontal displacement increments in x direction; (right) incremental shear strains

the bottom of the mesh. Soil below the cone shows smaller incremental vertical displacements than the surrounding soil. The region colored dark blue that extends 0.5 D below the cone tip represents displacements of up to 0.8 δu_y. At 2 D below the cone tip, incremental displacements lie at 0.9 δu_y. The horizontal displacements shown in the center reach a maximum value of approximately 0.3 δu_y. The region colored dark red represents displacements between 0.1 and 0.3 δu_y. Beyond a distance of 2 D, horizontal displacements subside to less than 5 percent of the maximum horizontal displacement. Incremental shear strains, also shown in Figure 6.17, likewise concentrate in the vicinity of the cone. Here, shear strain is defined as the square root of the second invariant of the deviatoric strain tensor. A comparison of incremental deformations of different computations is not of much use here as the magnitudes of displacements and strains depend on the varying sizes of the applied prescribed displacement increments.

In the following, results of the effective stress analyses II.2 and II.4 with I_r = 101 will be shown. With computation II.2, a smooth penetrometer surface is considered, with computation II.4 fully rough contact is considered.

Figure 6.18 depicts the accumulated shear strains for these two effective stress analyses. Raw shaded material point data is shown. White spots near the top soil surface represent gaps in the material point discretisation. The region colored red represents shear strains beyond 20 percent and up to 700 percent for the smooth contact surface, up to 900 percent for the fully rough contact surface. In case of the smooth contact surface, the large accumulated shear strains originate solely from the previously shown incremental shearing of soil around the cone. The sheared material then moves upwards along the smooth penetrometer surface. For adhesive contact, the soil is additionally subjected to shearing while moving along the penetrometer surface. Clearly, the zone of heavily sheared soil is wider in case of the fully rough contact surface compared to

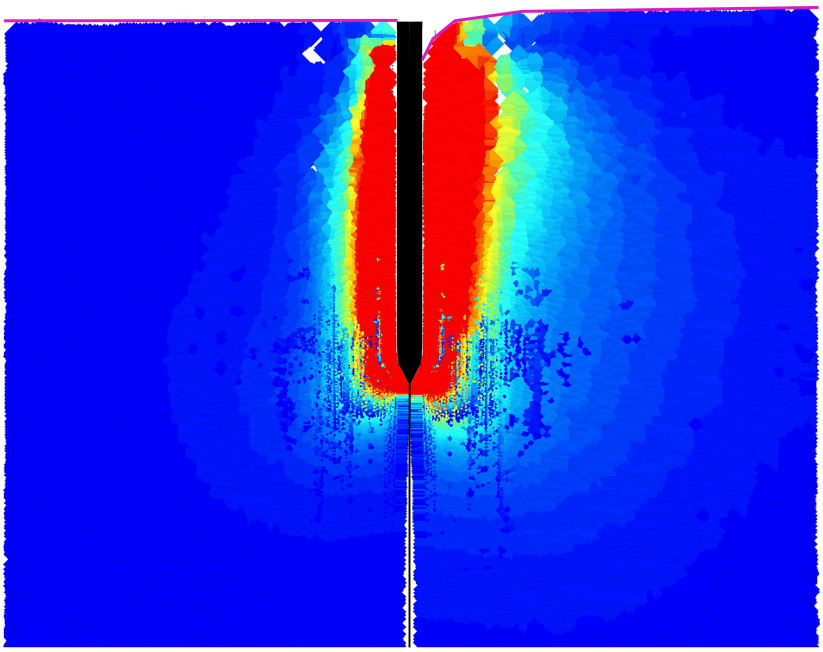

Figure 6.18: Accumulated shear strains for effective stress analyses; (left) II.2 with smooth contact surface; (right) II.4 with fully rough contact surface

the smooth surface. For the smooth contact surface, the zone of shear strains beyond 20 percent has a width of approximately 1.5 D, whereas for fully rough contact the shear zone has a width of 2.5 D.

With the fully rough contact surface, soil particles that adhere to the penetrometer surface are pulled downwards. This shows in the formation of a funnel around the penetrometer whereas for smooth contact the top soil surface is horizontal. In Figure 6.18 this is emphasised by purple lines drawn along the top soil surface.

Figures 6.19 and 6.20 show the principal stresses at the very tip of the cone and in the vicinity of the cone for the effective stress analyses with smooth and fully rough contact surfaces. In case of smooth contact, principal stresses σ_1 are oriented perpendicular to the penetrometer surface, while they are inclined by 45° towards the penetrometer surface for fully rough contact. Because the principal stresses are plotted at a distance from the contact surface, the shown inclinations for rough contact lie below 45°. The principal stresses correspond well to results found by Lu *et al.* [40]. Clearly visible is the radial alignment of principal stresses further away from the cone. The principal stresses are oriented towards a point that lies about 0.5 D below the cone base.

Figure 6.21 shows the deviatoric stress measure corresponding to the square root of the second invariant of the deviatoric stress tensor for the effective stress analyses with smooth and rough contact surface (II.2 and II.4). For the specified soil strength, a maximum deviatoric stress of 40 kPa is obtained which corresponds to the region colored red in Figure 6.21. The shape of the plastic zone agrees well to the shape predicted by amongst others Lu *et al.* who refer to cavity expansion theory as a reference. Accord-

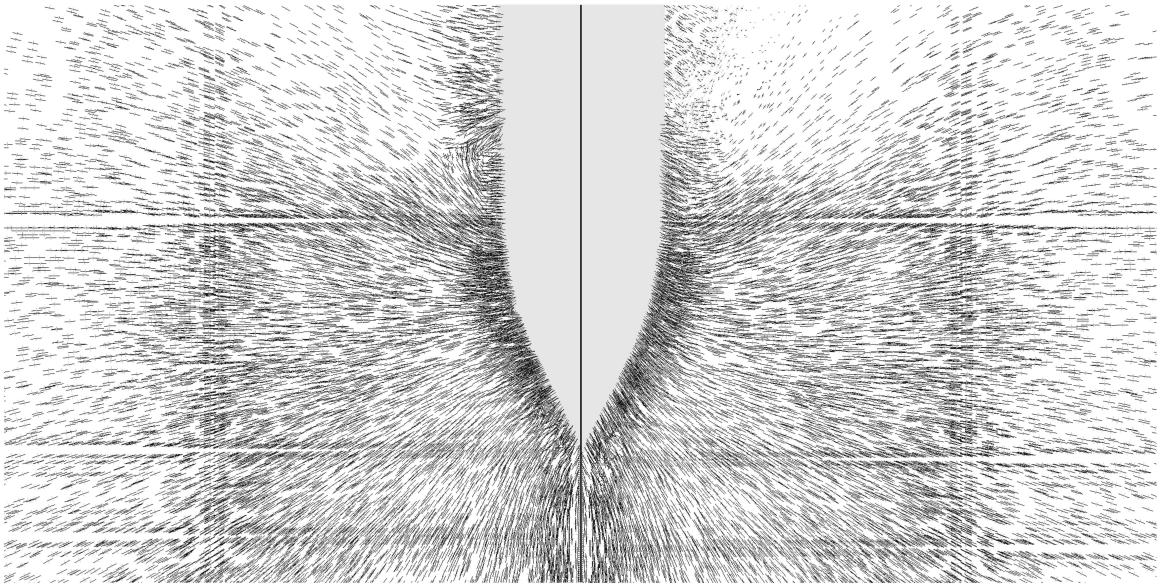

Figure 6.19: Principal stresses in the vicinity of the cone for effective stress analyses scaled down by a factor of 45E-6; (left) II.2 with smooth contact surface; (right) II.4 with fully rough contact surface

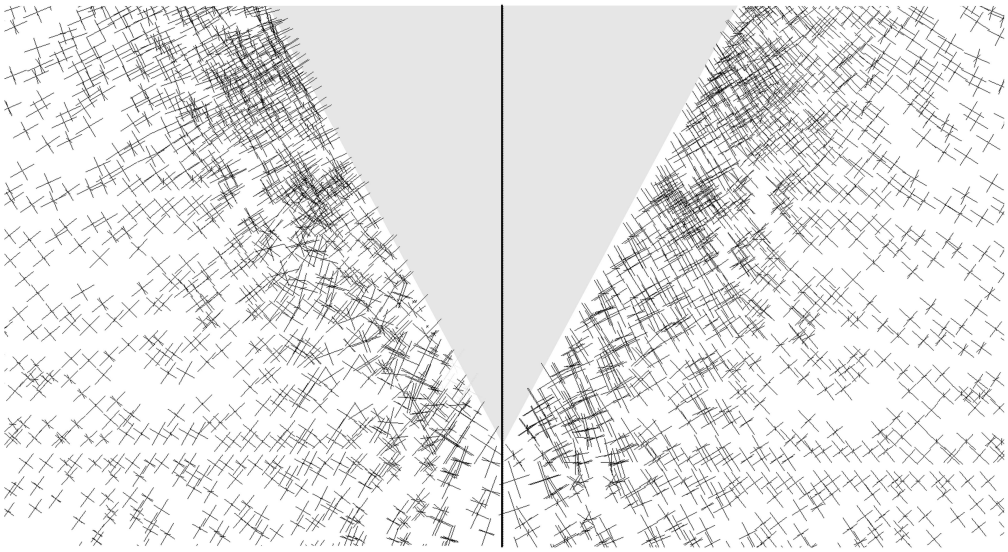

Figure 6.20: Close-up of principal stresses at cone tip for effective stress analyses scaled down by a factor of 90E-6; (left) II.2 with smooth contact surface; (right) II.4 with fully rough contact surface

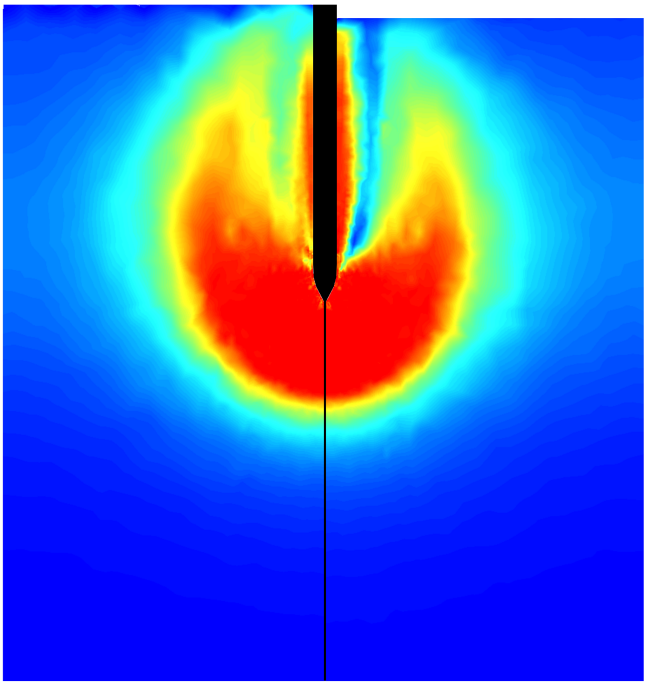

Figure 6.21: Deviatoric stress measure q^* for effective stress analyses; (left) II.2 with smooth contact surface; (right) II.4 with fully rough contact surface

ing to their research, the shape and extend of the plastic zone depends on the rigidity index and to a lesser extend on initial stress anisotropy, while the roughness of the penetrometer surface has no significant impact on the size and shape of the plastic zone. For the chosen soil parameters and initial stresses a nearly circular shape is found that extends approximately 5.5 D below the tip and 5.5 D to the sides for smooth as well as fully rough contact surface. Lu *et al.* predict for a rigidity index of 100 a smaller plastic zone. According to their results, plastic deformations extend 2.5 D below a point that lies slightly below the cone base and 3 D to the sides of the penetrometer. Furthermore, they report that the lower the rigidity index, the more circular the shape of the plastic zone, which corresponds well to the found rounded shape of the plastic zone. With all performed computations, large deviatoric stresses occur in a thin band along the penetrometer surface for smooth as well as adhesive contact.

Total horizontal and vertical stresses σ_{xx} and σ_{yy} are plotted in Figure 6.22 for the effective stress analyses II.2 and II.4. This figure also shows total horizontal and vertical stresses obtained by Van den Berg at a cone tip displacement of 14.6 D for the reference computation with $I_r \approx 101$ with a smooth contact surface. The maximum horizontal stress is somewhat higher for the smooth contact surface compared to the fully rough contact surface (-247 kPa compared to -215 kPa). Small tensile stresses occur in a region below the cone tip. In case of the fully rough contact surface, horizontal stresses decrease with a larger gradient along the penetrometer shaft compared to the smooth contact surface. For the fully rough contact surface, vertical stresses show a sharp decrease just

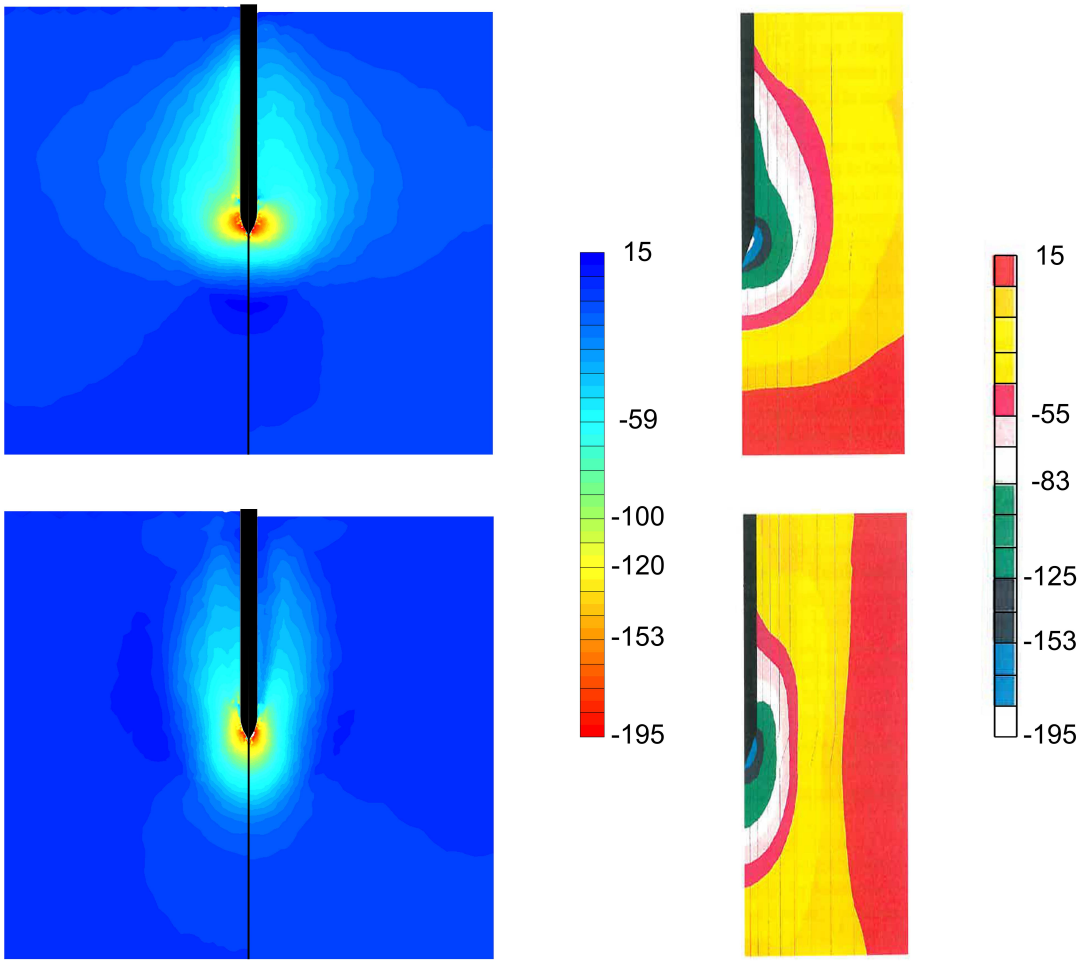

Figure 6.22: (top) Total horizontal stresses σ_{xx}: (left) effective stress analyses II.2 with smooth contact surface and II.4 with fully rough contact surface; (right) total stress analysis with smooth contact surface by Van den Berg [56]; (bottom) total vertical stress: (left) effective stress analyses II.2 with smooth contact surface and II.4 with fully rough contact surface; (right) total stress analysis with smooth contact surface by Van den Berg in [kPa]

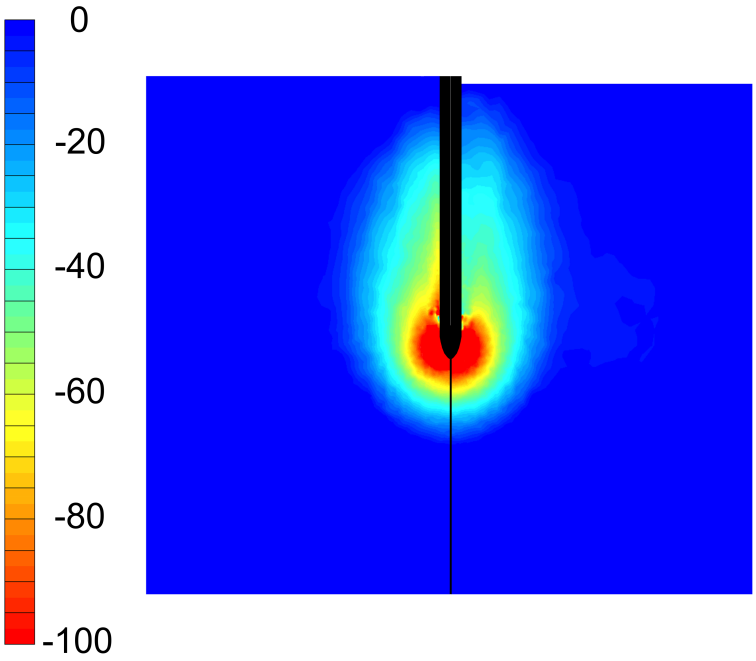

Figure 6.23: Total mean stresses for effective stress analyses; (left) II.2 with smooth contact surface; (right) II.4 with fully rough contact surface in [kPa]

above the cone base. The computation with smooth contact surface exhibits a slightly larger maximum vertical stress than the computation with fully rough contact surface (-245 kPa compared to -231 kPa). Van den Berg obtained somewhat lower values for the maximum total horizontal and vertical stress of -195 kPa, -180 kPa respectively. Lu *et al.* note that a concave shape of the vertical stress bulb towards the outer side indicates the transformation from downward vertical displacement of soil below the cone to upward vertical displacement. Below the concavity, soil is pushed to the sides and downward, above it, soil moves to the sides in an upward direction. Obviously, some of the vertical compression previously applied on soil particles that pass along the penetrometer must consequently be released at this location. This can also be observed with the results of the quasi-static MPM analyses as well as the results obtained by Van den Berg. The extend of the horizontal and vertical stress bulbs below the cone and to its sides is approximately identical.

As with the total vertical and horizontal stresses, the total mean stresses for smooth and fully rough contact shown in Figure 6.23 distinguish through a difference in stresses along the penetrometer surface above the cone. With fully rough contact, total mean stresses subside in the narrow band where soil is sheared along the rough contact surface while the total mean stresses remain at an elevated level in case of smooth contact. The region colored red indicates total mean stresses between -100 and -216 kPa for fully rough contact and -100 and -239 kPa for smooth contact.

Results shown so far are basically identical for the total and effective stress analyses I.2 and II.2, I.4 and II.4 respectively. In the following, results of the effective stress anal-

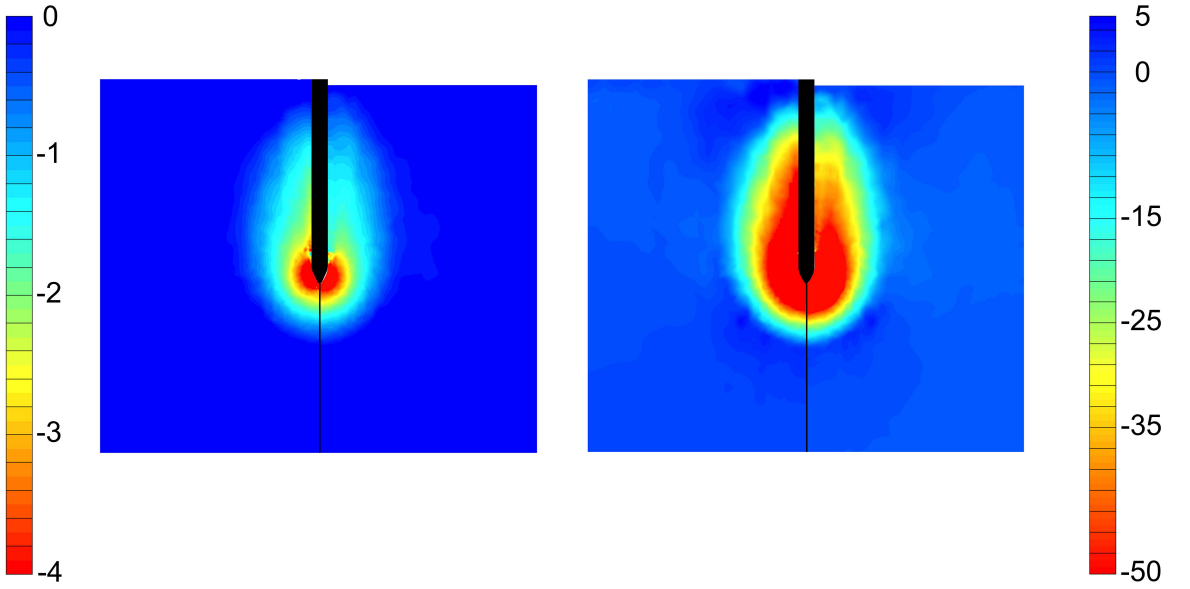

Figure 6.24: (left) Effective mean stresses and (right) excess pore pressures each for II.2 with smooth contact surface on left half and II.4 with fully rough contact surface on right half in [kPa]

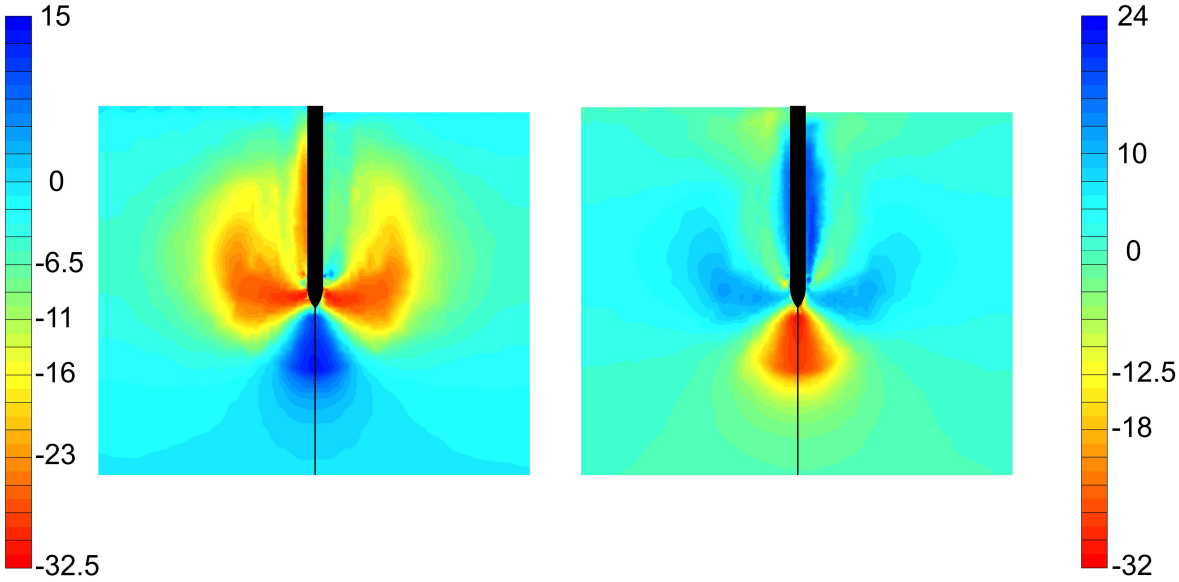

Figure 6.25: (left) Effective horizontal stresses σ'_{xx} and (right) vertical stresses σ'_{yy} each for II.2 with smooth contact surface on left half and II.4 with fully rough contact surface on right half in [kPa]

yses are shown which give some more insight into the evolving stress field around the penetrometer for the considered undrained conditions.

Figure 6.24 (left) shows the effective mean stresses for smooth and fully rough contact. The region colored red represents compression beyond -4 kPa. For both, smooth and fully rough contact, the maximum mean stress lies at -8 kPa. Due to the slight compressibility allowed with the performed computations (ν_u = 0.49), the mean stresses acting on the soil skeleton do change. However, mean effective stresses represent only a small fraction of the mean total stresses of -239 kPa for smooth contact, -216 kPa respectively for fully rough contact. Consequently, the excess pore pressure distribution must correspond to the total mean stresses presented in Figure 6.23. The image on the right shows excess pore pressures for smooth and fully rough contact. The results for smooth contact show a maximum value of -230 kPa and results for fully rough contact show a maximum pore pressure of -209 kPa. The region colored red indicates pore pressures below -50 kPa. The extend of the pore pressure bulb does not differ much for smooth and fully rough contact. The decrease of excess pore pressures above the cone base next to the penetrometer surface occurs with a larger gradient in case of the fully rough contact compared to the smooth contact.

Figure 6.25 shows the horizontal and vertical effective stresses σ'_{xx} and σ'_{yy}. Clearly visible below the cone tip is a region of horizontal tensile stresses with a maximum value of 15 kPa that does not differ neither in magnitude nor in extension for smooth and fully rough contact. Wing-shaped horizontal stress bulbs develop next to the penetrometer. The extend of this region of large horizontal stresses and its magnitude with a maximum value of -32 kPa is approximately the same for smooth and fully rough contact. In case of the smooth penetrometer surface, soil particles maintain large horizontal stresses along the penetrometer surface. A similar arrangement of stress bulbs is observed for effective vertical stresses. Again, except for the region in the vicinity of the penetrometer surface above the cone, the observed pattern is nearly identical for smooth and fully rough contact surfaces. In the region of horizontal tensile stresses, vertical compression occurs with a maximum value of -245 kPa for smooth contact and -208 kPa for fully rough contact. The region of large horizontal stresses shows slight vertical tensile stresses. Near the penetrometer surface, vertical tensile stresses occur. These stresses are more pronounced in case of the fully rough contact, which reflects the fact that soil particles are pulled downwards by the penetrating bar.

The horizontal and vertical stress distributions can be derived from the pear-shaped distributions of total stresses and excess pore pressures shown above in Figures 6.22 and 6.24. Excess pore pressures are introduced through compression of the soil in the vicinity of the penetrometer. In regions where the negative excess pore pressures exceed the negative total horizontal or vertical stresses, tensile (positive) effective vertical or horizontal stresses appear. Below the cone, strong vertical compression introduces large excess pore pressures which result in tensile effective horizontal stresses. As mentioned above, the total vertical stress distribution shows a concavity where the movement of soil particles changes from a downward to an upward movement. Here, obviously, large horizontal compaction of the soil shows up in excess pore pressures that lead to tensile vertical stresses within the soil skeleton. The same holds true for the thin band along the

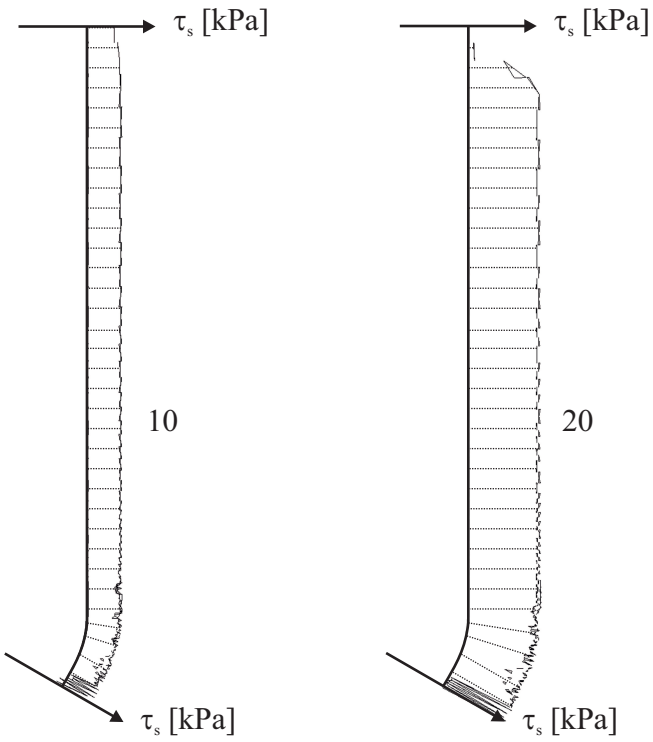

Figure 6.26: Interface shear traction for effective stress analyses; (left) II.3 with $a = s_u/2$; (right) II.4 with $a = s_u$

penetrometer shaft.

Figures 6.26 and 6.27 show tractions of the interface elements placed along the penetrometer surface for the effective stress analyses II.3 and II.4. Shear tractions for both adhesive contact with $a = s_u/2$ = 10 kPa and $a = s_u$ = 20 kPa are shown. Clearly, the found distributions comply with the specified shear strengths. Some oscillations occur at the tip of the cone. The total normal tractions for fully rough contact surface show a considerable peak at the cone tip. However, its extend is limited to the very tip of the cone. The total normal traction of -241 kPa slightly above the very cone tip lies in the range of magnitude of σ_1 obtained in the vicinity of the cone tip. The sharp decrease of normal traction just above the base of the cone complies with results for total horizontal stresses shown in Figure 6.22. The excess pore pressures shown on the right side of Figure 6.27 correspond well with the excess pore pressures within the soil shown in Figure 6.24. Just above the cone base, excess pore pressures exhibit a sharp decrease and further up a more gradual decrease from -45 kPa to 0 kPa.

6.3.2 Analysis with the Mohr-Coulomb material model

The analysis of cone penetration testing with the Mohr-Coulomb model presented in this section forms an intermediate step before introducing the AUC model in the following Section 6.3.3. With the Mohr-Coulomb as with the AUC model, the undrained shear

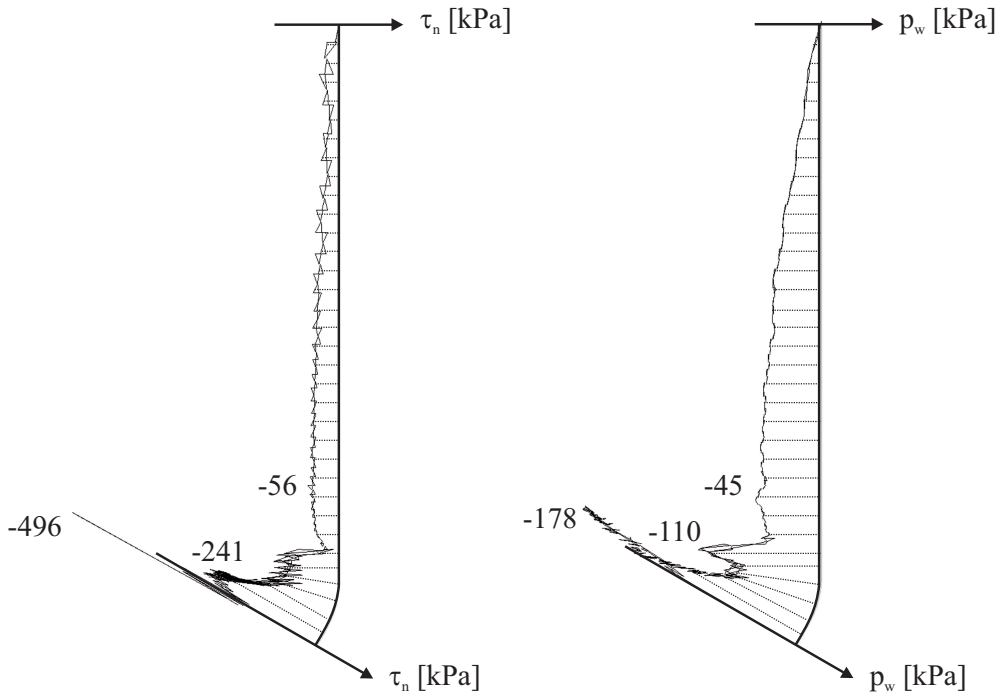

Figure 6.27: (left) Interface total normal traction and (right) interface excess pore pressures for II.4 with $a = s_u$

strength depends on the effective stress state and the loading type — in contrast to the Tresca model, which assumes a unique constant undrained shear strength.

Therefore, in the following computations a vertical traction of 10 kPa is applied on the top soil surface. Here, K_0 is set to 0.5 in order to generate an initial stress typical for a normally-consolidated clay. Only a small traction is applied because higher loads caused numerical problems with the present implementation of the quasi-static MPM.

In contrast to the computations presented above, only smooth contact between penetrometer surface and soil is considered. The iterative procedure used for solving the equilibrium equations reached its limits with computations that involve both adhesive contact as well as the more complex AUC model.

Results obtained with the Mohr-Coulomb model are compared to results of a computation that uses the Tresca model but which is otherwise identical. In the next section, these results will be compared with those obtained with the AUC model.

The soil properties of the performed computations using the Mohr-Coulomb and Tresca model are provided in Table 6.4. In Section 5.3.4, the undrained shear strengths for triaxial compression, extension and simple shear were computed by means of numerical analyses for the Mohr-Coulomb, Tresca and AUC model for these material parameters and the specified surcharge. For the Mohr-Coulomb model, $s_{\mathrm{u\,compression}}$ is 4 kPa, $s_{\mathrm{u,\,extension}}$ is 2.8 kPa and for simple shear $s_{\mathrm{u,\,simpleshear}}$ is 3.8 kPa. The cohesion of 4 kPa specified with the Tresca model thus coincides with the undrained shear strength under triaxial compression specified with the Mohr-Coulomb model.

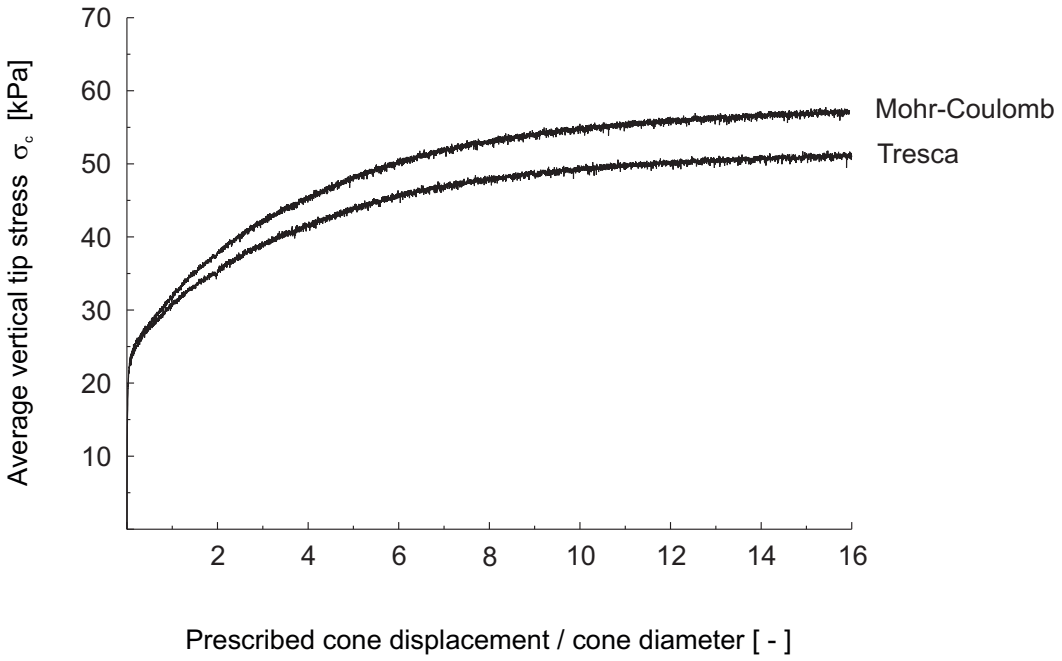

Figure 6.28: Average vertical tip stress plotted over the relative cone displacement for the computations with the Mohr-Coulomb and Tresca model

A check analysis has been performed with the Mohr-Coulomb model with the cone initially placed above the soil rather than inside. This check has been performed for an undrained Poisson ratio of 0.485 because the computation with ν_u = 0.49 requires significantly more computational time than for a lower undrained Poisson ratio. A tip resistance of 60 kPa is obtained when placing the cone initially inside the soil and a tip resistance of 61 kPa is obtained when placing the cone initially above the soil. Results differ by 2 percent. Thus, the initial location of the cone has no significant impact on results when using the Mohr-Coulomb model. This agrees with the results of computations presented in Section 6.3.1 in which the Tresca model is used and no surface traction is applied.

Material model	E	ν	c'	ϕ'	ν_u	K_w/n	a
	$[\mathrm{kN/m^2}]$	$[-]$	$[\mathrm{kN/m^2}]$	$[^\circ]$	$[-]$	$[\mathrm{kN/m^2}]$	$[\mathrm{kN/m^2}]$
Mohr-Coulomb	6,000	0.25	1E-4	30	0.49	110,300	0
Tresca	6,000	0.25	4	0	0.49	110,300	0

Table 6.4: Soil material parameters for the performed computations

Evaluation of results Figure 6.28 shows results obtained for the Mohr-Coulomb and Tresca model. The Mohr-Coulomb model gives a higher tip resistance of 57 kPa than the

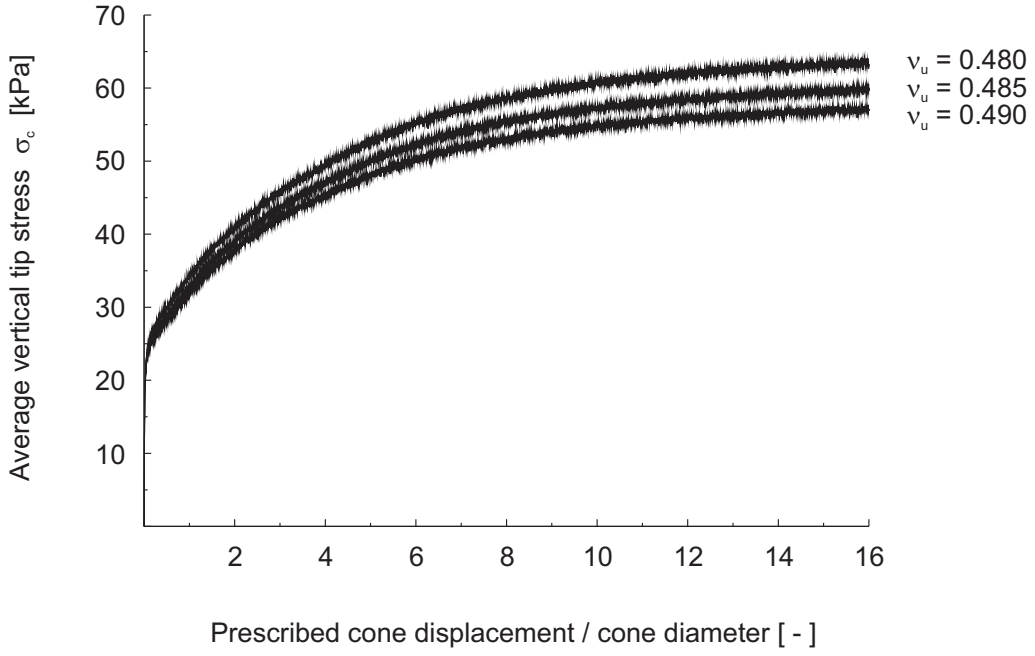

Figure 6.29: Average vertical tip stress plotted over the relative cone displacement for the Mohr-Coulomb computation with ν_u = 0.48, ν_u = 0.485 and ν_u = 0.49

Tresca model which renders a tip resistance of 51 kPa. This can be explained by a slight increase of the effective mean stresses during the simulation with the Mohr-Coulomb model due to the specified undrained Poisson ratio.

Figure 6.29 shows results for a variation of the undrained Poisson ratio ν_u for the computation with the Mohr-Coulomb material model. Setting ν_u to 0.48 results in a bulk modulus of the pore water of 55.7 MN/m^2, ν_u = 0.485 gives a bulk modulus of the pore water of 76 MN/m^2 compared to K_w/n = 110.3 MN/m^2 for ν_u = 0.49. For ν_u = 0.48 a tip resistance of 64 kPa is obtained, for ν_u = 0.485 a tip resistance of 60 kPa and for ν_u = 0.49 a tip resistance of 57 kPa. In case of relatively low values for ν_u, the effective mean stresses change despite the assumed undrained conditions. With the Mohr-Coulomb model this results in an increase of the undrained shear strength of the soil and thus in a higher tip resistance, in contrast to the computations with the Tresca model. Extrapolation to ν_u = 0.495 results in a tip resistance of approximately 56 kPa. Thus, with increasing undrained Poisson ratio the tip resistance obtained for the Mohr-Coulomb model corresponds reasonably well to the tip resistance obtained with the Tresca material model of 51 kPa. However, an undrained Poisson ratio beyond 0.49 could not be used with the Mohr-Coulomb due to numerical problems.

With the specified undrained shear strength of 4 kPa, the computation with the Tresca model gives a cone factor of 12.75. Equation 6.3 of Lu *et al.* renders for I_r = 600 and Δ = 0.625 a cone factor of 12.45 close to the computed value. With the Mohr-Coulomb model, more than one undrained shear strength might determine the tip resistance. The proximity of the tip resistances found with the Mohr-Coulomb model and the Tresca model indicates that in both computations the same undrained shear strength dominates

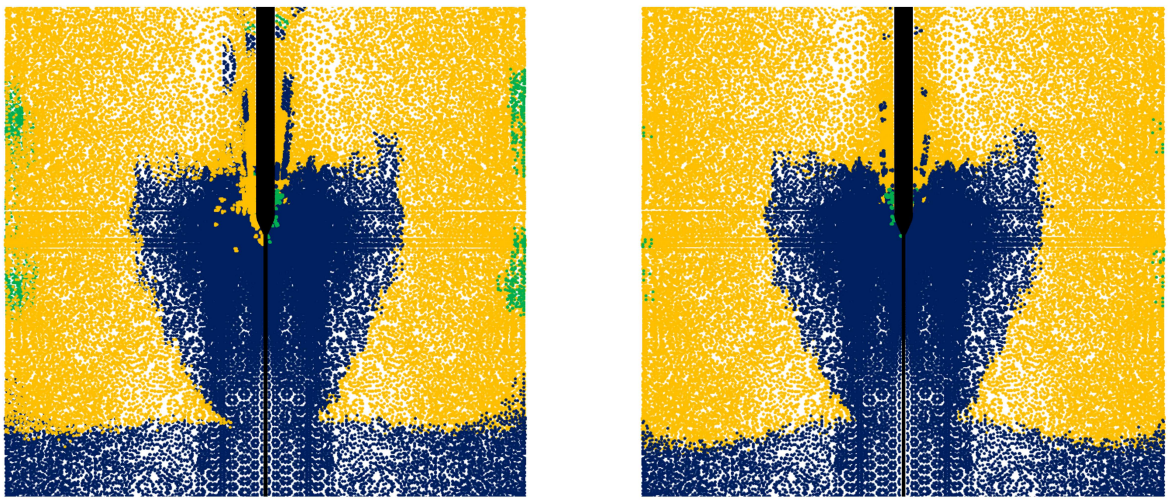

Figure 6.30: (left) Regions of triaxial compression, extension and isotropic stresses and (right) regions of identical Lode angle each for the computation with the Tresca model on the left half and the computation with the Mohr-Coulomb model on the right half

the failure mechanism.

Figure 6.30 illustrates the loading types found within the soil body. The image on the left has been generated by coloring Gauss points dark blue for which $\sigma_2' \approx \sigma_3'$ and $\sigma_1' \neq \sigma_2'$ indicating triaxial compression, Gauss points for which $\sigma_1' \approx \sigma_2'$ and $\sigma_2' \neq \sigma_3'$ are colored green indicating triaxial extension and Gauss points for which $\sigma_1' \approx \sigma_2' \approx \sigma_3'$ are colored red. Of the latter, only a very small number occurs. Gauss points for which no principal stresses are equal are colored orange. The tolerated difference between principal stresses is chosen as 10 percent of the minimum of the two compared stress values. The image on the right considers the Lode angle. Blue indicates Gauss points with Lode angles between 0 and 3° (triaxial compression), green indicates Lode angles between 60 and 57° (triaxial extension) and orange indicates Lode angles between these two values. Results are approximately identical for the computations with the Mohr-Coulomb and Tresca model. For both the Tresca and the Mohr-Coulomb model, triaxial compression occurs in the vicinity of the cone. In case of the computations with the Tresca and Mohr-Coulomb model, triaxial extension occurs in small patches at the mesh boundary due to boundary effects. However, effective stresses at this distance from the penetrometer nearly correspond to the initial stresses so that this region plays no significant role in the penetration mechanism. Clearly, with the Mohr-Coulomb model, the undrained shear strength for triaxial compression determines the tip resistance.

In the following section, further results obtained with the Mohr-Coulomb model will be compared to results obtained with the AUC model. The depicted stress plots are approximately the same for the computations with the Tresca and Mohr-Coulomb model so that results of the former are skipped.

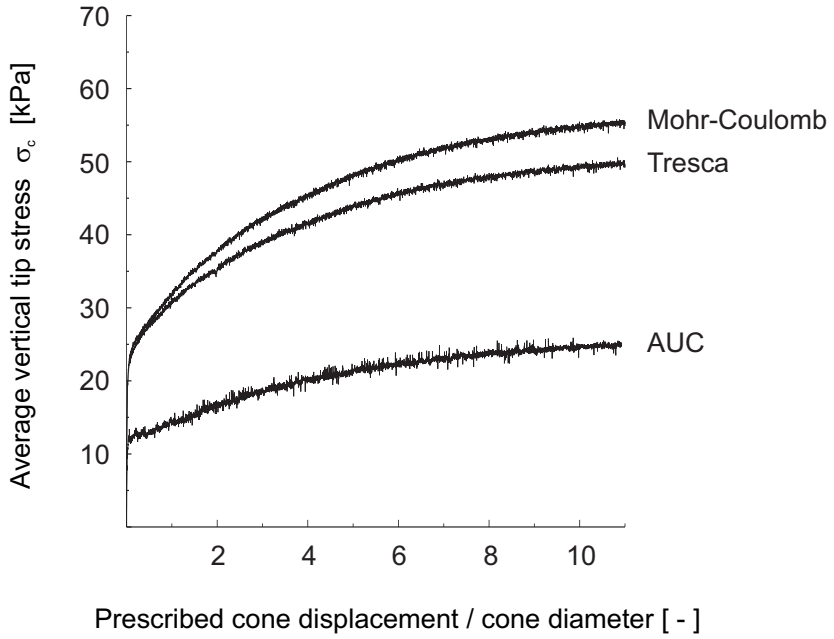

Figure 6.31: Average vertical tip stress plotted over the relative cone displacement for the computations with the Tresca, Mohr-Coulomb and AUC models

6.3.3 Analysis with the Anisotropic Undrained Clay model

In the following, the AUC model is introduced to the analysis of cone penetration testing in order to take into account the shear-induced generation of excess pore pressures and the anisotropic strength of undrained clay.

The same boundary conditions are applied for this analysis with the AUC model as for the analyses of the previous section. Normally-consolidated clay is considered, the overconsolidation ratio is 1. The computation with the AUC model uses the same effective strength and stiffness parameters as the computation with the Mohr-Coulomb model presented above in Table 6.4. Here, of course, ϕ'_{cs} rather than ϕ' is set to 30°. The factor M of the yield surface being equal to M_c then has a value of 1.2. In contrast to the Tresca and Mohr-Coulomb computations, the computation with the AUC model was performed with an undrained Poisson ratio of 0.495 instead of 0.49 resulting in a bulk modulus of the pore water of 235.2 MN/m^2. The chosen soil parameters render for the AUC model a value α_0 of -0.458 and an isotropic preconsolidation pressure of -7.1 kPa (see Figure 5.19). The numerical analyses presented in Section 5.3.4 render for the AUC model with these material parameters undrained shear strengths of 3 kPa for triaxial compression, 1.2 kPa for triaxial extension and 2.15 kPa for simple shear.

The computation with the AUC model and the higher undrained Poisson ratio requires considerably more time and memory consumption than the other two computations. It was therefore stopped at a penetration depth of 11 D instead of proceeding up to 16 D as with the Tresca and Mohr-Coulomb model.

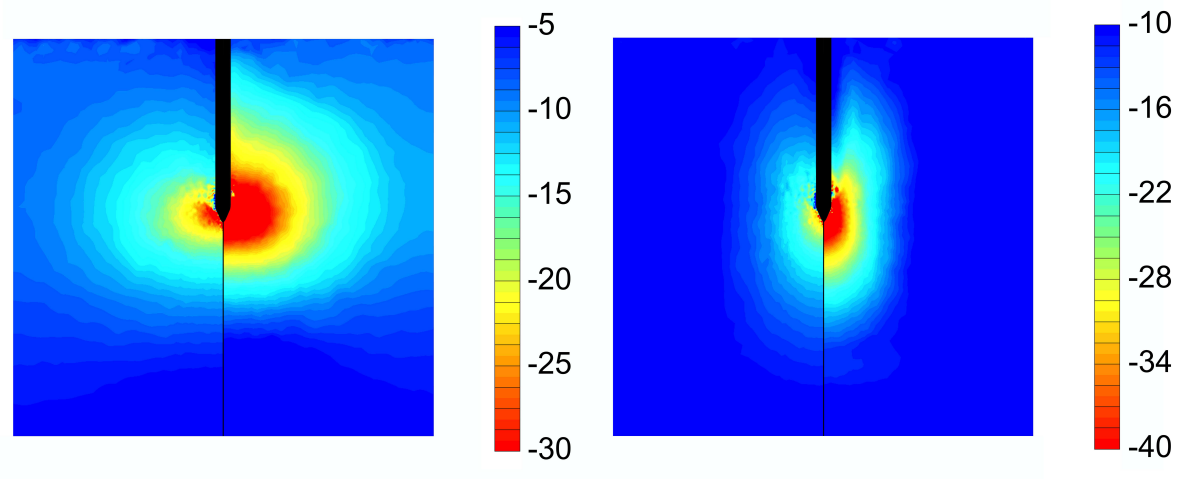

Figure 6.32: (left) Total horizontal stresses σ_{xx} and (right) total vertical stresses σ_{yy} each for the computation with AUC model on the left half and Mohr-Coulomb model on the right half in [kPa]

Evaluation of results In Figure 6.31, results obtained for the AUC model are added to Figure 6.28. The AUC model predicts a significantly lower tip resistance than the Tresca and Mohr-Coulomb model, 25 kPa instead of 50 kPa, a tip resistance of 55.5 kPa respectively (at 11 D). For a penetration depth of 16 D, a tip resistance of approximately 26 kPa is obtained through extrapolation. In the following, results obtained with the AUC model are investigated in more detail.

The stress plots presented in the following are generated identically to those shown in Section 6.3.1. The left half of each plot shows stresses being obtained with the AUC model, the mirrored right half shows stresses being obtained with the Mohr-Coulomb model. When relating (negative) compressive stresses, terms such as 'below', 'higher than' relate to absolute values as it seems more intuitive.

Figure 6.32 shows total horizontal stresses σ_{xx} on the left and vertical stresses σ_{yy} on the right for the computations with the AUC and Mohr-Coulomb model. For the Mohr-Coulomb model, the total horizontal stresses range between 0 and -85 kPa and the total vertical stresses between 0 and -87 kPa. For the Tresca model, the total horizontal stresses lie between 0 and -78 kPa and the total vertical stresses between 0 and -78 kPa. For the AUC model, the maximum total stresses are lower than those obtained with the Mohr-Coulomb and Tresca models. The total horizontal stresses lie between 0 and -57 kPa and the total vertical stresses range for the AUC model from 0 to -55 kPa. For the Tresca and Mohr-Coulomb model the stress bulbs for total horizontal and vertical stresses ressemble those obtained for the above presented computations without overburden stress. Compared to the Tresca and Mohr-Coulomb model, the total stresses decrease with a larger gradient above the cone base in case of the AUC model. For all three computations, the distribution of total vertical stresses shows the same concavity that has been described in Section 6.3.1. The ratios of the maximum total vertical stresses correspond as is to be expected approximately to the ratios of the tip stresses of these three computations.

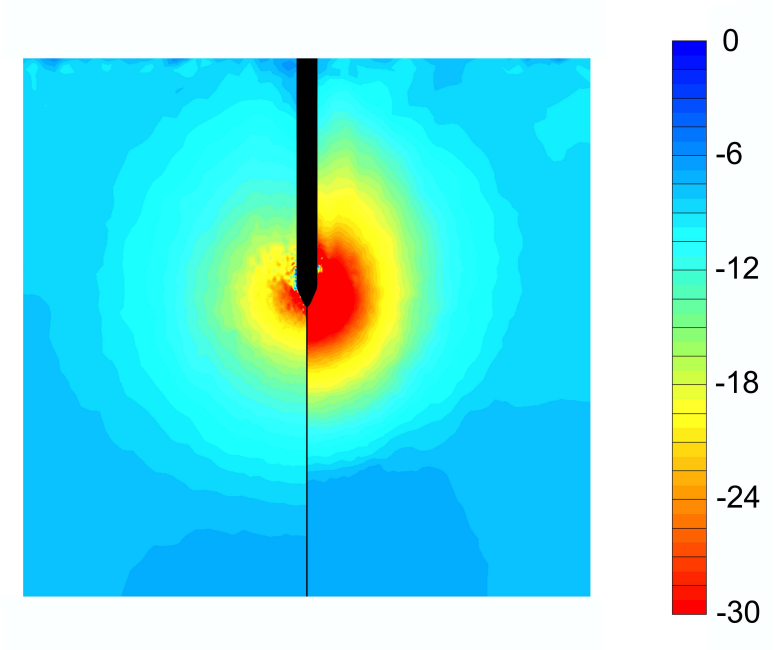

Figure 6.33: Total mean stresses; (left) computation with AUC model; (right) computation with Mohr-Coulomb model in [kPa]

Figure 6.33 shows the total mean stresses for the computations with the AUC and Mohr-Coulomb model. Stresses range from 0 to -83 kPa for the Mohr-Coulomb model, from 0 to -76 kPa for the Tresca model and from 0 to -55 kPa for the AUC model.

Figure 6.34 shows on the left the effective mean stresses for the computations with the AUC and Mohr-Coulomb model and on the right the excess pore pressures obtained for these two computations. The effective mean stresses range for both the Mohr-Coulomb and Tresca model from 0 to -9 kPa and for the AUC model from 0 to -6.7 kPa. The excess pore pressures range from 0 to -74 kPa for the Mohr-Coulomb model, from 0 to -67 kPa for the Tresca model and from 0 to -53 kPa for the AUC model. A maximum effective mean stress that lies above the initial mean stress of -6.7 kPa is found with the Mohr-Coulomb and Tresca model. As mentioned above, this increase can be explained by the choice of the undrained Poisson ratio of 0.49 which allows for a slight change of effective stresses. With the AUC model, the initial effective mean stress is not exceeded as a higher undrained Poisson ratio of 0.495 is specified. The AUC model predicts a significant decrease of the effective mean stress in the vicinity of the cone. The wing-shaped bulb of effective mean stresses has its lowest value at the height of the cone base. This reduction of the effective mean stress implies that the change of excess pore pressures exceeds the change of total mean stresses in this region of the soil.

Figure 6.35 shows on the left effective horizontal stresses σ'_{xx} for the AUC and Mohr-Coulomb model and on the right effective vertical stresses σ'_{yy}. With the Mohr-Coulomb model, effective horizontal stresses range from 0 to -15.5 kPa, for the Tresca model from 0 to -14 kPa and for the AUC model from 0 to -7 kPa. Effective vertical stresses range for the Mohr-Coulomb model from 0 to -14 kPa, for the Tresca model from 0 to -13 kPa and

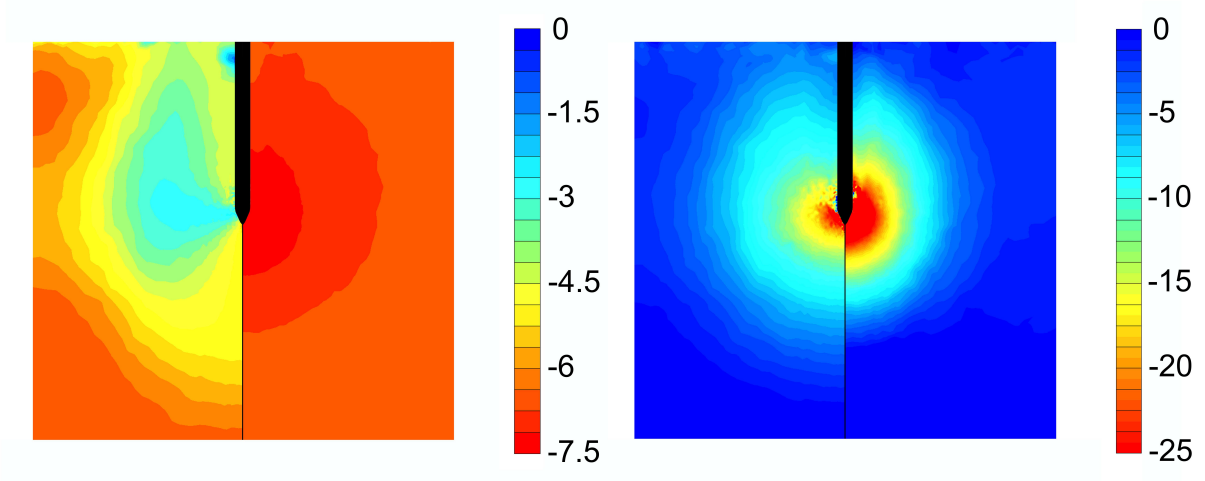

Figure 6.34: (left) Effective mean stresses and (right) excess pore pressures each for computation with AUC model on left half and Mohr-Coulomb model on the right half in [kPa]

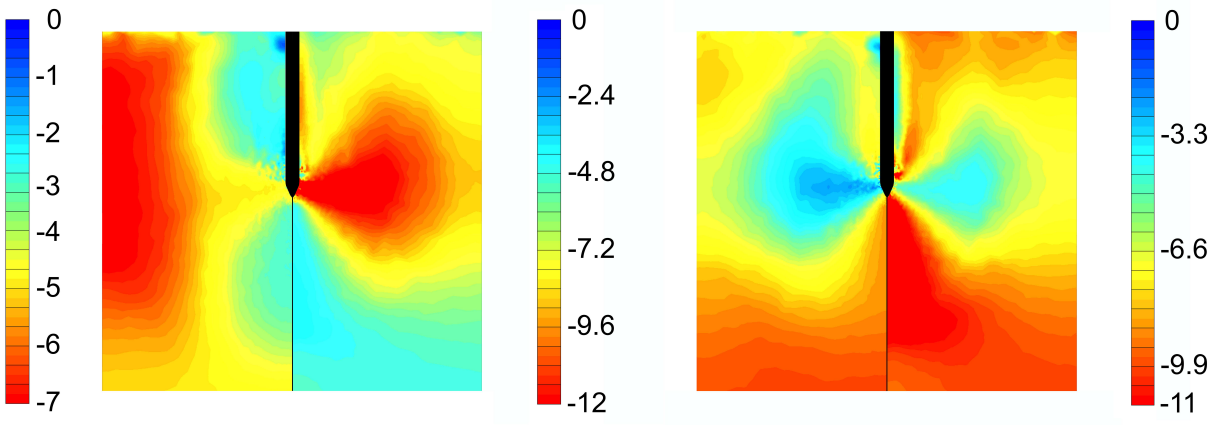

Figure 6.35: (left) Effective horizontal stresses σ'_{xx} and (right) effective vertical stresses σ'_{yy} each for computation with AUC model on the left half and Mohr-Coulomb model on the right half in [kPa]

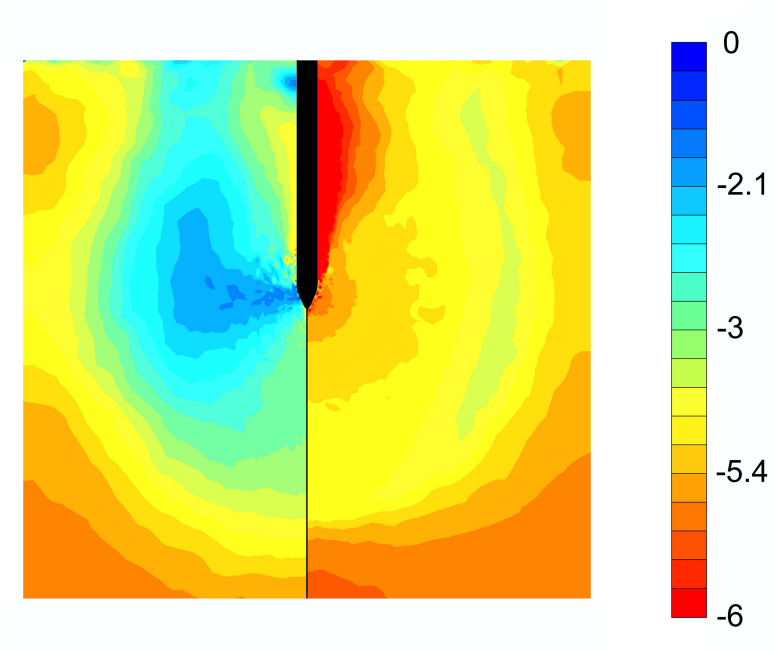

Figure 6.36: Effective circumferential stresses; (left) computation with AUC model; (right) computation with Mohr-Coulomb model in [kPa]

for the AUC model from 0 to -10 kPa. Figure 6.36 shows the effective circumferential stresses for the two computations which range for the Mohr-Coulomb and Tresca model from 0 to -11 kPa and for the AUC model from 0 to -5.7 kPa. The stress distributions for the Mohr-Coulomb and Tresca model correspond to the wing-shaped stress bulbs described in Section 6.3.1. Clearly visible is that regions of minimum vertical stress correspond to regions of maximum horizontal and circumferential stress and vice versa. With the AUC model, the shape and location of bulbs of low vertical and circumferential effective stresses coincide. In contrast to the Mohr-Coulomb and Tresca computations, horizontal effective stresses only deviate slightly from the initial horizontal effective stress with the AUC model. Below and above the cone tip a zone of somewhat lower horizontal stresses is found. A peak of horizontal stresses occurs at the height of the cone base at a distance of 8.5 D measured from the penetrometer axis.

The shown plots of effective stresses indicate a boundary effect. However, the difference between initial effective as well as total stresses and effective/total stresses at a penetration depth of 11 D is rather small along the boundary. Furthermore, check computations showed that an increase of the mesh width from 14 to 19 D does not influence the tip stress.

The deviatoric stress measure plotted in Figure 6.37 lies for the Mohr-Coulomb model between 0 and 11 kPa, for the Tresca model between 0 and 8 kPa and for the AUC model between 0 and 6 kPa. The initial deviatoric stress is 5 kPa. With regard to the Mohr-Coulomb model, deviatoric stresses above a limit value of 8 kPa defined through the chosen strength parameters and initial stresses are found as is to be expected in the vicinity of the cone where effective mean stresses exceed the initial mean stress of -6.7 kPa.

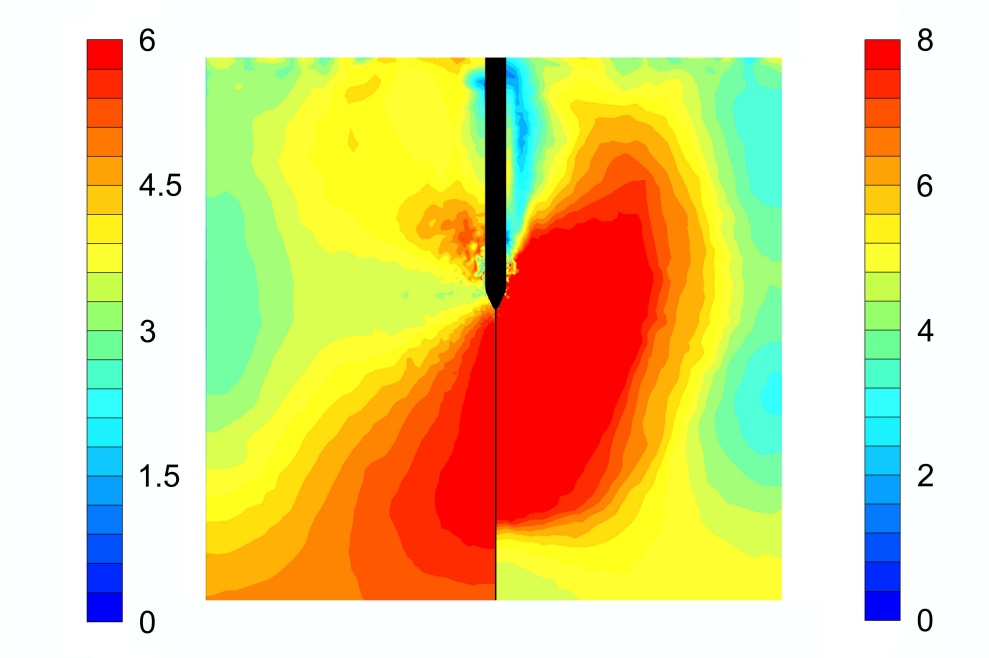

Figure 6.37: Deviatoric stress measure q^*; (left) computation with AUC model; (right) computation with Mohr-Coulomb model in [kPa]

Of course, with the Tresca model, deviatoric stresses must lie at or below the specified limit of 2 s_u. With the AUC model, the maximum deviatoric stress is equal to twice the undrained shear strength for triaxial compression which gives 6 kPa. Deviatoric stresses in this range are found below and above the cone tip. A bulb of low deviatoric stresses extends from the cone base into the soil.

Figure 6.38 illustrates the loading types found within the soil body. The figure has been generated identically to Figure 6.30 through comparison of principal stresses and evaluation of the Lode angle. Compared to the Mohr-Coulomb model, triaxial compression occurs with the AUC model in a much smaller region below the cone. A clear association between tip resistance and undrained shear strength as with the Mohr-Coulomb model therefore seems not possible.

Figure 6.39 shows that the soil in the vicinity of the cone tip is in a state of yielding. Gauss points whose stresses lie on the yield surface (f > -1E-4) are colored black when soil is in triaxial compression and green when soil is in another stress state. Almost the entire soil body is in a plastic state as normally-consolidated soil is considered. The zone at the bottom of the mesh would seem to be in an elastic state, but this can be attributed to numerical inaccuracies.

Figure 6.40 shows in the left image Gauss point stresses of the soil body plotted in the p'-q^*-plane and on the right plotted in the deviatoric plane for the computation with the AUC model. Only Gauss points with a plastic state are plotted. Furthermore, only stress states in the vicinity of the cone tip are considered. The considered rectangular region is indicated in Figure 6.39. It extends 2.5 D above the cone tip, 11 D below the cone tip and 9 D to the side of the cone tip. The coloring of the stress states corresponds to

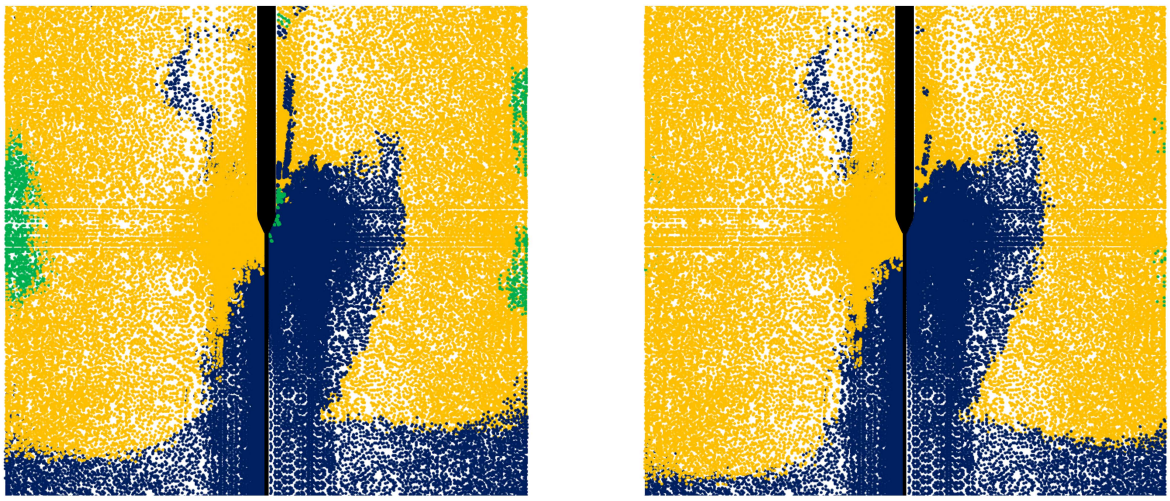

Figure 6.38: (left) Regions of triaxial compression colored blue and extension colored green; (right) regions of identical Lode angle each for computation with AUC model on left half and computation with Mohr-Coulomb model on right half

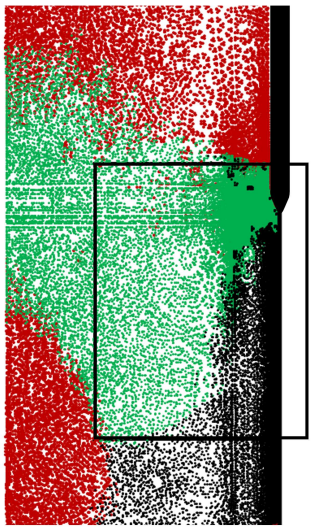

Figure 6.39: Region of soil with stress states on the yield surface for computation with the AUC model

that of Figure 6.39. The effective stresses are limited by the initial stress and by the yield function which takes for triaxial compression the shape of an ellipse.

The maximum deviatoric stress is restricted by the yield surface to values between 5 and 6 kPa for triaxial compression, at which the effective mean stress reduces from the initial value of -6.7 kPa to -5 kPa. In the deviatoric plane, all stress states lie in the upper left section. Stress states close to the vertical axis correspond to triaxial compression. Those close to the inclined axis correspond to triaxial extension. The chart indicates that triaxial extension does not occur in the vicinity of the cone as also seen in Figure 6.38.

The presented results provide some insight into the mechanical processes in the region surrounding the cone that determine the tip resistance found with the AUC model.

Below the cone, where soil is compacted vertically through the advancing cone, soil is in a state of triaxial compression as shown in Figure 6.38. As can be seen from Figure 6.37, deviatoric stresses increase in this region from 5 kPa to the maximum stress of 6 kPa which corresponds to the undrained shear strength for triaxial compression. Because stress states are limited by the elliptic yield locus, the effective mean stresses decrease with increasing deviatoric stress down to a value of -5 kPa as illustrated in Figure 6.40. This decrease corresponds to results shown in Figure 6.34 (left). Consequently, horizontal and vertical effective stresses decrease in this region as shown in Figure 6.35.

Next to the cone, low vertical and horizontal effective stresses σ'_{yy} and σ'_{zz} occur, whereas σ'_{xx} increases slightly. This can be explained as in Section 6.3.1 by the reduction of vertical compaction once soil leaves the 'shadow' of the penetrating cone and the increase of compaction in x direction which reaches a peak at the height of the cone base. As a consequence, the mean effective stresses decrease in this region as shown in Figure 6.34 — in contrast to computations with the Tresca and Mohr-Coulomb model which prohibit any change of the effective mean stress. As shown in Figure 6.37, deviatoric stresses decrease with decreasing effective mean stresses. These stress paths correspond to soil yielding in a critical state: stress states in this region follow the critical state line. They do not correspond to triaxial compression nor triaxial extension here as also shown in Figure 6.38.

Clearly, with the AUC model, in contrast to the computation with the Mohr-Coulomb model, the tip resistance is not entirely determined through triaxial compression. Such loading is with the AUC model confined to a wedge below the cone. As shown in Figure 6.37, soil yields in the vicinity of the cone at deviatoric stresses as low as 3 kPa which explains the lower tip resistance found with the AUC model. In addition, the undrained shear strength for triaxial compression is somewhat lower with the AUC model than with the Mohr-Coulomb model, 3 kPa instead of 4 kPa, which contributes somewhat to the found lower tip resistance.

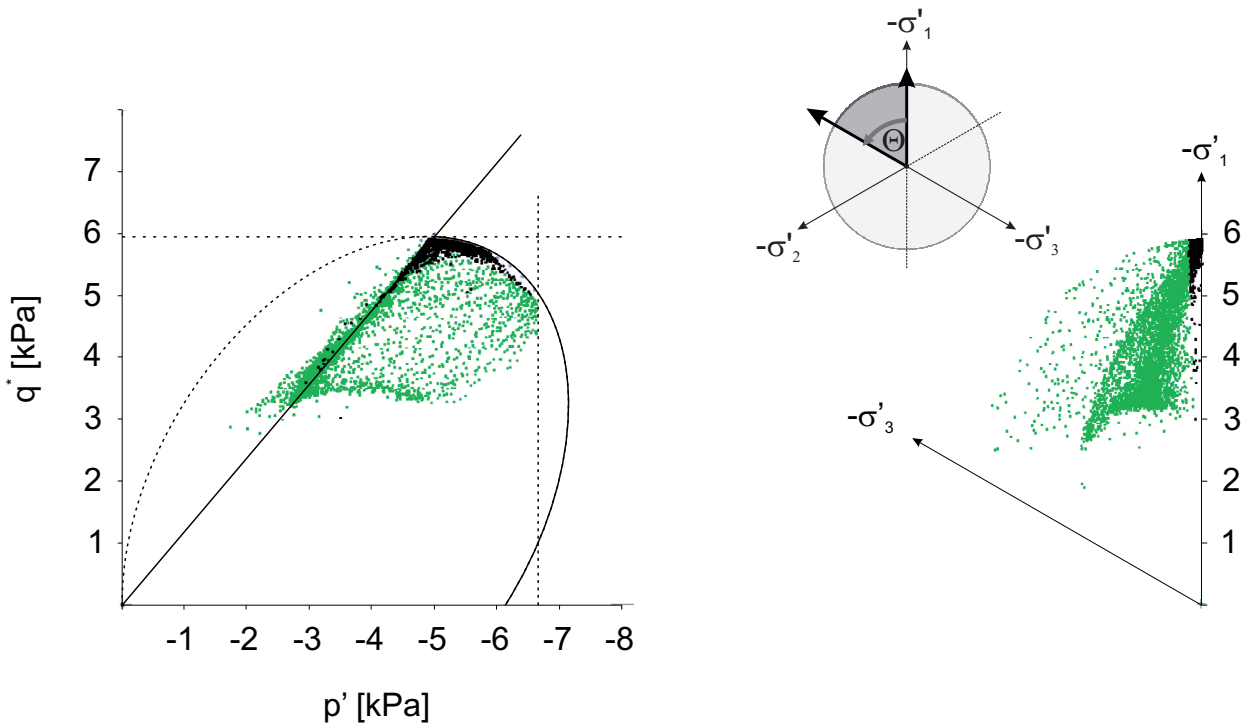

Figure 6.40: Evaluation of stress states on the yield surface in the vicinity of the cone: (left) Gauss point stresses plotted in p'-q^*-plane; (right) projection of Gauss point stresses onto the deviatoric plane for computations with the AUC model; stress states of triaxial compression are colored black, other stress states are colored green)

Chapter 7

Conclusions

A new numerical approach has been presented for quasi-static analyses of geotechnical problems involving large deformations of soil. Existing MPM codes are based on explicit time integration using a mass matrix, whereas the new quasi-static MPM code is based on implicit time integration. Several other novel extensions were made to the Material Point Method in order to improve the applicability and accuracy of the method.

- Material point based integration over finite elements has been successfully extended by Gaussian integration.
- In order to accomodate for the accurate application of boundary conditions, a mesh adjustment scheme has been devised. Instead of resetting the mesh at the end of a load step to its initial configuration, the mesh follows the movement of a relatively stiff structure such as a retaining wall. Thereby, boundaries of the structure coincide throughout the computation with boundaries of finite elements.
- The insertion and removal of (virtual) material points has been introduced to the method in order to ensure an even distribution of material points within a solid body.
- So far, most implementations of the MPM are based on regular finite element grids. For complex structures, being represented by a cloud of material points within a grid, this would require a special CAD-type preprocessor. On the other hand, existing user-friendly preprocessors can be used in combination with non-regular and non-structured finite element meshes. Furthermore, the use of non-structured meshes allows for local mesh refinement. Therefore, the presented MPM formulation applies to structured as well as non-structured meshes. Prismatic and tetrahedral low-order as well as high-order elements are considered.
- Interface elements are of great importance for analysing the interaction between soil and structures such as piles. In this study, interface elements commonly used in conventional small-strain FEM have been extended to simulate slip between soil and structure. They proved to be easy-to-use and to provide accurate results.

The quasi-static MPM can be used in combination with the 3D Plaxis-GiD pre-processor and a Plaxis 3D post-processor. Within this study, the post-processing application has been extended for visualisation of material point data. Moreover, mapping of state parameters from material points to nodes has been added to the post-processor for the

generation of shaded plots of stresses and other state parameters. In combination with the pre- and post-processor, the quasi-static MPM provides ample and relatively easy-to-use means for investigating three-dimensional geomechanical problems. It allows to investigate problems such as the simulation of on- and off-shore foundation techniques, the jacking of piles, the installation of bucket foundations and spudcans. Likewise, longterm deformation processes of soil, for example of slopes, can be investigated with this method.

Certainly, various possibilities exist to further broaden the applicability of the developed method. The following works seem to render at present the most obvious improvements:

- As yet, multi-layered soil has not been considered. This would at first require to assess possible approaches with regard to numerical accuracy.
- At present, interface elements can only be used with rigid structures. Extending the present implementation to accomodate for deforming structures requires refinement of the available mesh adjustment scheme.
- Parallelisation of the code would allow to greatly reduce the required computational time.

Application of the implemented quasi-static MPM to a series of benchmark problems proves that the presented method allows accurate simulations of large deformation problems. A deforming cantilever beam and slope have been analysed as well as a retaining wall and a block sliding across a flat surface. Furthermore, the quasi-static MPM has been validated through the simulation of cone penetration testing. Here, the relationship between cone tip resistance and the strength of undrained clay has been investigated. Results of analyses based on the Tresca model comply well with results reported by Van den Berg [56] and in great detail with a correlation assembled by Lu *et al.* [40]. Beyond validation purposes, the performed effective stress analyses provide new insight into the generation of excess pore pressures during cone penetration.

At present, the use of the Tresca model represents the state-of-the-art in numerical analyses of cone penetration in undrained clay. However, this model does not take into account that the undrained shear strength of clay depends heavily on the type of loading and that natural clay is anisotropic. With the performed computation based on the Mohr-Coulomb model, the load type dependency of the undrained shear strength is considered. The computation based on the AUC model takes into consideration the load type dependency of the undrained shear strength as well as the influence of the anisotropic fabric of clay on its undrained shear strength. Results obtained with the AUC model indicate that the failure mechanism relevant for cone penetration in undrained clay differs significantly from predictions based on the Tresca and Mohr-Coulomb model. Results show that for normally-consolidated clay, taking the average of the undrained shear strengths of triaxial compression, extension and simple shear as also done by Aas *et al.* [1] gives a good estimate of the soil's undrained shear strength relevant for cone penetration

testing. Certainly, further numerical analyses are necessary to deepen the understanding of the mechanical processes that occur during cone penetration testing.

This requires to ready the AUC model for heavily over-consolidated clay. Eventually, such analyses would lead to the development of a theoretical correlation between the soil parameters of the AUC model and a computed tip resistance. That way, in-situ measurements of tip resistance in combination with estimates of soil strength and stiffness would allow to estimate the soil's OCR. When used together with the AUC model, such a correlation would greatly simplify the numerical analyses of geotechnical problems involving undrained clay.

Bibliography

[1] G Aas, S Lacasse, T Lunne, and K Hoeg. Use of In Situ Tests for Foundation Design on Clay. In *Proceedings of In Situ Special Conference on the Use of In Situ Tests in Geotechnical Engineering*, volume 6, pages 1–30. ASCE, New York, 1986.

[2] SG Bardenhagen, JU Brackbill, and D Sulsky. The material point method for granular materials. *Computer Methods in Applied Mechanics and Engineering*, 187(3-4): 529–541, 2000. ISSN 0045-7825.

[3] SG Bardenhagen, JE Guilkey, KM Roessig, JU Brackbill, WM Witzel, and JC Foster. An improved contact algorithm for the material point method and application to stress propagation in granular material. *CMES: Computer Modeling in Engineering & Sciences*, 2(4):509–522, 2001.

[4] P Barentsen. Short description of a field testing method with cone–shaped sounding apparatus. In *Proceedings of the 1st International Conference on Soil Mechanics and Foundation Engineering*, volume 1, pages 6–10, 1936.

[5] HK Begemann. The Friction Jacket Cone as an Aide in Determining the Soil Profile. In *Proceedings of the 6th International Conference on Soil Mechanics and Foundation Engineering*, volume 1, pages 17–20. University of Toronto Press, 1965.

[6] T Belytschko, Y Krongauz, D Organ, M Fleming, and P Krysl. Meshless methods: an overview and recent developments. *Computer Methods in Applied Mechanics and Engineering*, 139(1-4):3–47, 1996.

[7] T Belytschko, WK Liu, and B Moran. *Nonlinear Finite Elements for Continua and Structures*. John Wiley and Sons Ltd, 2000.

[8] L Beuth, T Benz, PA Vermeer, CJ Coetzee, P Bonnier, and P Van Den Berg. Formulation and validation of a quasi-static Material Point Method. In *Proceedings of the 10th International Symposium on Numerical Methods in Geomechanics*, volume 10, pages 189–195. Taylor & Francis Group, 2007.

[9] L Beuth, Z Więckowski, and PA Vermeer. Solution of quasi-static large-strain problems by the material point method. *International Journal for Numerical and Analytical Methods in Geomechanics*, 35(13):1451–1465, 2011.

[10] AW Bishop. The influence of an undrained change in stress on the pore pressure in porous media of low compressibility. *Geotechnique*, 23(3):435–442, 1973.

[11] L Bjerrum. Problems of soil mechanics and construction on soft clays and structurally unstable soils (collapsible, expansive and others). In *Proceedings of the 8th International Conference on Soil Mechanics and Foundation Engineering*, volume 3, pages 111–159, 1973.

[12] RBJ Brinkgreve. *Plaxis 3D Foundation Scientific Manual Version 2*. Plaxis BV, 2007.

[13] JR Bruggeman, CN Zangar, and JHA Brahtz. *Memorandum to Chief Designing Engineer, Subject, Notes on Analytic Soil Mechanics*. US Dept. of the Interior, Bureau of Reclamation, 1939.

[14] ASK Buisman. De weerstand van paalpunten in zand. *De Ingenieur*, 50:25–28, 1935.

[15] D Burgess, D Sulsky, and JU Brackbill. Mass matrix formulation of the FLIP particle–in–cell method. *Journal of Computational Physics*, 103(1):1–15, 1992.

[16] RG Campanella, DG Gillespie, and PK Robertson. *Pore pressures during cone penetration testing*. Dept. of Civil Engineering, University of British Columbia, 1981.

[17] CJ Coetzee. *The modelling of granular flow using the particle–in–cell method*. PhD thesis, University of Stellenbosch, Republic of South Africa, 2004.

[18] CJ Coetzee, PA Vermeer, and AH Basson. The modelling of anchors using the material point method. *International Journal for Numerical and Analytical Methods in Geomechanics*, 29(9):879–895, 2005.

[19] YF Dafalias. Anisotropic critical state clay plasticity model. In *Proceedings of the 2nd International Conference on Constitutive Laws for Engineering Materials, Tucson, Arizona*, volume 1, pages 513–521. Elsevier, 1987.

[20] EA de Souza Neto, D Periæ, and DRJ Owen. *Computational methods for plasticity: theory and applications*. John Wiley and Sons Ltd, 2008.

[21] C Detournay and E Dzik. Nodal mixed discretization for tetrahedral elements. In *Proceedings of the 4th International FLAC Symposium, Numerical Modeling in Geomechanics. Minnesota Itasca Consulting Group, Inc.*, number 07-02, 2006.

[22] J Donea. Arbitrary Lagrangian–Eulerian finite element methods. *Computational Methods for Transient Analysis(A 84-29160 12-64)*, pages 473–516, 1983.

[23] JE Guilkey and JA Weiss. Implicit time integration for the material point method: Quantitative and algorithmic comparisons with the finite element method. *International Journal for Numerical Methods in Engineering*, 57(9):1323–1338, 2003.

[24] LA Hansen and GW Clough. Characterization of the Undrained Anisotropy of Clays. In *Application of Plasticity and Generalized Stress-strain in Geotechnical Engineering*, pages 253–276. ASCE New York, 1980.

[25] FH Harlow. The particle–in–cell computing method for fluid dynamics. *Methods in Computational Physics*, 3:319–343, 1964.

[26] DJ Henkel. The shear strength of saturated remolded clays. In *Proceedings of the Research Conference on Shear Strength of Cohesive Soils*, pages 533–554. ASCE New York, 1960.

[27] R Hill. Some basic principles in the mechanics of solids without a natural time. *Journal of the Mechanics and Physics of Solids*, 7(3):209–225, 1959.

[28] Y Hu and MF Randolph. A practical numerical approach for large deformation problems in soil. *International Journal for Numerical and Analytical Methods in Geomechanics*, 22(5):327–350, 1998.

[29] J Huétink. Analysis of Metal Forming Processes Based on a Combined Eulerian–Lagrangian Finite Element Formulation. *Numerical Methods in Industrial Forming Processes*, pages 501–509, 1982.

[30] J Huétink. *On the simulation of thermo–mechanical forming processes*. PhD thesis, University of Twente, 1986.

[31] TJR Hughes, WK Liu, and TK Zimmermann. Lagrangian–Eulerian finite element formulation for incompressible viscous flows. *Computer Methods in Applied Mechanics and Engineering*, 29(3):329–349, 1981.

[32] TK Huizinga. Application of results of deep penetration tests to foundation piles. In *Proceedings of the Building Research Congress*, volume 1, pages 173–179, 1951.

[33] M Jamiolkowski, CC Ladd, J Germaine, and R Lancellotta. New developments in field and lab testing of soils. In *Proceedings of the 11th International Conference on Soil Mechanics and Foundation Engineering*, volume 1, pages 57–153, 1985.

[34] WT Koiter. *General theorems for elastic–plastic solids*. North–Holland, 1960.

[35] KH Korhonen and M Lojander. Yielding of Perno clay. In *Proceedings of the 2nd International Conference on Constitutive Laws for Engineering Materials, Tucson, Arizona*, volume 2, pages 1249–1255. Elsevier, 1987.

[36] M Leoni, M Karstunen, PA Vermeer, EC MRTN-CT, et al. Anisotropic creep model for soft soils. *Geotechnique*, 58(3):215–266, 2009.

[37] S Li and WK Liu. Meshfree and particle methods and their applications. *Applied Mechanics Reviews*, 55:1–34, 2002.

[38] GR Liu. *Mesh free methods: moving beyond the finite element method*. CRC, 2009.

[39] WK Liu, T Belytschko, and H Chang. An arbitrary Lagrangian–Eulerian finite element method for path–dependent materials. *Computer Methods in Applied Mechanics and Engineering*, 58(2):227–245, 1986.

[40] Q Lu, MF Randolph, Y Hu, and IC Bugarski. A numerical study of cone penetration in clay. *Geotechnique*, 54(4):257–267, 2004.

[41] T Lunne, PK Robertson, and JJM Powell. *Cone penetration testing in geotechnical practice*. Taylor & Francis Group, 1997. ISBN 041923750X.

[42] LE Malvern. *Introduction to the Mechanics of a Continuous Medium*. Prentice–Hall, 1969.

[43] RM McMeeking and JR Rice. Finite–element formulations for problems of large elastic–plastic deformation. *International Journal of Solids and Structures*, 11(5):601–616, 1975.

[44] JM Ortega and WC Rheinboldt. *Iterative solution of nonlinear equations in several variables*. Number 30 in 3. Society for Industrial Mathematics, 2000.

[45] PK Robertson and RG Campanella. Interpretation of cone penetration tests. Part II: Clay. *Canadian Geotechnical Journal*, 20(4):734–745, 1983.

[46] JA Schneider, MF Randolph, PW Mayne, and NR Ramsey. Analysis of factors influencing soil classification using normalized piezocone tip resistance and pore pressure parameters. *Journal of Geotechnical and Geoenvironmental Engineering*, 134:1569, 2008.

[47] A Schofield and P Wroth. *Critical state soil mechanics*. McGraw–Hill New York, 1968.

[48] D Sheng. Finite element modelling of penetration problems in geomechanics. In *Proceedings of the 10th International Symposium on Numerical Models in Geomechanics*, volume 10, pages 239–245. Taylor & Francis Group, 2007.

[49] P Silvester and McGill Univ Montreal (Quebec). *Symmetric quadrature formulae for simplexes*. Defense Technical Information Center, 1969.

[50] D Stolle, I Jassim, and PA Vermeer. Simulation of Incompressible Problems in Geomechanics. *Computer Methods in Mechanics*, pages 347–361, 2010.

[51] D Sulsky and HL Schreyer. Axisymmetric form of the material point method with applications to upsetting and Taylor impact problems. *Computer Methods in Applied Mechanics and Engineering*, 139(1-4):409–429, 1996.

[52] D Sulsky, Z Chen, and HL Schreyer. A particle method for history–dependent materials. *Computer Methods in Applied Mechanics and Engineering*, 118(1-2):179–196, 1994.

[53] D Sulsky, SJ Zhou, and HL Schreyer. Application of a particle–in–cell method to solid mechanics. *Computer Physics Communications*, 87(1-2):236–252, 1995.

[54] D Sulsky, HL Schreyer, K Peterson, R Kwok, and M Coon. Using the material point method to model sea ice dynamics. *Journal of Geophysical Research*, 112(C2):C02S90, 2007.

[55] K Terzaghi, RB Peck, and G Mesri. *Soil mechanics in engineering practice*. Wiley–Interscience, 1996.

[56] P Van den Berg. *Analysis of soil penetration*. PhD thesis, Technical University Delft, The Netherlands, 1994.

[57] J van Kan, A Segal, and F Vermolen. *Numerical methods in scientific computing*. VSSD, 2005.

[58] H Van Langen. *Numerical analysis of soil–structure interaction*. PhD thesis, Technical University Delft, The Netherlands, 1991.

[59] H Van Langen and PA Vermeer. Automatic step size correction for non–associated plasticity problems. *International Journal for Numerical Methods in Engineering*, 29(3): 579–598, 1990.

[60] PA Vermeer. *PLAXIS 2D Reference Manual Version 5*. Balkema, Rotterdam / Brookfield, 1993.

[61] PA Vermeer. Elastoplastic Soil Modelling COMMAS E7. Institute of Geotechnical Engineering University of Stuttgart, June 2011. Lecture notes.

[62] PA Vermeer and JAM Teunissen. Internal communications, 2010 – 2011.

[63] PA Vermeer and H Van Langen. Soil collapse computations with finite elements. *Archive of Applied Mechanics*, 59(3):221–236, 1989.

[64] PA Vermeer, Y Yuan, L Beuth, and P Bonnier. Application of interface elements with the Material Point Method. In *Proceedings of the 18th International Conference on Computer Methods in Mechanics*, volume 18, pages 477–478. Polish Academy of Sciences, 2009.

[65] PA Vermeer, I Jassim, and F Hamad. Need and performance of a new undrained clay model, 2010.

[66] SJ Wheeler, A Näätänen, M Karstunen, and M Lojander. An anisotropic elastoplastic model for soft clays. *Canadian Geotechnical Journal*, 40(2):403–418, 2003.

[67] Z Więckowski. The material point method in large strain engineering problems. *Computer Methods in Applied Mechanics and Engineering*, 193(39-41):4417–4438, 2004.

[68] Z Więckowski, SK Youn, and JH Yeon. A particle–in–cell solution to the silo discharging problem. *International Journal for Numerical Methods in Engineering*, 45(9): 1203–1225, 1999. ISSN 1097-0207.

[69] II York, R Allen, D Sulsky, and HL Schreyer. The material point method for simulation of thin membranes. *International Journal for Numerical Methods in Engineering*, 44(10):1429–1456, 1999. ISSN 1097-0207.

Appendix A

Finite element specifications

A.1 Specification of 15-noded prismatic elements

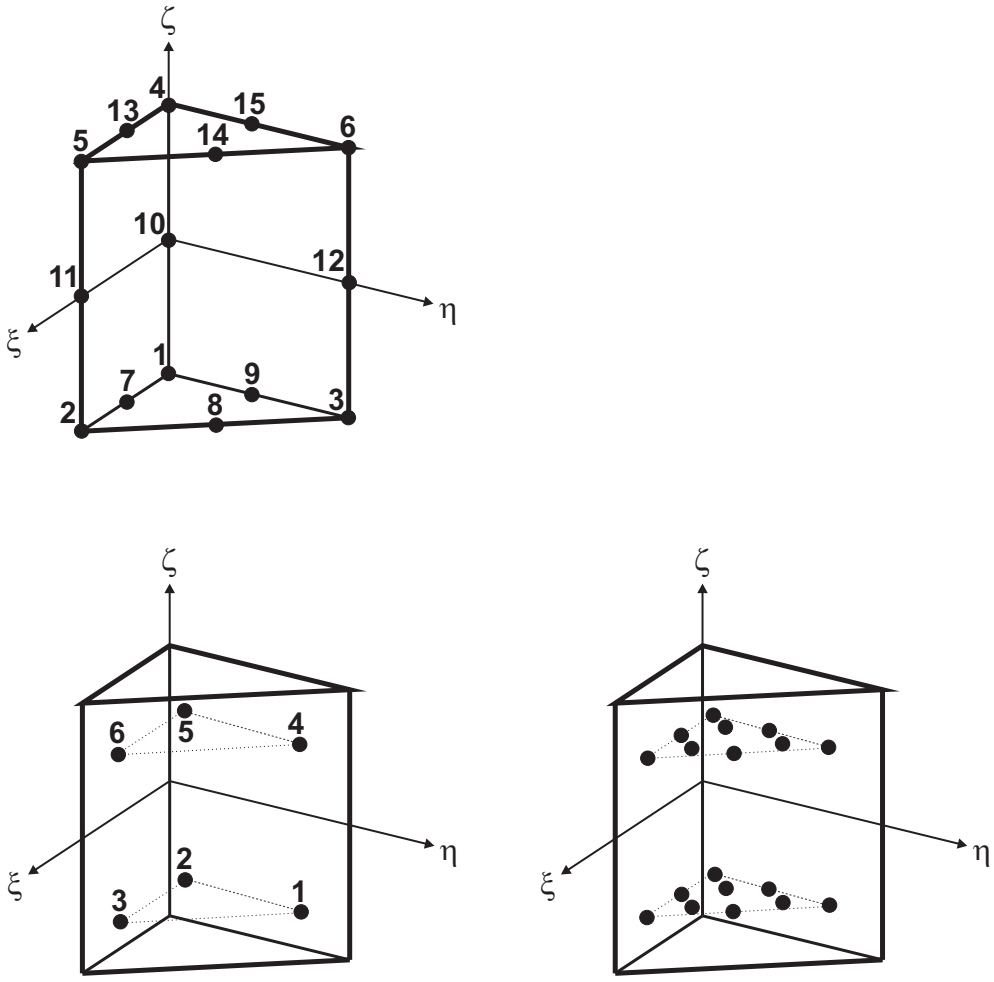

Figure A.1: 15-noded prismatic element: (top) local numbering and positioning of nodes; (bottom left) of Gaussian integration points; (bottom right) initial positioning of material points

The shape functions N_i of the 15 nodes and the interpolation functions H_j used to map data from the 6 Gaussian integration points to material points are as follows. The indices relate to the local numbering of nodes, Gaussian integration points respectively, as specified in Figure A.1.

$$
\begin{aligned}
N_1 &= -\left(1-\xi-\eta\right)\left(1-\zeta\right)\left(2\,\xi+2\,\eta+\zeta\right)/2\\
N_2 &= -\xi\left(1-\zeta\right)\left(2-2\,\xi-\zeta\right)/2\\
N_3 &= -\eta\left(1-\zeta\right)\left(2-2\,\eta+\zeta\right)/2\\
N_4 &= -\left(1-\xi-\eta\right)\left(1+\zeta\right)\left(2\,\xi+2\,\eta-\zeta\right)/2\\
N_5 &= -\xi\left(1+\zeta\right)\left(2-2\,\xi+\zeta\right)/2\\
N_6 &= -\eta\left(1+\zeta\right)\left(2-2\,\eta-\zeta\right)/2\\
N_7 &= \left(1-\xi-\eta\right)\xi\left(1-\zeta\right)2\\
N_8 &= \xi\,\eta\left(1-\zeta\right)2\\
N_9 &= \eta\left(1-\xi-\eta\right)\left(1-\zeta\right)2\\
N_{10} &= \left(1-\xi-\eta\right)\left(1-\zeta\right)\left(1+\zeta\right)\\
N_{11} &= \xi\left(1-\zeta\right)\left(1+\zeta\right)\\
N_{12} &= \eta\left(1-\zeta\right)\left(1+\zeta\right)\\
N_{13} &= \left(1-\xi-\eta\right)\xi\left(1+\zeta\right)2\\
N_{14} &= \xi\,\eta\left(1+\zeta\right)2\\
N_{15} &= \eta\left(1-\xi-\eta\right)\left(1+\zeta\right)2
\end{aligned}
$$

$$
\begin{aligned}
H_1 &= -\frac{1}{6}+\eta+\frac{1}{2\sqrt{3}}\,\xi-\sqrt{3}\,\eta\,\xi\\
H_2 &= \frac{5}{6}-\zeta-\eta-\frac{5}{2\sqrt{3}}\,\xi+\sqrt{3}\,\zeta\,\xi+\sqrt{3}\,\eta\,\xi\\
H_3 &= -\frac{1}{6}+\zeta+\frac{1}{2\sqrt{3}}\,\xi-\sqrt{3}\,\zeta\,\xi\\
H_4 &= -\frac{1}{6}+\eta-\frac{1}{2\sqrt{3}}\,\xi+\sqrt{3}\,\eta\,\xi\\
H_5 &= \frac{5}{6}-\zeta-\eta+\frac{5}{2\sqrt{3}}\,\xi-\sqrt{3}\,\zeta\,\xi-\sqrt{3}\,\eta\,\xi\\
H_6 &= -\frac{1}{6}+\zeta-\frac{1}{2\sqrt{3}}\,\xi+\sqrt{3}\,\zeta\,\xi
\end{aligned}
$$

Gauss points	ξ	η	ζ	Weight ω
1	$1/6$	$2/3$	$-1/\sqrt{3}$	$1/6$
2	$1/6$	$1/6$	$-1/\sqrt{3}$	$1/6$
3	$2/3$	$1/6$	$-1/\sqrt{3}$	$1/6$
4	$1/6$	$2/3$	$1/\sqrt{3}$	$1/6$
5	$1/6$	$1/6$	$1/\sqrt{3}$	$1/6$
6	$2/3$	$1/6$	$1/\sqrt{3}$	$1/6$
Material points				
1	$1/9$	$1/9$	$-1/2$	$1/18$
2	$2/9$	$2/9$	$-1/2$	$1/18$
3	$4/9$	$1/9$	$-1/2$	$1/18$
4	$1/9$	$4/9$	$-1/2$	$1/18$
5	$5/9$	$2/9$	$-1/2$	$1/18$
6	$2/9$	$5/9$	$-1/2$	$1/18$
7	$4/9$	$4/9$	$-1/2$	$1/18$
8	$7/9$	$1/9$	$-1/2$	$1/18$
9	$1/9$	$7/9$	$-1/2$	$1/18$
10	$1/9$	$1/9$	$1/2$	$1/18$
11	$2/9$	$2/9$	$1/2$	$1/18$
12	$4/9$	$1/9$	$1/2$	$1/18$
13	$1/9$	$4/9$	$1/2$	$1/18$
14	$5/9$	$2/9$	$1/2$	$1/18$
15	$2/9$	$5/9$	$1/2$	$1/18$
16	$4/9$	$4/9$	$1/2$	$1/18$
17	$7/9$	$1/9$	$1/2$	$1/18$
18	$1/9$	$7/9$	$1/2$	$1/18$

Table A.1: Local coordinates and weights of Gaussian integration points and initial local coordinates and weights of material points for 15-noded prismatic elements

A.2 Specification of 10-noded tetrahedral elements

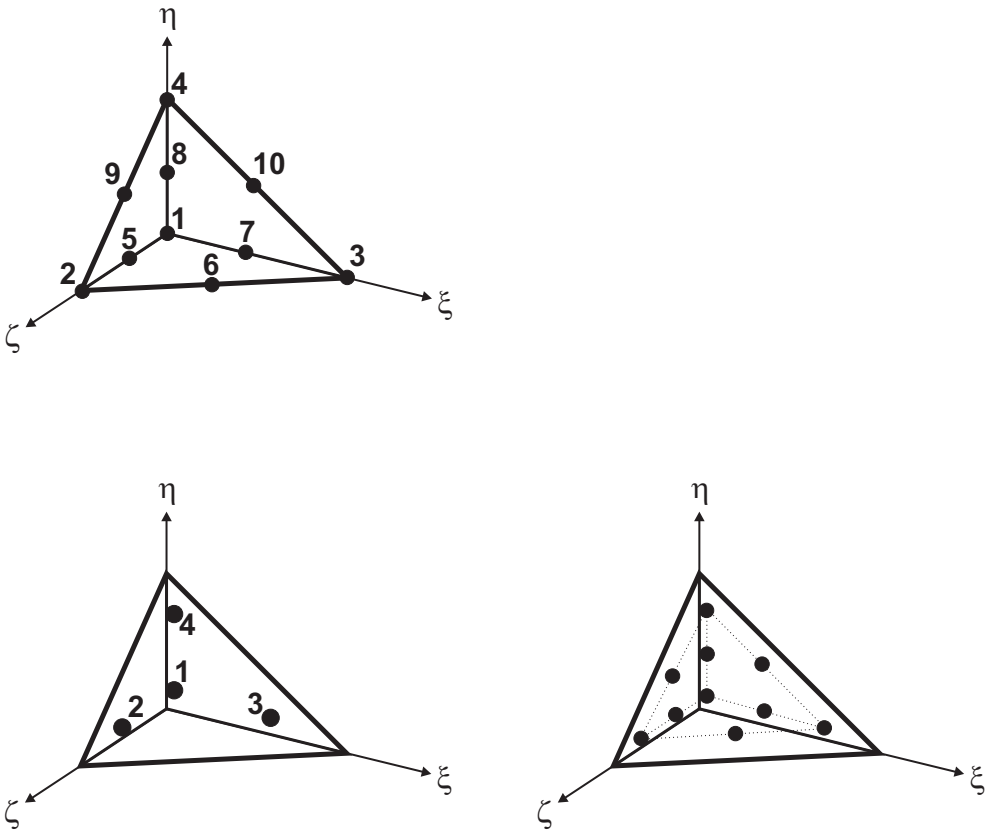

Figure A.2: 10-noded tetrahedral element: (top) local numbering and positioning of nodes; (bottom left) of Gaussian integration points; (bottom right) initial positioning of material points

The shape functions N_i of the 10 nodes and the interpolation functions H_j used to map data from the 4 Gaussian integration points to material points are as follows. The indices relate to the local numbering of nodes, Gaussian integration points respectively, as specified in Figure A.2.

$$
\begin{aligned}
N_1 &= (1 - \xi - \eta - \zeta)\,(1 - 2\xi - 2\eta - 2\zeta) \\
N_2 &= \zeta\,(2\zeta - 1) \\
N_3 &= \xi\,(2\xi - 1) \\
N_4 &= \eta\,(2\eta - 1) \\
N_5 &= 4\zeta\,(1 - \xi - \eta - \zeta) \\
N_6 &= 4\xi\zeta \\
N_7 &= 4\xi\,(1 - \xi - \eta - \zeta) \\
N_8 &= 4\eta\,(1 - \xi - \eta - \zeta) \\
N_9 &= 4\eta\zeta \\
N_{10} &= 4\xi\eta
\end{aligned}
$$

$$
\begin{aligned}
H_1 &= 5\sqrt{5}\left(\frac{3}{20} + \frac{1}{20\sqrt{5}}\right) - \sqrt{5}\,\xi - \sqrt{5}\,\eta - \sqrt{5}\,\zeta \\
H_2 &= 5\sqrt{5}\left(-\frac{1}{20} + \frac{1}{20\sqrt{5}}\right) + \sqrt{5}\,\zeta \\
H_3 &= 5\sqrt{5}\left(-\frac{1}{20} + \frac{1}{20\sqrt{5}}\right) + \sqrt{5}\,\xi \\
H_4 &= 5\sqrt{5}\left(-\frac{1}{20} + \frac{1}{20\sqrt{5}}\right) + \sqrt{5}\,\eta
\end{aligned}
$$

Gauss points	ξ	η	ζ	Weight ω
1	$1/4 - 1/20\sqrt{5}$	$1/4 - 1/20\sqrt{5}$	$1/4 - 1/20\sqrt{5}$	$1/24$
2	$1/4 - 1/20\sqrt{5}$	$1/4 - 1/20\sqrt{5}$	$1/4 + 3/20\sqrt{5}$	$1/24$
3	$1/4 + 3/20\sqrt{5}$	$1/4 - 1/20\sqrt{5}$	$1/4 - 1/20\sqrt{5}$	$1/24$
4	$1/4 - 1/20\sqrt{5}$	$1/4 + 3/20\sqrt{5}$	$1/4 - 1/20\sqrt{5}$	$1/24$
Material points				
1	$1/4 - 1/20\sqrt{5}$	$1/4 - 1/20\sqrt{5}$	$1/4 - 1/20\sqrt{5}$	$1/60$
2	$1/4 - 1/20\sqrt{5}$	$1/4 - 1/20\sqrt{5}$	$1/4 + 3/20\sqrt{5}$	$1/60$
3	$1/4 + 3/20\sqrt{5}$	$1/4 - 1/20\sqrt{5}$	$1/4 - 1/20\sqrt{5}$	$1/60$
4	$1/4 - 1/20\sqrt{5}$	$1/4 + 3/20\sqrt{5}$	$1/4 - 1/20\sqrt{5}$	$1/60$
5	$1/4 - 1/20\sqrt{5}$	$1/4 - 1/20\sqrt{5}$	$1/4 + 1/20\sqrt{5}$	$1/60$
6	$1/4 + 1/20\sqrt{5}$	$1/4 - 1/20\sqrt{5}$	$1/4 - 1/20\sqrt{5}$	$1/60$
7	$1/4 - 1/20\sqrt{5}$	$1/4 + 1/20\sqrt{5}$	$1/4 - 1/20\sqrt{5}$	$1/60$
8	$1/4 + 1/20\sqrt{5}$	$1/4 - 1/20\sqrt{5}$	$1/4 + 1/20\sqrt{5}$	$1/60$
9	$1/4 - 1/20\sqrt{5}$	$1/4 + 1/20\sqrt{5}$	$1/4 + 1/20\sqrt{5}$	$1/60$
10	$1/4 + 1/20\sqrt{5}$	$1/4 + 1/20\sqrt{5}$	$1/4 - 1/20\sqrt{5}$	$1/60$

Table A.2: Local coordinates and weights of Gaussian integration points and initial local coordinates and weights of material points for 10-noded tetrahedral elements

A.3 Specification of 4-noded tetrahedral elements

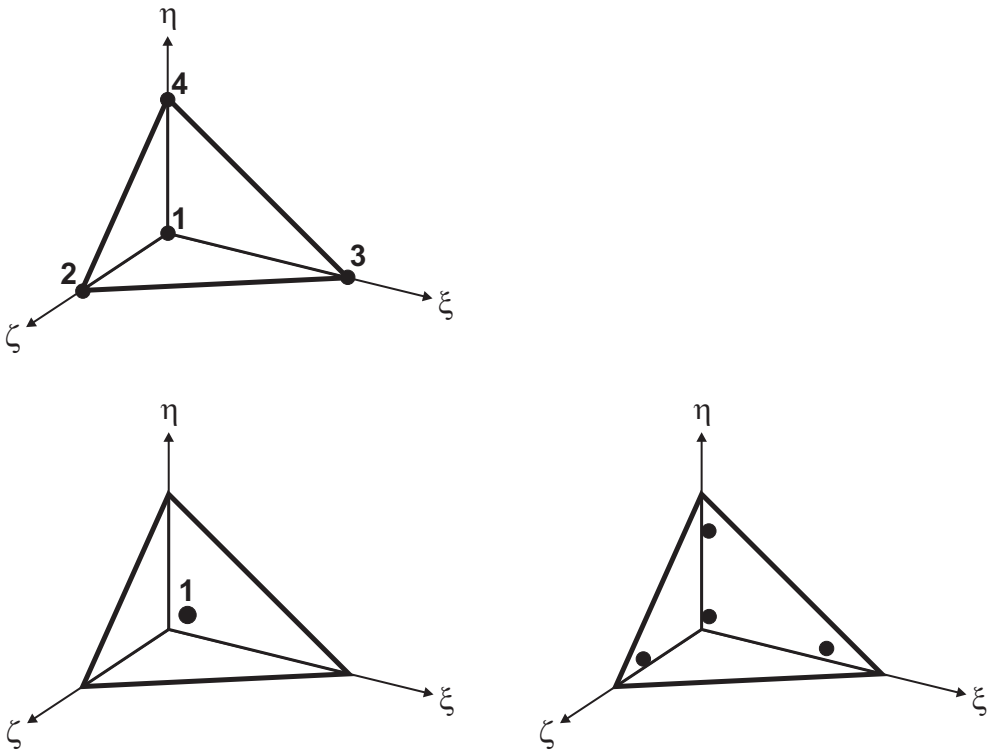

Figure A.3: 4-noded tetrahedral element: (top) local numbering and positioning of nodes; (bottom left) of Gaussian integration points; (bottom right) initial positioning of material points

The shape functions N_i of the 4 nodes are as follows. The index relates to the local numbering of nodes as specified in Figure A.3.

$$
\begin{aligned}
N_1 &= (1 - \xi - \eta - \zeta) \\
N_2 &= \zeta \\
N_3 &= \xi \\
N_4 &= \eta
\end{aligned}
$$

The initial locations and weights of the 4 material points coincide with those of the Gaussian integration points of the 10-noded tetrahedral element.

Gauss point	ξ	η	ζ	Weight ω
1	$1/4$	$1/4$	$1/4$	$1/6$

Table A.3: Local coordinates and weight of the Gaussian integration point for 4-noded tetrahedral elements

A.4 Specification of 6-noded interface elements

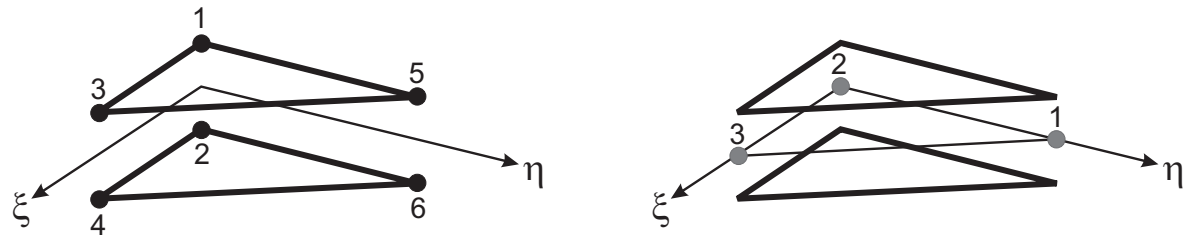

Figure A.4: 6-noded interface element: (left) local numbering and positioning of nodes and (right) of Newton-Cotes integration points

The shape functions of the 6 nodes are as follows. The index relates to the local numbering of nodes as specified in Figure A.4.

$$
\begin{aligned}
N_{1/2} &= (1 - \xi - \eta) \\
N_{3/4} &= \xi \\
N_{5/6} &= \eta
\end{aligned}
$$

Evaluation of the shape functions at the location of integration points gives

$$
\begin{aligned}
N_{1/2}(IP_1) &= 0 & N_{1/2}(IP_2) &= 1 & N_{1/2}(IP_3) &= 0 \\
N_{3/4}(IP_1) &= 0 & N_{3/4}(IP_2) &= 0 & N_{3/4}(IP_3) &= 1 \\
N_{5/6}(IP_1) &= 1 & N_{5/6}(IP_2) &= 0 & N_{5/6}(IP_3) &= 0
\end{aligned}
$$

Integration points	ξ	η	Weight ω
1	0.0	1.0	1/6
2	0.0	0.0	1/6
3	1.0	0.0	1/6

Table A.4: Local coordinates and weights of Newton-Cotes integration points for 6-noded interface elements [49]

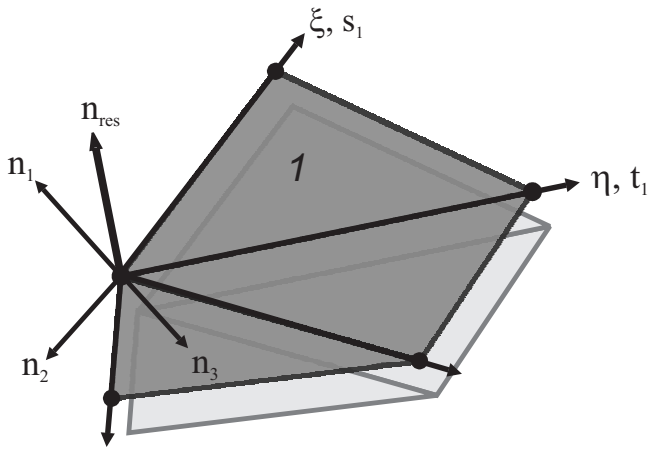

Figure A.5: Determination of the normal vector of interface elements

Computation of the normal vectors and integration weights of interface elements At first, the normal vector of an interface element is determined as illustrated in Figure A.5 for an element number 1. Because the geometry of interface elements having no real width corresponds to the one of triangular elements, the normal vector $\boldsymbol{n}_1$ can be determined from the vectors $\boldsymbol{s}_1$ and $\boldsymbol{t}_1$ tangential to the element surface by means of

$$\boldsymbol{n}_1 \;=\; \boldsymbol{s}_1 \times \boldsymbol{t}_1 \tag{A.1}$$

where the tangential vectors can be computed from

$$\boldsymbol{s}_1 \;=\; \sum_{j=1}^{n_{nodes}} \frac{\partial N_{ij}}{\partial \xi} \boldsymbol{x}_j \qquad\qquad \boldsymbol{t}_1 \;=\; \sum_{j=1}^{n_{nodes}} \frac{\partial N_{ij}}{\partial \eta} \boldsymbol{x}_j \tag{A.2}$$

Here, n_{nodes} denotes the number of nodes j of one element face, $\boldsymbol{x}_j$ are the coordinates of node j and N_{ij} is the shape function value of node j evaluated at a point i.

The weight of an integration point i is then computed from the norm of the normal vector and the integration weight ω_i by

$$\Delta S_i \;=\; \omega_i \,|\, \boldsymbol{n}_1 \,| \tag{A.3}$$

Curved slip surfaces are taken into account by adjusting the normal vectors at interface dual nodes and thus Newton-Cotes integration points. This is done by computing a new normal vector $\boldsymbol{n}_{res}$ at each interface node as the norm of the resultant of the normal vectors of all interface elements connected to a considered node.

Curriculum vitæ

8 July 1975	Born in Langen, Germany
1995 – 2004	Graduate program in civil engineering at the Technical University of Kaiserslautern, graduation as Diplomingenieur
1997	Intermediate Diploma
1997 – 1998	Study stay in France at the ESITC Cachan
1998 – 2000	Student Assistant at the Chair of Information Science in Civil Engineering
2004 – 2006	Software Developer at Plaxis B.V. in Delft
2006 – 2011	Scientific Assistant at the Institute of Geotechnical Engineering, University of Stuttgart
2009 – 2011	Secondment in the frame of the EU funded research project GEO-INSTALL at Deltares in Delft
since 2012	Software Developer at Plaxis B.V. in Delft
14. 02. 2012	Graduation